Proceedings of the

10th Patras Workshop On Axions, WIMPs and WISPs

June 29 – July 4, 2014
CERN Geneva
Switzerland

Editors:
Emmanuel Tsesmelis
Marios Maroudas

VERLAG DEUTSCHES ELEKTRONEN-SYNCHROTRON

Proceedings of the

10th Patras Workshop on Axions, WIMPs and WISPs

PATRAS 2014

June 29 – July 4, 2014

CERN Geneva, Switzerland

Editors: Emmanuel Tsesmelis, Marios Maroudas

Verlag Deutsches Elektronen-Synchrotron

Impressum

Proceedings of the 10th Patras Workshop on Axions, WIMPs and WISPs (PATRAS 2014)
June 29 – July 4, 2014, CERN Geneva, Switzerland

Conference homepage
`http://axion-wimp2014.desy.de/`

Slides at
`http://axion-wimp2014.desy.de/e222615/`

Online proceedings at
`http://www-library.desy.de/confprocs.html`

Editors:
Emmanuel Tsesmelis and Marios Maroudas
December 2014
DESY-PROC-2014-03
ISBN 978-3-935702-59-1
ISSN 1435-8077

Published by
Verlag Deutsches Elektronen-Synchrotron
Notkestraße 85
22607 Hamburg
Germany

Printed by
Kopierstelle Deutsches Elektronen-Synchrotron

Organizing Committee

Vassilis Anastassopoulos and Konstantin Zioutas
Department of Physics
University of Patras
26504 Patras
Greece

Ignatios Antoniadis
Theory Division
CERN
CH-1211 Geneva 23
Switzerland

Laura Baudis
Physik Institut
University of Zurich
Winterthurerstr. 190
8057 Zurich
Switzerland

Joerg Jaeckel
Institut für theoretische Physik
Universität Heidelberg
Philosophenweg 16
69120 Heidelberg
Germany

Axel Lindner and Andreas Ringwald
Deutsches Elektronen Synchrotron (DESY)
Notkestraße 85
D-22607 Hamburg
Germany

Marc Schumann
Albert Einstein Center for Fundamental Physics
University of Bern
Sidlerstrasse 5
3012 Bern
Switzerland

Emmanuel Tsesmelis (Chairman)
CERN CH-1211
Genève 23
Switzerland

Conference Secretary and Local Organization

Ulla Tihinen
CERN CH-1211
Genève 23
Switzerland

Barbara Wittmann
Deutsches Elektronen Synchrotron (DESY)
Notkestraße 85
D-22607 Hamburg
Germany

Marios Maroudas
Panachaikou 23
26224 Patras
Greece

10th Patras Workshop on Axions, WIMPs and WISPs

29th June - 4th July 2014

CERN Geneva, Switzerland

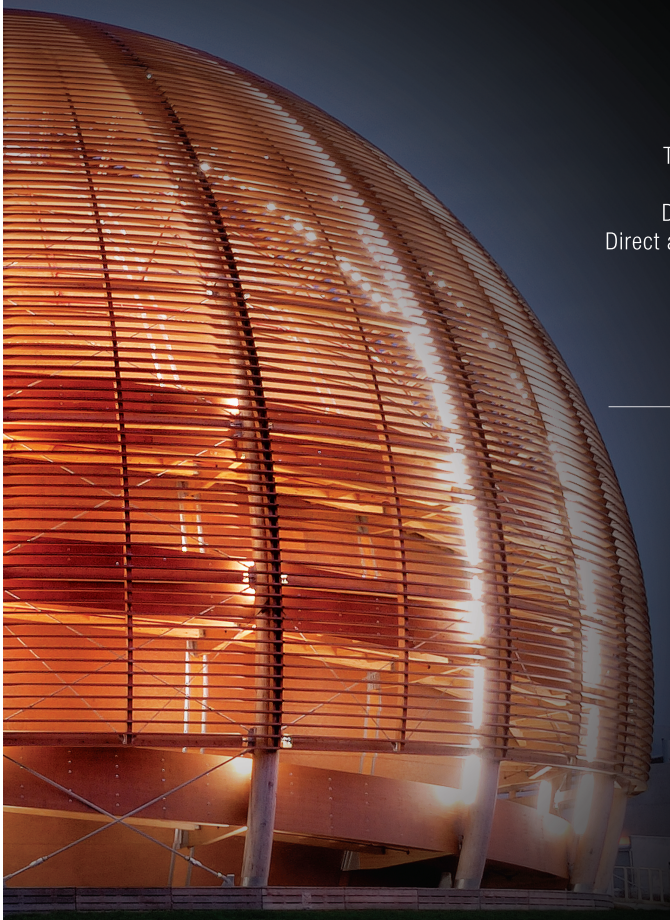

The physics case for WIMPS, Axions, WISPs
Searches for Hidden Sector Photons
Direct and indirect searches for Dark Matter
Direct and indirect searches for Axions and WISPs
Signals from astrophysical sources
Review of collider experiments
New theoretical developments
Scalar Dark Energy, theory and experiment

Organizing committee:
Vassilis Anastassopoulos (University of Patras)
Ignatios Antoniadis (CERN)
Laura Baudis (University of Zurich)
Joerg Jaeckel (University of Heidelberg)
Axel Lindner (DESY)
Andreas Ringwald (DESY)
Marc Schumann (University of Bern)
Emmanuel Tsesmelis (CERN, Chairman)
Konstantin Zioutas (University of Patras & CERN)

Conference secretary:
Ulla Tihinen (CERN)

This workshop is supported by

http://axion-wimp.desy.de

CERN | DESY | AEC UNIVERSITY OF BERN | UNIVERSITY OF PATRAS | UNIVERSITY OF HEIDELBERG | UNIVERSITÄT ZÜRICH | CAST

Preface

The search for the elusive dark matter particles continues. WIMPs and axions remain the two most promising candidates and the worldwide efforts to spot these (or eventually other) particles remain among the biggest challenges in physics. We do not know when the breakthrough will happen but we do know already that we are living in an exciting time. After all, our active astroparticle physics community is aiming for nothing less than to find out how our Universe works, from its early epoch until the present time. This also includes dark energy, which remains among the biggest mysteries in physics even though much effort and many ideas are put forward to decipher its nature. Laboratory experiments along with astrophysical observations, as well as new developments in theory, are pushing to unravel the unknown.

These exciting topics and many more important aspects of particle and astroparticle physics were openly discussed between experimentalists and theorists at the 10th Patras Workshop on Axions, WIMPs, and WISPs. The event took place from June 29 - July 4, 2014 at CERN, the actual birth place of this workshop series. As in the previous years, it was a very fruitful and lively meeting in an inspiring and cooperative atmosphere, which allowed for many open and constructive discussions also on controversial topics.

The spirit of the workshop and its atmosphere cannot be brought to paper, but many of its scientific highlights are collected in these proceedings. We are looking forward to the 11th Patras Workshop, which will be held in Zaragoza (Spain) from June 21 - 26, 2015.

Marc Schumann, Emmanuel Tsesmelis (Chairman) and Konstantin Zioutas

Acknowledgements

The organizers would like to thank the University of Patras, CAST, DESY, CERN, the IPPP Durham, the University of Zurich and the AEC of the University of Bern for support. Special thanks also to Soultana Kotsopoulou, Marios Maroudas and Yannis Tsagris for their real help. All participants recognized the perfect organization and full engagement of Ulla Tihinen (CERN) for the workshop. The support by Barbara Wittmann (DESY) for creating the online presence of the conference is also acknowledged.

The organizing committee

Contents

Chapter 1

WIMP Dark Matter

Observations are confirming the WIMP paradigm

Csaba Balázs[1], *Tong Li*[1], *and Jayden L. Newstead*[2]

[1]Centre of Excellence for Particle Physics, Monash University, Melbourne, VIC 3800, Australia
[2]Department of Physics, Arizona State University, Tempe, Arizona 85287, USA

DOI: http://dx.doi.org/10.3204/DESY-PROC-2014-03/balazs_csaba

We present a model independent analysis of thermal dark matter constraining its mass and interaction strengths with data from astro- and particle physics experiments. We show that the observationally favored dark matter particle mass region is 1-1000 GeV with effective interactions that have a cut-off in the range of 1-10 TeV.

1 Introduction

We present the results of a model independent analysis of dark matter constraining its mass and interaction strengths with data from astro- and particle physics experiments. We use the effective field theory approach to describe interactions of thermal dark matter particles of the following types: real and complex scalars, Dirac and Majorana fermions, and vector bosons. Using Bayesian inference we calculate posterior probability distributions for the mass and interaction strengths for the various spin particles. The observationally favoured dark matter particle mass region is 1-1000 GeV with effective interactions that have a cut-off at 1-10 TeV. This mostly comes from the requirement that the thermal abundance of dark matter not exceed the observed value. Thus thermal dark matter in the light of present data implies new physics most likely under 10 TeV.

2 The effective field theory framework

We follow a minimalistic, model independent approach regarding the microscopic properties of dark matter. Relying on a few major tenets, we assume

- a single dark matter particle,
- annihilating with its anti-particle,
- reaching its relic abundance by thermal freeze-out.

We represent the interactions between the dark matter particle and standard fermions with effective, four particle vertices depicted in Figure 1. These interactions can be represented with a Lagrangian containing all Lorentz and gauge invariant operators of dimension-5 for real or complex scalar and vector boson, and dimension-6 for Dirac or Majorana fermion dark matter particles

$$\mathcal{L}_\chi = \sum_{i,f} C_i \mathcal{O}_{i,f}. \tag{1}$$

Here C_i and $\mathcal{O}_{i,f}$ denote a set of coefficients and operators relevant to different structures of χ interacting with SM fields. The explicit expressions of C_i and $\mathcal{O}_{i,f}$ are shown in Table 1 for

the various spin dark matter particles. For generality we couple the dark matter field to over all standard fermions f with the exception of the neutrinos.

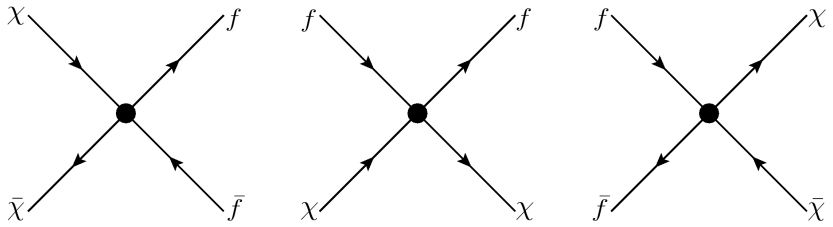

Figure 1: Effective interaction between a dark matter particle χ, its anti-particle $\bar{\chi}$, a standard matter particle f, and its anti-matter partner $\bar{f}$. The three different orientation of the same diagram shows the three different ways of observing dark matter: indirect detection (left), direct detection (middle) and collider production (right).

3 Constraint on the scale of new physics

Using the effective field theory framework the thermally averaged annihilation cross section of dark matter into standard fermions can approximately be calculated using

$$\langle \sigma_{\rm ann} v_{\rm rel} \rangle_{avg} = \frac{1}{\sqrt{8\pi}} \int_2^\infty \sigma_{\chi\chi\to f\bar{f}}(x) x^{3/2} (x^2-4) F_{x_F}(x) dx, \tag{2}$$

where the function $F_{x_F}(x)$ and the total annihilation cross section $\sigma_{\chi\chi\to f\bar{f}}$ are given in Ref. [1] for the various dark matter candidates we consider here.

With increasing dark matter mass and interaction cut-off scales either the relic abundance becomes too high or the resulting theory cannot be described as effective. There is thus a maximal cut-off scale at which the correct relic density can be satisfied in the effective field theory framework.

Model	m_χ (GeV)	Λ (GeV)
DF	3.0×10^4	4.7×10^3
MF	8.8×10^4	1.4×10^4
CS	4.5×10^4	7.1×10^3
RS	1.1×10^4	1.6×10^3
VB	4.8×10^4	7.7×10^3

Table 2: The maximal values for the dark matter mass and cut-off scale satisfying relic density constraint in the five considered models.

To find the approximate upper limit of the cut-off scale, we take a universal Λ in all operators for a given dark matter candidate. Then we perform the integration in Eq. (2) with a typical $x_F \equiv m_\chi/T = 30$ with T being the freeze out temperature. In order to guarantee the validity of the effective field theory framework, the cut-off scale has to be larger than the dark matter mass, i.e. $\Lambda > \frac{m_\chi}{2\pi}$. We thus set $m_\chi = 2\pi\Lambda$ in the calculation. This choice also gives the allowed upper limit of m_χ. The obtained upper limits of universal Λ and m_χ for the various dark matter models are summarized in Table 2. One can see that the upper limits of Λ are at the level of $10^3 - 10^4$ GeV with the consequent $m_\chi \sim 10^4$ GeV. The approximate numbers in Table 2 agree well with the more precise values we obtain numerically. During our numerical analysis we determine the preferred Λ ranges based on a micrOmegas calculation of the relic abundance.

Label	Operator $\mathcal{O}_{i,f}$	Coefficient C_i
D1	$\bar{\chi}\chi\bar{f}f$	$\frac{m_f}{\Lambda^3_{D1}}$
D2	$\bar{\chi}\gamma_5\chi\bar{f}f$	$\frac{im_f}{\Lambda^3_{D2}}$
D3	$\bar{\chi}\chi\bar{f}\gamma_5 f$	$\frac{im_f}{\Lambda^3_{D3}}$
D4	$\bar{\chi}\gamma_5\chi\bar{f}\gamma_5 f$	$\frac{m_f}{\Lambda^3_{D4}}$
D5	$\bar{\chi}\gamma^\mu\chi\bar{f}\gamma_\mu f$	$\frac{1}{\Lambda^2_{D5}}$
D6	$\bar{\chi}\gamma^\mu\gamma_5\chi\bar{f}\gamma_\mu f$	$\frac{i}{\Lambda^2_{D6}}$
D7	$\bar{\chi}\gamma^\mu\chi\bar{f}\gamma_\mu\gamma_5 f$	$\frac{i}{\Lambda^2_{D7}}$
D8	$\bar{\chi}\gamma^\mu\gamma_5\chi\bar{f}\gamma_\mu\gamma_5 f$	$\frac{1}{\Lambda^2_{D8}}$

Label	Operator $\mathcal{O}_{i,f}$	Coefficient C_i
V1	$\chi^\mu\chi_\mu\bar{f}f$	$\frac{m_f}{2\Lambda^2_{V1}}$
V2	$\chi^\mu\chi_\mu\bar{f}\gamma_5 f$	$\frac{im_f}{2\Lambda^2_{V2}}$
V3	$X^{\mu\nu}X_{\mu\nu}\bar{f}f$	$\frac{m_f}{4\Lambda^4_{V3}}$
V4	$X^{\mu\nu}X_{\mu\nu}\bar{f}\gamma_5 f$	$\frac{im_f}{4\Lambda^4_{V4}}$

Label	Operator $\mathcal{O}_{i,f}$	Coefficient C_i
M1	$\bar{\chi}\chi\bar{f}f$	$\frac{m_f}{2\Lambda^3_{M1}}$
M2	$\bar{\chi}\gamma_5\chi\bar{f}f$	$\frac{im_f}{2\Lambda^3_{M2}}$
M3	$\bar{\chi}\chi\bar{f}\gamma_5 f$	$\frac{im_f}{2\Lambda^3_{M3}}$
M4	$\bar{\chi}\gamma_5\chi\bar{f}\gamma_5 f$	$\frac{im_f}{2\Lambda^3_{M4}}$
M5	$\bar{\chi}\gamma^\mu\gamma_5\chi\bar{f}\gamma_\mu f$	$\frac{1}{2\Lambda^2_{M5}}$
M6	$\bar{\chi}\gamma^\mu\gamma_5\chi\bar{f}\gamma_\mu\gamma_5 f$	$\frac{1}{2\Lambda^2_{M6}}$

Label	Operator $\mathcal{O}_{i,f}$	Coefficient C_i
R1	$\chi\chi\bar{f}f$	$\frac{m_f}{2\Lambda^2_{R1}}$
R2	$\chi\chi\bar{f}\gamma_5 f$	$\frac{im_f}{2\Lambda^2_{R2}}$
C1	$\chi^\dagger\chi\bar{f}f$	$\frac{m_f}{\Lambda^2_{C1}}$
C2	$\chi^\dagger\chi\bar{f}\gamma_5 f$	$\frac{im_f}{\Lambda^2_{C2}}$
C3	$\chi^\dagger\partial_\mu\chi\bar{f}\gamma^\mu f$	$\frac{1}{\Lambda^2_{C3}}$
C4	$\chi^\dagger\partial_\mu\chi\bar{f}\gamma^\mu\gamma_5 f$	$\frac{1}{\Lambda^2_{C4}}$

Table 1: Utilized operators $\mathcal{O}_{i,f}$ and coefficients C_i, in the context of Eq. (1), for a pair of Dirac and Majorana fermion (labeled with D1-8 and M1-6), vector boson (V1-4), real and complex scalar (R1-2 and C1-4) dark matter coupling to SM fermions.

4 Preferred dark matter mass and new phyiscs scale

Using dark matter abundance, direct and indirect detection data we infer the most likely values of the dark matter mass m_χ and new physics scale Λ_i. To find the central value and credibility interval of the parameter values we use Bayesian parameter estimation. Further details of our analysis, including our likelihood function, priors and details of the evidence calculation can be found in Ref. [1].

The resulting posterior probability distributions, marginalized to the minimal cut-off scale and the dark matter mass, are shown in Figure 2. The minimal cut-off is taken to capture the dominant operator, contributing the most to the relic abundance or the direct detection cross section, at each point in the parameter space. As Figure 2 shows a light dark matter mass is favoured, in the region of 10-100 GeV. The scale where new physics cuts off the effective theory is predicted to be $10^3 - 10^4$ GeV at 1σ credible level.

5 Acknowledgments

The work of C.B. and T.L. was supported by the ARC Centre of Excellence for Particle Physics at the Terascale. J.N. was supported by an Australian Postgraduate Award and the U.S. DOE.

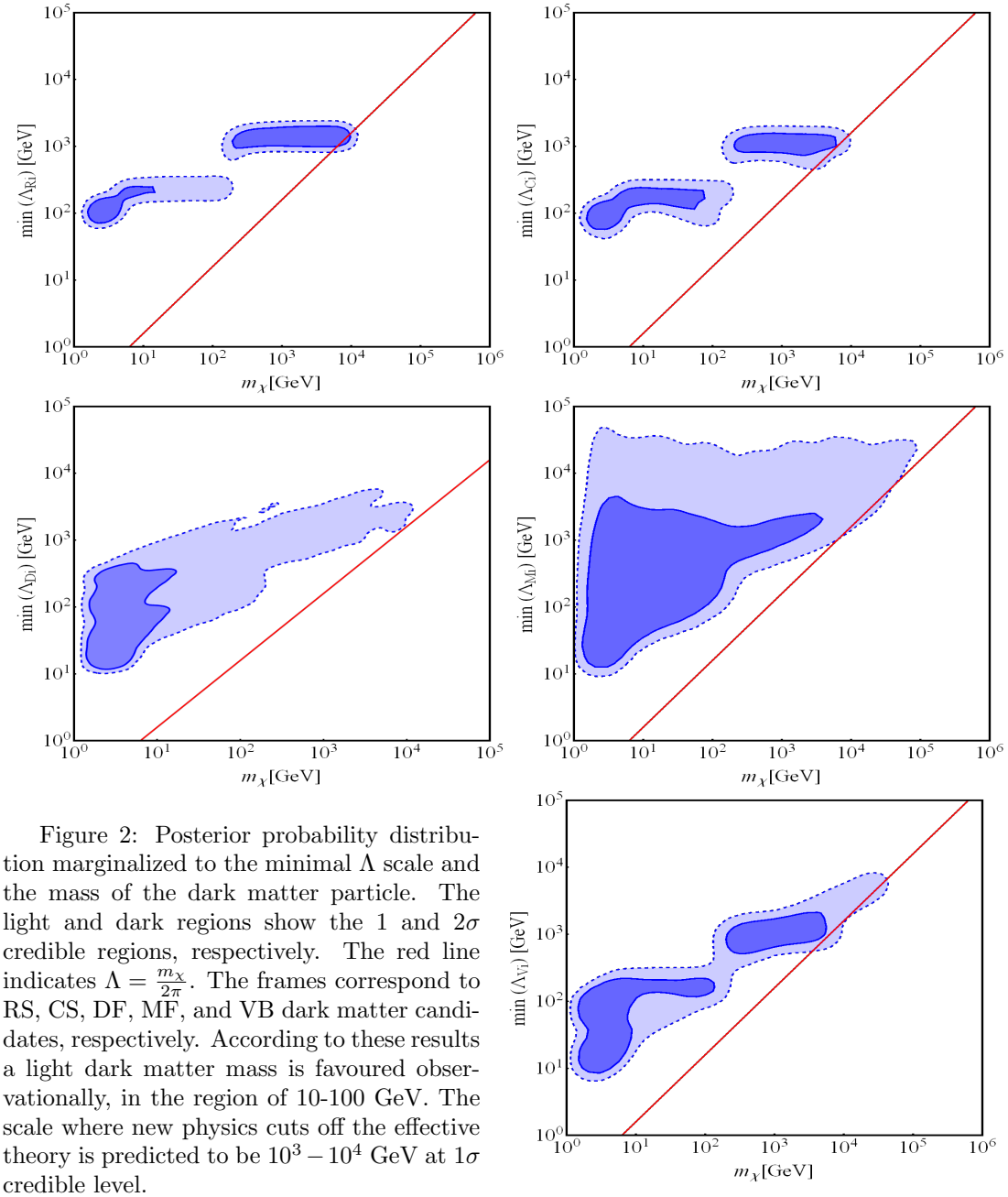

Figure 2: Posterior probability distribution marginalized to the minimal Λ scale and the mass of the dark matter particle. The light and dark regions show the 1 and 2σ credible regions, respectively. The red line indicates $\Lambda = \frac{m_\chi}{2\pi}$. The frames correspond to RS, CS, DF, MF, and VB dark matter candidates, respectively. According to these results a light dark matter mass is favoured observationally, in the region of 10-100 GeV. The scale where new physics cuts off the effective theory is predicted to be $10^3 - 10^4$ GeV at 1σ credible level.

References

[1] C. Balázs, T. Li and J. L. Newstead, JHEP **1408**, 061 (2014) [arXiv:1403.5829 [hep-ph]].

Status of the XENON1T Dark Matter Search

Daniel Coderre[1] *for the XENON Collaboration*

[1]Albert Einstein Center for Fundamental Physics (AEC), Bern, Switzerland
daniel.coderre@lhep.unibe.ch

DOI: http://dx.doi.org/10.3204/DESY-PROC-2014-03/coderre_daniel

The XENON1T experiment is under construction at the Laboratori Nazionali del Gran Sasso in Italy. Building on an extremely successful program pioneered by the XENON10 and XENON100 experiments, XENON1T will provide the most sensitive measurement of the spin-independent WIMP-nucleon cross section to date, reaching sensitivities down to $2 \times 10^{-47}\mathrm{cm}^2$ after two years of data taking. We report on the design of the experiment as well as the current status of construction. The commissioning phase of XENON1T is expected to start in early 2015.

1 Dark Matter

Dark matter is postulated to be a new form of non-luminous matter that interacts very weakly with visible matter [1]. To date there is no direct evidence of the existence of dark matter particles. However there exists a wealth of indirect evidence that makes the inference of some of the properties of dark matter possible. This evidence includes the rotation curves of galaxies, the interaction of galaxy clusters, gravitational lensing measurements of galactic collisions, and precision measurements of the cosmic microwave background.

Several interpretations have been suggested to explain these and other observations including axions, sterile neutrinos, and weakly interacting massive particles (WIMPs) [2]. The WIMP is a particularly attractive candidate and is the main subject of the XENON1T experiment.

The hypothesized WIMP would be a new type of stable particle with a sizable mass and weak-scale interactions with normal matter and other WIMPs. In addition to the tiny interaction cross section this particle would interact with normal matter through gravity, providing explanations for many anomalous astrophysical observations.

The explanation of the dark matter phenomenon is one of the most important open questions in physics and has led to a worldwide hunt for the dark matter particle in which the XENON collaboration is taking a leading role [3].

2 The XENON1T Experiment

The search for an unknown particle with an extremely weak interaction cross section requires both an incredibly sensitive detector and very low background conditions. The XENON1T experiment is under construction at the Laboratori Nazionali del Gran Sasso (LNGS) in Italy.

This laboratory is built under 1400 m (3600 meters water equivalent) of rock, providing a factor of 10^6 reduction in the muon flux compared to the surface.

The XENON1T detector itself follows a scaled up design of the successful XENON10 [4] and XENON100 [5] detectors and is a dual-phase liquid xenon time projection chamber (TPC). XENON1T contains 3.3 tons (2.0 tons active volume) of high-purity liquid xenon instrumented from both above and below with low-background photomultiplier tubes. The volume is kept under a homogeneous electric field of about 1.0 kV/cm causing electrons freed in an interaction to drift towards the top of the TPC.

If an incoming WIMP interacts with a nucleus in the target volume it will produce both scintillation light (S1) and ionization electrons (S2). S1 signals are detected immediately while S2 signals are delayed due to the drift time of the electrons. The S2 is detected via proportional scintillation in the gas phase above the liquid target and provides a localized signal, allowing reconstruction of the (x,y) position of the interaction. The z position of the collision is derived from the time difference between the S1 and the S2.

WIMPs are expected to interact with the xenon nuclei while most background reactions interact with the electrons surrounding the nucleus. Liquid xenon TPCs provide excellent discrimination of electronic and nuclear collisions. The ratio of the charge (S2) to light (S1) signal is different for both collision types, allowing them to be separated in the analysis. During operation the detector is repeatedly calibrated using both gamma and neutron sources in order to study the detector response to electronic and nuclear recoils, respectively. The actual dark matter data is kept blinded in the signal region during the analysis.

A noteworthy aspect of a liquid xenon TPC is liquid xenon's excellent self-shielding capability. Because it is so dense the outer volume of xenon effectively shields the inner volume from background interactions originating from outside the TPC. However for WIMPs this effect is negligible. Therefore when performing the analysis only an inner fiducial volume of xenon is selected. The dimensions of this volume are optimized by studying the expected background distribution. A 10 cm fiducial cut in XENON1T will translate to a fiducial mass of ~ 1 ton.

3 Technical Developments and Sensitivity

Each iteration of the XENON experiment has been designed to provide about two orders of magnitude increase in sensitivity. To build a more sensitive liquid xenon TPC two things are required: a larger target mass and lower background levels. Realizing both of these features has been the subject of a continuous intensive research and development campaign performed by the XENON Collaboration.

A larger target mass provides obvious benefits on sensitivity and self-shielding. However creating a functional TPC with arbitrarily large size is not trivial. For XENON1T the main challenge was providing a stable 1.0 kV/cm electric field over a drift distance of 1m. This has been demonstrated using the XENON1T demonstrator, a 1m long TPC containing up to 60 kg of xenon in operation at Columbia University [9]. The development of this large-scale test apparatus has also allowed tests of the cryogenic and circulation systems.

The best sensitivity in a low-rate counting experiment is achieved with zero background, so the goal for XENON1T is to keep the background as close to zero as possible. One source of nuclear recoil backgrounds originate from cosmic muons which produce neutrons as secondary products as they pass near the detector. Though the muon flux is already very low at LNGS, muon induced neutrons could still cause a sizable background in the signal region. For this

reason the XENON1T detector is surrounded by a 10m by 10m water Cerenkov detector [6]. When this detector sees a signal from a passing muon the data surrounding this signal will be vetoed. This reduces the muon induced background to negligible levels (about 0.01 events/year).

Radiogenic backgrounds provide the largest challenge to a low background experiment like XENON1T. Every detector component is a potential source of radiation. Radiogenic background from within the underground cavern are effectively reduced by the passive shielding provided by the water tank and the outer volume of xenon. To keep background originating from detector components low, a comprehensive material screening campaign is being performed in order to choose the most radio pure raw materials for the detector construction. The stainless steel used to construct the cryostat and parts of the TPC was specially selected by screening many samples. Special low background photomultiplier tubes from Hammamatsu have been manufactured using carefully selected components and extensively tested [7, 8]. A minimalist approach has been undertaken on the design and construction on the detector side in order to keep material, and thus material-induced backgrounds, to a minimum. Some background from the detector materials is unavoidable and so each component used in the construction of the detector has been carefully measured using high purity germanium detectors in order to provide an accurate background prediction for simulations. The predicted background from material contamination in the WIMP search region is about 0.25 events/year.

Other backgrounds come from the xenon itself. When ultra-pure xenon is ordered from a manufacturer it contains krypton as a contaminant on the ppb level. The unstable isotope ^{85}Kr comprises only a factor of $\sim 10^{-11}$ of natural krypton but its β-decays cause a significant background for a dark matter detector. Such impurities within the xenon volume itself are not rejected by fiducialization or analysis and must be removed physically. For XENON1T a krypton distillation column is used to remove krypton impurities from the xenon. This reduces levels of krypton to below the ppt level (target 0.5×10^{-12} Kr/Xe). Electronegative impurities such as O_2, N_2, and H_2O are filtered using getters. A predicted background of 0.15 events/year in the WIMP search region originates from impurities in the xenon.

Two final sources of irreducible background are the solar neutrino background and the double beta decay of ^{136}Xe (about 10% of natural xenon). Both of these backgrounds together contribute an estimated 0.09 events/year, making the full background prediction from all sources about 0.5 events/year.

The expected sensitivity of the XENON1T experiment has been computed with realistic assumptions on the detector performance and analysis efficiency. The background estimates provided above make the assumption that the XENON1T analysis will have similar acceptance and background rejection to the XENON100 analysis. The assumptions are a one ton fiducial volume, 5-50 keV search window for nuclear recoils, rejection of 99.5% of electonic recoil events, and acceptance of 50% of nuclear recoil events. The sensitivity to the spin-independent WIMP-nucleon cross section is shown in Figure 1.

4 Conclusion and Beyond XENON1T

XENON1T will be the most sensitive dark matter experiment in the world when it is completed in 2015. The detector sensitivity depends strongly on the target mass and XENON1T will reach its design sensitivity after two years of stable operation. For this reason a plan has been developed to reuse most of the detector installation to house a TPC with a larger volume of active xenon.

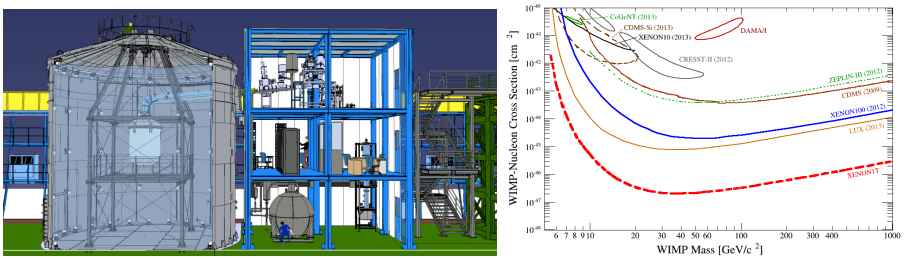

Figure 1: Left: a drawing of the XENON1T facility. Right: the projected spin-independent WIMP-nucleon cross section sensitivity compared to some existing experiments.

The XENONnT project will contain about 7 tons of xenon and has to goal of 20 ton-years of exposure. This will allow a sensitivity down to 10^{-48}cm^2 in the spin-independent WIMP-nucleon cross section. Development and construction will run in parallel to the operation of XENON1T with installation starting as early as 2018.

The main cost of the experiment will be procurement of additional xenon and photodetectors. However the large physical installations at the XENON1T facility have been designed to accomodate the new detector without modification. A new inner vessel will fit within the existing outer cryostat within the existing water tank. Signal and high voltage cables for the new photodetectors have already been installed within the cable pipes connecting the detector to the outside electronics and the existing DAQ, slow control, and computing infrastructure will be reused. The cryogenic and purification systems will also be repurposed for the operation of the new detector.

The XENON1T experiment itself is under construction at Gran Sasso. It is currently on schedule with commissioning planned for early 2015 and first results for later that year. With XENON1T and the planned upgrade, the XENON collaboration plans to remain at the forefront of WIMP direct detection.

References

[1] N. Jarosik et al., Astrophys. J. Suppl. Ser. 192, 14 (2011);
G. Bertone (ed.), *Particle Dark Matter*, Cambridge University Press, 2010.

[2] E. Kolb and M. Turner, *The Early Universe*, Westview Press, 1994.

[3] L. Baudis, Phys. Dark. Univ. 1, 94 (2012).

[4] Angle, J. et al. First Results from the XENON10 Dark Matter Experiment at the Gran Sasso National Laboratory. Phys. Rev. Lett. 100, 021303 (2008)

[5] Aprile, E. et al. Limits on Spin-Dependent WIMP-Nucleon Cross Sections from 225 Live Days of XENON100 Data. Phys. Rev. Lett. 111, 021301 (2013)

[6] Aprile, E., Agostini, F., Alfonsi, M., et al. 2014, arXiv:1406.2374

[7] Baudis, L. et al. Performance of the Hamamatsu R11410 photomultiplier tube in cryogenic xenon environments. JINST 8, P04026 (2013)

[8] Lung, K. et al. Characterization of the Hamamatsu R11410-10 3-in. photomultiplier tube for liquid xenon dark matter direct detection experiments. Nucl. Inst. and Meth. A 696, 32-39 (2012)

[9] Aprile, E., Beck, M., Bokeloh, K., Budnik, R., Choi, B., Contreras, H. A., Weinheimer, C. Measurement of the quantum efficiency of Hamamatsu R8520 photomultipliers at liquid xenon temperature. Journal of Instrumentation, 7(10), P10005 (2012)

[10] Aprile, E., Agostini, F., Alfonsi, M., et al. 2014, arXiv:1406.2374

The XMASS experiment

K. Ichimura[1] *for the XMASS collaboration*

[1]Kamioka Observatory, Institute for Cosmic Ray Research, the University of Tokyo, Higashi-Mozumi, Kamioka, Hida, Gifu 506-1205, Japan,
Kavli Institute for Physics and Mathematics of the Universe, the University of Tokyo, Kashiwa, Chiba 277-8582, Japan

DOI: http://dx.doi.org/10.3204/DESY-PROC-2014-03/ichimura_koichi

The XMASS project is a multi purpose low background experiment with large volume of liquid xenon (LXe) scintillator. The current stage with a 835 kg LXe detector was started in 2010. After the commissioning data taking, we have refurbished the detector to reduce PMT related background and resumed data taking. The physics results obtained with commissioning run and the current status of the XMASS are reported.

1 Introduction

The XMASS project [1] was proposed to observe rare events such as elastic scattering of electron by *pp* solar neutrinos, neutrino-less double beta decay, and elastic scattering of nuclei by dark matter particles with a single phase LXe detector. In the XMASS detector, scintillation lights from LXe are observed by photo-multiplier tubes (PMTs) arranged around the LXe volume. LXe is suitable for the rare event search since LXe has high atomic number and density, so it is worked as shield material against external radiation. XMASS-I, the first stage of the XMASS project aims at the search for the dark matter. The XMASS-I detector was constructed in 2010 with 835 kg of LXe in the pentakis-dodecahedral copper vessel, and commissioning runs were conducted from 2010 to 2012. The performance of XMASS-I detector is summarized in Ref. [2].

2 Physics results from XMASS-I commissioning run

2.1 Search for light WIMPs

Since deposit energy by WIMPs is small, the lower energy threshold of XMASS is advantageous for detecting them. In some of the commissioning runs were taken in a low threshold setting. The analysis threshold was set to four hits of PMTs which correspond to 0.3 keV$_{ee}$. We used 6.7 days with 835 kg entire LXe volume with applying simple cut to reduce Cherenkov background events that occur in quartz windows of PMTs. To constrain light WIMPs, we compare each expected energy spectrum of a certain mass of light WIMPs with the observed data. XMASS excludes part of the parameter space favored by other experiments [3].

2.2 Search for solar axions

The axion is a hypothetical particle introduced by Pecci and Quinn for solving the CP problem in strong interaction. The search for axion as well as axion-like particles (ALPs) focuses on coupling to photons, nucleons and electrons. The signals XMASS searched for are produced by the Compton scattering of photons on electrons and the bremsstrahlung of axions from electrons in the Sun. They can couple to electrons and cause the axio-electric effect to deposit their total energy in the XMASS-I detector. With the same data set of search for light WIMPs, the model independent limit on the coupling for mass $\ll 1$ keV is $\mid g_{aee} \mid < 5.4 \times 10^{-11}$ (90 % C.L.) was obtained. The obtained bounds on the axion mass for the DFSZ and KSVZ axion models are 1.9 and 250 eV, respectively [4].

2.3 Search for inelastic WIMP nucleus scattering on ^{129}Xe

Inelastic scattering that excites low-lying nuclear states in suitable target nuclei provides another avenue to probe for WIMP dark matter. ^{129}Xe is suitable for search for inelastic scattering since it has the lowest-lying excited nuclear state at 39.58 keV among the xenon isotopes. The lifetime of its excited state is short (τ = 1ns), so we searched for a peak at 39.58 keV γ-ray with high energy tail due to the recoil of the ^{129}Xe nucleus. We applied various cuts to reduce the background events as shown in the Figure 1 (left) for sensitive search. We apply a cut based on reconstructed vertex positions, timing information and PMT hit pattern information to reject surface events which are misidentified as inner events. We achieved a low background $\sim 3\times10^{-4}$/day/kg/keV$_{ee}$ with 41 kg of LXe fiducial volume. The dominant contribution to the remained events is ^{214}Pb from ^{222}Rn. We observed no significant excess in 165.9 live days data and derived upper limit of inelastic cross section on ^{129}Xe nuclei. We also obtained an upper limit for spin dependent WIMP-nucleus cross section shown in Figure 1 (right). This limit is the first derived exclusively from data on inelastic scattering [5].

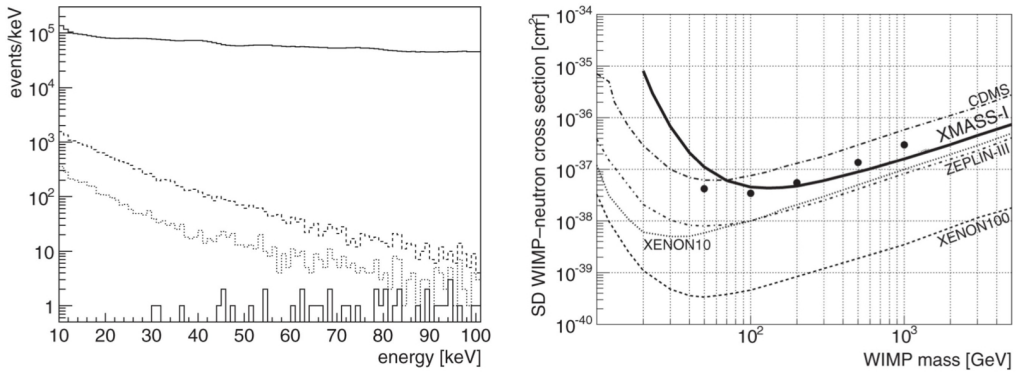

Figure 1: (Left)Energy spectra of the observed events after each reduction step. From top to bottom, the observed energy spectrum after pre-selection (solid), radius cut (dashed), timing cut (dotted) and hit pattern cut (solid), respectively. (Right) The upper limit on the spin-dependent WIMP-neutron cross section from our search for inelastic scattering of WIMPs on ^{129}Xe. The thick line with its gray shaded systematic uncertainty band represents our limit using the form factors of Ref. [7], and the dots represent our limits following Ref. [8] .

2.4 Search for Bosonic Superweakly Interacting Massive Dark Matter Particles

Bosonic super weakly interacting massive particles (super-WIMPs) are a candidate for lukewarm dark matter. For vector boson case, it is called as dark photon, hidden photon and so on. With the absorption of such a boson by a xenon atom, these dark matter candidate would deposit their total energy equivalent to their rest mass in the detector. We search for super-WIMPs in the mass range between 40 and 120 keV. The data set and the reduction method is same as the search for inelastic scattering from ^{129}Xe. We optimized the cut parameters in the reduction steps for each rest mass of super-WIMPs to obtain the best sensitivity. Figure 2 (left) shows the energy spectra of the observed events and simulated events. No significant excess above background, which mostly comes from the radon daughter ^{214}Pb, was observed. Figure 2 (right) shows the limits on coupling constant for pseudoscalar bosons and vector bosons at 90 % C.L. This is the first direct detection experiment exploring the vector super-WIMPs and the obtained limit for the vector super-WIMPs excludes the possibility that such particles constitute all of the dark matter [6].

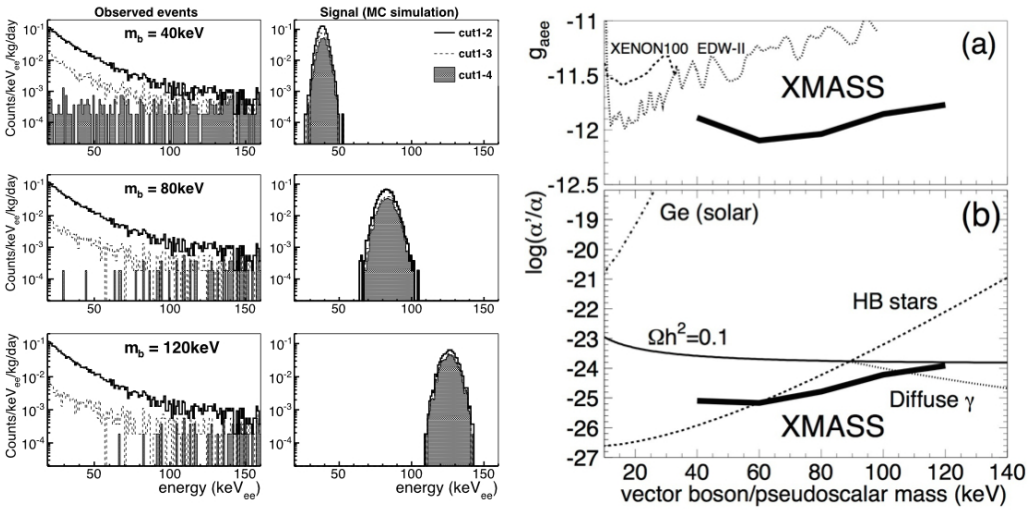

Figure 2: (Left)Energy spectra of the observed events and simulated events after each reduction step for each vector boson mass. Hatched histogram shows remaining events after applying radius cut, timing cut and hit pattern cut. (Right)Limits on coupling constants for (a)electrons and pseudoscalar bosons and (b) electrons and vector bosons at 90% C.L. (thick solid line)

3 Refurbishment of XMASS-I detector and the current status

During the commissioning run we conducted detailed studies on XMASS-I and found that the radioisotopes of ^{210}Pb and ^{238}U in the aluminum seal of the PMT windows is the majority of observed events. To reduce these background, we covered the PMTs with copper ring and high

purity aluminum is evaporated on the side of PMT quartz window to minimize the scintillation lights from the aluminum seal. The other issue is background events at blind corners of PMTs are frequently mimic events within the fiducial volume. Thin copper plates were installed to minimize the gaps between the PMT rings. After the refurbishment work was accomplished in November 2013, DAQ was resumed and now we already accumulated about 200 days data. Figure 3 shows the photographs of PMT before and after refurbishment. Now we are working on the detailed analysis of data for deeper understanding of remained backgrounds and for better sensitivities. A result of a quick check are shown in Figure 3. One order of magnitude reduction above 5 keV for entire volume is achieved.

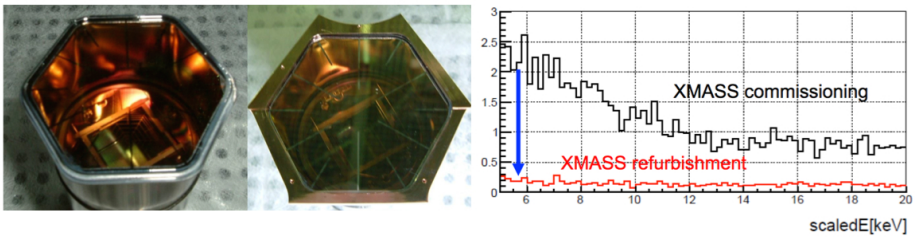

Figure 3: (Left and Middle)The photographs of PMT before and after refurbishment. The aluminum seal of the PMT window is covered with the copper ring to prevent scintillation photon from radioisotopes. (Right)Energy spectrum for entire volume before and after refurbishment. The vertical axis is counts/day/kg/keV$_{ee}$. One order of magnitude reduction is achieved.

4 Summary

The goal of the XMASS project is to observe the various rare events with a large volume of LXe. The current XMASS-I detector has the largest target mass (835 kg) and achieve the very low energy threshold (0.3 keV$_{ee}$). We discussed the physics results of the XMASS-I from the commissioning runs. The refurbishment work for the XMASS-I detector and the current status of the XMASS experiment are also reported.

References

[1] Y. Sizuki, arXiv:hep-ph/0008296.

[2] K. Abe *et al.*, Nucl. Instr. Meth. A **716**, 78-85 (2013)

[3] K. Abe *et al.*, Phys. Lett. B **719**, 78-82 (2013)

[4] K. Abe *et al.*, Phys. Lett. B **724**, 46-50 (2013)

[5] H. Uchida *et al.*, Prog. Theor. Exp. Phys. **063C01** (2014)

[6] K. Abe *et al.*, Phys. Rev. Lett. **113**, 121301 (2014)

[7] L. Baudis *et al.*, Phys. Rev. D **88**, 115014 (2013)

[8] J. D. Vergados, H. Ejiri, and K. G. Savvidy, Nucl. Phys. B **877**, 36 (2013)

On the Validity of Effective Operators for WIMP searches in t-channel models

Thomas Jacques[1]

[1]Section de Physique, Université de Genève,
24 quai E. Ansermet, CH-1211 Geneva, Switzerland

DOI: http://dx.doi.org/10.3204/DESY-PROC-2014-03/jacques_thomas

It is now clear that there are sever limitations to the validity of the effective operator description for dark matter interactions at the LHC. We extend recent analyses by investigating the case in which Dirac dark matter couples to standard model quarks via t-channel exchange of a scalar mediator. We measure the validity of the effective operator description of this model, at both $\sqrt{s} = 8$ TeV and 14 TeV. We also point out the general trend that in the regions where the effective operator description is valid, the dark matter relic abundance is typically large.

1 Introduction

The LHC is searching for direct DM production at unprecedented energies, yet it has proven difficult to constrain the WIMP sector in a model-independent way. One potential solution is the use of Effective Field Theories (EFTs), where a DM-SM interaction is written as a single effective operator, integrating out the mediator. This has the advantage of reducing the parameter space to a single mass ($m_{\rm DM}$) and an energy scale (Λ), and reducing the number of WIMP models down to a small basis set. EFTs are inherently an approximation to a full UV-complete theory, and hence must be used with caution. Given that the LHC is operating at very large energies, it is important to ensure that constraints on EFTs are internally consistent and fall in a region where the EFT approximation is valid.

This issue has been investigated in Refs. [1, 2] where the validity of the EFT has been tested in the s-channel. It was found that only a small fraction of events were at energies where the EFT approximation is valid. In addition, Refs. [3, 4] have compared constraints on some EFTs to those on simplified models, and found that constraints on Λ using UV complete models can either be substantially stronger or substantially weaker than those on EFTs, depending on the choice of parameters.

In this article we extend the analysis of Refs. [1, 2] to the t-channel. We consider a model where Dirac DM couples to SM quarks via t-channel exchange of a scalar mediator. Our goal is to determine in what regions of parameter space the EFT approach is a valid description of this model. The EFT approximation is made by integrating out the mediator, and combining the mediator mass M with the coupling strength g into a single energy scale, $\Lambda \equiv M/g$. This is done by expanding the propagator term for the mediator in powers of $Q_{\rm tr}^2/M^2$ and truncating

at the lowest order, where $Q_{\rm tr}$ is the momentum carried by the mediator:

$$\frac{g^2}{Q_{\rm tr}^2 - M^2} = -\frac{g^2}{M^2}\left(1 + \frac{Q_{\rm tr}^2}{M^2} + \mathcal{O}\left(\frac{Q_{\rm tr}^4}{M^4}\right)\right) \simeq -\frac{1}{\Lambda^2}. \tag{1}$$

Clearly, this approximation is only valid when $Q_{\rm tr}^2 \ll M^2$; yet this condition is impossible to test precisely in the true EFT limit, since M has been combined with g to form Λ. Instead, an assumption about g must be made. There is no lower limit to the coupling strength, so regardless of the scale of Λ, it is always possible that M is small enough that the EFT approximation does not apply.

Alternatively, the most optimistic choice is to assume that $g \simeq 4\pi$, the maximum possible coupling strength such that the model still lies in the perturbative regime. As a middle ground, we test whether the EFT approximation is valid for values of $g \gtrsim 1$, a natural scale for the coupling in the absence of any other information. In this case, the condition for the validity of the EFT approximation becomes $Q_{\rm tr}^2 \lesssim \Lambda^2$, which we will adopt in the following to assess the validity of the use of EFT at LHC for DM searches.

2 Validity of the EFT: analytical approach

2.1 Operators and cross sections

In this article we will consider the following effective operator describing the interactions between Dirac dark matter χ and left-handed quarks q

$$\mathcal{O} = \frac{1}{\Lambda^2}\left(\bar{\chi}P_L q\right)\left(\bar{q}P_R\chi\right). \tag{2}$$

Only the coupling between dark matter and the first generation of quarks is considered.

The operator in Eq. (2) can be viewed as the low-energy limit of a simplified model describing a quark doublet Q_L coupling to DM, via t-channel exchange of a scalar mediator S_Q,

$$\mathcal{L}_{\rm int} = g\,\bar{\chi}Q_L S_Q^* + h.c. \tag{3}$$

and integrating out the mediator itself. We consider only coupling to the first generation of quarks, $Q_L = (u_L, d_L)$. This model is popular as an example of a simple DM model with t-channel couplings, which exist also in well-motivated models such as supersymmetry where the mediator particle is identified as a squark, and the DM is a Majorana particle.

The standard search channel for such a scenario is missing energy plus a single jet, although there are other promising complementary search channels. The dominant process contributing to the missing energy plus monojet signal is $q\bar{q} \to \chi\bar{\chi}g$. We have calculated the differential cross section for these processes.

2.2 Results and discussion

To test whether the EFT approximation is valid in monojet searches, we define the ratio of the cross section truncated so that all events pass the condition, to the total cross section:

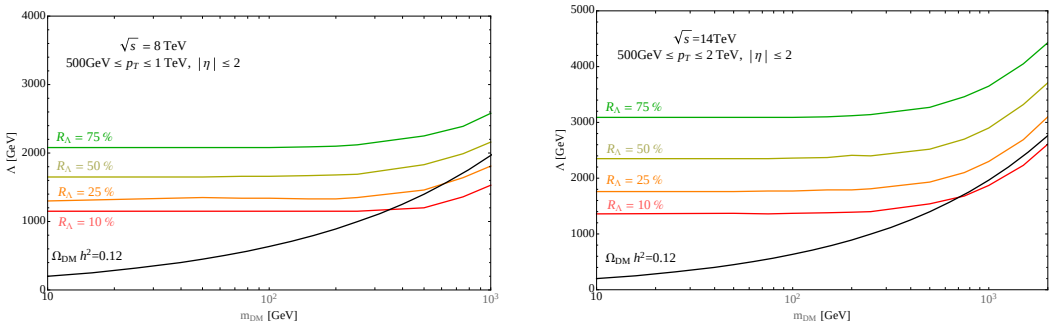

Figure 1: Contours for R_Λ. The black solid curves indicates the correct relic abundance.

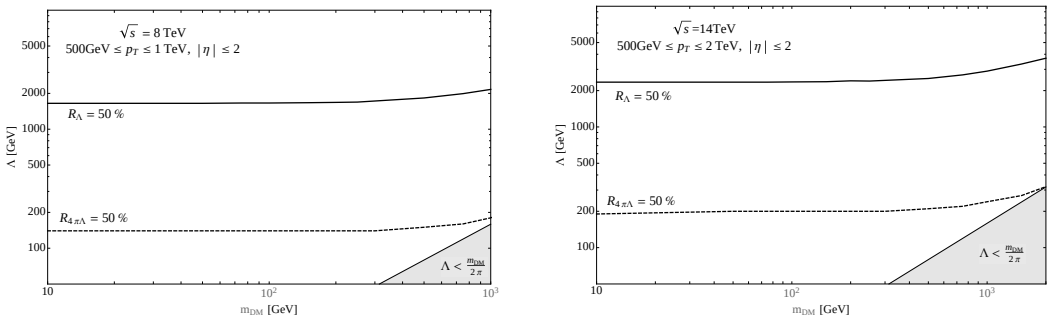

Figure 2: Contours for R_Λ, varying the cutoff $Q_{\rm tr} < \Lambda$ and $Q_{\rm tr} < 4\pi\Lambda$. The grey shaded area shows $\Lambda < m_{\rm DM}/(2\pi)$, often used as a benchmark for the validity of the EFT.

$$R_\Lambda \equiv \frac{\sigma|_{Q_{\rm tr}<\Lambda}}{\sigma} = \frac{\int_{p_{\rm T}^{\rm min}}^{p_{\rm T}^{\rm max}} {\rm d}p_{\rm T} \int_{-2}^{2} {\rm d}\eta \left.\frac{{\rm d}^2\sigma}{{\rm d}p_{\rm T}{\rm d}\eta}\right|_{Q_{\rm tr}<\Lambda}}{\int_{p_{\rm T}^{\rm min}}^{p_{\rm T}^{\rm max}} {\rm d}p_{\rm T} \int_{-2}^{2} {\rm d}\eta \frac{{\rm d}^2\sigma}{{\rm d}p_{\rm T}{\rm d}\eta}}. \tag{4}$$

The integration limits on these quantities are chosen to be comparable to those used in standard searches for WIMP DM by the LHC collaborations (see, for instance, Ref. [5]).

In Fig. 1 we plot isocontours of four fixed values of R_Λ as a function of both $m_{\rm DM}$ and Λ. Contrasted with the s-channel case [1, 2], the ratio has less DM mass dependence, being even smaller than in the s-channel case at low DM masses and larger at large DM masses, without becoming large enough to save EFTs.

In Fig. 1 we also show the curves corresponding to the correct DM relic density. For given $m_{\rm DM}$, larger Λ leads to a smaller self-annihilation cross section and therefore to larger relic abundance. It is evident that the large-Λ region where the EFT is valid typically leads to an unacceptably large DM density.

In the most optimistic scenario for EFTs, the coupling strength g takes the maximum value (4π) such that the model remains in the perturbative regime. To demonstrate how our results depend on the coupling strength, in Fig. 2 we plot isocontours for $R = 50\%$, for two cases:

1) the standard requirement that $Q_{\rm tr}^2 < \Lambda^2$, equivalent to requiring $g \simeq 1$, and **2)** requiring $Q_{\rm tr}^2 < (4\pi\Lambda)^2$, equivalent to requiring $g \simeq 4\pi$.

The grey shaded area indicates the region where $\Lambda < m_{\rm DM}/(2\pi)$. This is often used as a benchmark for the validity of the EFT approximation, since in the s-channel, $Q_{\rm tr}$ is kinematically forced to be greater than $2m_{\rm DM}$.

3 Conclusions

In this article we have extended the investigation of the validity of the EFT approach for DM searches at the LHC. We have considered here the case of Dirac DM couplings to the standard model via the t-channel.

We have computed the relic density over the parameter space of the model, assuming that the only interactions between DM and the SM are those mediated by the t-channel operator (2), and found that the region of EFT validity corresponds to an overly large relic density. This conclusion is rather general and may be evaded by assuming additional DM annihilation channels.

Similar to what happens in the s-channel case, our findings indicate that in the t-channel the range of validity of the EFT is significantly limited in the parameter space $(\Lambda, m_{\rm DM})$, reinforcing the need to go beyond the EFT at the LHC when looking for DM signals. This is especially true for light mediators as they can be singly produced in association with a DM particle, leading to a qualitatively new contribution to the mono-jet processes. Mediators can even be pair-produced at the LHC through both QCD processes and DM exchange processes. All of this rich dynamics leads to stronger signals (and therefore, in the absence thereof, to tighter bounds) than the EFT approach.

Acknowledgments

This article is based on Ref. [6], done in collaboration with Giorgio Busoni, Andrea De Simone, Enrico Morgante and Antonio Riotto.

References

[1] G. Busoni, A. De Simone, E. Morgante, and A. Riotto, Phys.Lett. **B728**, 412 (2014), arXiv:1307.2253.

[2] G. Busoni, A. De Simone, J. Gramling, E. Morgante, and A. Riotto, (2014), arXiv:1402.1275.

[3] P. J. Fox, R. Harnik, J. Kopp, and Y. Tsai, Phys.Rev. **D85**, 056011 (2012), arXiv:1109.4398.

[4] O. Buchmueller, M. J. Dolan, and C. McCabe, JHEP **1401**, 025 (2014), arXiv:1308.6799.

[5] ATLAS Collaboration, ATLAS-CONF-2012-147, (2012).

[6] G. Busoni, A. De Simone, T. Jacques, E. Morgante, and A. Riotto, (2014), arXiv:1405.3101.

LHC Dark Matter Searches

Felix Kahlhoefer

Rudolf Peierls Centre for Theoretical Physics, University of Oxford,
1 Keble Road, Oxford OX1 3NP, United Kingdom

DOI: http://dx.doi.org/10.3204/DESY-PROC-2014-03/kahlhoefer_felix

We review the experimental and theoretical status of dark matter searches at the LHC and the interplay with direct detection experiments. A particular emphasis is placed on discussing the usefulness and validity of effective operators and possible ways to go beyond this simple approach. Moreover, we consider cases where loop contributions are important for the comparison of collider searches and direct detection experiments.

1 Introduction

It is a remarkable fact that one of the leading experiments for the detection of weakly interacting massive particles (WIMPs) is the CERN Large Hadron Collider (LHC). Although any WIMPs produced at the LHC will escape from the detector unnoticed, we may observe large amounts of missing transverse energy ($\not{E}_T$) if one or more Standard Model (SM) particles are produced in association with the WIMPs. In particular, the LHC has the potential to produce WIMPs via their direct couplings to SM particles [1], i.e. by inverting the annihilation of WIMPs that occurred in the early Universe. In this case, one can obtain an observable signal if additional SM particles are produced via SM interactions, for example a single jet from initial state radiation.

Experimental searches for mono-jet events have been performed at the LHC by both CMS [2] and ATLAS [3]. To reduce backgrounds, experimental collaborations typically require both $\not{E}_T$ and the transverse momentum (p_T) of the primary jet to be large, i.e. of order of a few hundred GeV. Secondary jets with high p_T are usually also permitted, provided the two jets are not back-to-back. The dominant remaining backgrounds arise from $Z + j$ with invisibly decaying Z and from leptonically decaying $W + j$ with unidentified charged lepton.

Unfortunately, these backgrounds are rather large and the p_T spectrum of the signal — although slightly harder than the background — is essentially featureless. Consequently, mono-jet searches typically cannot provide conclusive information concerning the mass of the WIMPs. Nevertheless, the resulting bounds on the production cross section allow to directly constrain the couplings of WIMPs to quarks, which also determine the WIMP scattering cross section in direct detection experiments [4, 5].

Although mono-jet searches typically give the strongest constraints on the interactions of WIMPs, a convincing discovery of WIMPs at the LHC would require the observation of an excess in more than one search channel. Promising alternatives are mono-photon searches, mono-W searches, mono-Z searches, and searches for two jets or two heavy quarks in association with $\not{E}_T$. Observing an excess in several of these search channels would enable us to disentangle the couplings of WIMPs to various SM particles.

In this article, we want to address two questions: How do we make predictions (such as signal distributions) in order to optimize experimental cuts? And how do we interpret LHC searches in order to compare them with other experiments (such as direct detection)? To answer these questions, we need to specify the Lorentz structure of the assumed WIMP-quark interactions. In many cases, however, it is not necessary to specify the details of the mediator of the interaction.

2 From effective operators to simplified models

For sufficiently large mediator mass, we can integrate out the heavy mediator to obtain effective four-fermion interactions. For example, the vector operator $\mathcal{O}_\mathrm{V} \equiv \frac{1}{\Lambda_\mathrm{V}^2} (\bar{\chi}\gamma_\mu \chi) (\bar{q}\gamma^\mu q)$ could arise from integrating out a vector mediator with mass M_R and couplings g_q and g_χ to quarks and WIMPs, so that the suppression scale Λ associated with the scale of new physics would be given by $\Lambda^2 = M_R^2/(g_q\, g_\chi)$.

If the mediator is sufficiently heavy ($m_R \gg 1$ TeV), the effective interaction introduced above remain valid even at LHC energies. Both mono-jet cross sections and direct detection cross sections will then be proportional to Λ^{-4}, so that we can directly translate bounds from one kind of search to the other. For the vector operator and light WIMPs, for example, current LHC searches find $\Lambda \gtrsim 800$–900 GeV, corresponding to $\sigma_N \lesssim 10^{-39}\,\mathrm{cm}^2$ [2, 3]. This bound implies that LHC searches are superior to direct detection experiments for $m_\chi \lesssim 5$ GeV, since collider searches do not suffer from a limitation for light WIMPs in contrast to direct detection experiments. On the other hand, LHC constraints are inferior for heavier WIMPs, since for spin-independent (SI) interactions direct detection experiments benefit from a coherent enhancement proportional to the square of the target nucleus mass. A similar bound on Λ is found for the axialvector operator, which is stronger than the typical constraints on spin-dependent (SD) interactions from direct detection experiments up to WIMP masses of a TeV. For larger masses, present collider searches cease to be constraining because of kinematics.

Because of their simplicity, effective operators can be very valuable tools to study the qualitative behaviour of different types of WIMP interactions and to develop an intuition for the relevant effects in mono-jet searches and direct detection experiments. For these reasons, there is an extensive literature on the interpretation of WIMP searches using effective operators (see e.g. [4, 6]). Nevertheless, there are reasons to be cautious when applying effective operators to LHC searches for WIMPs [5]. In particular, the UV completion should have perturbative couplings, meaning that $g_{q,\chi} \lesssim \sqrt{4\pi}$. Consequently, for $\Lambda = 900$ GeV, the mediator mass has to be smaller than about 3.2 TeV. Once the centre-of-mass energy $\sqrt{s}$ becomes comparable to this scale, we can no longer rely on an effective operator description, because the mediator may be produced on-shell (see e.g. [7, 8]).

Similarly, effective operators run into problems with unitarity [9]. For the vector operator and the process $q\bar{q} \to \chi\bar{\chi}$ one finds $\mathcal{M} = 2\sqrt{3}\, s/\Lambda^2$, so unitarity is violated for $\sqrt{s} > 1.9$ TeV, implying that new physics must appear below this scale. The conclusion is that effective operators may not be valid at the LHC, because the mediator may be accessible for LHC energies. Once the mediator can be produced on-shell, it becomes necessary to depart from an effective field theory description and specify the properties of the mediator (such as couplings, mass and decay width).

As a specific example we consider the case of a new massive gauge boson Z' arising from an additional broken $U(1)_X$ symmetry [10]. In particular, we consider an effective Lagrangian

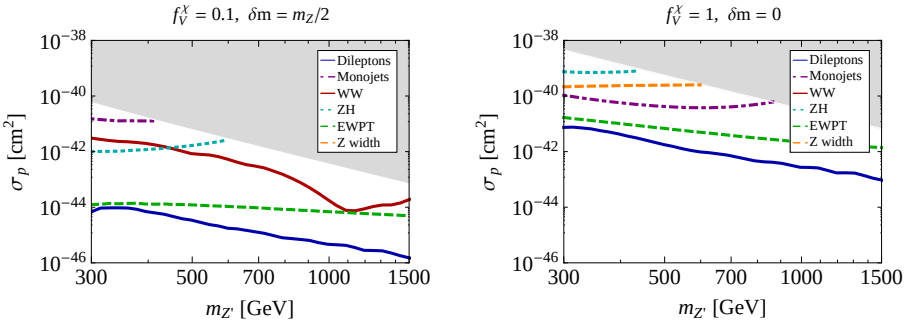

Figure 1: Bounds on the direct detection cross section for different choices of f_χ^V and δm. The grey shaded regions correspond to $\sin\epsilon > 0.8$.

that includes kinetic mixing and mass mixing [11]:

$$\mathcal{L} \supset -\frac{1}{2}\sin\epsilon\,\hat{B}_{\mu\nu}F'^{\mu\nu} + \delta m^2\,\hat{Z}_\mu Z'^\mu - f_\chi^{\mathrm{V}}\,Z'^\mu\,\bar{\chi}\gamma_\mu\chi\,.$$

There are 5 new parameters in this model: the mixing parameters $\sin\epsilon$ and δm^2, the direct coupling f_χ between the Z' and the WIMP, the Z' mass $m_{Z'}$ and the WIMP mass m_χ.

In addition to the mono-jet searches discussed above, there are three further interesting search channels at the LHC: dilepton resonances, WW resonances and ZH production [12]. The resulting bounds directly constrain the mixing parameters ϵ and δm^2. For fixed mass mixing and fixed direct couplings, these constraints can thus be interpreted as bounds on $\sin\epsilon$ as a function of $m_{Z'}$, which in turn can be translated into bounds on the WIMP direct detection cross section. The resulting constraints are presented in Figure 1 (taken from [12]).

We observe that for $f_\chi^V = 0.1$ the LHC gives strong constraints on the direct detection cross section, comparable to the best bounds from current direct detection experiments. Increasing f_χ^V relaxes all bounds from the LHC since now smaller quark couplings — and therefore smaller mixing parameters — are sufficient to obtain similar direct detection cross section. At the same time the invisible partial width of Z' is increased so that decays of Z' into SM particles are additionally suppressed. Monojet searches, on the other hand, become significantly more constraining. Thus, even for $f_\chi^V = 1$, direct detection cross section above $10^{-41}\,\mathrm{cm}^2$ are excluded by dilepton and mono-jet searches as well as electroweak precision tests (EWPT).

This example illustrates that once we move away from effective operators there may be additional experimental signatures apart from mono-jet signals that may give strong bounds on the interactions of the dark mediator. There has been a lot of recent activity in constructing sets of simplified models in order to investigate these effects more systematically [7, 8]. In addition to s-channel mediators like a Z', there has also been much interest in models with t-channel mediators, which give rise to a somewhat different phenomenology [13, 14].

3 The importance of heavy-quark loops

So far, we have neglected an important complication, which is important for both effective operators and simplified models. While the LHC produces WIMPs with energies of up to

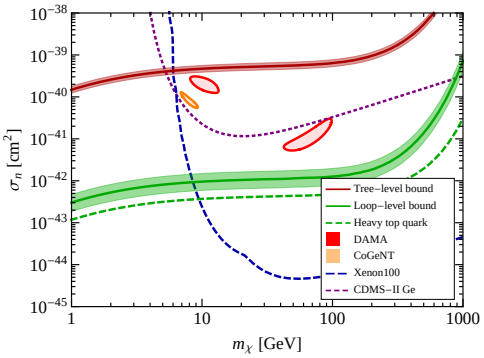

Figure 2: LHC mono-jet bounds on the WIMP-proton cross section for Yukawa-like couplings at tree-level (red) and loop-level (green) compared to various results from direct detection experiments.

several TeV, the WIMPs in the Galactic halo are non-relativistic with $v/c \sim 10^{-3}$ and the typical momentum transfer in direct detection experiments is of the order of a few MeV. To calculate direct detection cross sections, we must therefore evolve all operators from the TeV scale down to the hadronic scale. In the process, new interactions may be induced at loop level, leading to additional operators, which are assumed to be absent (or small) at the TeV scale.

As an example, we consider the exchange of a new heavy scalar or pseudoscalar mediator with Yukawa-like couplings to quarks [15]. Using tree-level diagrams alone, the suppression scale Λ is very difficult to constrain with LHC mono-jet searches [4, 5, 6] since the initial state contains (apart from gluons) only light quarks, which by assumption have small couplings to WIMPs. The situation changes dramatically beyond tree level, since now loop graphs involving virtual top quarks give rise to a $j + \not{E}_T$ signal [15]. The inclusion of these heavy-quark loops leads to a dramatic increase in the predicted mono-jet cross section and therefore a significant improvement of the bounds from LHC searches.

This observation is illustrated in Figure 2 (taken from [15]). We find that including the loop-level processes in the calculation increases the predicted mono-jet cross sections by a factor of about 500. Consequently, the inclusion of loop-level processes gives a pertinent improvement of the mono-jet bounds on the WIMP scattering cross section, in particular because it independently excludes the possibility that the CoGeNT excess or the DAMA modulation arise from the interactions of a heavy scalar mediator with Yukawa-like couplings.

It is also possible that the converse situation occurs, namely that LHC mono-jet searches give very strong bounds at tree level, because direct detection cross sections are SD. However, loop contributions can significantly boost direct detection bounds whenever they induce SI interactions. In fact, a rigorous classification of WIMP-nucleon interactions into SI and SD (or momentum suppressed) is not possible in general, as such a distinction is unstable under radiative corrections. This effect is most striking for tensor interactions, which induce magnetic dipole moments at loop level [16]. These loop-induced interactions lead to an SI part in the differential cross section that is additionally enhanced in the infrared due to the photon pole.

Bounds on the differential event rate from direct detection experiments can be used to infer strong bounds on the WIMP magnetic dipole moment. We can then convert these bounds into limits on the new-physics scale Λ entering the definition of the tensor operator and compare

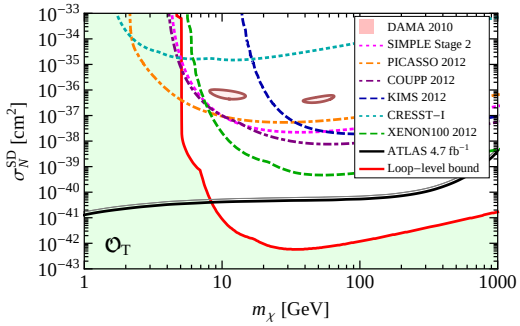

Figure 3: Bounds on the SD WIMP-nucleon cross section from direct detection experiments compared to the constraints resulting from loop-induced dark dipole moments and LHC searches for $j + \not{E}_T$.

these 'indirect' bounds on $\sigma_N^{\rm SD}$ with the conventional constraints on SD interactions from direct detection experiments with an odd number of protons or neutrons in the target atoms.

The resulting bounds and best-fit regions are shown in Figure 3 (from [16]). The solid red curve indicates the combined bound from loop-induced SI interactions. As expected, if WIMP interactions proceed via the tensor operator, experiments sensitive for SD interactions cannot currently probe the parameter region allowed by LHC mono-jet searches. Our central observation is, however, that even if we neglect the bounds from the LHC, the accessible parameter region is already excluded by constraints on the WIMP magnetic dipole moment unless $m_\chi < 5\,\text{GeV}$. In other words, for $m_\chi \geq 5\,\text{GeV}$ there is no need for target nuclei with spin in order to constrain the tensor operator.

A related question concerns the magnitude of QCD corrections for mono-jet searches. These effects have been systematically investigated in [17] using MCFM and POWHEG. For most operators, next-to-leading order (NLO) corrections are small once parton showering (PS) is included. Nevertheless, these corrections are important, because they reduce scale dependencies and hence the theoretical uncertainty of the signal prediction.

4 Outlook

The LHC is in good shape to continue its search for WIMPs in the next few years. A recent ATLAS study concluded that with a centre-of-mass energy of 14 TeV the vector operator can be probed up to new physics scales of 2.3 TeV (corresponding to $\sigma_p \approx 3 \times 10^{-41}\,\text{cm}^2$), provided even tighter cuts on $\not{E}_T$ will be applied to reduce systematic uncertainties [18]. Similarly, a 5σ discovery of vector interactions should be possible for $\sigma_p \approx 2 \times 10^{-40}\,\text{cm}^2$.

In conclusion, the LHC is very well suited for constraining the WIMP production cross section and therefore probing the same interactions as direct and indirect detection experiments. A wide range of possible search channels has been investigated both by the theory community and the experimental collaborations. Although effective operators provide a convenient framework to interpret these searches, the description becomes inaccurate whenever the intermediate particles can be on-shell. As a first step to go beyond effective operators, there have been recent efforts to analyse LHC searches using simplified models (for example a Z' vector mediator).

At the same time, there has been important progress in our understanding of the importance of heavy-quark loops and NLO corrections and there are now public codes that are capable of including the resulting effects in future analyses.

Acknowledgments

FK would like to thank the CERN theory group for hospitality and to acknowledge support from a Leathersellers' Company Scholarship at St Catherine's College, Oxford.

References

[1] M. Beltran, D. Hooper, E. W. Kolb, Z. A. C. Krusberg and T. M. P. Tait, "Maverick dark matter at colliders," JHEP **1009**, 037 (2010) [arXiv:1002.4137 [hep-ph]].

[2] CMS Collaboration, S. Chatrchyan et al., "Search for dark matter and large extra dimensions in monojet events in pp collisions at $\sqrt{s} = 7$ TeV," JHEP **1209**, 094 (2012) [arXiv:1206.5663 [hep-ex]].

[3] ATLAS Collaboration, G. Aad et al., "Search for dark matter candidates and large extra dimensions in events with a jet and missing transverse momentum with the ATLAS detector," JHEP **1304**, 075 (2013) [arXiv:1210.4491 [hep-ex]].

[4] J. Goodman, M. Ibe, A. Rajaraman, W. Shepherd, T. M. P. Tait et al., "Constraints on Dark Matter from Colliders," Phys. Rev. **D82**, 116010 (2010) [arXiv:1008.1783 [hep-ph]].

[5] P. J. Fox, R. Harnik, J. Kopp and Y. Tsai, "Missing Energy Signatures of Dark Matter at the LHC," Phys. Rev. **D85**, 056011 (2012) [arXiv:1109.4398 [hep-ph]].

[6] J. March-Russell, J. Unwin and S. West, "Closing in on Asymmetric Dark Matter I: Model independent limits for interactions with quarks," JHEP **1208**, 029 (2012) [arXiv:1203.4854 [hep-ph]].

[7] G. Busoni, A. De Simone, E. Morgante and A. Riotto, "On the Validity of the Effective Field Theory for Dark Matter Searches at the LHC," Phys. Lett. **B728**, 412-421 (2014) [arXiv:1307.2253 [hep-ph]].

[8] O. Buchmueller, M. Dolan and C. McCabe, "Beyond Effective Field Theory for Dark Matter Searches at the LHC," JHEP **1401**, 025 (2014) [arXiv:1308.6799 [hep-ph]].

[9] I. M. Shoemaker and L. Vecchi, "Unitarity and Monojet Bounds on Models for DAMA, CoGeNT, and CRESST-II," Phys. Rev. **D86**, 015023 (2012) [arXiv:1112.5457 [hep-ph]].

[10] K. S. Babu, C. F. Kolda and J. March-Russell, "Implications of generalized Z - Z-prime mixing," Phys. Rev. **D57**, 6788-6792 (1998) [arXiv:hep-ph/9710441].

[11] M. T. Frandsen, F. Kahlhoefer, S. Sarkar and K. Schmidt-Hoberg, "Direct detection of dark matter in models with a light Z'," JHEP **1109**, 128 (2011) [arXiv:1107.2118 [hep-ph]].

[12] M. T. Frandsen, F. Kahlhoefer, A. Preston, S. Sarkar and K. Schmidt-Hoberg, "Direct detection of dark matter in models with a light Z'," JHEP **1207**, 123 (2012) [arXiv:1204.3839 [hep-ph]].

[13] H. An, L.-T. Wang and H. Zhang, "Dark matter with t-channel mediator: a simple step beyond contact interaction," Phys. Rev. **D89**, 115014 (2014) [arXiv:1308.0592 [hep-ph]].

[14] A. DiFranzo, K.-I. Nagao, A. Rajaraman and T. M. P. Tait, "Simplified Models for Dark Matter Interacting with Quarks," JHEP **1311**, 014 (2013) [arXiv:1308.2679 [hep-ph]].

[15] U. Haisch, F. Kahlhoefer and J. Unwin, "The impact of heavy-quark loops on LHC dark matter searches," JHEP **1307**, 125 (2013) [arXiv:1208.4605 [hep-ph]].

[16] U. Haisch and F. Kahlhoefer, "On the importance of loop-induced spin-independent interactions for dark matter direct detection," JCAP **1304**, 050 (2013) [arXiv:1302.4454 [hep-ph]].

[17] U. Haisch, F. Kahlhoefer and E. Re, "QCD effects in mono-jet searches for dark matter," JHEP **1312**, 007 (2013) [arXiv:1310.4491 [hep-ph]].

[18] ATLAS Collaboration, "Sensitivity to WIMP Dark Matter in the Final States Containing Jets and Missing Transverse Momentum with the ATLAS Detector at 14 TeV LHC," ATL-PHYS-PUB-2014-007 (2014).

The DAMIC-100 dark matter detection experiment with CCDs at SNOLAB

Ben Kilminster[1], *Alexis Aguilar-Arevalo*[2], *Dan Amidei*[3], *Xavier Bertou*[4], *Melissa Butner*[5,8], *Gustavo Cancelo*[5], *Alvaro E. Chavarria*[6], *Juan Carlos D'Olivo*[2], *Juan Estrada*[5], *Guillermo Fernandez Moroni*[5], *Federico Izraelevitch*[5], *Yashmanth Langisetty*[3], *Junhui Liao*[1], *Jorge Molina*[7], *Paolo Privitera*[6], *Carolina Salazar*[2], *Youssef Sarkis*[2], *Vic Scarpine*[5], *Tom Schwarz*[3], *Miguel Sofo Haro*[4], *Javier Tiffenberg*[5], *Frederic Trillaud*[2], *Jing Zhou*[6]

[1] Universität Zürich Physik Institut, Zurich, Switzerland
[2] Universidad Nacional Autónoma de México, México D.F., México
[3] University of Michigan, Ann Arbor, MI, United States
[4] CNEA/CONICET, Centro Atomico Bariloche, San Carlos de Bariloche, Argentina
[5] Fermi National Accelerator Laboratory, Batavia, IL, United States
[6] Kavli Institute for Cosmological Physics and The Enrico Fermi Institute, The University of Chicago, Chicago, IL, United States
[7] Facultad de Ingenieria, Universidad Nacional de Asuncion (FIUNA), Asuncion, Paraguay
[8] Northern Illinois University, DeKalb, IL, USA

DOI: http://dx.doi.org/10.3204/DESY-PROC-2014-03/kilminster_ben

The DAMIC (Dark Matter in CCDs) experiment uses the fully depleted silicon of CCDs (Charge Coupled Devices) as a target for galactic dark matter. The ionization energy threshold for detecting nuclear recoils of dark matter reaches down to 50 eV_{ee}, resulting in better sensitivity to dark matter with mass below 5 GeV than other direct dark matter detection experiments. Installation of the DAMIC-100 experiment at SNOLAB is ongoing and we present our expected sensitivity, which will extend the reach to low-mass dark matter cross sections within a year of operation.

1 Introduction

The mass and interaction type and strength of dark matter particles is yet unknown. It has been suggested that, to explain why the dark matter density is so similar to the baryon density, the lepton-baryon asymmetry was transferred to dark matter in the early universe, resulting in a natural mass of the dark matter particle of $5 \cdot M_{proton} \sim 5$ GeV [2, 3, 4]. This dark matter particle would interact weakly with matter, and could therefore be detected through its nuclear recoil with the target of a low-background detector. Several experiments searching for dark matter have reported statistically significant excesses consistent with this expected signal [5, 6].

DAMIC (Dark Matter in CCDs) uses the fully depleted silicon of CCDs (charge-coupled devices) [1] as a target for coherent dark-matter nucleus elastic scattering. Due to the low electronics noise (2e-) of its minimalistic readout scheme, the CCD is an ideal detector for searching for the low energy recoil expected from dark matter with mass ~ 5 GeV. Improvements in the resistivity of silicon substrates have allowed scientific CCDs to achieve thicknesses of 675

μm [7], more than 30 times that of commercial CCDs, resulting in improved near-infrared light detection for telescope imaging [8], and more massive targets for direct dark matter detection.

First results for DAMIC were reported in Ref. [9]. The experiment used a shallow underground site (350' deep) and one 0.5-gram CCD detector developed for DECam, and with 107 g-days total exposure, achieved the best upper limits on the cross-section for weakly interacting dark matter particles below 4 GeV. Subsequently, DAMIC has been moved to SNOLAB (6800' deep), and the construction of the next phase of the experiment, DAMIC-100 is underway. More information about DAMIC-100 can be found in Ref. [10].

DAMIC CCDs were originally designed and fabricated at the Lawrence Berkeley National Laboratory MicroSystems Lab for the Dark Energy Survey (DES) camera (DECam) [7]. They make use of a three-phase, triple poly-silicon gate structure with a p-channel implant to collect holes from the fully depleted n-type silicon substrate which has a resistivity of 10–20 kΩ cm. A CCD has up to 16 Mpixels, each with a transverse size of $15\,\mu\text{m} \times 15\,\mu\text{m}$, and a thickness of at least 250 μm. CCDs are fully depleted with a 20 (50) V substrate voltage for 250 (675) μm thickness which causes ionization produced from nuclear recoils in the active region to be accelerated toward anode gates on the backside of the CCD, where charge is collected near a p-n junction. The substrate voltage also controls the level of lateral diffusion of the charge carriers as they drift the thickness of the CCD. The depth of an interaction inside the CCD can be determined from a measurement of the lateral sharing of charge among the pixels which record charge from the interaction.

DAMIC-100 CCDs are operated at 133 K, resulting in a dark current due to thermal excitations in the silicon substrate of $\sim 1\, e^-$/pix/day. The RMS noise in each pixel measurement is $\sim 1.9\ e^-$ which corresponds to 7 eV energy. Pixels are measured by shifting charge row-by-row, column-by column to a low capacitance output gate via phased potential wells generated by the three-phase gate structure. Charge is converted to an output voltage of $\sim$ 3 μV/e- that is compared to the pedestal value for each pixel in order to determine the signal level. High frequency electronics noise is reduced by increasing the integration time of each readout, so that pixels are read out at $\sim$1 Mpixels per minute. Long exposure times ($>$ 10 hours) are used to reduce the total number of times the readout noise is incurred per dataset. DAMIC does not have timing resolution, and therefore cannot veto background events through timing coincidence with supplemental detectors as in other experiments.

Calibrations of the CCDs with fluorescence X-rays from a Kapton target exposed to the ^{55}Fe source or αs from ^{241}Am were performed. Figure 1(a) demonstrates the linearity of the CCD in the measurement of ionization energy, while Figure 1(b) quantifies the energy resolution of the CCD. For these calibrations the CCD was illuminated from the back, which, due to charge diffusion, leads to a larger dynamic range and worse energy resolution than if the CCD had been illuminated from the front.

The ionization efficiency of nuclear recoils is a fraction of that of electrons. Previous measurements have been done down to energies of 3–4 keV_r [11], yielding results in agreement with Lindhard theory [12]. From this, DAMIC's nominal 50 eV_{ee} threshold corresponds to $\sim$0.5 keV_r. Given the significant uncertainty in the extrapolation, and the importance of precise nuclear recoil scale calibration for dark matter searches, we are undergoing a series of experiments to measure this value down to the threshold [10].

DAMIC-100 consists of eighteen, 675 μm thick, 16 Mpixel LBNL CCDs with a total mass of 100 g in a vacuum vessel with copper, lead, and polyethylene shielding at SNOLAB. The CCDs will be installed on high-purity silicon supports, immediately surrounded by OFHC copper. The radioactive background from the CCD packaging is expected to be $\ll 1$ events/(keV_{ee}·kg·d)

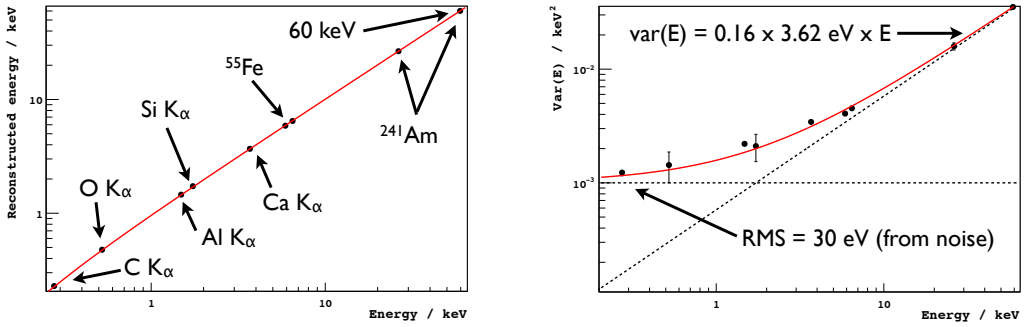

(a) Linearity of the ionization energy scale

(b) Energy resolution

Figure 1: a) Reconstructed energy of X-ray lines compared to true energy from ^{55}Fe and ^{241}Am sources. The labeled K_α markers are fluorescence lines from elements in the Kapton target and other materials in the CCD setup. Linearity is demonstrated from 0.3 keV$_{ee}$ to 60 keV$_{ee}$. b) Variance of X-ray lines as a function of energy yielding a Fano factor of 0.16 typical for a CCD [1]. The resolution of 30 eV$_{ee}$is for maximal diffusion since the calibration was performed on the backside of the detector.

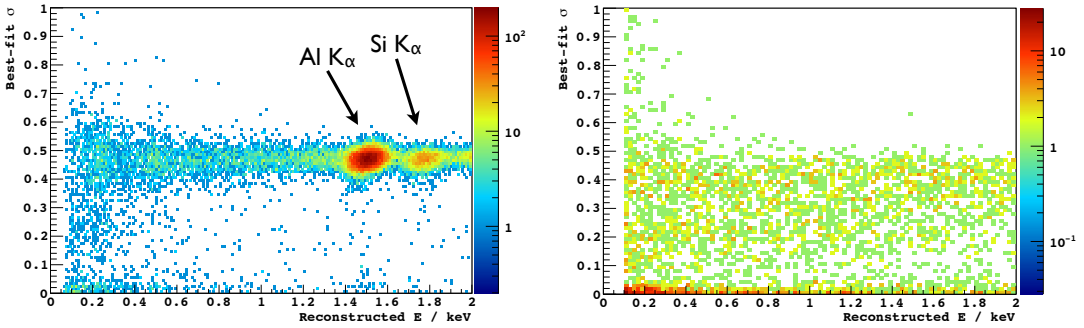

(a) Low energy X-rays from the back

(b) ^{252}Cf source (uniform)

Figure 2: The RMS size of pixel clusters (in pixels) as a function of energy from (a) fluorescence X-rays from a Kapton target exposed to a ^{55}Fe source and (b) fast neutrons from a ^{252}Cf source. X-rays are absorbed in $<10\,\mu$m of the back side, resulting in large lateral diffusion, and an RMS of about 0.5 pixels or 7.5 μm. The neutron interaction length is much larger than the thickness of the CCDs, resulting in a uniform depth of interaction, as is expected for dark matter.

and the count rate should be dominated by Compton scattering from external γ-rays, at a predicted rate of 0.5 events/(keV$_{ee}$·kg·d). Operation of the new detector should start early 2015. We use an MCNP simulation to model the backgrounds and a possible signal expected in the CCD detectors based on measurements of the radioactivity of the limiting backgrounds in the experiment. Fig. 3 shows the expected reach of DAMIC-100 and the magnitude of the possible signal from the light WIMP scenario suggested by CDMS-Si [5].

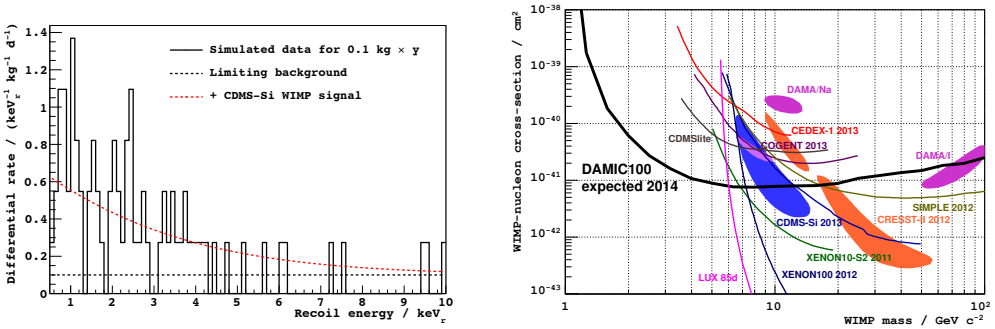

Figure 3: a) Simulated energy spectrum of DAMIC-100, considering a dark matter candidate with the mass and interaction cross-section of the best-fit to the CDMS-Si signal (M_χ=8.6 GeV and $\sigma_{\chi N}$=1.9×10^{-41} cm^2) [5], standard halo parameters (ρ_χ=0.3 GeV/cm^3, v_0=220 m/s, v_E=232 m/s, v_{esc}=544 m/s) and a 0.1 kg·y exposure. The expected limiting background of 0.5 events/(keV$_{ee}$·kg·d) corresponds to 0.1 events/(keV$_r$·kg·d) due to the assumption of an ionization efficiency of 0.2. b) We present an expected 90% exclusion plot which would result in the best limits on spin-independent WIMP-nucleon elastic scattering for M_χ<6 Gev.

References

[1] J. Janesick, Press Monographs, The International Society for Optical Engineering, 2001.

[2] D. B. Kaplan, Phys. Rev. Lett. **68**, 741 (1992).

[3] D. E. Kaplan, M. A. Luty and K. M. Zurek, Phys. Rev. D **79**, 115016 (2009) [arXiv:0901.4117 [hep-ph]].

[4] T. Cohen, D. J. Phalen, A. Pierce and K. M. Zurek, Phys. Rev. D **82**, 056001 (2010) [arXiv:1005.1655 [hep-ph]].

[5] R. Agnese *et al.* [CDMS Collaboration], Phys. Rev. Lett. **111**, 251301 (2013) [arXiv:1304.4279 [hep-ex]].

[6] R. Bernabei *et al.* [DAMA and LIBRA Collaborations], Eur. Phys. J. C **67**, 39 (2010) [arXiv:1002.1028 [astro-ph.GA]].

[7] S.E. Holland, D.E. Groom, N.P. Palaio, R. J. Stover, and M. Wei, IEEE Trans. Electron Dev., **50** 225 (2003), LBNL-49992.

[8] J. Estrada & R. Schmidt , Scientific Detectors for Astronomy 2005, Edited by J.E. Beletic, J.W. Beletic and P. Amico, Springer, (2006).

[9] J. Barreto *et al.* [DAMIC Collaboration], Phys. Lett. B **711**, 264 (2012) [arXiv:1105.5191 [astro-ph.IM]].

[10] A. Chavarria, J. Tiffenberg, A. Aguilar-Arevalo, D. Amidei, X. Bertou, G. Cancelo, J. C. D'Olivo and J. Estrada *et al.*, arXiv:1407.0347 [physics.ins-det].

[11] G. Gerbier, E. Lesquoy, J. Rich, M. Spiro, C. Tao, D. Yvon, S. Zylberajch and P. Delbourgo *et al.*, Phys. Rev. D **42**, 3211 (1990).

[12] J. Lindhard, V. Nielsen, M. Scharff, and P.V. Thomsen, Mat. Fys. Medd. Dan. Selsk **33**, 10 (1963).

Direct Dark matter search with the Edelweiss experiment

Valentin Kozlov[1] *on behalf of the EDELWEISS Collaboration*

[1]Karlsruhe Institute of Technology, Institut für Kernphysik, Postfach 3640, 76021 Karlsruhe, Germany

DOI: http://dx.doi.org/10.3204/DESY-PROC-2014-03/kozlov_valentin

The EDELWEISS experiment searches for Dark Matter particles by means of Ge-bolometers with a powerful rejection of background. The setup is installed in the Modane underground laboratory (LSM, France) in French-Italian Alps. The second phase of the experiment was completed in 2011, and results are published setting new limits on the spin-independent WIMP-nucleon scattering cross-section. The same data set was also analyzed to search for axion-induced electron recoils down to 2.5 keV. We set new limits on ALP parameters for different scenarios, some of which provide one of the best bounds for direct axion searches. Recently the setup was upgraded towards significantly higher sensitivity and 36 new Ge-detectors of 800 g each were installed. The detector background rejection capabilities and performances, and improvements of the background will be presented. The status and scientific goals of the current EDELWEISS program will be described as well as further plans for a next generation experiment, EURECA.

1 Overview of the Edelweiss experiment

The primary goal of the EDELWEISS experiment is a direct search for the WIMP dark matter. As the expected rate of events is below 10^{-3}/kg/day, the experiment is located in the underground laboratory in Modane (France), which provides a very good shielding against cosmogenic background down to 5 μ/m^2/day. To reduce further the radioactive background the muon veto, external polyethylene and lead shields, and recently introduced internal polyethylene shield, are used in the experimental setup (Fig. 1). The volume inside the shields is flushed with de-radonized air to even more reduce the influence of the ambient background. Another important reduction of the background is possible due to the ability of the detectors to distinguish between nuclear recoils (expected from the WIMP interaction) and electron recoils (originate from ambient sources of background). The experiment uses bolometers of ultra pure germanium: Once these detectors are cooled to about 18 mK, both phonon and ionization signals can be simultaneously measured. The ratio of the two signals, called *ionization yield*, is different for nuclear and electron recoils allowing to separate these two types of recoils. Additional rejection power arises from the special electrode arrangement, called *interdigitized electrode design* (ID), which provides vetoing of *surface events* [1]. The EDELWEISS experiment finished its second phase (Sec. 2), and the upgrade to EDELWEISS-III is nearly completed (Sec. 3). The scientific goal of EDELWEISS-III is to reach a sensitivity of about 10^{-45} cm^2 for the WIMP-nucleon spin-independent (SI) cross-section by 2015-2016 (Fig. 2).

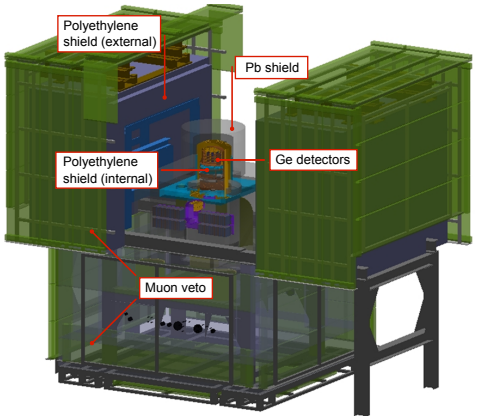

Figure 1: The EDELWEISS setup layout: in the center is the dilution refrigerator able to host up to 40 kg of detectors. The passive lead and polyethylene shields followed by the active muon-veto system protect the detectors against various backgrounds.

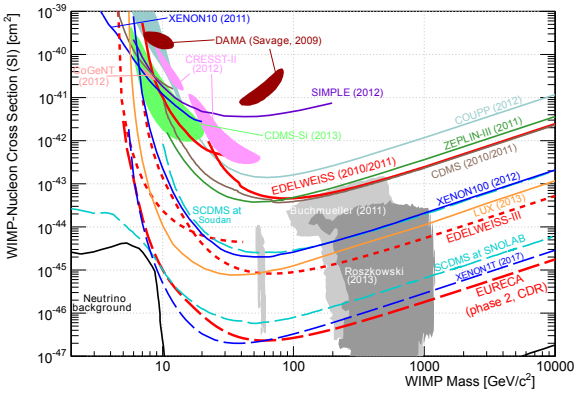

Figure 2: The upper limits on the WIMP-nucleon spin-independent cross-section as a function of WIMP mass. The EDELWEISS-II data are marked with thick solid red lines and correspond to Refs. [2, 3]. As dashed red lines are shown EDELWEISS-III projections for two cases: the standard WIMP, 12000 kg·day, and low-mass WIMP analysis, 1200 kg·day, HEMT-based front-end electronics. The EURECA projection, phase 2, is shown as the red long dashed line. The shaded areas correspond to theoretical SUSY predictions.

2 Summary of the phase II

In a period from April 2009 to May 2010 the EDELWEISS collaboration successfully operated ten 400-g ID detectors. The data set acquired during this period (with an addition of the run between July and November 2008) was analyzed for the 'standard' WIMP search, i.e. with a possible WIMP mass, m_χ, around or above 100 GeV [2], low-mass WIMP search with m_χ ~10 GeV [3], and thanks to the low-background environment and the ability to separate electron recoils out, we also searched for axion-induced signals [4].

The EDELWEISS primary goal is to search for the WIMP dark matter. However, as another possible dark matter candidate, axions, would lead to electron recoils which can be measured down to low energies because of the EDELWEISS very low background down to 2.5 keV and the ability to reject the surface events, four scenarios involving different hypotheses on the origin and couplings of axions were probed. This includes the Primakoff axion search, i.e. due to Primakoff axion production in the Sun (Fig. 3), a search for solar axions produced by Compton-bremsstrahlung and axion-recombination and deexcitation processes (C-B-RD), the search for solar axions emitted by ^{57}Fe, and the specific scenario in which the galactic dark matter halo is made of ALPs (axion like particles) with a keV-scale mass (Fig. 4). By combining all obtained results we exclude the mass range 0.92 eV $< m_A <$ 80 keV for DFSZ (Dine-Fischler-Srednicki-

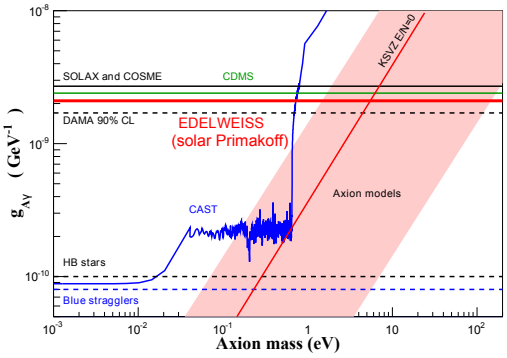

Figure 3: 95% C.L. constraint on the $g_{A\gamma}$ coupling from the solar Primakoff flux obtained by EDELWEISS-II (red thick line), compared to other crystal experiments.

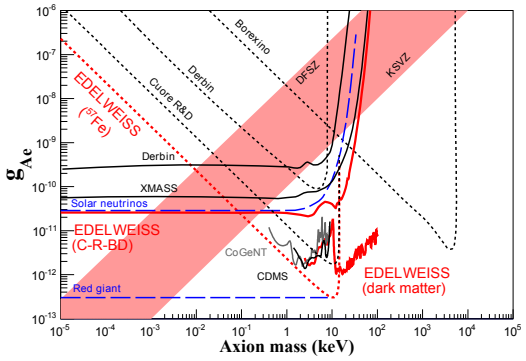

Figure 4: The limits obtained by EDELWEISS-II on the g_{Ae} axion coupling as a function of axion mass, m_A (red lines).

Zhitnitskii) axions and 5.78 eV $< m_A <$ 40 keV for KSVZ (Kim-Shifman-Vainstein-Zakharov) axions [4], which is a prominent result for a direct axion search from a single data set.

The obtained WIMP search limits are summarized on Fig. 2 (thick solid red lines): in the 'standard' WIMP search the analysis was optimized for the maximum exposure and resulted in the exclusion of the spin-independent WIMP-nucleon scattering cross-section of $4.4{\cdot}10^{-44}$ cm^2 at 90% C.L. for $m_\chi \sim$85 GeV (Fig. 2) [2]. For the low-mass WIMP search the detectors with the lowest possible thresholds and backgrounds were selected, such that the sensitivity to nuclear recoils down to 5 keV could be achieved. This leaded to a restricted data set but extended the sensitivity of EDELWEISS-II down to WIMP masses below 20 GeV (Fig. 2) [3].

In Refs. [5] and [6] general background conditions of EDELWEISS-II were investigated, and possible improvements were pointed out. Together with significantly increased target mass this leaded to the next phase of the experiment, EDELWEISS-III.

3 Phase III and beyond

EDELWEISS-III is the upgrade of the EDELWEISS-II towards enlarged target mass, more advanced detectors and reduced background environment. New FID800 detectors have about 800 g total mass, two NTD sensors to measure phonons, all surfaces are covered with interleaved electrodes to perform the surface event rejection. The fiducial volume is also increased, i.e. it is 75%, or 600 g per detector, compared to 40%, or 160 g, in previously used ID400 detectors. As follows from tests the γ-rejection factor of the new FID800 is improved by factor 5 compared to ID400, or $< 6 \cdot 10^{-6}$, while surface-event rejection is better by 33%, or $< 4 \cdot 10^{-5}$ for the recoil energy E_R >15 keV. As of autumn 2014, 36 FID800 detectors are installed in the cryogenic setup, while 24 are cabled and used in the just started WIMP search. The cabling between the detectors and the acquisition system as well as the connectors were exchanged by new ones, using less radioactive materials. In the 1 K zone of the cryostat additional polyethylene was installed to shield the detectors from the internally generated neutrons, e.g. due to (α,n). New copper thermal screens were produced out of higher radiopurity copper to lower the intrinsic

gamma background but also to fit the larger detector mass and new shielding. The cryogenic system was upgraded to reduce the microphonic noise. The analog front-end electronics placed at 100 K stage of the cryostat has been upgraded such that DAC-controlled mechanical relays are used instead of feedback resistors of charge sensitive preamplifiers [7]. A new data analysis framework improves the usability of the recorded data [8]. The EDELWEISS-III DAQ can read up to 60 bolometers and includes the readout of the muon veto timing. The system consists of a crate with FPGA based input cards which are able to do a real time analysis of the data stream in parallel for all channels. This is a highly scalable system and can be extended to include even more detectors in future. The readout electronics of one of the detectors is equipped with the prototype of a time resolved digitization card, which allows to read 2 ionization channels with a 400 times higher sampling rate of 40 MHz. The higher resolution on timing of the ionization signal would improve further the characterization of events, e.g. the discrimination between fiducial and surface events or double scattering events [1]. One more R&D is ongoing to use the HEMT-based front-end readout in order to lower the recoil energy threshold down to 3 keV and thus improve the low-mass WIMP search. The projected sensitivities of EDELWEISS-III for the 'standard' WIMP search and the low-mass case are shown on Fig. 2.

To go beyond the EDELWEISS-III sensitivity a next generation dark matter experiment, EURECA, is planned. In its 1^{st} phase EURECA will host a multi-nuclei target of about 150 kg, while in the 2^{nd} phase up to 1000 kg [9]. For the 1^{st} phase a closer collaboration with the SuperCDMS at SNOlab experiment is foreseen. EURECA in its 1-tonne version should probe a WIMP-nucleon SI interaction down to 10^{-47} cm^2 (Fig. 2).

Acknowledgments

The help of the technical staff of the Laboratoire Souterrain de Modane and the participant laboratories is gratefully acknowledged. The EDELWEISS project is supported in part by the French Agence Nationale pour la Recherche, by Science and Technology Facilities Council (UK) and the Russian Foundation for Basic Research (grant No. 07-02-00355-a) and by the Helmholtz Alliance for Astroparticle Physics (HAP) funded by the Initiative and Networking Fund of the Helmholtz Association. R&D activities within EDELWEISS towards EURECA are also supported in part by the German ministry of science and education (BMBF Verbundforschung ATP Proj.-Nr. 05A11VK2).

4 Bibliography

References

[1] A. Broniatowski *et al.*, Phys. Lett. B **681**, 305 (2009) [arXiv:0905.0753 [astro-ph.IM]].
[2] E. Armengaud *et al.*, Phys. Lett. B **702**, 329 (2011) [arXiv:1103.4070 [astro-ph.CO]].
[3] E. Armengaud *et al.*, Phys. Rev. D **86**, 051701(R) (2012) [arXiv:1207.1815 [astro-ph.CO]].
[4] E. Armengaud *et al.*, J. of Cosm. and Astropart. Phys. **11**, 067 (2013) [arXiv:1307.1488 [astro-ph.CO]].
[5] E. Armengaud *et al.*, Astropart. Phys. **47**, 1 (2013) [arXiv:1305.3628 [physics.ins-det]].
[6] B. Schmidt *et al.*, Astropart. Phys. **44**, 28 (2013) [arXiv:1302.7112 [astro-ph.CO]].
[7] B. Censier *et al.*, J. Low Temp. Phys. **167**, 645 (2012).
[8] G. A. Cox *et al.*, Nucl. Instr. and Meth. A **684**, 63 (2012).
[9] G. Angloher*et al.*, Phys. of the Dark Univ. **3**, 41 (2014).

Electroweak fragmentation functions for dark matter annihilation

Leila Ali Cavasonza[1], *Michael Krämer*[1,2], *and Mathieu Pellen*[1]

[1] *Institute for Theoretical Particle Physics and Cosmology, RWTH Aachen University, D-52056 Aachen, Germany*

[2] *SLAC National Accelerator Laboratory, Stanford University, Stanford, CA 94025, USA*

DOI: http://dx.doi.org/10.3204/DESY-PROC-2014-03/kraemer_michael

Electroweak corrections are relevant for dark matter indirect detection predictions. The quality of the fragmentation function approximation to describe electroweak gauge boson radiation is examined in two concrete models. For models with Majorana fermion dark matter annihilation into light fermions, the fragmentation function approximation does not work, due to the helicity suppression of the lowest-order cross section. For other models, like those with vector dark matter, fragmentation functions provide very reliable results for dark matter with masses $M_{\rm DM} \gtrsim 500\,\text{GeV}$.

1 Introduction

In dark matter indirect detection experiments one searches for dark matter annihilation products, including antimatter particles like positrons and antiprotons, which propagate through the galactic halo and which can be detected in astrophysical experiments at the earth.

As pointed out in the literature [1, 2, 3, 4, and refs. therein], electroweak (EW) radiation from the primary dark matter annihilation products can significantly alter the spectra of the secondary Standard Model particles, that may be detected at the earth. The decay of the EW bosons will modify the spectra of the primary annihilation products and, more importantly, will always produce the complete spectrum of stable SM particles, irrespective of the model-specific composition of the primary annihilation products.

Many models provide dark matter candidates with masses in the TeV-range. For such heavy dark matter, soft and collinear electroweak gauge boson emission from the relativistic final-state particles is enhanced by Sudakov logarithms $\ln^2(M_{\rm DM}^2/M_{\rm EW}^2)$ [5], where $M_{\rm DM}$ and $M_{\rm EW}$ are the mass of the dark matter candidate and of the electroweak gauge boson, respectively. The fragmentation function formalism [2, and refs. therein] provides a simple and model-independent approximation to describe the logarithmically enhanced contributions due to EW radiation. Note that the model-dependent gauge boson emission off initial and intermediate state particles is not reproduced by the fragmentation function approximation.

In the following we examine the quality of the fragmentation function approximation. To this end, we have compared the predictions obtained for the flux at the earth using the fragmentation function approximation against those obtained from an exact calculation of Z-boson emission. To perform the comparison we have chosen two concrete models of dark matter: a simplified

version of the Minimal Supersymmetric Model (MSSM) [6, 7], and a simplified Universal Extra Dimension (UED) model [8, 9]. In these models the dark matter candidates are a pure bino neutralino, $\tilde{\chi}^0$, and the first Kaluza-Klein excitation of the SU(2) gauge boson, $B^{(1)}$, *i.e.* a Majorana fermion and a vector boson, respectively. For simplicity we focus on the particular case where the dark matter particles annihilate at lowest order into electron-positron pairs only. To assess the quality of the fragmentation function approximation [10], which only describes the logarithmically enhanced contributions to Z-boson radiation off the finale state, we have performed comparisons of the energy spectra of the Z bosons and of the spectra of positrons and anti-protons at the earth after the propagation through the galactic halo. We have obtained the secondary particles fluxes using PYTHIA 8 [11, 12] and implemented the propagation through the galactic halo using a Green functions formalism [13, and refs. therein].

In this proceedings contribution we show that the fragmentation function approach reproduces well the exact result for vector dark matter annihilation (the UED case), while the approximation does not work for the annihilation of Majorana fermion dark matter into light fermions (the MSSM case). This is due to the fact that the annihilation of neutralinos into a lepton pair is helicity suppressed [14, 15, 16] and that the emission of soft and collinear gauge bosons from the final state particles, included in the fragmentation function approximation, is not sufficient to lift this helicity suppression [3]. Hence, the fragmentation function approximation provides a simple and reliable technique to obtain realistic predictions for dark matter indirect detection for models where the annihilation is not suppressed at the lowest order.

2 Comparison and results

The fragmentation function approximation does not reproduce the correct result for Majorana fermion annihilation as anticipated [10]. Therefore, we consider here only the spectra for positrons and antiprotons from the annihilation of vector dark matter in the universal extra dimension model after propagation through the galactic halo. We compare the results from the full $(2 \to 3)$ calculation, $B^{(1)}\,B^{(1)} \to e^+e^-(Z \to \text{SM particles})$ and the fragmentation function approximation. In Fig. 1 the positron spectra after parton shower and propagation are displayed. The fragmentation function approximation provides an accurate description of the positrons from the Z-boson decay. However, as the cross section of the $(2 \to 3)$ process is a genuine electroweak higher-order contribution of $\mathcal{O}(\alpha \ln^2(M_{\rm DM}^2/m_Z^2))$, and thus highly suppressed by comparison to the leading-order annihilation, the amount of additional positrons is small compared to those produced in the $(2 \to 2)$ process The small dip in the fragmentation function prediction at high energies is a remnant of the kinematics of the $(2 \to 2)$ process and is disappearing as $M_{\rm DM}/m_Z$ increases. In our simple leptophilic model set-up, antiprotons are generated exclusively from Z-boson decay. As the fragmentation function provides a good approximation to the Z-boson spectrum of the exact calculation [10], the flux of antiprotons is also expected to be reproduced well. This is indeed born out by the explicit calculation presented in Fig. 2. We find that the exact $(2 \to 3)$ calculation and the fragmentation function approach agree within 10% for $M_{\rm DM} \gtrsim 500\,\text{GeV}$. This result is further supported by the comparison of the fragmentation function result against the analytical expression for the exact $(2 \to 3)$ calculation, see Ref.[10].

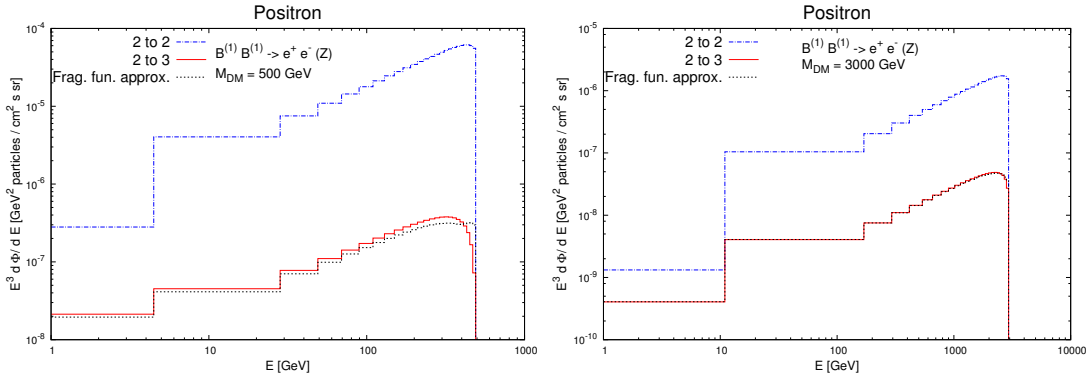

Figure 1: Positron energy spectra for $M_{\rm DM} = 500$, 3000 GeV in the UED case after propagation.

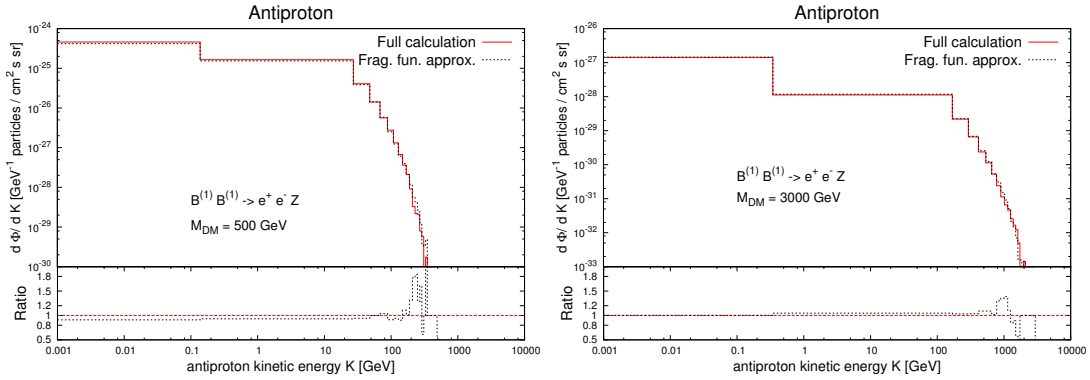

Figure 2: Antiproton spectra for $M_{\rm DM} = 150$, 3000 GeV in the UED case after propagation.

3 Conclusions

We have examined the quality of the fragmentation function approximation for two specific simple DM models [10], by comparing the primary energy spectra and fluxes after the evolution of the annihilation products and propagation through the galactic halo. We find that fragmentation functions fails to reproduce the behaviour of the complete calculation for models with Majorana fermion annihilation into light fermions. This is due to the fact that the soft/collinear contribution to Z-boson radiation, included in the fragmentation function approximation, is not sufficient to lift the helicity suppression of the lowest-order cross section. By contrast, we find that the fragmentation function approach is working very well for models that do not suffer from helicity suppression at the lowest order, like vector dark matter annihilation in models with universal extra dimensions. Specifically, we find that the particle fluxes after probation through the galactic halo obtained from the exact ($2 \to 3$) calculation and the fragmentation function approach agree to better than 10% for $M_{\rm DM} \approx 500\,\text{GeV}$ and to better than 2% for $M_{\rm DM} \approx 1\,\text{TeV}$. The fragmentation function formalism thus provides a simple framework to obtain predictions for astrophysical experiments for models where the lowest-order annihilation cross section is not suppressed.

4 Acknowledgments

MK would like to thank the organisers of the 10th PATRAS workshop for hosting such an inspiring and pleasant event. We would like to thank Alexander Mück and Torbjörn Sjöstrand for useful discussions, and Angélina Bieler for her colaboration at earlier states of this work. MK is grateful to SLAC and Stanford University for their hospitality. This work was supported by the Deutsche Forschungsgemeinschaft through the graduate school "Particle and Astroparticle Physics in the Light of the LHC" and through the collaborative research center TTR9 "Computational Particle Physics", and by the U.S. Department of Energy under contract DE-AC02-76SF00515.

5 Bibliography

References

[1] P. Ciafaloni, A. Urbano, "TeV scale Dark Matter and electroweak radiative corrections," Phys. Rev. D **82**, 149 (2010) [arXiv:1001.3950 [hep-ph]].

[2] P. Ciafaloni, D. Comelli, A. Riotto, F. Sala, A. Strumia, and others, "Weak Corrections are Relevant for Dark Matter Indirect Detection," JCAP 1103, 019 (2011) [arXiv:1009.0224 [hep-ph]].

[3] P. Ciafaloni, M. Cirelli, D. Comelli, A. De Simone, a. Riotto, and others, "On the Importance of Electroweak Corrections for Majorana Dark Matter Indirect Detection," JCAP 1310, 031 (2013) [arXiv:1305.6391 [hep-ph]].

[4] P. Ciafaloni, D. Comelli, A. De Simone, E. Morgante, A. Riotto, and others, "The Role of Electroweak Corrections for the Dark Matter Relic Abundance," JCAP 1106, 018 (2011) [arXiv:1104.2996 [hep-ph]].

[5] P. Ciafaloni and D. Comelli, "Sudakov enhancement of electroweak corrections," Phys. Lett. B **446**, 278-284 (1999) hep-ph/9809321.

[6] J.R. Ellis, J.S. Hagelin, D.V. Nanopoulos, K.A. Olive, M. Srednicki, "Supersymmetric Relics from the Big Bang," Nucl. Phys. B **238**, 453-476 (1984)

[7] G. Jungman, M. Kamionkowski, K Griest, "Supersymmetric dark matter," Phys. Rept. 267, 195-373 (1996) hep-ph/9506380.

[8] H.C. Cheng, J.L. Feng, K.T.Matchev, "Kaluza-Klein dark matter," Phys. Rev. Lett. 89, 211-301 (2002) hep-ph/0207125.

[9] G. Servant, T.M.P. Tait, "Is the lightest Kaluza-Klein particle a viable dark matter candidate?," Nucl. Phys. B **650**, 391-419 (2003) hep-ph/0206071

[10] L. Ali Cavasonza, M. Krämer, M. Pellen, "Electroweak Fragmentation Functions for Dark Matter Annihilation," [arXiv:1409.8226 [hep-ph]].

[11] T. Sjostrand, S. Mrenna, P.Z. Skands, "PYTHIA 6.4 Physics and Manual," JHEP 0605, 026 (2006) [arXiv:0603175 [hep-ph]].

[12] T. Sjostrand, S. Mrenna, P.Z. Skands, "A Brief Introduction to PYTHIA 8.1," Comput.Phys.Commun. 178, 852-867 (2008) [arXiv:0710.3820 [hep-ph]].

[13] M. Cirelli, G. Corcella, A. Hektor, G. Hutsi, M. Kadastik, and others, "PPPC 4 DM ID: A Poor Particle Physicist Cookbook for Dark Matter Indirect Detection," JCAP 1103, 051 (2011) [arXiv:1012.4515 [hep-ph]].

[14] H. Goldberg, "Constraint on the Photino Mass from Cosmology," Phys. Rev. Lett. 50, 1419 (1983).

[15] N.F. Bell,J.B. Dent, T.D. Jacques, T.J. Weiler, "Electroweak Bremsstrahlung in Dark Matter Annihilation," Phys. Rev. D78, 083540 (2008) [arXiv:0805.3423 [hep-ph]].

[16] N.F. Bell, J.B. Dent, ,A.J. Galea, T.D. Jacques, L.M. Krauss, and others, "W/Z Bremsstrahlung as the Dominant Annihilation Channel for Dark Matter, Revisited," Phys. Lett. B706, 6-12 (2011) [arXiv:1104.3823 [hep-ph]].

XENON100 Results on WIMP and non-WIMP Searches

Nadav Priel on behalf of the XENON collaboration

Department of Particle Physics and Astrophysics, Weizmann Institute of Science, Rehovot, Israel

DOI: http://dx.doi.org/10.3204/DESY-PROC-2014-03/priel_nadav

XENON100 is the second phase of the XENON direct Dark Matter search program. It consists of an ultra-low background double phase (liquid-gas) xenon filled time projection chamber, and is installed at the Laboratori Nazionali del Gran Sasso. The results from the 224.6 live days of data taken between March 2011 and April 2012 are reported. The experiment sets one of the most stringent limits on the WIMP-nucleon spin-independent cross section, and the most stringent limit on the spin-dependent WIMP-neutron interaction. With the same dataset, XENON100 sets the best limit to date on the axion coupling to electrons for solar and for galactic axions.

1 Introduction

The Λ-Cold Dark Matter model states that only 5% of the energy of our universe comes from Baryonic matter. The remaining is split into *Dark Energy* (≈68%) and non-Baryonic *Dark Matter* (≈ 27%).

The nature of Dark Matter (DM) is still unknown, and possible candidates arise naturally in several extensions of the Standard Model of particle physics. Weakly Interacting Massive Particles (WIMPs) are the most prominent ones since they are cold, neutral, and can produce the correct relic density of DM observed today. Another prominent class of candidates are Axion-Like Particles (ALPs) generated in a non-thermal production mechanism in the early universe.

The several phases of underground detectors that constitute the XENON program is located at the Laboratori Nazionali del Gran Sasso (LNGS), Italy, at an average depth of 3600 m water equivalent. The ever growing detectors search for DM by detecting its scattering off a liquid xenon (LXe) atom, that leaves both ionization and excitation traces in the liquid. The current phase, XENON100, has been successfully operating since 2009 and achieved unprecedented sensitivity on WIMP-nucleon cross section [1], and on axion-electron coupling [2]. The next phase of the program, XENON1T, is a ton scale detector. XENON1T is in an advanced construction phase, and will become operational in the near future.

2 XENON100

The operational principle of XENON100 is depicted in Fig. 1. The detector is a double-phase time projection chamber (TPC), filled with 62 kg of LXe. A total of 178 low radioactivity, UV-sensitive photomultiplier tubes (PMTs) measure signals induced by particles interacting in the sensitive volume. An interaction in the detector produces both scintillation photons and ionization electrons. The electrons, moved from the interaction point by a 530 V/cm electric, are extracted from the liquid and accelerated in the gas by a 12 kV/cm field, producing proportional scintillation light. The direct scintillation signal ($S1$) and the amplified charge signal ($S2$) are detected by the PMTs. The time difference between the $S1$ and the $S2$ signals is used to estimate the z-coordinate of the interaction, while the $S2$-hit-pattern on the PMTs is employed to estimate the (x , y) - coordinate. In addition, the $S2/S1$ ratio, serves as a separator between the expected WIMP-induced nuclear recoil events (NR) and the electromagnetic induced events (ER). A detailed description of the instrument is given in [3].

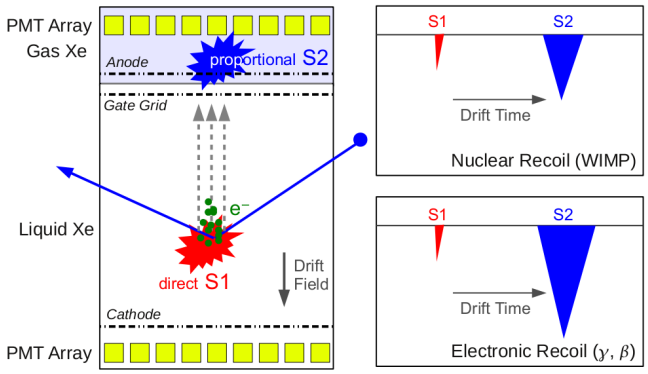

Figure 1: Operational principle of the XENON TPC. The ratio S2/S1 provides separation between nuclear and electromagnetic recoils.

3 WIMP search

The XENON100 data presented here, includes 34 kg fiducial mass and 224.6 live days, collected between March 2011 and April 2012. Compared to the previous data set, this run has a longer exposure, a significantly lower intrinsic ^{85}Kr contamination, an improved electronic noise condition and a lower trigger threshold.

The expected background comes from the leakage of ER events (originating from the detector materials and from intrinsic radioactivity), and by NRs induced by neutrons. The ER background is estimated from calibration data, while the NR background is determined by a detailed Monte Carlo simulation.

A Profile Likelihood (PL) approach is used to test the background-only and signal hypotheses. The systematic uncertainties in the energy scale and in the background expectation are treated as nuisance parameters and represented in the limit. Poisson fluctuations in the number of PEs dominate the S1 energy resolution and are also taken into account along with the single

PE resolution of the PMTs. For the signal model, we assume an isothermal halo with a local density of 0.3 GeV/cm^3, a local circular velocity of 220 km/s, and a Galactic escape velocity of 544 km/s.

WIMPs in the halo of our Galaxy are non-relativistic and their interactions with nuclei can be characterized in terms of scalar (or spin-independent, SI) and axial-vector (or spin-dependent, SD) couplings. This led to the 90% confidence level (CL) limits shown in Fig. 2 for spin-independent, and in Fig. 3 for spin-dependent interactions. The $1\sigma(2\sigma)$ uncertainty on the sensitivity of this run is shown as a green(yellow) band.

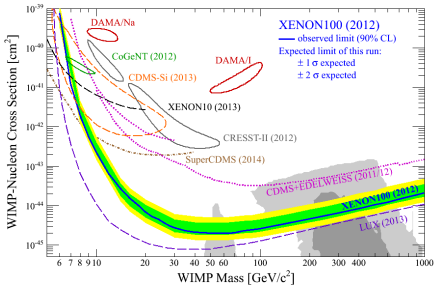

Figure 2: Spin-independent WIMP-nucleon cross section exclusion limit (90% CL) [1].

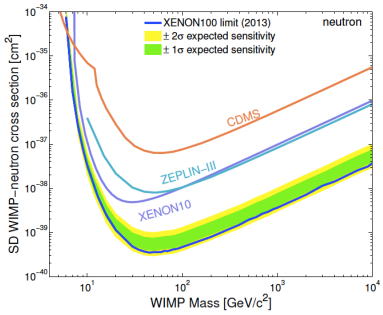

Figure 3: Spin-dependent WIMP-neutron cross section exclusion limit (90% CL) [4].

4 Axion searches

Axions were introduced in the Peccei-Quinn solution of the strong CP problem as pseudo-Nambu-Goldstone bosons emerging from the breaking of a global U(1) symmetry. Although this original model has been ruled out, "invisible" axions (arising from a higher symmetry-breaking energy scale) are still allowed, as described, for example, in the DFSZ and KSVZ models. In addition to QCD axions, axion-like particles (ALPs) are pseudoscalars that do not necessarily solve the strong CP problem, but which have been introduced by many extensions of the Standard Model of particle physics. Axions as well as ALPs are well motivated cold dark matter candidates.

The Sun is an intense source of axions and ALPs, where they can be produced via Bremsstrahlung, Compton scattering, axio-recombination and axio-deexcitation [5] (referred to as solar axions). Additionally, searches can be conducted for ALPs that may have been generated via a non-thermal production mechanism in the early universe and which now constitute the dark matter in our galaxy (referred to as galactic ALPs).

Axions and ALPs may give rise to observable signatures in XENON100 through their coupling to electrons. The coupling g_{Ae}, may be tested via scattering off the electron of a target, through the axio-electric effect [6]. This process is the analogue of the photo-electric effect with the absorption of an axion instead of a photon.

We report on the first axion searches performed with the XENON100 detector, using the same data set used for the WIMP-searches, with an exposure of 224.6 live days and 34 kg

fiducial mass. The expected interaction rate is obtained by the convolution of the flux and the axio-electric cross section. The solar axion flux has recently been recalculated in [5]. This incorporates four production mechanisms that depend upon g_{Ae}: Bremsstrahlung, Compton scattering, atomic recombination, and atomic deexcitation. For ALPs in the galaxy, assuming that they constitute the whole dark matter halo density ($\rho_{DM} \sim 0.3$ GeV/cm^3), the total flux is given by $\phi_{\rm ALP} = c\beta_A \times \rho_{DM}/m_A$, where m_A is the ALP mass.

Fig.4 shows the new XENON100 exclusion limit on g_{Ae}, at 90% CL [2]. The sensitivity is shown by the green/yellow band ($1\sigma/2\sigma$). For comparison, we also present recent experimental constraints. Astrophysical bounds and theoretical benchmark models are also shown. For solar axions with masses below 1 keV/c^2, XENON100 is able to set the strongest constraint on the coupling to electrons, excluding values of g_{Ae} larger than 7.7×10^{-12} (90% CL).

Fig.5 shows the XENON100 90% CL exclusion limit [2]. The XENON100 result is shown compared to other experimental constraints. Astrophysical bounds and a theoretical benchmark model are also presented. The expected sensitivity is shown by the green/yellow bands ($1\sigma/2\sigma$). In the 5 - 10 keV/c^2 mass range, XENON100 sets the best upper limit, excluding an axion-electron coupling $g_{Ae} > 1 \times 10^{-12}$ at the 90% CL, assuming that ALPs constitute all of the galactic dark matter.

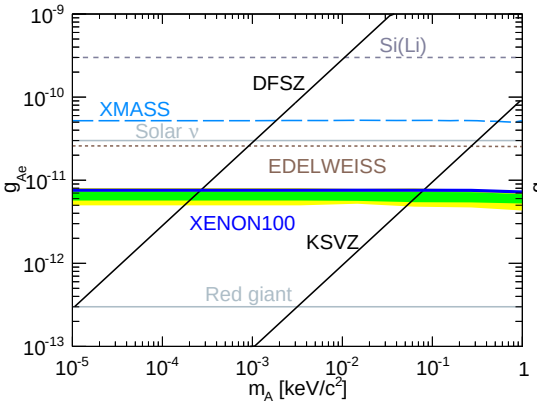

Figure 4: XENON100 limit (90% CL) on solar axions [2].

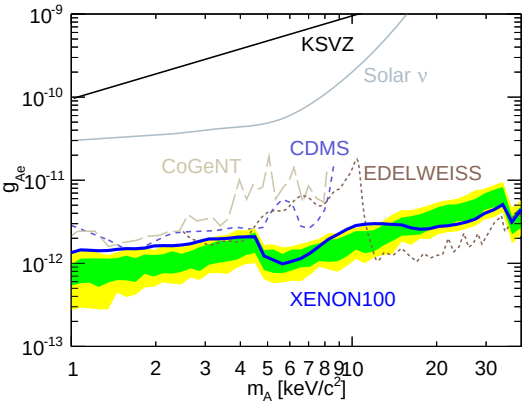

Figure 5: XENON100 limit (90% CL) on galactic ALPs [2].

References

[1] E. Aprile *et al.* [XENON100 Collaboration], Phys. Rev. Lett. **109** (2012) 181301 [arXiv:1207.5988 [astro-ph.CO]].

[2] E. Aprile *et al.* [XENON100 Collaboration], Phys. Rev. D **90** (2014) 062009 [arXiv:1404.1455 [astro-ph.CO]].

[3] E. Aprile *et al.* [XENON100 Collaboration], Astropart. Phys. **35** (2012) 573 [arXiv:1107.2155 [astro-ph.IM]].

[4] E. Aprile *et al.* [XENON100 Collaboration], Phys. Rev. Lett. **111** (2013) 2, 021301 [arXiv:1301.6620 [astro-ph.CO]].

[5] J. Redondo, JCAP **1312** (2013) 008 [arXiv:1310.0823 [hep-ph], arXiv:1310.0823].

[6] S. Dimopoulos, G. D. Starkman and B. W. Lynn, Mod. Phys. Lett. A **1** (1986) 491.

First results from CRESST-II Phase 2

Raimund Strauss[1], *for the CRESST Collaboration*

[1]Max-Planck-Institut für Physik, D-80805 München, Germany

DOI: http://dx.doi.org/10.3204/DESY-PROC-2014-03/strauss_raimund

The CRESST-II (Cryogenic Rare Event Search with Superconducting Thermometers) experiment, currently in its second phase, aims at the direct detection of WIMPs. Compared to previous runs the intrinsic radiopurity of $CaWO_4$ crystals and the capability to reject recoil events from alpha-surface contamination were significantly improved. Data from 29 kg-days of exposure acquired by a single $\sim$ 250 g $CaWO_4$ detector provide competitive limits on the spin-independent WIMP-nucleon cross section, particularly for low-mass WIMPs, and probe a new region of parameter space for WIMP masses below 3 GeV/c^2.

1 Introduction

Direct searches for dark matter in form of Weakly Interacting Massive Particles (WIMPs) have significantly improved the sensitivity to spin-independent WIMP-nucleon scattering within the last two decades. Possible hints for low-mass WIMPs with masses of $\mathcal{O}(10\,\mathrm{GeV/c^2})$ which recently arose [1, 2, 3, 4] are, however, clearly excluded by a variety of experiments [5, 6, 7, 8, 9, 10]. During the last years, these non-conclusive experimental results and theoretical dark matter models (see e.g. [11]) drew the attention to WIMPs with masses of $\lesssim 10\,\mathrm{GeV/c^2}$.

2 Results of the detector module TUM40

The CRESST-II (Cryogenic Rare Event Search with Superconducting Thermometers) experiment uses scintillating $CaWO_4$ crystals as target material for dark matter particles [1]. The modular detectors of 200-300 g each are based on a two-channel detector readout: 1) The target crystal itself is operated as a cryogenic detector at mK temperatures to measure the total deposited energy of particle interactions. This phonon channel is read-out by transition edge sensors (TES) realized by thin W-films. 2) A separate light detector (silicon-on-sapphire disc), also equipped with a TES, measures the scintillation light output induced by particles. Due to light quenching [12] this additional information provides identification of the type of particle interaction. Thus, beta/gamma background events can be discriminated from possible WIMP-induced nuclear-recoil events which, to a certain extent, can further be tagged as O, Ca and W recoils [13].

CRESST-II Phase 2 has started in July 2013 with a total target mass of $\sim$ 5 kg using 18 detector modules of four different detector designs [15]. In this paper, one single detector module (called TUM40) of a new design, with the best performance among the detectors installed in CRESST-II Phase 2, is described. A block-shaped $CaWO_4$ crystal with a mass of 249 g is held by sticks made of $CaWO_4$, for details see [14]. Together with a polymeric foil the sticks provide a

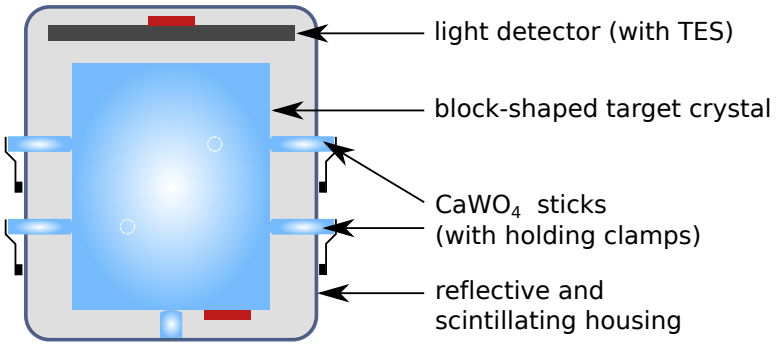

Figure 1: Scheme of the new detector module based on $CaWO_4$ sticks fed through the scintillating housing (polymeric foil). Inside the housing only scintillating material is present in order to reject surface-alpha background, see [14]. Unlike in the conventional design the bronze clamp are located outside.

detector housing with fully-scintillating inner surface (see Fig. 1). Using this design, previously observed backgrounds from surface-alpha decays are rejected with high efficiency [14]. For the first time, $CaWO_4$ crystals from in-house production at the Technische Universität München [16] are operated in the CRESST-II setup. Using one of these crystals, the intrinsic background level could be reduced significantly to an average beta/gamma rate of 3.44/[kg keV day] in the region of interest at 1-40 keV [17, 18]. An energy threshold of $\sim$ 600 eV and a resolution of σ_{ph}=(0.090±0.010) keV (at 2.60 keV) were reached with TUM40. With the silicon-on-sapphire light detectors (diameter: 40 mm, thickness: 500 μm) used, a baseline resolution of $\sigma_l \sim 5$ eV is achieved.
In the first TUM40 data with 29 kg-days of exposure, all events observed in the region-of-interest for dark matter search are compatible with leakage of beta/gamma background. No indications for additional events above this background are observed. Therefore, a limit on the spin-independent WIMP-nucleon scattering cross section is derived (see Fig. 2) [17]. A new region of parameter space for WIMP masses below 3 GeV/c^2 is probed. An excess signal as observed by the previous results of CRESST-II [1] is not confirmed.

3 Conclusion and Outlook

The results of CRESST-II Phase 2 [17] demonstrate the potential of phonon-light detectors using scintillating crystals, in particular, for low-mass WIMP search. A new detector concept which provides an efficient veto against surface-alpha backgrounds has been successfully operated in the CRESST setup. The first data of CRESST-II Phase 2 with a moderate exposure of 29 kg-days acquired by a single detector module set a new limit on spin-independent WIMP-nucleon scattering cross section. A new region of parameter space is probed for WIMP masses below 3 GeV/c^2.
Concerning the search for higher WIMP masses ($\gtrsim$ 10 GeV/c^2), the discrimination capability of the present detector performance is sufficient. Above an energy of $\sim$ 12 keV, no leakage of beta/gamma events is expected in CRESST-II detectors of this new design, even for a possible ton-scale experiment ($< 10^{-4}$ events per detector and year [18]) as far as no other backgrounds

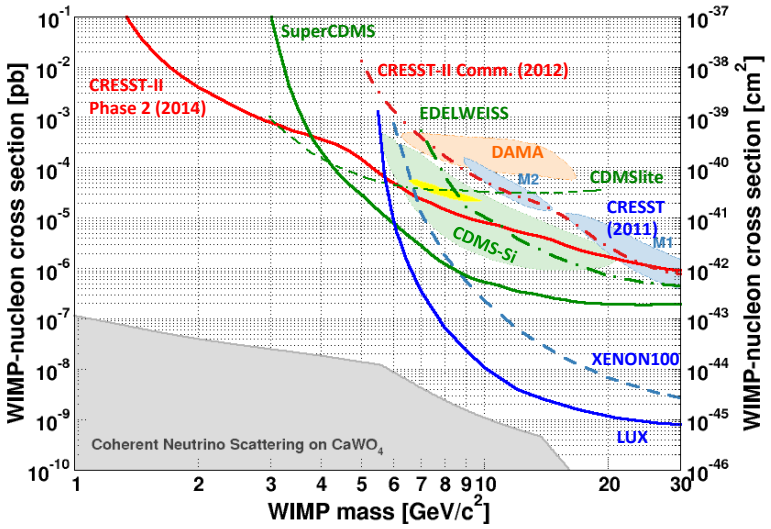

Figure 2: Spin-independent WIMP-nucleon cross section plotted against the WIMP mass with selected experimental results from direct dark matter searches [1, 2, 4, 5, 6, 7, 8, 9, 10]. The results of CRESST-II Phase 2 [17] (red full line) give the presently best limit below WIMP masses of $\sim$3 GeV/c^2. It disfavours a WIMP-interpretation of the previous results of CRESST-II [1].

appear.
To increase the sensitivity to low-mass WIMPs (masses below 10 GeV/c^2) the performance of the detectors must be further improved. In particular, efforts to reduce the energy threshold, to improve the optical quality of the $CaWO_4$ crystals and to lower the background level are ongoing. There is a high potential to further investigate the low-mass WIMP region with future CRESST detectors and, for the first time, sensitivities to detect coherent neutrino-nucleus scattering might be in reach with exposures of $\sim$ 300 kg-years [19].

Acknowledgments

This research was supported by the DFG cluster of excellence: Origin and Structure of the Universe, the DFG Transregio 27: Neutrinos and Beyond, the Helmholtz Alliance for Astroparticle Phyiscs, the Maier-Leibnitz-Laboratorium (Garching), the Science & Technology Facilities Council (UK) and by the BMBF: Project 05A11WOC EURECA-XENON. We are grateful to LNGS for their generous support of CRESST, in particular to Marco Guetti for his constant assistance.

References

[1] G. Angloher, et al., Eur.Phys.J. **C72**(4), 1 (2012)

[2] R. Bernabei, et al., Eur.Phys.J. **C67**, 39 (2010)

[3] C. Aalseth, et al., (2012). URL `http://arxiv.org/abs/1208.5737`

[4] R. Agnese, et al., Phys. Rev. Lett. **111**, 251301 (2013)
[5] D. Akerib, et al., Phys.Rev.Lett. **112**, 091303 (2014)
[6] E. Aprile, et al., Phys.Rev.Lett. **109**, 181301 (2012)
[7] R. Agnese, et al., Phys.Rev.Lett. **112**, 241302 (2014)
[8] R. Agnese, et al., Phys.Rev.Lett. **112**, 041302 (2014)
[9] E. Armengaud, et al., Phys.Rev. **D86**, 051701 (2012)
[10] A. Brown, S. Henry, H. Kraus, C. McCabe, Phys. Rev. D **85**, 021301 (2012)
[11] P. Cushman, et al., (2013). URL `http://arxiv.org/abs/arXiv:1310.8327`
[12] J. Birks, *The Theory and Practice of Scintillation Counting* (Pergamon Press, 1964)
[13] R. Strauss, et al., Eur.Phys.J. **C74**(7), 2957 (2014)
[14] R. Strauss, et al., (2014). URL `http://arxiv.org/abs/1410.1753`
[15] F. Reindl, et al., *Astropart., Part., Space Phys. and Detect. for Phys. Appl.* (2014), chap. 45, pp. 290–296
[16] A. Erb, J.-C. Lanfranchi, CrystEngComm **15**, 2301 (2013)
[17] G. Angloher, et al., (2014). URL `http://arxiv.org/pdf/1407.3146v1.pdf`
[18] R. Strauss, et al., to be published (2014)
[19] A. Gütlein, et al., (2014). URL `http://arxiv.org/abs/1408.2357`

Chapter 2

Axion Dark Matter and Searches for Axions and WISPs

Axion Dark Matter at the Time of Big Bang Nucleosynthesis

Raffaele Tito D'Agnolo[1]

[1]School of Natural Sciences, Institute for Advanced Study, Princeton, NJ, 08540

DOI: http://dx.doi.org/10.3204/DESY-PROC-2014-03/dagnolo_raffaeletito

We discuss a new constraint on the parameter space of axion dark matter that was first presented in [1]. The axion increases the neutron-proton mass difference at neutron freeze-out. The precise measurements of ^{4}He produced during Big Bang Nucleosynthesis (BBN) sets meaningful bounds on its parameter space.

1 Introduction

In 1977 Peccei and Quinn proposed what would become the classic solution to the strong CP problem [2, 3]. Later it was noted by Weinberg and Wilczek that it implied the existence of a light degree of freedom, the axion [4, 5]. If a $U(1)$ symmetry, anomalous under QCD, is spontaneously broken at an high scale f_a, the QCD θ parameter

$$\mathcal{L}_{QCD} \supset -\frac{\theta}{32\pi^2} G^{a\mu\nu}\tilde{G}^a_{\mu\nu}\,, \tag{1}$$

can dynamically be set to zero through the minimization of the axion (the $U(1)$ pseudo-Goldstone boson) potential.

The axion is a motivated dark matter candidate [6]. In this work we focus on relic axions produced through the so-called misalignment mechanism [7, 8, 9, 10]. In order to solve the strong CP problem, the leading contribution to the axion potential must come from the QCD chiral anomaly. This contribution is generated during the QCD phase transition and earlier in the history of the universe we can consider the axion potential to be zero. As it turns on, the initial condition for the axion field does not need to coincide with the minimum of the potential. So after the QCD phase transition the axion can be described as an oscillating classical field

$$a(t) = a_0 \cos(m_a t) = \frac{\sqrt{2\rho_{DM}}}{m_a}\cos(m_a t)\,, \tag{2}$$

with an amplitude proportional to the initial misalignment. In the last equality we fix the initial condition by requiring that the axion makes up all of the observed dark matter energy density ρ_{DM}. In the simple setting described above, the axion mass m_a is not a free parameter, but is given by the QCD relation $f_a\, m_a = f_\pi m_\pi \sqrt{m_u m_d}/(m_u + m_d)$ [4, 5], in terms of the decay constant f_a. However axion-like particles for which this equality is violated are common in a variety of models [11, 12]. For brevity in the following we designate with "axion" both the QCD axion and these generalizations.

As stated above the axion coupling to gluons is the one responsible for the solution of the strong CP problem. Current constraints on this coupling leave open many orders of magnitude to m_a and f_a. The axion interactions with the electromagnetic field are more strongly constrained [6], but the coupling is much more model dependent and given an f_a can span over orders of magnitude. Therefore we find interesting to explore in more detail axion-gluon interactions. This is particularly important in view of the recent proposal of new experiments aimed at detecting these interactions [15, 16]. In the next section we show how the measurement of the primordial ^{4}He abundance greatly limits the parameter space available to the axion, largely overlapping with the projected sensitivity of the proposed experiments. We conclude by giving a fine-tuning argument that disfavors an even larger fraction of this parameter space.

2 The three graces of Big Bang Nucleosynthesis

Big Bang Nucleosynthesis is an ideal setting for constraining axion dark matter for three simple physical reasons. First, the effects of the axion field are amplified by the redshirting of the axion field $a \sim \sqrt{\rho_{DM}} \sim (1+z)^{3/2}$, $z_{\rm BBN} \approx 10^{10}$. Second we have precise measurements of quantities generated at that time. For instance, the fractional error on ^{4}He abundance, Y_p, is $\delta Y_p/Y_p \approx 10\%$ at 3σ [6]. Last and most important, Y_p is exponentially sensitive to the axion interaction with gluons. This was first shown in [1] following a known result on the constant QCD θ parameter [17]. Here we briefly review the steps that led to this conclusion.

The most general Lagrangian connecting the axion with Standard Model fields charged under $SU(3)_c$ can be written as

$$\mathcal{L} = -\frac{a}{f_a}\frac{G^a_{\mu\nu}\tilde{G}^{a\mu\nu}}{32\pi^2} - \frac{\partial_\mu a}{f_a}\sum_\psi c_\psi \bar{\psi}\bar{\sigma}^\mu\psi\,, \tag{3}$$

where we have ignored possible flavor violation in the c_ψ's that is irrelevant for what follows. We have indicated with ψ all possible quark fields taken as left-handed Weyl spinors. Using the methods of Chiral Perturbation Theory it is easy to show that these interactions, below the QCD confinement scale, generate

$$\mathcal{L}_{\rm QCDCh} \supset \quad -\tfrac{1}{2}\tfrac{f_\pi^2 m_\pi^2 m_u m_d}{(m_u+m_d)^2}\left(\tfrac{a}{f_a}\right)^2 \tag{4}$$

$$- \quad \bar{N}\pi\cdot\sigma\left(i\gamma^5 g_{\pi NN} - 2\,\bar{g}_{\pi NN}\tfrac{a}{f_a}\right)N \tag{5}$$

$$+ \quad \tfrac{f_\pi\,\bar{g}_{\pi NN}}{2}\tfrac{m_d-m_u}{m_d+m_u}\left(\tfrac{a}{f_a}\right)^2\bar{N}\sigma^3 N\,. \tag{6}$$

where we have introduced the nucleon field $N = (p\ n)^T$ and the pions π. Clearly there are many more terms in the QCD Chiral Lagrangian that contain also the axion, but the three above are sufficient for our purposes. The first is the axion mass term mentioned in the introduction, the second generates an oscillating nucleon electric dipole moment (EDM) at one loop [18] that the experiments in [15, 16] intend to detect. The third and last term generates a neutron-proton mass difference

$$m_n - m_p = Q_0 + \delta Q\,,$$
$$\delta Q \approx \tfrac{f_\pi\,\bar{g}_{\pi NN}}{2}\left(\tfrac{m_d-m_u}{m_d+m_u}\right)\left(\tfrac{a}{f_a}\right)^2 \approx (0.37\ \text{MeV})\left(\tfrac{a}{f_a}\right)^2\,, \tag{7}$$

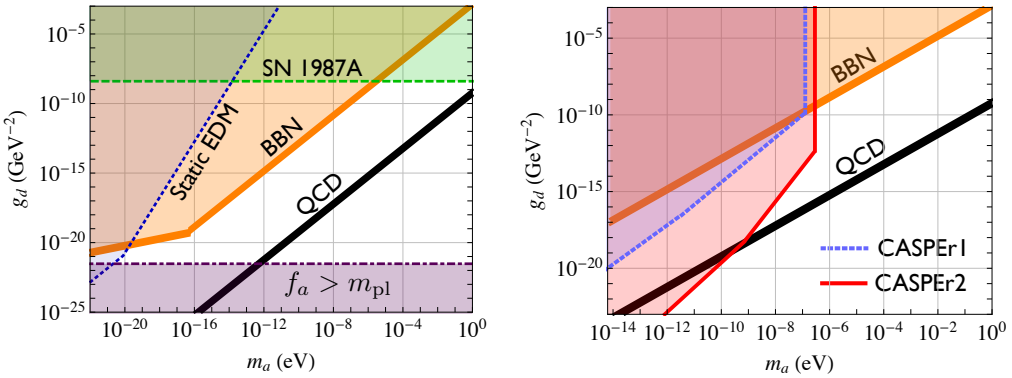

Figure 1: Taken from [1]. Left panel: In orange we show the BBN excluded region in the (g_d, m_a) plane. The blue shaded region is excluded by static EDM searches. The green region from excess SN 1987A cooling. Both were estimated conservatively in [16, 19]. We shade in purple the area where $f_a > m_{\rm pl}$. Right panel: The projected sensitivity of the oscillating EDM search of [15, 16]. CASPEr1 and CASPEr2 are the two generations of the experiment. The black line in both panels represents the QCD axion, $f_a\, m_a \approx \Lambda^2_{\rm QCD}$.

where we have taken $\bar{g}_{\pi NN} \approx 0.023$ as measured from baryon decays [17, 18]. It is this effect that feeds into the measured ^{4}He abundance though the neutron to proton ratio at freeze-out, $(n/p)_{\text{freeze-out}} \approx e^{-Q_{\rm F}/T_{\rm F}}$. Here Q_F is the value of $Q_0 + \delta Q$ at $T_F \approx 0.8$ MeV. The neutron to proton ratio stays approximately constant until the time of nucleosynthesis, when almost all neutrons bind into ^{4}He nuclei: $Y_p \approx 2(n/p)_{\rm Nuc}/(1 + (n/p)_{\rm Nuc})$.

Imposing conservatively $\delta Y_p/Y_p < 10\%$, we find the constraint $f_a\, m_a \gtrsim 10^{-9}$ GeV^2. A full numerical calculation gives $f_a\, m_a \gtrsim 1.3 \times 10^{-9}$ [1]. In the left panel of Figure 1 we compare this bound with known constraints from static EDM measurements [13, 14, 16] and the excess cooling of SN 1987A [19, 16] and in the right panel with the sensitivity of the experiments proposed in [15, 16]. Note that this comparison is meaningful because the c_ψ in the UV Lagrangian do not appear at leading order in f_π/f_a in (5) and (6). So the nucleon EDM and proton-neutron mass difference are dominated by the $G\tilde{G}$ coupling of the axion and thus proportional to each other. The y-axis is given by a rescaling of the axion decay constant $g_d \approx \big(2.4 \times 10^{-16}$ e cm$\big)/f_a$. We can clearly see that the bound adds on known results and strongly overlaps with the sensitivity of future experiments. For more details we refer to [1].

3 Conclusion and fine-tuning

We have shown that the measurement of the ^{4}He abundance from BBN sets a strong constraint on the axion dark matter parameter space. This bound overlaps with most of the sensitivity of projected experiments for the measurement of an oscillating nucleon EDM [15, 16].

It is worth to notice that the whole parameter space above the QCD line in Figure 1, albeit not excluded, is strongly disfavored by fine-tuning arguments. In that region $m_a \ll m_a^{\rm QCD}$, so we are implicitly adding a Lagrangian term $\Delta\mathcal{L}(a) \propto \delta m^2 (a + \delta\theta)^2$, to cancel the QCD contribution to the axion mass. The tuning required by the mass cancellation can be estimated

as: $\Delta_{mass} \sim f_a^2\, m_a^2 / f_\pi^2 m_\pi^2 \sim 10^{-14} \left(f_a\, m_a / 10^{-9}\ \mathrm{GeV}^2 \right)^2$. At the same time $\delta\theta$ must also be tuned to avoid reintroducing the strong CP problem. It is not possible to avoid these tunings by introducing multiple axions [1]. However the experiments in [15, 16] have a concrete chance of being built. Furthermore tuning arguments in other sectors of the Standard Model Lagrangian have started to appear less reliable since LEP and the trend seems to be confirmed by the LHC. So we find useful to give solid observational bounds such as the one discussed in this note.

Acknowledgments

The content of this work is based on [1] written together with Kfir Blum, Mariangela Lisanti and Benjamin R. Safdi. The author is supported by the NSF grant PHY-0907744.

References

[1] K. Blum, R. T. D'Agnolo, M. Lisanti and B. R. Safdi, "Constraining Axion Dark Matter with Big Bang Nucleosynthesis," arXiv:1401.6460 [hep-ph].

[2] R. D. Peccei and H. R. Quinn, "Constraints Imposed by CP Conservation in the Presence of Instantons," Phys. Rev. D **16** (1977) 1791.

[3] R. D. Peccei and H. R. Quinn, "CP Conservation in the Presence of Instantons," Phys. Rev. Lett. **38** (1977) 1440.

[4] S. Weinberg, "A New Light Boson?," Phys. Rev. Lett. **40** (1978) 223.

[5] F. Wilczek, "Problem of Strong p and t Invariance in the Presence of Instantons," Phys. Rev. Lett. **40** (1978) 279.

[6] K. A. Olive *et al.* [Particle Data Group Collaboration], "Review of Particle Physics," Chin. Phys. C **38** (2014) 090001.

[7] L. F. Abbott and P. Sikivie, "A Cosmological Bound on the Invisible Axion," Phys. Lett. B **120** (1983) 133.

[8] J. Preskill, M. B. Wise and F. Wilczek, "Cosmology of the Invisible Axion," Phys. Lett. B **120** (1983) 127.

[9] M. Dine and W. Fischler, "The Not So Harmless Axion," Phys. Lett. B **120** (1983) 137.

[10] M. S. Turner, "Cosmic and Local Mass Density of Invisible Axions," Phys. Rev. D **33** (1986) 889.

[11] J. Jaeckel and A. Ringwald, "The Low-Energy Frontier of Particle Physics," Ann. Rev. Nucl. Part. Sci. **60** (2010) 405 [arXiv:1002.0329 [hep-ph]].

[12] A. Arvanitaki, S. Dimopoulos, S. Dubovsky, N. Kaloper and J. March-Russell, "String Axiverse," Phys. Rev. D **81** (2010) 123530 [arXiv:0905.4720 [hep-th]].

[13] C. A. Baker, D. D. Doyle, P. Geltenbort, K. Green, M. G. D. van der Grinten, P. G. Harris, P. Iaydjiev and S. N. Ivanov *et al.*, "An Improved experimental limit on the electric dipole moment of the neutron," Phys. Rev. Lett. **97** (2006) 131801 [hep-ex/0602020].

[14] P. G. Harris, C. A. Baker, K. Green, P. Iaydjiev, S. Ivanov, D. J. R. May, J. M. Pendlebury and D. Shiers *et al.*, "New experimental limit on the electric dipole moment of the neutron," Phys. Rev. Lett. **82** (1999) 904.

[15] D. Budker, P. W. Graham, M. Ledbetter, S. Rajendran and A. Sushkov, "Cosmic Axion Spin Precession Experiment (CASPEr)," Phys. Rev. X **4** (2014) 021030 [arXiv:1306.6089 [hep-ph]].

[16] P. W. Graham and S. Rajendran, "New Observables for Direct Detection of Axion Dark Matter," Phys. Rev. D **88** (2013) 035023 [arXiv:1306.6088 [hep-ph]].

[17] L. Ubaldi, "Effects of theta on the deuteron binding energy and the triple-alpha process," Phys. Rev. D **81** (2010) 025011 [arXiv:0811.1599 [hep-ph]].

[18] R. J. Crewther, P. Di Vecchia, G. Veneziano and E. Witten, "Chiral Estimate of the Electric Dipole Moment of the Neutron in Quantum Chromodynamics," Phys. Lett. B **88** (1979) 123 [Erratum-ibid. B **91** (1980) 487].

[19] G. G. Raffelt, "Astrophysical axion bounds," Lect. Notes Phys. **741** (2008) 51 [hep-ph/0611350].

The Pressure of Misalignment Axions: a Difference from WIMPs in Galaxy Formation?

Sacha Davidson[1]

[1]IPN de Lyon/CNRS, Université Lyon 1, Villeurbanne, France

DOI: http://dx.doi.org/10.3204/DESY-PROC-2014-03/davidson_sacha

Two populations of axions can contribute to cold dark matter: the classical field produced via the misalignment mechanism, and the modes produced in the decay of strings. The classical field has extra pressure, as compared to WIMPs, which could have observable consequences in non-linear galaxy formation.

1 Introduction

It is interesting to study whether axion dark matter could be distinguished from WIMP dark matter, using Large Scale Structure (LSS) data. It is well known that axion dark matter can be composed of two components[1]: the misalignment axions and the non-relativistic modes radiated by strings (here taken to be cold particles). Both redshift like CDM, and grow linear density inhomogeneities like WIMPs. However, as pointed out by Sikivie [2], the misalignment axions have a different pressure from WIMPs, which could be relevant during non-linear stucture formation. The consequences of this additional pressure could be reliably addressed by the numerical galaxy formation community. The aim of this proceedings, which is based on [3], is to clarify the relevant variables and equations for studying non-linear stucture formation with axions.

There has been considerable confusion in the literature about whether axion dark matter is a Bose Einstein condensate. In a scenario proposed by Sikivie, the dark matter axions "thermalise" via their gravitational interactions, and therefore form a Bose Einstein condensate due to the high occupation number of the low momentum modes. Then, Sikivie and collaborators hypothesize that a galactic halo made of condensate could form vortices, which could be observed as caustics in the dark matter distribution. This interesting scenario, which proposes an observable signature for axion dark matter in LSS data, has been studied by many people: Saikawa and collaborators[4] confirmed in Q uantum Field Theory and General Relativity, the gravitational interaction rate estimated by Sikivie and collaborators. However, with Martin Elmer[5], we could not confirm that the interaction rate was a thermalisation rate (= generated entropy). Rindler-Daller and Shapiro[6] studied rotating halos of non-relativistic scalar field, and found that vortices were energetically favoured for much lighter bosons than the QCD axion, or for scalars with repulsive self-interactions (opposite to axions, whose self-interactions are attractive). This proceedings will argue that the notion of Bose Einstein condensation is an unneccessary confusion, somewhat akin to trying to describe a classical electromagnetic field in terms of photons. The misalignment axions are a classical scalar field, as such they have a

different pressure from WIMPs, and this could allow them to leave distinctive features in LSS data. First, I review the formalism and results of [3], and discuss the relation to Bose Einstein condensation after eqn (1).

Structure formation within the horizon is a classical gravity problem, so at first sight, a Quantum Field Theory treatment seems unneccessary. However, the classical field and classical particle limits of a QFT are different, and dark matter axions are composed of both. So to obtain a self-consistent and well-defined formalism, where approximations can be catalogued, and particles and fields can be included simultaneously, this proceedings starts from the path integral. A very beautiful earlier treatment of axion dark matter in field theory is [7]. We will find that it is straightforward to describe axion dark matter as a classical field (the misalignment axions) plus cold axion particles (produced by strings). The leading order gravitational interactions of the axion field and particles are simply found by computing their contributions to the stress-energy tensor. And while cold axion particles, in the limit of negligeable velocity, have the stress-energy as WIMPs, the classical axion field has extra contributions to the pressure, which could be relevant during non-linear stucture formation.

Finally, in section 3, I discuss the rate at which gravity can move axions between the field and the cold particle bath.

2 Formalism

From a theoretical perspective, it should be true that "the path integral knows everything": our world is usually at a saddle-point of the effective action. This perspective is rarely useful, because the path integral cannot be solved. However, I imagine to follow it here for two reasons: first, it gives an formal framework which can describe all aspects of axion behaviour, and second, the axion is so feebly coupled that the path integral could be computed pertubatively, which organises the various corrections to the classical= leading order solutions.

I imagine to write the path integral for the axion field, and evalulate it in a closed-time-path (CTP) formalism, as a perturbative expansion in Newton's constant G_N and the axion self-interaction parameter m_a^2/f_{PQ}^2. The path integral offers to decribe axions via n-point functions. I am particularily interested in the one-point function, which is the classical axion field, and the two-point function, which in CTP formalism includes the number distribution f of axion particles. Higher point functions can be neglected because the axion is so feebly coupled.

Next, equations of motion are required. Since we are interested in the gravitational interactions of axions, the leading order (= classical) equations are Einstein's Equations, with contributions to the stress-energy tensor from the axion field and particle density. These contributions will be obtained in second-quantised Field Theory in flat space-time, for simplicity. The details of the calculation can be found in [3]. The order G_N^2 effects will be discussed in section 3.

For cold axion particles, self-interactions are $\sim \lambda^2 \sim (m_a/f_{PQ})^4$ which is negligeable, so $T_{\mu\nu}$ has the form expected for non-relativistic non-interacting particles (the same as for WIMPs):

$$T_{\mu\nu} = \rho U_\mu U_\nu = \begin{bmatrix} \rho & -\rho\vec{v} \\ -\rho\vec{v} & \rho v^i v^j \end{bmatrix} \qquad \text{where} \qquad \rho(x) = \int \frac{d^3q}{(2\pi)^3} m_a f(x,q) \quad ,$$

which is the expected classical particle result, with matter four-velocity $U^\mu = (1, \vec{v})$.

For the non-relativistic classical field $\phi = \eta e^{-i(mt+S)}$, $T_{\mu\nu}$ is of the form

$$T_{\mu\nu} = \begin{bmatrix} \rho & -\rho\vec{v} \\ -\rho\vec{v} & \rho v^i v^j + \Delta T_{ij} \end{bmatrix} \qquad \begin{aligned} \Delta T_{ij} &= 2\partial_i\eta\partial_j\eta - \delta_{ij}\nabla\eta\cdot\nabla\eta \\ &\quad -\delta_{ij}\left(\rho|\vec{v}|^2 - 2m\eta^2\partial_t S + \lambda\eta^4\right) \end{aligned} \tag{1}$$

where $\rho \simeq 2m^2\eta^2$, $v_j \simeq \partial_j S/m$, and ΔT_{ij} is the extra pressure intrinsic to the classical scalar field. There is a part related to the field gradients, sometimes refered to as "quantum pressure"[8], and a part due to self-interactions, which is linear in the four-axion coupling $\lambda = -m_a^2/(12f_{PQ}^2)$. Since the self-interaction pressure of axions is *negative*, it causes axions to clump (like gravity). Rindler-Daller and Shapiro [6] argue that this negative pressure discourages vortices in axion halos.

Notice that the pressure excess ΔT_{ij} arises because the misalignment axions are a classical field. There is no additional requirement of "bose einstein condensation". In calculations, Bose Einstein condensates are described at leading order as non-relativistic classical fields[8]; since this is what the misalignment axions are, one could also say the misalignment axions are a bose einstein condensate. However, in my opinion, this comes with baggage of un-useful [1] intuitions from classical equilibrium statistical mechanics, and from well-known strongly interacting Bose Einstein condensates such as ^4He. So its simpler and clearer to refer to misalignment axions as a classical scalar field.

The pressure excess ΔT_{ij} confirms Sikivie's expectation that axions could differ from WIMPs during non-linear structure formation. This can most easily be seen from the "continuity" and "Euler" equations obtained from $T^{\nu\mu}_{\ ;\mu} = 0$:

$$\begin{aligned} \partial_t\rho + \nabla\cdot(\rho\vec{v}) &= 0 && \text{continuity} \\ \rho\partial_t\vec{v} + \rho(\vec{v}\cdot\nabla)\vec{v} &= -\rho\nabla\psi - \rho\nabla Q - \nabla P_{SI} && \text{Euler} \quad , \end{aligned}$$

where ψ is the Newtonian gravitational potential, $Q = -\frac{1}{2m\eta}\nabla^2\eta$ describes the "quantum kinetic energy" related to the "quantum pressure" of the classical field, and $P_{SI} = 2\lambda\eta^4$ is proportional to the pressure arising from the Self Interactions of the field. The point is that the extra pressures generate extra forces on the dark matter distribution. It would be interesting to numerically simulate galaxy formation using fluid equations for the dark matter, rather than N-body. This could allow to identify differences between galaxies made of classical axion field versus cold particles.

3 Gravitational evaporation of the field?

An important question remains, before studying galaxy formation in the the presence of the classical axion field: can gravity move axions between the field and the particle bath? One could imagine that during violent moments of galaxy formation, the field gets stirred up, and evaporates into particles. Or maybe the particles condense to the field, due to their high occupation numbers?

This process of "decay" of the field into particles should arise somewhere in the path integral formalism. For instance, in the case of a $\lambda\phi^4$ interaction, this "decay" of the field will arise as an

[1] Statistical mechanics is un-useful because its about the classical particle limit of QFT, and ^4He is a poor analogy because axions are feebly coupled.

imaginary part of loop corrections to the potential, in a 2 Particle Irreducible Closed-Time-Path evaluation of the path integral. A more simple-minded estimate was performed in [3].

First, notice that classical gravity, at $\mathcal{O}(G_N)$, does not move the particles between the field and the bath, because the field and particles contribute independently to the stress-energy tensor:

$$T_{\mu\nu} = T^{(\phi_c)}_{\mu\nu} + T^{(part)}_{\mu\nu} \quad .$$

Then, one can estimate the $\mathcal{O}(G_N^2)$ cross-section for axion scattering via graviton exchange, $aa \to aa$. If one of the incident axions is in the classical field, and both final state axions are free particles, this would correspond to field "evaporation. The cross-section is infra-red divergent, so the choice of infra-red cut-off is crucial. I claim that a reasonable IR cutoff is the inverse axion momentum, because on much larger distances, the graviton will not see individual axions, but rather will interact coherently with a large number of axions. Therefore the the two-axion scattering process, $aa \to aa$, only occurs when the momentum exchange is of order the axion momentum. In this case, the rate for the field to evaporate to particles via gravitational interactions is found to be negligeably small, because it is suppressed by $(m_a/m_{pl})^3$.

4 Summary

The axion misalignment field has additional contributions to the pressure, as compared to a bath of cold particles. This is automatic, no dynamical process of Bose Einstein condensation is required. As suggested by Sikivie, this extra pressure could give observational signatures in the structure of galaxies. It would be interesting to numerically simulate galaxy formation with a fluid code which allowed the dark matter to have pressure, to discover whether galaxies made of axion dark matter look different.

References

[1] See the proceedings of K. Saikawa at this conference.

[2] P. Sikivie and Q. Yang, "Bose-Einstein Condensation of Dark Matter Axions," Phys. Rev. Lett. **103** (2009) 111301 [arXiv:0901.1106 [hep-ph]].

[3] S. Davidson, "Axions: Bose Einstein Condensate or Classical Field?," arXiv:1405.1139 [hep-ph].

[4] K. 'i. Saikawa and M. Yamaguchi, "Evolution and thermalization of dark matter axions in the condensed regime," Phys. Rev. D **87** (2013) 085010 [arXiv:1210.7080 [hep-ph]]. T. Noumi, K. 'i. Saikawa, R. Sato and M. Yamaguchi, "Effective gravitational interactions of dark matter axions," arXiv:1310.0167 [hep-ph].

[5] S. Davidson and M. Elmer, "Bose Einstein condensation of the classical axion field in cosmology?," JCAP **1312** (2013) 034 [arXiv:1307.8024].

[6] T. Rindler-Daller and P. R. Shapiro, "Finding new signature effects on galactic dynamics to constrain Bose-Einstein-condensed cold dark matter," arXiv:1209.1835 [astro-ph.CO]. *ibid.* "Angular Momentum and Vortex Formation in Bose-Einstein-Condensed Cold Dark Matter Haloes," arXiv:1106.1256 [astro-ph.CO]. *ibid.* "Vortices and Angular Momentum in Bose-Einstein-Condensed Cold Dark Matter Halos," arXiv:0912.2897 [astro-ph.CO].

[7] Y. Nambu and M. Sasaki, "Quantum Treatment Of Cosmological Axion Perturbations," Phys. Rev. D **42** (1990) 3918.

[8] F Dalfovo, S Giorgini, L.P. Pitaevskii, S. Stingari, "Theory of Bose-Einstein condensation in trapped gases", Rev. Mod Phyis. **71** (1999), 463.

New limit on the mass of 9.4-keV solar axions emitted in an M1 transition in ^{83}Kr nuclei

A.V. Derbin[2], *A.M. Gangapshev*[1], *Yu.M. Gavrilyuk*[1], *V.V. Kazalov*[1], *H.J. Kim*[5], *Y.D. Kim*[6], *V.V. Kobychev*[4], *V.V. Kuzminov*[1], *Luqman Ali*[5], *V.N. Muratova*[2], *S.I. Panasenko*[1,3], *S.S. Ratkevich*[1,3], *D.A. Semenov*[2], *D.A. Tekueva*[1], *S.P. Yakimenko*[1], *E.V. Unzhakov*[2]

[1] Institute for Nuclear Research, RAS, Moscow, Russia
[2] Petersburg Nuclear Physics Institute, St. Petersburg, Russia
[3] Kharkov National University, Kharkov, Ukraine
[4] Institute for Nuclear Research of NAS Ukraine, Kiev, Ukraine
[5] Department of Physics, Kyungpook National University, Daegu, Republic of Korea
[6] Institute of Basic Science, Daejeon, Republic of Korea

DOI: http://dx.doi.org/10.3204/DESY-PROC-2014-03/derbin_alexander

A search for resonant absorption of the solar axion by ^{83}Kr nuclei was performed using the proportional counter installed inside the low-background setup at the Baksan Neutrino Observatory. The obtained model independent upper limit on the combination of isoscalar and isovector axion-nucleon couplings $|g_3 - g_0| \leq 1.69 \times 10^{-6}$ allowed us to set the new upper limit on the hadronic axion mass of $m_A \leq 130$ eV (95% C.L.) with the generally accepted values S=0.5 and z=0.56.

1 Introduction

If axions do exist, then the Sun should be an intense source of these particles. In 1991 Haxton and Lee calculated the energy loss of stars along the red-giant and horizontal branches due to the axion emission in nuclear magnetic transitions in ^{57}Fe, ^{55}Mn, and ^{23}Na nuclei [1]. In 1995 Moriyama proposed experimental scheme to search for 14.4 keV monochromatic solar axions that would be produced when thermally excited ^{57}Fe nuclei in the Sun relax to its ground state and could be detected via resonant excitation of the same nuclide in a laboratory [2]. Searches for resonant absorption of solar axions emitted in the nuclear magnetic transitions were performed with ^{57}Fe, ^{7}Li and ^{83}Kr (see [3] and refs therein).

In this paper we present the results of the search for solar axions using the resonant absorption by ^{83}Kr nuclei [4]. The energy of the first excited $7/2^+$ nuclear level is equal to 9.405 keV, lifetime $\tau = 2.23 \times 10^{-7}$ s, internal conversion coefficient $\alpha = 17.0$ and the mixing ratio of 1 and 2 transitions is $\delta = 0.013$.

In accordance with indirect estimates the abundance of the krypton in the Sun (Kr/H) = 1.78×10^{-9} atom/atom [5] that corresponds to $N = 9.08 \times 10^{13}$ of ^{83}Kr atom per 1 g material in the Sun. The axion flux from a unit mass is equal

$$\delta\Phi(T) = N \frac{2\exp(-\beta_T)}{1 + 2\exp(-\beta_T)} \frac{1}{\tau_\gamma} \frac{\omega_A}{\omega_\gamma}, \quad (1)$$

where N - number of ^{83}Kr atoms in 1 g of material in the Sun, $\beta_T = E_\gamma/kT$, τ_γ - lifetime of the nuclear level, ω_A/ω_γ - represents the branching ratio of axions to photons emission. The ratio ω_A/ω_γ was calculated in [6, 7, 1] as

$$\frac{\omega_A}{\omega_\gamma} = \frac{1}{2\pi\alpha}\frac{1}{1+\delta^2}\left[\frac{g_0\beta + g_3}{(\mu_0 - 0.5)\beta + \mu_3 - \eta}\right]^2 \left(\frac{p_A}{p_\gamma}\right)^3, \tag{2}$$

where μ_0 and μ_3 - isoscalar and isovector magnetic moments, g_0 and g_3 - isoscalar and isovector parts of the axion-nucleon coupling constant g_{AN} and β and η - nuclear structure dependent terms.

In case of the ^{83}Kr nucleus, which has the odd number of nucleons and an unpaired neutron, in the one-particle approximation the values of β and η can be estimated as $\beta \approx$-1.0 and $\eta \approx$0.5.

In the hadronic axion models, the g_0 and g_3 constants can be represented in the form [8]:

$$g_0 = -\frac{m_N}{6f_A}[2S + (3F - D)\frac{1+z-2w}{1+z+w}], \tag{3}$$

$$g_3 = -\frac{m_N}{2f_A}[(D + F)\frac{1-z}{1+z+w}]. \tag{4}$$

where D and F denote the reduced matrix elements for the SU(3) octet axial vector currents and S characterizes the flavor singlet coupling. The parameter S characterizing the flavor singlet coupling still remains a poorly constrained one [3]. The most stringent boundaries ($0.37 \leq S \leq 0.53$) and ($0.15 \leq S \leq 0.5$) were found in [9] and [10], accordingly.

The axion flux was calculated for the standard solar model BS05 [11] characterized by a highmetallicity [12]. The differential flux at the maximum of the distribution is

$$\Phi_A(E_{M1}) = 5.97 \times 10^{23}\left(\frac{\omega_A}{\omega_\gamma}\right) \mathrm{cm}^{-2}\mathrm{s}^{-1}\mathrm{keV}^{-1}. \tag{5}$$

The width of the resulting distribution, which is described well by a Gaussian curve, is $\sigma =$ 1.2 eV. This value exceeds substantially the recoil-nucleus energy and the intrinsic and Doppler widths of the level of ^{83}Kr target nuclei. The cross section for resonance axion absorption is given by an expression similar to the expression for the photon-absorption cross section, the correction for the ratio ω_A/ω_γ being taken into account.

$$\sigma(E_A) = 2\sqrt{\pi}\sigma_{0\gamma}\exp\left[-\frac{4(E_A - E_M)^2}{\Gamma^2}\right]\left(\frac{\omega_A}{\omega_\gamma}\right), \tag{6}$$

where $\sigma_{0\gamma} = 1.22\times10^{-18}\mathrm{cm}^2$ is the maximum cross section of the γ -ray resonant absorption and $\Gamma = 1/\tau$. The total cross section for axion absorption can be obtained by integrating $\sigma(E_A)$ over the axion spectrum. The expected rate of resonance axion absorption by the ^{83}Kr nucleus as a function of ω_A/ω_γ, $(g_3 - g_0)$ and m_A can be represented in the form ($S = 0.5$, $z = 0.56$):

$$R_A[\mathrm{g}^{-1}\mathrm{day}^{-1}] = 4.23 \times 10^{21}(\omega_\mathrm{A}/\omega_\gamma)^2 \tag{7}$$

$$= 8.53 \times 10^{21}(g_3 - g_0)^4(p_A/p_\gamma)^6 \tag{8}$$

$$= 2.41 \times 10^{-10}(m_A)^4(p_A/p_\gamma)^6. \tag{9}$$

2 Experimental setup

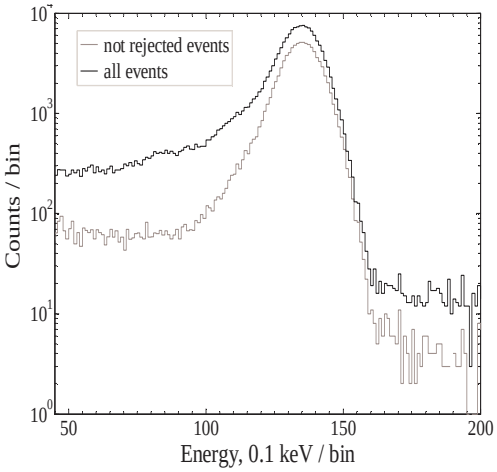

Figure 1: Original energy spectrum and spectrum after rejection of the events with pulse rise time $\geq 3.8\mu$s and $\lambda \leq 0.115$

To register γ-quantum and conversion electrons appearing after deexcitation of the ^{83}Kr nuclei a large proportional counter (LPC) with a casing of copper is used. The gas mixture Kr(99.55%)+Xe(0.45%) is used as working media, krypton consisted of 58.2% of ^{83}Kr. The LPC is a cylinder with inner diameters of 137 mm. A gold-plated tungsten wire of 10 μm in diameter is stretched along the LPC axis and is used as an anode. To reduce the influence of the counter edges on the operating characteristics of the counter, the end segments of the wire are passed through the copper tubes electrically connected to the anode. The fiducial length of the LPC is 595 mm, and the corresponding volume is 8.77 L. Gas pressure is 5.6 bar, and corresponding mass of the ^{83}Kr-isotope in fiducial volume of the LPC is 101 g.

The LPC is surrounded by passive shield made of copper (∼20 cm), lead (∼20 cm) and polyethylene (8 cm). The setup is located in the Deep Underground Low-Background Laboratory at BNO INR RAS [13], at the depth of 4900 m w.e., where the cosmic ray flux is reduced by $\sim 10^7$ times in comparison to that above ground, and evaluated as $(3.0 \pm 0.1) \times 10^{-9}$ cm^{-2}s^{-1} [14].

3 Results

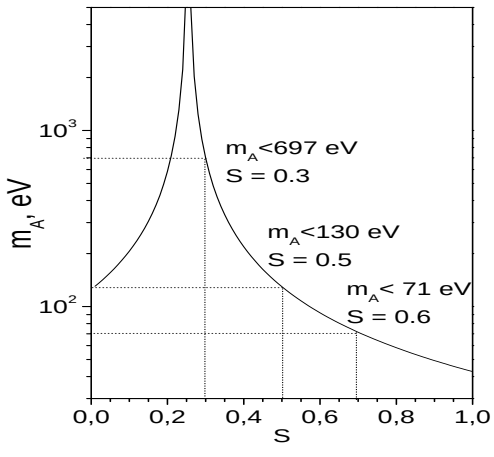

Figure 2: Upper limits on the hadronic-axion mass versus parameter S (z=0.56)

The background spectra collected during 26.5 days and fit result curve are presented in Fig.1. The peak of 13.5 keV from K-capture of ^{81}Kr is well seen. ^{81}Kr is a cosmogenic isotope. The distributions of the events versus pulse rise time and parameter λ (the ratio of amplitudes of secondary and primary pulses) are were investigated [15]. The pulses with rise time longer 4.4 μs are mostly events from the inner surface of the cathode or multisite events. The events with $\lambda < 115$ are mostly close to the edge of the fiducial volume or out of it .

Thus, as we are looking for single site events in the inner volume of the detector. The events with pulse rise time longer 3.8 μs and λ lower then 0.115 are rejected. The resulting spectrum in comparison with original one is presented in Fig.1. There is no visible peak around 9.4 keV from axions. The upper limit on the excitation rate of ^{83}Kr by solar hadronic axions is defined as

$R_{exp} = 0.069$ g^{-1}day^{-1}. This relation $R_A \leq R_{exp}$ limits the region of possible values of the coupling constants g_0, g_3 and axion mass m_A. In accordance with Eqs. (7-9), and on condition that $(p_A/p_\gamma) \cong 1$ provided for $m_A < 3$ keV one can obtain:

$$|g_3 - g_0| \leq 1.69 \times 10^{-6}, \text{ and} \tag{10}$$

$$m_A \leq 130 \text{ eV} \quad \text{at } 95\% \text{ C.L.} \tag{11}$$

The limit (11) is stronger than the constrain obtained with 14.4 keV ^{57}Fe solar axions - ($m_A \leq 145$ eV [3]) and is significantly stronger than previous result obtained in ^{83}Kr experiment [16]. As in the case of ^{57}Fe nucleus the obtained limit on axion mass strongly depends on the exact values of the parameters S and z (Fig.2).

The work is supported by Russian Foundation of Basic Research (Grants No. 14-02-00258A, 13-02-01199A and 13-02-12140-ofi-m).

References

[1] Haxton W.C. and Lee K.Y. Phys. Rev. Lett. 66, 2557 (1991)

[2] Moriyama S. Phys. Rev. Lett. 75,3222 (1995)

[3] Derbin A.V. et al. Phys. At. Nucl. 74, 596 (2011)

[4] Gavrilyuk Yu. M. et al. arXiv:1405.1271

[5] Asplund M.et al. Ann. Rev. of Astronomy and Astrophys. 47, 481 (2009)

[6] Donnelly T.W. et al. Phys. Rev. D18, 1607 (1978)

[7] Avignone III F.T. et al. Phys. Rev. D37, 618 (1988)

[8] Srednicki M. NP B260,689 (1985); Kaplan D.B. NP B260, 215 (1985)

[9] Altarelli G., et al. Phys. Lett. B46,337 (1997)

[10] Adams D. et al. Phys. Rev. D56, 5330 (1997)

[11] Bahcall J.H., Serenelli A.M., Basu S., Astrophys. J. 621, L85 (2005)

[12] Grevesse N., Sauval A.J. Space Sci. Rev. 85, 161 (1998)

[13] Gavriljuk Ju.M. et al.NIM A729, 576 (2013)

[14] Gavrin V.N. et al. Preprint INR RAS P-698 (1991)

[15] Gavrilyuk Yu.M. et al. Instr.Exper.Techn. 53, 57 (2010), Phys. Rev. C87, 035501 (2013)

[16] Jakovčić K. et al. Radiat.Phys.Chem. 74, 93 (2004) arXiv:nucl-ex/0402016v1

Intermediate Scale Accidental Axion and ALPs

Alex G. Dias

Universidade Federal do ABC – Centro de Ciências Naturais e Humanas, Santo André, Brasil

DOI: http://dx.doi.org/10.3204/DESY-PROC-2014-03/dias_alex

We discuss the problem of constructing models containing an axion and axion-like particles, motivated by astrophysical observations, with decay constants at the intermediate scale ranging from 10^9GeV to 10^{13}GeV. We present examples in which the axion and axion-like particles arise accidentally as pseudo Nambu-Goldstone bosons of automatic global chiral symmetries, in models having exact discrete symmetries.

Pseudoscalar bosons very weakly interacting and having low mass – below the eV scale for example – are common in the particle spectra of theories aiming to answer questions left open by the Standard Model (SM) like, for example, the CP conservation of the strong interactions, and the nature of dark matter. The axion is a prominent example occurring in extensions of the SM constructed to solve the strong CP problem [1, 2, 3]. Not connected with this last problem, but with interactions similar to the axion, are the axion-like particles (ALPs). For a review see [4].

Axions and ALPs arise in models containing global symmetries that, besides being spontaneously broken, are also explicitly broken conferring small masses for those particles characterizing them as pseudo Nambu-Goldstone bosons. There are astrophysical phenomena motivating the construction of models containing at last one ALP in addition to the axion [5]. Thus, we consider first a simple case of SM extensions containing two global chiral symmetries, $\mathrm{U}(1)_1 \times \mathrm{U}(1)_2$ with each factor broken spontaneously by vacuum expectation values (vev) $\langle\sigma_i\rangle = v_i/\sqrt{2}$ of SM singlets complex $\sigma_i(x) = [v_i + \rho_i(x)]e^{i\,a'_i(x)/f_{a'_i}}/\sqrt{2}$, $i = 1, 2$, where the decay constants $f_{a'_i}$ depend on v_i and the vev of other scalar fields carrying charge of the $\mathrm{U}(1)_{is}$. At energies much below the scales $v_i \sim f_{a'_i}$, the low energy effective Lagrangian contains the $a'_i(x)$ fields interactions with the gluons and electromagnetic field, through the field strengths $G_{\mu\nu}$ and $F_{\mu\nu}$,

$$\mathcal{L} \supset \frac{1}{2}\sum_{i=1}^{2}\partial_\mu a'_i\,\partial^\mu a'_i - \frac{\alpha_s}{8\pi}\sum_{i=1}^{2}C_{ig}\frac{a'_i}{f_{a'_i}}\,G^a_{\mu\nu}\tilde{G}^{a,\mu\nu} - \frac{\alpha}{8\pi}\sum_{i=1}^{2}C_{i\gamma}\frac{a'_i}{f_{a'_i}}\,F_{\mu\nu}\tilde{F}^{\mu\nu}\,. \tag{1}$$

We have omitted the $a'_i(x)$ interactions with fermionic fields since we are not going to discuss them here. The anomaly coefficients, C_{ig} and $C_{i\gamma}$ are model dependent but typically of order one in common models [5]. It is observed in Eq. (1) that the fields $a'_i(x)$ can be made very weakly interacting if the decay constants $f_{a'_i}$ are sufficiently high – much above the electroweak scale ~ 246 GeV. Equation (1) has the axion as the particle excitation of the field $A(x) = C_{1g}\,a'_1(x)f_A/f_{a'_1} + C_{2g}\,a'_2(x)f_A/f_{a'_2}$, with the ALP the one of the field $a(x) = C_{2g}\,a'_1(x)f_a/f_{a'_2}$ - $C_{1g}\,a'_2(x)f_a/f_{a'_2}$, and the decay constants $1/f_A^2 = 1/f_a^2 = (C_{1g}/f_{a'_1})^2 + (C_{2g}/f_{a'_2})^2$. The axion and the ALP couplings with the photon are defined through $-\frac{g_{\phi\gamma}}{4}\,\phi\,F_{\mu\nu}\widetilde{F}^{\mu\nu}$, where $\phi = A$, a, from Eq. (1) as $g_{A\gamma} = \frac{\alpha\,f_A}{2\pi}\left(C_{1g}C_{1\gamma}/f_{a'_\gamma} + C_{2g}C_{2\gamma}/f_{a'_\gamma} - 1.95\right)$ and $g_{a\gamma} = \frac{\alpha\,f_A}{2\pi}\left(C_{1g}C_{2\gamma} - C_{1\gamma}C_{2g}\right)/f_{a'_1}f_{a'_2}$.

The number -1.95 in the above is a universal contribution from the axion-neutral pion mixing. $g_{A\gamma}$ and $g_{a\gamma}$ are the main couplings of the axion and ALPs, respectively, giving rise to notable phenomena like photon-axion/ALP oscillations [4]. Intermediate energy scales for the decay constants such that $10^9\text{GeV} \lesssim f_{a'_i} \lesssim 10^{13}\text{GeV}$ are specially interesting. This furnishes the values of $g_{A\gamma}$ and $g_{a\gamma}$ within the ranges to be probed directly in new experiments, required to potentially explain some phenomena hinted by astrophysical observations. Depending on their masses, the axion and the ALP could also be cold dark matter candidates.

The pseudo-Nambu-Goldstone field $A(x)$ is associated to the Peccei-Quinn symmetry, $\text{U}(1)_{PQ}$ ($\subset \text{U}(1)_1 \times \text{U}(1)_2$), which is a chiral global symmetry with the special property of being anomalous – explicitly broken by non-perturbative effects – in the quarks sector leading to the interaction term $\frac{1}{f_A} A\, G^a_{\mu\nu}\tilde{G}^{a,\mu\nu}$. This allows the elimination of the CP violation term $\bar{\theta}\, G^a_{\mu\nu}\tilde{G}^{a,\mu\nu}$ absorbing the $\bar{\theta}$-parameter into the axion field as $A+\bar{\theta}\, f_A \to A$ [1]. Also, it is generated a potential $V(A) \simeq m_A^2 f_A^2 \left[1-\cos\left(\frac{A}{f_A}\right)\right]$, in which the axion mass is $m_A = \frac{m_\pi f_\pi}{f_A}\frac{\sqrt{z}}{1+z} \simeq 6\,\text{meV}\times\left(\frac{10^9\,\text{GeV}}{f_A}\right)$, with m_π the mass of the pion, f_π its decay constant, and $z \approx 0.56$ [2]. $V(A)$ leads to the result that the effective CP violation parameter turns out to be zero by the fact that $\langle\frac{A}{f_A}\rangle = \theta_{eff} = 0$. This solves the strong CP problem, which is a fine tuning problem once $\bar{\theta}$ must be very small, arising due the non-observation of a electric dipole moment of the neutron, whose actual measurements limits $|\bar{\theta}| \lesssim 10^{-10}$ [6].

Differently from the axion the ALP remains massless – as Nambu-Goldstone boson of the combined $\text{U}(1)_i$ out of $\text{U}(1)_{PQ}$ – unless there are additional interactions explicitly breaking its associate global symmetry and, thus, generating an extra potential $\delta V(a'_i)$. Massive ALPs have been implemented in ultra-violet completions of the SM for several purposes [5]. But the explicit breakdown of the global symmetries must occur in a controlled way to get appropriate ALPs masses and preserve the solution of the strong CP problem. In fact, it is not expected that gravitational interactions conserve global symmetries. It is known that operators suppressed by the Planck scale M_{Pl} like $\sigma_1^n\sigma_2^k/M_{\text{Pl}}^{D-4}$, with $D = n+k > 4$, might bring corrections to the axion potential such that $\delta\bar{\theta} > 10^{-10}$ if not forbidden until a certain dimension $D \gtrsim 9/\left[1-0.1\log\left(f_A/10^9\text{GeV}\right)\right]$ [7]. Discrete gauge symmetries Z_N [8], with $N = D+1$, have been used to resolve the problem of having dangerous effective operators in axion models [9], and also in models containing axion plus ALPs [5]. Another compelling reason for these Z_N symmetries is that if they are appropriately postulate anomalous symmetries like $\text{U}(1)_{PQ}$ may arise as automatic quasi exact symmetries. This avoids the non-natural impositions of global continuous symmetries which are already explicitly broken, as is the case of the $\text{U}(1)_{PQ}$ symmetry.

A model in which the axion and ALPs have their masses and couplings controlled by discrete symmetries is the $\mathbb{Z}_{13}\otimes\mathbb{Z}_5\otimes\mathbb{Z}'_5$ model proposed in [5]. It is a hybrid of invisible axion models [10] plus an ALP. The field content of the model beyond the SM one is: four SM Higgs doublets H_b, an $\text{SU}(2)_L$ triplet T, a vector-like color triplet (Q_L, Q_R), three right-handed neutrinos N_{iR}, and two SM singlet fields $\sigma_{1,2}$. The fields charges of the imposed discrete symmetry $\mathbb{Z}_{13}\otimes\mathbb{Z}_5\otimes\mathbb{Z}'_5$ are shown in Table 1. It can be shown that both the Yukawa interaction terms and the renormalizable scalar potential of this model have two accidental global chiral symmetries and, thus, an axion and one ALP. Additionally, the interaction terms $\overline{L}_i\widetilde{H}_N N_{jR}$ and $\overline{(N_{iR})^c}\sigma_1 N_{jR}$, allowed by the discrete symmetries of the model lead to a seesaw mechanism for generating small masses to the active neutrinos.

The lowest dimensional effective operator invariant by the discrete symmetry, but breaking $\text{U}(1)_1\otimes\text{U}(1)_2$ explicitly is $\frac{g}{M_{\text{Pl}}^{10}} H_N^\dagger H_d \sigma_1^{*5}\sigma_2^7$. This generates a tiny mass $m_a \sim 10^{-33}$ eV to

ψ_i	q_L	u_R	d_R	L	N_R	l_R	H_u	H_d	H_l	H_N	σ_2	T	Q_L	Q_R	σ_1
$\mathbb{Z}_{13}$	ω_{13}^5	ω_{13}^3	ω_{13}^8	ω_{13}^9	ω_{13}^3	ω_{13}^7	ω_{13}^{11}	ω_{13}^{10}	ω_{13}^2	ω_{13}^7	ω_{13}^{12}	ω_{13}^9	1	ω_{13}^6	ω_{13}^7
$\mathbb{Z}_5$	1	ω_5	ω_5^4	1	ω_5	ω_5^4	ω_5	ω_5	ω_5	ω_5	1	ω_5^2	ω_5	ω_5^3	ω_5^3
$\mathbb{Z}_5'$	1	ω_5^4	1	1	ω_5^2	ω_5^4	ω_5^4	1	ω_5	ω_5^2	ω_5	ω_5^3	1	ω_5^4	ω_5

Table 1: $\mathbb{Z}_N$ charges of the $\mathbb{Z}_{13} \otimes \mathbb{Z}_5 \otimes \mathbb{Z}_5'$ model, where $\omega_{13} \equiv e^{i2\pi/13}$ and $\omega_5 \equiv e^{i2\pi/5}$.

the ALP, assuming the values $v_1 \simeq f_A \simeq 10^{10}$ GeV, $v_1 \simeq 7.5 \times 10^{10}$ GeV, taking the Higgses doublets vevs $v_W \simeq 100$ GeV, the Planck scale $M_{\rm Pl} = 10^{19}$ GeV, and $g = 1$. The axion mass is approximately $m_a \simeq 0.6$ meV, not been affected in a significantly manner by the Planck suppressed effective operators. For the couplings $g_{A\gamma}$, $g_{a\gamma}$, the coefficients entering in them are $C_{1g} = 1$, $C_{2g} = 3$, $C_{1\gamma} = 6$, $C_{2\gamma} = 4$, where we assume the electric charge of $Q_{L,R}$ equal to one. This furnishes $|g_{A\gamma}| \simeq 4 \times 10^{-13}$ GeV^{-1}, and $|g_{a\gamma}| \simeq 2 \times 10^{-13}$ GeV^{-1}. With these values for the coupling to photons and mass the axion can be a dark matter candidate, but still outside the region to be probed directly by present experiments. The ALP in this model has the coupling to photons and mass within the range required explanation for the soft X-ray excess from Coma cluster [11], and also being in the reach of proposed experiments [5].

We present another construction containing, in addition to the axion, two photophilic ALPs is the $Z_{11} \otimes Z_9 \otimes Z_7$ model. It is motivated by distinct ranges of coupling to photons and mass required to explain the anomalous transparency of the Universe [12] (see [5] and references therein), and the unidentified X-ray line of 3.55 keV found in recent observations [13]. With the latter supposed to be due a two photon decay of a dark matter ALP with mass of 7.1 keV [15]. The field content of the $Z_{11} \otimes Z_9 \otimes Z_7$ model has beyond the SM fields: one vector-like color triplet (Q_L, Q_R); two noncolored vectorial charged fermions $(E_L,\, E_R)$, $(E_L',\, E_R')$; three right-handed neutrinos N_{iR}; and three SM singlet fields σ_i. The fields charges of the discrete symmetry are shown in Table 2.

	q_L	u_R	d_R	L	l_R	N_R	H	Q_L	Q_R	σ_1	σ_2	E_L	E_R	σ_3	E_L'	E_R'
$\mathbb{Z}_7$	1	ω_7^3	ω_7^4	1	ω_7^4	ω_7^3	ω_7^3	ω_7^5	ω_7^3	ω_7	1	ω_7^5	ω_7^4	ω_7^1	ω_7^5	ω_7^3
$\mathbb{Z}_9$	1	ω_9^5	ω_9^4	ω_9^6	ω_9	ω_9^2	ω_9^5	1	ω_9^8	ω_9^5	ω_9	ω_9^6	1	1	ω_9^1	ω_9^5
$\mathbb{Z}_{11}$	1	ω_{11}^3	ω_{11}^8	ω_{11}^2	ω_{11}^{10}	ω_{11}^5	ω_{11}^3	ω_{11}^9	ω_{11}^7	ω_{11}	1	1	ω_{11}^{10}	1	ω_{11}^{10}	ω_{11}^9

Table 2: $\mathbb{Z}_N$ charges of the $\mathbb{Z}_7 \otimes \mathbb{Z}_9 \otimes \mathbb{Z}_{11}$ model.

It is shown in [5] that the Yukawa interaction terms and the renormalizable scalar potential allowed by the discrete symmetry have three global chiral symmetries, $\mathrm{U}(1)_1 \otimes \mathrm{U}(1)_2 \otimes \mathrm{U}(1)_3$. Each one of them is spontaneously broken by the respective singlet vevs $\langle \sigma_i \rangle = v_1/\sqrt{2}$, with the axion being related to related to $\mathrm{U}(1)_1$, the ALP a_2 to $\mathrm{U}(1)_2$, and the ALP a_3 to $\mathrm{U}(1)_3$. There is no one relevant Planck suppressed operator correcting the axion mass. The lowest dimension operators breaking $\mathrm{U}(1)_2$ and $\mathrm{U}(1)_3$ are $\frac{g}{M_{\rm Pl}^5}(\sigma_2)^9$ and $\frac{g'}{M_{\rm Pl}^3}(\sigma_2)^7$, respectively. In order to give an example we set $v_2 = 10^9$ GeV, $v_3 = 3 \times 10^9$ GeV, $g = 1$, and $g' \approx 0.1$. This furnishes $m_{a_2} \approx 10^{-7}$ eV, $g_{a_2\gamma} \approx 2.2 \times 10^{-11}$ GeV^{-1} to the ALP a_2 making it able to explain the anomalous transparency of the Universe [12], and also in the search range of the experiment

ALPS II [14]; and $m_{a_3} \approx 7.1$ keV, $g_{a_3\gamma} \approx 7.7 \times 10^{-13}$ GeV^{-1} to the ALP a_3 so that it can explain the 3.55 keV line through its two photons decay [15].

For other developments on discrete symmetries originating from string theory see [16].

Acknowledgments – This work is partially supported by CNPq (grant 303094/2013-3) and FAPESP (grant 2013/22079-8). The author thanks the support of workshop organizers.

References

[1] R. D. Peccei, H. R. Quinn, "CP Conservation in the Presence of Instantons," Phys. Rev. Lett. 38 (1977) 1440;

[2] S. Weinberg, "A New Light Boson?," Phys. Rev. Lett. 40 (1978) 223.

[3] F. Wilczek, "Problem of Strong P and T Invariance in the Presence of Instantons," Phys. Rev. Lett. 40 (1978) 279.

[4] J. Jaeckel and A. Ringwald, "The Low-Energy Frontier of Particle Physics," Ann. Rev. Nucl. Part. Sci. **60** (2010) 405 [arXiv:1002.0329 [hep-ph]].

[5] A. G. Dias *et al.*, "The Quest for an Intermediate-Scale Accidental Axion and Further ALPs", JHEP **1406**, 037 (2014) [arXiv:1403.5760 [hep-ph]].

[6] C. A. Baker *et al*, "An Improved experimental limit on the electric dipole moment of the neutron", Phys. Rev. Lett. 97 (2006) 131801.

[7] S. Ghigna, M. Lusignoli and M. Roncadelli, "Instability of the invisible axion," Phys. Lett. B **283**, 278 (1992); R. Holman *et al*, "Solutions to the strong CP problem in a world with gravity," Phys. Lett. B **282**, 132 (1992) [hep-ph/9203206]; M. Kamionkowski and J. March-Russell, "Planck scale physics and the Peccei-Quinn mechanism," Phys. Lett. B **282**, 137 (1992) [hep-th/9202003]; S. M. Barr and D. Seckel, "Planck scale corrections to axion models," Phys. Rev. D **46**, 539 (1992).

[8] L. M. Krauss, F. Wilczek, "Discrete Gauge Symmetry in Continuum Theories", Phys. Rev. Lett. 62 (1989) 1221.

[9] A. G. Dias, V. Pleitez and M. D. Tonasse, "Naturally light invisible axion and local Z(13) x Z(3) symmetries," Phys. Rev. D **69**, 015007 (2004) [hep-ph/0210172]; A. G. Dias, V. Pleitez and M. D. Tonasse, "Naturally light invisible axion in models with large local discrete symmetries," Phys. Rev. D **67**, 095008 (2003) [hep-ph/0211107]; L. M. Carpenter, M. Dine and G. Festuccia, "Dynamics of the Peccei Quinn Scale," Phys. Rev. D **80**, 125017 (2009) [arXiv:0906.1273 [hep-th]]; K. Harigaya *et al*, "The Peccei-Quinn Symmetry from a Gauged Discrete R Symmetry," arXiv:1308.1227 [hep-ph]; J. E. Kim and H. P. Nilles, "Dark energy from approximate $U(1)_{\rm de}$ symmetry," arXiv:1311.0012 [hep-ph].

[10] J. E. Kim, "Weak Interaction Singlet and Strong CP Invariance," Phys. Rev. Lett. 43 (1979) 103; M. A. Shifman, A. I. Vainshtein, V. I. Zakharov, "Can Confinement Ensure Natural CP Invariance of Strong Interactions?," Nucl. Phys. B 166 (1980) 493; M. Dine, W. Fischler, M. Srednicki, "A Simple Solution to the Strong CP Problem with a Harmless Axion," Phys. Lett. B 104 (1981) 199; A. R. Zhitnitsky, "On Possible Suppression of the Axion Hadron Interactions," Sov. J. Nucl. Phys. 31 (1980) 260 [Yad. Fiz. 31 (1980) 497].

[11] J. P. Conlon and M. C. D. Marsh, "Searching for a 0.1-1 keV Cosmic Axion Background," Phys. Rev. Lett. **111**, 151301 (2013) [arXiv:1305.3603 [astro-ph.CO]]; S. Angus *et al*, "Soft X-ray Excess in the Coma Cluster from a Cosmic Axion Background," arXiv:1312.3947 [astro-ph.HE].

[12] M. Meyer, D. Horns and M. Raue, "First lower limits on the photon-axion-like particle coupling from very high energy gamma-ray observation," Phys. Rev. D **87**, 035027 (2013) [arXiv:1302.1208 [astro-ph.HE]].

[13] E. Bulbul *et al*, "Detection of An Unidentified Emission Line in the Stacked X-ray spectrum of Galaxy Clusters," arXiv:1402.2301 [astro-ph.CO]; A. Boyarsky *et al*, "An unidentified line in X-ray spectra of the Andromeda galaxy and Perseus galaxy cluster," arXiv:1402.4119 [astro-ph.CO].

[14] R. Bahre *et al.* [ALPS Collaboration], "Any light particle search II - Technical Design Report," JINST **8**, T09001 (2013) [arXiv:1302.5647 [physics.ins-det]].

[15] T. Higaki, K. S. Jeong and F. Takahashi, "The 7 keV axion dark matter and the X-ray line signal," arXiv:1402.6965 [hep-ph]; J. Jaeckel, J. Redondo and A. Ringwald, "A 3.55 keV hint for decaying axion-like particle dark matter," arXiv:1402.7335 [hep-ph].

[16] J. E. Kim, "QCD Axion and Dark Energy", arXiv:1409.3609 [hep-ph].

First sensitivity limits of the ALPS TES detector

Jan Dreyling-Eschweiler[1], *for the ALPS-II collaboration*

[1]Deutsches Elektronen-Synchrotron (DESY), Hamburg, Germany

DOI: http://dx.doi.org/10.3204/DESY-PROC-2014-03/dreyling-eschweiler_jan

The Any Light Particle Search II (ALPS II) requires a sensitive detection of 1064 nm photons. Thus, a low dark count rate (DC) and a high detection efficiency (DE) is needed. ALPS has set up a transition-edge sensor (TES) detector system, namely the ALPS TES detector. It is found that thermal photons from room temperature surfaces are the main contribution of dark counts for 1064 nm photon signals. Furthermore, the current setup of the ALPS TES detector shows an improvement compared to using the ALPS I detector.

1 Introduction

ALPS II is a light-shining-through-a-wall experiment based on an optical laser [1]. Compared to ALPS I, the overall experimental sensitivity will be increased by extending the magnetic length, improving the optical system and setting up a more sensitive photon detector.[1] According to the latter, a detection of low-flux single 1064 nm photons is required [2]. Therefore, we have set to work on developing a TES detector system [3]. In the last year, the completed setup has been characterized concerning its experimental sensitivity for the first time [4].

2 ALPS detector sensitivity

The ALPS II experiment asks for a detection of low rates of single 1064 nm photons. The sensitivity of the axion-like particle-photon coupling, $g_{\mathrm{a}\gamma}$, concerning only the ALPS detector is defined as [5]:

$$\mathcal{S}_{\mathrm{detector}}(g_{\mathrm{a}\gamma}) = \left(\sqrt{DC}/DE\right)^{1/4} \tag{1}$$

where DC is the dark count[2] rate and DE is the (overall) detection efficiency of the detector. The smaller this figure of merit the higher the gain for the ALPS experiment.

The ALPS I detector was a commercial state-of-the-art silicon-based charged-coupled device (CCD) [6]. Using this CCD camera to detect 1064 nm light, the sensitivity is limited due to $DE_{\mathrm{CCD}} = 1.2$ % [7]. With $DC_{\mathrm{CCD}} = 1.2 \cdot 10^{-3}$ s^{-1} [7] it results:

$$\mathcal{S}_{\mathrm{CCD}} = 1.303 \text{ s}^{-1/8} \tag{2}$$

The goal of a new detector is to reach a higher sensitivity or lower figure of merit, $\mathcal{S}_{\mathrm{detector}}$.

[1]These improvements can be illustrated by the board game "Axionator", see the corresponding slides or contact the author.

[2]A dark count is defined as an event which cannot be distinguished from signals.

3 The ALPS TES detector

Detectors based on transition-edge sensors (TESs) can reach a high sensitivity [8]. TESs are operated within the superconducting transition of the sensor's material. Thus, small temperature changes like by a photon cause measurable changes of the electrical resistance.

For the ALPS TES detector, we are using a tungsten-based TES from NIST [9]. These kind of sensors are optimized for detecting single photons around 1064 nm. Single mode fibers are attached to NIST TES chips [10]. For 1064 nm signals, a detection efficiency of $DE = 97$ % $\pm$ 2 % syst. $\pm$ 1 % stat. was measured [11]. Exact measurements of ALPS TES detector's DE are underway within the collaboration. For the considered dark count rate in this paper (Sec. 5), we conservatively estimate [4]

$$DE_{\mathrm{TES}} = 18\ \% \tag{3}$$

which includes a low analysis efficiency due to necessary cuts on the signal region (Sec. 5).

We are operating the NIST TES at a bath temperature of $T_{\mathrm{bath}} = 80\ \mathrm{mK} \pm 25\ \mu\mathrm{K}$ due to the superconducting transition $T_{\mathrm{c}} \approx 140$ mK of the TES [4]. The bath is provided by an adiabatic demagnetization refrigerator (ADR) system. The 2.5 K-precooling is provided by a pulse tube cooler. The subsequent mK-cooling is provided by a 6 T magnet and a salt pills unit, which allows to establish a continuous 80 mK-operation for > 20 h. The low-noise current read-out of the TES circuit is provided by an dc 2-stage SQUID from PTB [12]. For signal calibration as well as for long-background measurements, we have used an oscilloscope DPO7104C from Tektronix as data acquisition system (DAQ).

4 Signals and thermal photonic background

Applying an attenuated laser for single photon source, we consider the distribution of the pulse heights PH (Fig. 1). We observe three event classes [4]:

- Signal photons: 1064 nm photons normally distribute around $PH \approx -55$ mV. Fitting a Gaussian distribution allows to define a signal region and to determine an energy resolution of a 1064 nm photon signal. We observe $(\Delta E/E)_{1064\ \mathrm{nm}} = 7 - 8$ %.

- Sensor noise: The signal peak is clearly separated from the noise peak around $PH = 0$ mV. The noise is mainly caused by the fundamental TES noise.

- Thermal photons: Thermal photon events are observed due to the warm fiber end at room temperature. The optical transmittance of the single mode fiber and the TES absorptivity cause an effective peak between 1550 and 2000 nm. Thermal photons through the fiber are confirmed by operating the TES in a < 4 K-environment without optical fiber link. Thermal photons are also observed by other groups as a reasonable background source [13].

While the intrinsic noise is no possible source for dark counts of 1064 nm signals, the spectrum of thermal photons can reach the 1064 nm signal region and result in a dark count. Further background events, like intrinsic, are well discriminated by a proper pulse shape analysis [4]. To estimate an expected dark count rate, we consider a conservative model: 300 K black body spectrum, no optical losses and an overall energy resolution of $\Delta E/E = 10$ %. Furthermore,

we only consider the high-energetic 3σ-region of 1064 nm signals which corresponds to photon wavelength between 818 and 1064 nm (Sec. 5). This results in a photon rate of $3.4 \cdot 10^{-4}$ s^{-1} due to a room-temperature black body spectrum. This number is compared to long-term measurements in the next section.

5 Dark count rate

To determine the dark count rate of a fiber-coupled TES, the warm fiber end outside the cryostat was adequately covered, so that no ambient light can couple into the open fiber end. We have analyzed each trigger event of two long-term measurements (> 14 h) offline. Only events showing a single photon pulse shape were taken into account [4].

Furthermore, as mentioned above, we only consider the high-energetic half 3σ-region of 1064 nm signals due to the used trigger level. This is necessary because of the used DAQ: A corresponding low trigger level around a PH of 1550 nm photons results in a too high trigger rate due to the thermal spectrum, which would cause dead time effects. For this setup, we determine a dark count rate of

$$DC_{\mathrm{TES}} = 8.6 \cdot 10^{-3}\ \mathrm{s}^{-1} \qquad (4)$$

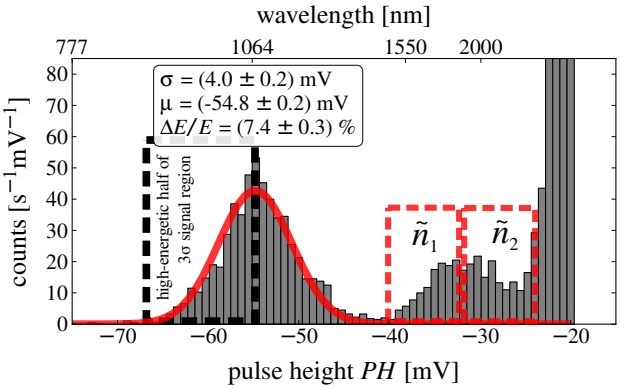

Figure 1: Exemplary pulse height distribution: Pulse heights PH of trigger events are negatively plotted in mV-units of the DAQ (bottom x-axis) and in nm-units of wavelength (top x-axis). Signal photons are around 1064 nm (red Gaussian shape). For the results, the high-energetic half of the 3σ-region is considered (dashed black box). Sensor noise is distributed around 0 mV. Thermal photons from room temperature surfaces are roughly found between 1550 and 2000 nm. For a pile-up estimate, the thermal peak is split in two contributions $\tilde{n}_1$ and $\tilde{n}_2$ (dashed red boxes).

Comparing this rate to the estimate rate due to a black body spectrum (Sec. 4) the measured rate is ∼1.5 orders of magnitude higher than the expected rate. It is found that a plausible explanation are pile-up events of thermal photons [4]. A first-order pile-up rate $\tilde{n}_{\mathrm{eff}}$ can be estimated by a formula describing accidental coincidences [14]: $\tilde{n}_{\mathrm{eff}} = 2\,\tau\,\tilde{n}_1\,\tilde{n}_2$ where τ is the resolving time and $\tilde{n}_1$ and $\tilde{n}_2$ uncorrelated rates. The time resolution of the current setup is constrained by the analysis method and is conservatively estimated by $\tau \approx 0.5\ \mu$s. The rates $\tilde{n}_1$ and $\tilde{n}_2$ are estimated from Fig. 1: We split the thermal peak in two parts and assume that two photons from each part can effectively combine to a 1064 nm signal event. It is $\tilde{n}_1 \approx \tilde{n}_2 \approx 10^2$ s^{-1}. Thus, the rate for first-order pile-ups imitating 1064 nm events is $\tilde{n}_{\mathrm{eff}} \simeq 10^{-2}$ s^{-1}. $\tilde{n}_{\mathrm{eff}}$ is in the same order of magnitude as the measured rate DC_{TES} (Eq. 4).

6 Conclusion

Using the ALPS TES detector, the experimental sensitivity (Eq. 1) results in

$$\mathcal{S}_{\mathrm{TES}} = 0.847\ \mathrm{s}^{-1/8} \tag{5}$$

where we used the estimated DE_{TES} (Eq. 3) and the measured DC_{TES} (Eq. 4). Compared to the CCD (Eq. 2), this results in a sensitivity gain of $\mathcal{S}_{\mathrm{CCD}}/\mathcal{S}_{\mathrm{TES}} = 1.54$ for the ALPS experiment. This proves the gain of using a TES-based detector instead of the CCD camera system to detect single 1064 nm photons. Furthermore, we are motivated to improve the ALPS TES detector. Most promising is to reduce the thermal background by using an optical bandpass filter and an improved analysis for pile-up rejection.

Acknowledgments

The ALPS collaboration wants to thank the PTB and NIST for the support of their superconducting devices.

References

[1] F. Januschek for the ALPS-II collaboration, "Review on LSW with lasers", these proceedings.

[2] R. Bähre *et al.*, "Any Light Particle Search II – Technical Design Report", JINST 1309, T09001 (2013) [arXiv:1302.5647].

[3] J. Dreyling-Eschweiler *et. al.*, "Detecting an infrared Photon within an Hour – Transition-Edge Detector at ALPS-II", Proceedings of 9th Patras Workshop 2013 [arXiv:1309.5024]

[4] J. Dreyling-Eschweiler, "A superconducting microcalorimeter for low-flux detection of near-infrared single photons", DESY-THESIS-2014-016, ISSN 1435-8085.

[5] J. E. von Seggern, "Overview on Low-flux Detectors", Proceedings of 9th Patras Workshop 2013 [arXiv:1310.0660]

[6] K. Ehret *et al.*, "New ALPS Results on Hidden-Sector Lightweights", Phys. Lett. B 689, 149 (2010) [arXiv:1004.1313].

[7] J. E. von Seggern, "Constraining Weakly Interacting Slim Particles with a Massive Star and in the Laboratory", DESY-THESIS-2014-001, ISSN 1435-8085.

[8] K. D. Irwin and G. C. Hilton, "Transition-Edge Sensors", In: C. Enss, "Cryogenic Particle Detectors", Springer-Verlag Berlin Heidelberg (2005)

[9] A. E. Lita *et al.*, "Superconducting transition-edge sensors optimized for high-efficiency photon-number resolving detectors", SPIE Conf. Ser. 7681 (2010)

[10] A. J. Miller *et al.*, "Compact cryogenic self-aligning fiber-to-detector coupling with losses below one percent", Opt. Express 19(10) (2012)

[11] A. E. Lita, Private communication (2013)

[12] D. Drung *et al.*, "Highly Sensitive and Easy-to-Use SQUID Sensors", IEEE Transactions on Applied Superconductivity 17:699704 (2007)

[13] A. J. Miller *et al.*, "Superconducting photon number resolving detectors: Performance and promise", Proceedings of the 8th international conference on quantum communication, measurement and computing (NICT Press, 2007)

[14] C. Eckart and F. R. Shonka, "Accidental Coincidences in Counter Circuits", Phys. Rev., 53:752756 (1938)

New PVLAS model independent limit for the axion coupling to $\gamma\gamma$ for axion masses above 1 meV

F. Della Valle[1], *A. Ejlli*[2], *U. Gastaldi*[3], *G. Messineo*[2], *E. Milotti*[1], *R. Pengo*[4], *L. Piemontese*[2], *G. Ruoso*[4], *G. Zavattini*[2]

[1] INFN, Sezione di Trieste and Dipartimento di Fisica, Università di Trieste, Italy
[2] INFN, Sezione di Ferrara and Dipartimento di Fisica, Università di Ferrara, Italy
[3] INFN, Sezione di Ferrara, Ferrara, Italy
[4] INFN, Laboratori Nazionali di Legnaro (PD), Italy

DOI: http://dx.doi.org/10.3204/DESY-PROC-2014-03/gastaldi_ugo

During 2014 the PVLAS experiment has started data taking with a new apparatus installed at the INFN Section of Ferrara, Italy. The main target of the experiment is the observation of magnetic birefringence of vacuum. According to QED, the ellipticity generated by the magnetic birefringence of vacuum in the experimental apparatus is expected to be $\psi^{(\mathrm{QED})} \approx 5 \times 10^{-11}$. No ellipticity signal is present so far with a noise floor $\psi^{(\mathrm{noise})} \approx 2.5 \times 10^{-9}$ after 210 hours of data taking. The resulting ellipticity limit provides the best model independent upper limit on the coupling of axions to $\gamma\gamma$ for axion masses above 10^{-3} eV.

1 Introduction

Several experimental efforts have been set up with the main goal of observing magnetic birefringence of vacuum [1, 2, 3]. This effect is expected to generate ellipticity on a linearly polarized light beam which propagates in vacuum in the presence of a magnetic field **B** orthogonal to the direction of the light beam. Magnetic birefringence of vacuum is a manifestation of nonlinear electrodynamic effects [4] due to vacuum fluctuations and predicted before the full formulation of QED. It results from the interaction of incoming laser photons with virtual photons of the magnetic field. Magnetic birefringence of vacuum is closely related to elastic light-by-light interaction [5]; neither effect has yet been observed. Detection of the magnetic birefringence of vacuum is of major importance because it would represent the first direct observation of the interactions between gauge bosons present both in the initial and the final states.

Spin zero light particles which couple to two photons may also contribute to birefringence [6]: observation of a magnetic birefringence different from the value predicted by QED could indicate the existence of light scalar or pseudoscalar particles [axions [7] or axion-like particles (ALPs)] of paramount importance for cosmology and for QCD. A limit on the ellipticity generated in an apparatus like the PVLAS ellipsometer gives a model independent indication on the axion mass m_a and the coupling constant g_a to two photons. Much better limits reported by CAST [8] depend, instead, on the assumed density of spin zero particles that traverse the apparatus.

2 Apparatus and Method

A new set up is installed in Ferrara, Italy, featuring a tabletop ellipsometer with two identical permanent dipole magnets each with a maximum field of 2.5 T over a 0.8 m length rotating up to 10 Hz. Figure 1, top panel, gives a schematic top view of the apparatus, whereas Fig. 1, lower panel, shows a photograph of the apparatus. The principle of the experiment follows the

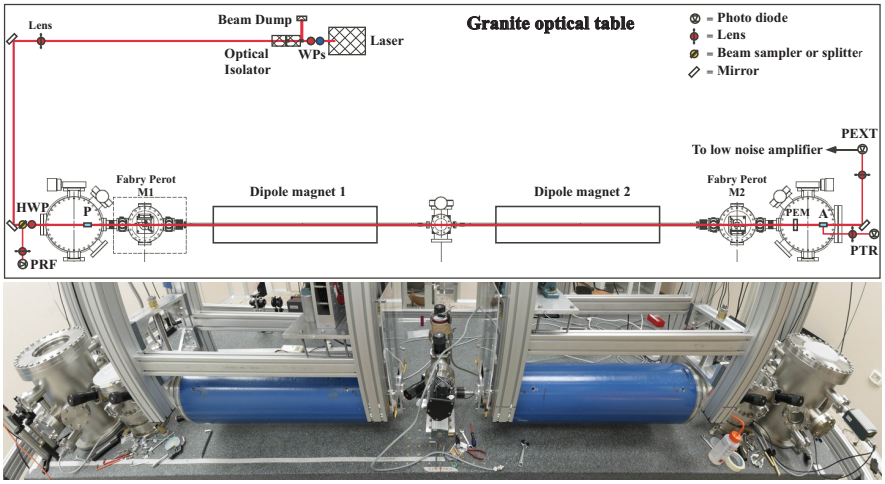

Figure 1: Upper panel: scheme of the apparatus. Lower panel: wide-angle picture of the PVLAS apparatus. The two blue cylinders are the dipole permanent magnets.

measurement scheme proposed in 1979 by Iacopini and Zavattini [9]. Linearly polarized light is injected in the ellipsometer, which is installed in a UHV enclosure. The ellipsometer consists of an entrance polarizer P and an analyzer A set to maximum extinction. Between P and A are installed the entrance mirror M1 and the exit mirror M2 of a Fabry-Perot cavity FP with ultra-high finesse $\mathcal{F}$ [10]. The laser source is frequency locked to the cavity [11]. The light stored between the two FP mirrors travels through the magnetic field region making typically $N = \frac{2\mathcal{F}}{\pi} = 4.3 \times 10^5$ reflections (corresponding to a path of about 800 km). When the fields of the two magnets are parallel, the ellipticity ψ induced on the linearly polarized light beam is

$$\psi = N\psi_{\rm single} = N\frac{\pi\Delta n_u^{(\rm vac)}\int_0^L B^2 dl}{\lambda}\sin 2\vartheta \approx 5\times 10^{-11}\ \sin 2\vartheta$$

where $\lambda = 1064$ nm is the laser wavelength, $L = 1.6$ m the length of the path through the two magnets, ϑ is the angle between the light polarization vector and the magnetic field vector and $\Delta n_u^{(\rm vac)} = 3.97 \times 10^{-24}$ T^{-2} is the unitary birefringence of vacuum predicted by QED. To measure such a small quantity, a heterodyne technique is used: a photoelastic modulator PEM introduces a time dependent carrier ellipticity with amplitude $\eta \approx 10^{-3}$ at a frequency $\nu_{\rm PEM} \approx 50$ kHz and the magnets are set in rotation at the same frequency $\nu_{\rm mag} \approx 3$ Hz. The ellipticity generated by the magnets is modulated at twice the magnet rotation frequency. In the frequency spectrum of the signals detected by the photodiode PEXT the beating of the magnet and PEM ellipticities generate signals with amplitudes proportional to $2\eta\psi \approx 10^{-13}$ at the frequencies $\nu_{\rm PEM} \pm 2\nu_{\rm mag}$ (see ref. [3]).

3 Results

The calibration of the apparatus has been done by measuring the Cotton-Mouton effect of helium gas at several pressures and controlling the consistency of the results with the values present in the literature. The left panel of Fig. 2 shows the Fourier spectrum of PEXT signals demodulated around $\nu_{\rm PEM}$ for a 5.7 hours run with 32 μbar He in the UHV enclosure and the magnets rotating at $\nu_{\rm mag} = 3$ Hz. The spectrum features a clear peak at $2\nu_{\rm mag}$ corresponding to a Cotton-Mouton ellipticity $\psi(\text{He @ } 32\mu\text{bar}) = 1.13 \times 10^{-7}$. The baseline ellipticity noise around 6 Hz is of the order of 1.5×10^{-8}. The right panel of Fig. 2 shows the ellipticity signal generated by He at three different pressures.

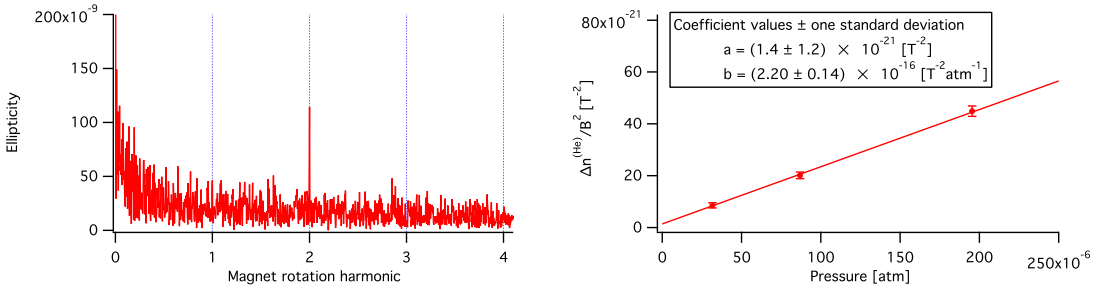

Figure 2: Left: Fourier spectrum of the measured ellipticity $\psi(t)$ with 32 μbar pressure of He after demodulation at $\Omega_{\rm PEM}$. The integration time was T = 5.7 hours. The vacuum magnetic birefringence predicted by QED is equivalent to a He pressure of ~ 20 nbar. Right: measured $\Delta n^{(\rm He)}/B^2$ as a function of pressure P. The error bars correspond to a 1σ statistical error. The data are fitted with a linear function $a + bP$.

With the ellipsometer in vacuum 210 hours of data have been analyzed, taking into account amplitude and phase for the signal at $2\nu_{\rm mag}$ for each run [12]. No peak is present in the resulting spectrum. The baseline noise level around $2\nu_{\rm mag}$ is $\psi_{\rm noise} \approx 2.5 \times 10^{-9}$. Although this represents a major improvement compared to previous measurements, in view of the expected sugnal of the magnetic birefringence of vacuum $\psi \approx 5 \times 10^{-11}$, we have still to recover a missing factor ≈ 50. This will be done identifying and reducing the sources of noise, which is presently far above the shot-noise limit.

The ellipticity induced by low mass axions can be expressed as [1]:

$$\psi_{\rm axion} = \frac{N\pi L}{\lambda} \frac{g_a^2 B^2}{2m_a^2} \left(1 - \frac{\sin 2x}{2x}\right)$$

where m_a is the axion mass, L the magnetic field length, $x = \frac{Lm_a^2}{4\omega}$ and ω is the energy of the laser photons. The measured ellipticity noise $\psi_{\rm noise} \approx 2.5 \times 10^{-9}$ gives an upper limit for $\psi_{\rm axion}$, represented as an exclusion plot for the coupling constant g_a as a function of the axion mass m_a. Figure 3 updates the limits given by model independent laser experiments. One may notice that the limits derived by PVLAS-Fe are the most restrictive in the m_a mass region above 10^{-3} eV.

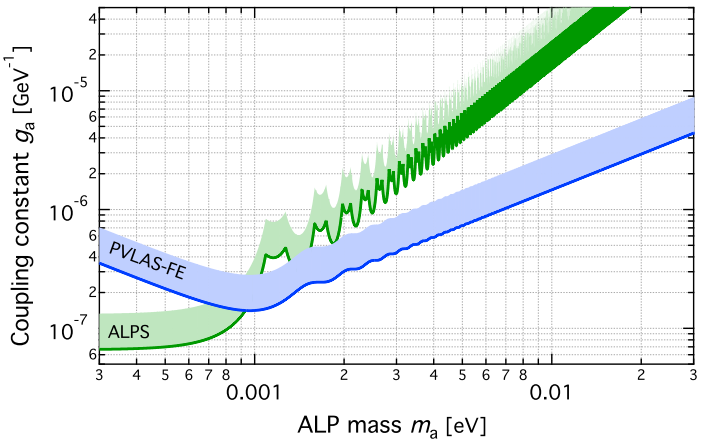

Figure 3: Exclusion plot at 95 % c.l. for axion-like particles for model independent experiments. In green, limits from the ALPS collaboration [13]; in blue the new bounds presented here.

References

[1] R. Cameron *et al.* (BFRT collaboration), Phys. Rev. D **47**, 3707 (1993).

[2] E. Zavattini *et al.* (PVLAS collaboration), Phys. Rev. D **77**, 032006 (2008); M. Bregant *et al.* (PVLAS collaboration), *ibid.* **78**, 032006 (2008); H.-H. Mei *et al.* (Q & A collaboration), Mod. Phys. Lett. A **25**, 983 (2010); OSQAR Annual Report 2013, CERN-SPSC-2013-030 / SPSC-SR-125; A. Cadène *et al.* (BMV collaboration), Eur. Phys. J. D **68**, 16 (2014).

[3] G. Zavattini *et al.* (PVLAS collaboration), Int. J. Mod. Phys. A **27**, 1260017 (2012); F. Della Valle *et al.* (PVLAS collaboration), New J. Phys. **15**, 053026 (2013); Nucl. Instrum. Methods Phys. Res. A **718**, 495 (2013).

[4] H. Euler and B. Kochel, Naturwiss. **23**, 246 (1935); W. Heisenberg and H. Euler, Z. Phys. **98**, 718 (1936);V.S. Weisskopf, Kgl. Danske Vid. Sels., Math.-fys. Medd. **14**, 6 (1936); J. Schwinger, Phys. Rev. **82**, 664 (1951); R. Baier and P. Breitenlohner, Acta Phys. Austriaca **25**, 212 (1967); Nuovo Cimento **47**, 261 (1967); S.L. Adler, Ann. Phys. **67**, 559 (1971); Z. Bialynicka-Birula and I. Bialynicki-Birula, Phys. Rev. D **2**, 2341 (1970).

[5] F. Moulin, D. Bernard, and F. Amiranoff, Z. Phys. C **72**, 607 (1996); D. Bernard *et al.*, Eur. Phys. J. D **10**, 141 (2000); D. A. Dicus, C. Kao, and W. W. Repko, Phys. Rev. D **57**, 2443 (1998).

[6] P. Sikivie, Phys. Rev. Lett. **51**, 1415 (1983); L. Maiani, R. Petronzio, and E. Zavattini, Phys. Lett B **175**, 359 (1986); M. Gasperini, Phys. Rev. Lett **59**, 396 (1987); G. Raffelt and R. Stodolsky, Phys. Rev. D. **37**, 1237 (1988).

[7] R. D. Peccei and H. Quinn, Phys. Rev. Lett. **38**, 1440 (1977); Phys. Rev. D **16**, 1791 (1977); S. Weinberg, Phys. Rev. Lett. **40**, 223 (1978); F. Wilczek, Phys. Rev. Lett. **40**, 279 (1978).

[8] S. Andriamonje *et al.* (CAST collaboration), J. Cosm. Astrop. Phys. **04**, 010 (2007); E. Arik *et al.* (CAST collaboration), *ibid.* **02**, 008 (2009).

[9] E. Iacopini and E. Zavattini, Phys. Lett. **85B**, 151 (1979).

[10] F. Della Valle *et al.* (PVLAS collaboration), Opt. Expr. **22**, 11570 (2014).

[11] G. Cantatore *et al.* (PVLAS collaboration), Rev. Sci. Instrum. **66**, 2785 (1995).

[12] F. Della Valle *et al.* (PVLAS collaboration), arXiv:1406.65 [quant-ph].

[13] K. Ehret *et al.*, Phys. Lett. B **689**, 149 (2010).

Stellar Evolution Bounds on the ALP-Photon Coupling: new Results and Perspectives

Maurizio Giannotti

Barry University, Miami Shores, US

DOI: http://dx.doi.org/10.3204/DESY-PROC-2014-03/giannotti_maurizio

Stellar evolution considerations are of fundamental importance in our understanding of the axion/ALP-photon coupling, $g_{a\gamma}$. Helium burning stars are the best laboratories to study this coupling. Here, we will review the bounds from massive and low mass helium burning stars, and present a new analysis of the bound from the horizontal branch stars. The analysis provides the strongest bound to date on $g_{a\gamma}$ in a wide mass range.

1 Introduction

For several decades stellar evolutionary arguments have provided an invaluable tool to understand various properties of *light, weakly interacting* particles, offering an alternative to terrestrial experiments and often providing even stronger bounds over wide regions of the parameter space. Some of the most successful examples include the study of nonstandard neutrino properties [1, 2, 3, 4], majorons [5], novel baryonic or leptonic forces [6], unparticles [7], extra-dimensional photons [8], axions [9, 10, 11, 4, 12] and, in general, WISPs (Weakly Interacting Slim Particles) [13].

Here, we are interested in the axions, and in particular in its coupling to photons

$$L = -\frac{g_{a\gamma}}{4} a F \tilde{F} = g_{a\gamma} \mathbf{E} \cdot \mathbf{B} \,. \tag{1}$$

Standard (QCD) axions are expected to satisfy a simple relation between mass and coupling, $(m_a/1 \text{ eV}) = 0.5\,\xi\, g_{10}$, where $g_{10} = g_{a\gamma}/(10^{-10}\text{GeV}^{-1})$ and ξ is of order 1 in many motivated axion models. This defines the so called *axion-line* in the $m_a - g_{a\gamma}$ plane. However, models of QCD-axions which do not satisfy this relation existed for a long time [14, 15, 16]. In addition, recently a considerable attention has been devoted to the so-called Axion-Like-Particles (ALPs), light pseudoscalr particles, coupled to photons as in Eq. (1) but not necessarily on the axion-line. Such particles emerge naturally in various extensions of the Standard Model (for a recent review see [13]) and are phenomenologically motivated by a series of unexplained astrophysical observations (see, e.g., [17] and references therein).

Several experiments are currently involved in the axion/ALP search. In particular, the CERN Axion Solar Telescope (CAST) [18], a 3$^{\text{th}}$ generation axion helioscope based at CERN, provides the strongest terrestrial bound, $g_{10} \lesssim 0.88$, on light ALPs ($m_a <$ a few eV). A larger and more sensitive (4$^{\text{th}}$ generation) helioscope, the International Axion Observatory (IAXO, [19]), recently proposed, would allow the exploration of the parameter region about an order of magnitude below the current CAST bound on $g_{a\gamma}$ in a wider mass range.

However, the strongest current bounds on the axion photon coupling are derived from astrophysical considerations. In particular, the analysis of the evolution of intermediate mass stars, $M = 8 - 12\,M_\odot$, leads to the bound $g_{10} \leq 0.8$, while the analysis of globular cluster stars provides the constraint $g_{10} \leq 0.66$. Both bounds apply to a wide mass range, up to a few 10 keV.

2 Helium burning stars and axions

Axions or ALPs with mass below a few keV could be produced in stellar interiors via the Primakoff process – the conversion of a photon into an axion in the electric field of nuclei and electrons in the stellar plasma [9]. The Primakoff process is particularly efficient in the core of He burning stars, at a temperature of about 10^8K and density of $10^3 - 10^4$ g·cm^{-3}. At higher temperatures, though the axions production increases, the pair neutrino process starts dominating and, by the time Carbon burning processes start, it becomes the main cooling mechanism of the star.

Stars of low and high mass show qualitative differences during the core He-burning phase and it is interesting to study them separately.

2.1 Massive stars: the Cepheids bound

Stars a few times more massive than the sun go through the so called *blue loop* phase while burning helium. This stage starts with a contraction during which the star becomes hotter (bluer), followed by a new expansion and cooling which brings the star back to the red region to the right of the HR diagram.

Interestingly, the beginning of the blue loop is fairly independent from the details of the core burning and it is fairly unaffected by axion emission, at least in the range of coupling of interest to us. However, the end of the loop depends on the amount of helium in the core. The presence of an efficient cooling mechanism speeds up the helium consumption and so can induce the loop to terminate early or even prevent it from starting. Though known for several decades (see, e.g., [20]), this observation was applied to the axion case only recently [11] and it was shown that a value of $g_{10} \gtrsim 0.8$ would eliminate the blue loop evolution for all stars in the mass range $M \sim 8 - 12\,M_\odot$.

It is particularly interesting to note that the blue loop extends on the instability strip and so it is necessary to explain the existence of Cepheid stars, whose properties are well understood and very well measured. The absence of Cepheids of mass $M \sim 8 - 12\,M_\odot$ would imply a gap in the observed oscillation periods (mass and period of a Cepheid are related), a fact which is not observed [11].

The relation of this bound to the Cepheid stars makes it quite robust from an observational point of view, since the periods of these stars are very well measured. However, the numerical modeling does present various uncertainties, especially in relation to the convection prescription. Notably, some amount of overshooting would reduce the extension of the loop and eventually eliminate it. The perfect convection prescription is, unfortunately, not known. However, there are indications in favor a non-minimal overshooting (see, e.g., [21]). If so, the Cepheid bound on the axion photon coupling could be somewhat lowered. A full analysis of the uncertainties in this bound is, at the moment, missing.

2.2 Low mass stars: the HB bound

Low mass globular cluster (GC) stars are also very efficient laboratories to study the axion-photon coupling. GCs, gravitationally bound systems of stars populating the Galactic Halo, are among the oldest objects in the Milky Way. Hence only low mass stars ($M \lesssim 0.85\ M_\odot$) are still alive and, therefore, observable. A typical CG harbors a few millions stars, so that the various evolutionary phases are well populated and distinguished from each other. It was recognized early on that axions coupled to photons would significantly reduce the lifetime of stars in the horizontal branch (HB) evolutionary stage, corresponding to the core He burning phase, while producing negligible changes during the preceding red giant branch (RGB) evolution [10]. So, $g_{a\gamma}$ can be constrained by measurements of the R parameter, $R = N_{\rm HB}/N_{\rm RGB}$, which compares the numbers of stars in the HB ($N_{\rm HB}$) and in the upper portion of the RGB ($N_{\rm RGB}$).

The original analyses of the axion bound from HB stars were based on the assumption that the measured R parameter is well reproduced, within 30%, by models of GC stars without including axion cooling. This approach, however, neglects the effects of the initial helium mass fraction Y which also affects the value of the R parameter. Quantitatively we found [12],

$$R(g_{a\gamma}, Y) = 6.26\, Y - 0.41\, g_{10}^2 - 0.12\,.$$

According to the above relation, even a considerable decrease of the HB lifetime caused by a large value of $g_{a\gamma}$ could be compensated by a suitable increase in the assumed He content. Because of this evident degeneracy, a proper evaluation of the axion constraint from the R parameter relies on our knowledge of the He abundance in the GCs.

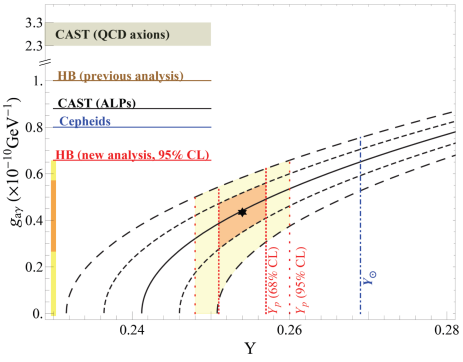

Figure 1: Constraints on $g_{a\gamma}$.

This effect has been taken into account in our recent work [12]. In this new analysis, the recent data for the R parameter [22] have been compared with measurements of the helium mass fraction Y in GCs [23, 24]. The results are shown in Fig. 1. The vertical lines indicate the 1σ and 2σ regions of Y and the dot-dashed vertical line the He abundance in the early solar system $Y_\odot$, provided here as a reference value (see discussion in [12]). The bent curves show $R_{\rm ave}$ and its 1σ and the 2σ ranges. The shaded area delimits the combined 68% CL (dark) and 95% CL (light) for Y and R. The vertical rectangles indicate the 68% CL (dark) and 95% CL (light) for $g_{a\gamma}$. Previous bounds are also shown.

The resulting constrain $g_{10} \leq 0.66$ (at 95% CL) represents the strongest limit on $g_{a\gamma}$ for QCD axions and ALPs in a wide mass range.

3 Discussion and conclusion

Helium burning stars are an excellent laboratory to study the ALP-photon coupling and provide the strongest bounds in a wide mass range which extends up to a few 10 keV.

The analysis from massive stars, which provides the bound $g_{10} \leq 0.8$, shows an interesting connection between Cepheids and particle physics and could possibly be applied to other scenarios in the low energy frontier.

The recent analysis of globular clusters stars provides an even stronger bound, $g_{10} \leq 0.66$ at 95% CL, and, for the first time, an analysis of the uncertainties.

From the Figure 1, it appears that a weakly coupled axion or axion-like particle could improve the relation between the observed R parameter and the helium mass fraction. However, the statistical significance of this result is very low and we prefer, for the moment, to use this analysis only to extract the upper bound on the coupling. Additional investigation may reveal if the effect is just due to poor statistics or indicates new physics. In any case, it is intriguing that the interesting parameter region is well in reach of the next generation experiments, notably ALPs II [25] and IAXO [19].

4 Bibliography

References

[1] J. Bernstein, M. Ruderman and G. Feinberg, Phys. Rev. **132** (1963) 1227.

[2] D. A. Dicus and E. W. Kolb, Phys. Rev. D **15** (1977) 977.

[3] A. Heger, A. Friedland, M. Giannotti and V. Cirigliano, Astrophys. J. **696** (2009) 608 [arXiv:0809.4703 [astro-ph]].

[4] N. Viaux, M. Catelan, P. B. Stetson, G. Raffelt, J. Redondo, A. A. R. Valcarce and A. Weiss, Phys. Rev. Lett. **111** (2013) 231301 [arXiv:1311.1669 [astro-ph.SR]].

[5] H. M. Georgi, S. L. Glashow and S. Nussinov, Nucl. Phys. B **193** (1981) 297.

[6] J. A. Grifols and E. Masso, Phys. Lett. B **173** (1986) 237.

[7] S. Hannestad, G. Raffelt and Y. Y. Y. Wong, Phys. Rev. D **76** (2007) 121701 [arXiv:0708.1404 [hep-ph]].

[8] A. Friedland and M. Giannotti, Phys. Rev. Lett. **100** (2008) 031602 [arXiv:0709.2164 [hep-ph]].

[9] G. G. Raffelt, Phys. Rev. D **33**, 897 (1986).

[10] G. G. Raffelt and D. S. P. Dearborn, Phys. Rev. D **36** (1987) 2211.

[11] A. Friedland, M. Giannotti and M. Wise, Phys. Rev. Lett. **110** (2013) 061101 [arXiv:1210.1271 [hep-ph]].

[12] A. Ayala, I. Dominguez, M. Giannotti, A. Mirizzi and O. Straniero, arXiv:1406.6053 [astro-ph.SR].

[13] K. Baker, G. Cantatore, S. A. Cetin, M. Davenport, K. Desch, B. Dbrich, H. Gies and I. G. Irastorza *et al.*, Annalen Phys. **525** (2013) A93 [arXiv:1306.2841 [hep-ph]].

[14] V. A. Rubakov, JETP Lett. **65** (1997) 621 [hep-ph/9703409].

[15] Z. Berezhiani, L. Gianfagna and M. Giannotti, Phys. Lett. B **500** (2001) 286 [hep-ph/0009290].

[16] L. Gianfagna, M. Giannotti and F. Nesti, JHEP **0410** (2004) 044 [hep-ph/0409185].

[17] G. Carosi, A. Friedland, M. Giannotti, M. J. Pivovaroff, J. Ruz and J. K. Vogel, arXiv:1309.7035 [hep-ph].

[18] S. Andriamonje *et al.* [CAST Collaboration], JCAP **0704**, 010 (2007) [hep-ex/0702006].

[19] I. G. Irastorza, F. T. Avignone, S. Caspi, J. M. Carmona, T. Dafni, M. Davenport, A. Dudarev and G. Fanourakis *et al.*, JCAP **1106** (2011) 013 [arXiv:1103.5334 [hep-ex]].

[20] D. Lauterborn, S. Refsdal and A. Weigert, Astron. Astrophys. **10**, 97 (1971).

[21] S. C. Keller, arXiv:0801.1342 [astro-ph].

[22] M. Salaris, M. Riello, S. Cassisi and G. Piotto, Astron. and Astrophys. **420**, 911 (2004) [astro-ph/0403600].

[23] Y. I. Izotov, G. Stasinska and N. G. Guseva, Astron. & Astroph. **558**, A57 (2013) [arXiv:1308.2100 [astro-ph.CO]].

[24] E. Aver, K. A. Olive, R. L. Porter and E. D. Skillman, JCAP **1311**, 017 (2013) [arXiv:1309.0047 [astro-ph.CO]].

[25] R. Bhre, B. Dbrich, J. Dreyling-Eschweiler, S. Ghazaryan, R. Hodajerdi, D. Horns, F. Januschek and E. -A. Knabbe *et al.*, JINST **8**, T09001 (2013) [arXiv:1302.5647 [physics.ins-det]].

Scalar Gauge Fields, C and CP violation, Global Scalar QED and Axions

Eduardo Guendelman[1]

[1]Physics Department, Ben Gurion University, Beer Sheva, Israel

DOI: http://dx.doi.org/10.3204/DESY-PROC-2014-03/guendelman_eduardo

We study the implications of using the gradient of a scalar field instead of a standard gauge field at various points: a) in minimal coupling and b) in coupling electromagnetism to a global charge. The implications in a) can be surprising, leading to possible mixing of this gauge field with Goldstone bosons, leading to low mass weakly coupled particles, C and CP violation and in case b) we arrive to a new scalar QED that reproduces features of axion photon physics.

1 Generalizing minimal coupling using scalar gauge fields

We introduce [1] a complex scalar field ϕ and consider the local phase symmetry of ϕ by introducing a real, scalar $B(x_\mu)$ in addition to a normal vector gauge field and two types of covariant derivatives as

$$D^A_\mu = \partial_\mu + ieA_\mu \quad ; \quad D^B_\mu = \partial_\mu + ie\partial_\mu B \ . \tag{1}$$

The gauge transformation of the complex scalar, vector gauge field and scalar gauge field have the following gauge transformation

$$\phi \to e^{ie\Lambda}\phi \quad ; \quad A_\mu \to A_\mu - \partial_\mu \Lambda \quad ; \quad B \to B - \Lambda \ . \tag{2}$$

It is easy to see that terms like $D^A_\mu\phi$ and $D^B_\mu\phi$, as well as their complex conjugates will be covariant under (2). Thus one can generate kinetic energy type terms like $(D^A_\mu\phi)(D^{A\mu}\phi)^*$, $(D^B_\mu\phi)(D^{B\mu}\phi)^*$, $(D^A_\mu\phi)(D^{B\mu}\phi)^*$, and $(D^B_\mu\phi)(D^{A\mu}\phi)^*$. Unlike A_μ where one can add a gauge invariant kinetic term involving only A_μ (i.e. $F_{\mu\nu}F^{\mu\nu}$) this is apparently not possible to do for the scalar gauge field B. However note that the term $A_\mu - \partial_\mu B$ is invariant under the gauge field transformation alone (i.e. $A_\mu \to A_\mu - \partial_\mu\Lambda$ and $B \to B - \Lambda$). Thus one can add a term like $(A_\mu - \partial_\mu B)(A^\mu - \partial^\mu B)$ to the Lagrangian which is invariant with respect to the gauge field part only of the gauge transformation in (2). This gauge invariant term will lead to both mass-like terms for the vector gauge field and kinetic energy-like terms for the scalar gauge field. In total a general Lagrangian which respects the new gauge transformation, has the form

$$\begin{aligned} \mathcal{L} &= c_1 D^A_\mu\phi(D^{A\mu}\phi)^* + c_2 D^B_\mu\phi(D^{B\mu}\phi)^* + c_3 D^A_\mu\phi(D^{B\mu}\phi)^* + c_4 D^B_\mu\phi(D^{A\mu}\phi)^* - V(\phi) \\ &- \frac{1}{4}F_{\mu\nu}F^{\mu\nu} + c_5(A_\mu - \partial_\mu B)(A^\mu - \partial^\mu B) \ , \end{aligned} \tag{3}$$

where c_i's are constants. The Maxwell field strength tensor appears in the equation above and is defined as

$$F_{\mu\nu} = \partial_\mu A_\nu - \partial_\nu A_\mu \ . \tag{4}$$

One can see that $F_{\mu\nu}$ is invariant under $A_\mu \to A_\mu - \partial_\mu \Lambda$.Later we will show that it is possible to add non-derivative , polynomial interaction terms for the B field. An interesting point to remark upon is that the last term in (3) will have a term of the form $A_\mu A^\mu$ which is a mass term for the vector gauge field. This term (contrary to the usual gauge transformation given in the introduction) does not violate the expanded gauge symmetry of (2).

2 Particle content, the generalized unitary gauge, C and CP violation

We devote this section to the discussion of the physical reality of the newly introduced scalar gauge field $B(x)$ and to discuss the particle content of the theory when we have spontaneous symmetry breaking i.e. when the scalar field ϕ develops a vacuum expectation value due to the form of the potential $V(\phi)$ in (3). At first glance one might conclude that $B(x)$ is not a physical field – it appears that one could "gauge" it away by taking $\Lambda = B(x)$ in (2). However one must be careful since this would imply that the gauge transformation of the field ϕ would be of the form $\phi \to e^{ieB}\phi$ i.e. the phase factor would be fixed by the gauge transformation of $B(x)$. In this situation one would no longer to able to use the usual unitary gauge transformation to eliminate the Goldstone boson in the case when one has spontaneous symmetry breaking.

The unitary gauge is the standard procedure to find the particle content of a spontaneously broken theory. Let us recall how the unitary gauge works: One writes the complex scalar field as an amplitude and phase – $\phi(x) = \rho(x)e^{i\theta(x)}$. The two fields $\rho(x)$ and $\theta(x)$ represent the initial fields of the system. If $\phi(x)$ develops a VEV due to the form of the potential, $V(\phi)$, then one can transform to the unitary gauge $\phi \to e^{ie\Lambda(x)}\phi(x)$ with $\Lambda = -\theta(x)/e$. In this way one removes the field $\theta(x)$ (which is "eaten" by the gauge boson) and is left with only the $\rho(x)$ field. With the introduction of the scalar gauge field, $B(x)$, one no longer can gauge away *both* $\theta(x)$ and $B(x)$, and in the end one is left with some real, physical field which is some combination of the original $B(x)$ and $\theta(x)$.

We now fix, as far as possible, the character of the c_i's in (3). First c_1, c_2 and c_5 must be real since $D^A_\mu\phi(D^{A\mu}\phi)^*$, $D^B_\mu\phi(D^{B\mu}\phi)^*$ and $(A_\mu - \partial_\mu B)(A^\mu - \partial^\mu B)$ are real. Next c_3 and c_4 must be complex conjugates (i.e. $c_3 = c_4^*$) in order that the combination of the two crossed covariant derivative terms in (3) (i.e. the terms $D^A_\mu\phi(D^{B\mu}\phi)^*$ and $D^B_\mu\phi(D^{A\mu}\phi)^*$) be real. Finally we require that $(c_1 + c_2 + c_3 + c_4) = (c_1 + c_2 + Re[c_3 + c_4]) = 1$. This condition ensures that the kinetic energy term for the scalar field ϕ has the standard form $\partial_\mu\phi\partial^\mu\phi^*$. One could accomplish this as well by rescaling ϕ, but here we chose to accomplish this by placing conditions on the c_i's. Taking into account these conditions (and in particular writing out c_3 and c_4 in terms of their real and imaginary parts $c_3 = a + ib$ and $c_4 = a - ib$) the Lagrangian in (3) becomes

$$\begin{aligned}
\mathcal{L} &= \partial_\mu\phi\partial^\mu\phi^* - V(\phi) - \frac{1}{4}F_{\mu\nu}F^{\mu\nu} + c_5 A_\mu A^\mu + c_5\partial_\mu B\partial^\mu B - 2c_5 A_\mu\partial^\mu B \\
&+ ie[\phi\partial_\mu\phi^* - \phi^*\partial_\mu\phi]\left((c_1 + a)A^\mu + (c_2 + a)\partial_\mu B\right) \\
&+ e^2\phi\phi^*\left(c_1 A_\mu A^\mu + c_2\partial_\mu B\partial^\mu B + 2a\partial_\mu B A^\mu\right) - eb\partial_\mu(\phi^*\phi)(A^\mu - \partial^\mu B) \ .
\end{aligned} \tag{5}$$

There are several interesting features of the Lagrangian in (5). First, the vector gauge field, A_μ, has a mass term (i.e. $c_5 A_\mu A^\mu$) which is allowed by the extended gauge symmetry (2). Thus in addition to the vector gauge field developing a mass through the term $e^2 c_1 \phi\phi^* A_\mu A^\mu$ if ϕ develops a vacuum expectation value (i.e. if $\langle\phi\phi^*\rangle = \rho_0^2$ with ρ_0 a constant), there is now an additional potential mass term for the vector gauge field, even in the absence of spontaneous symmetry breaking via ϕ. Second, the scalar gauge field appears to be a dynamical field through the presence of two possible kinetic energy terms. The term $c_5 \partial_\mu B \partial^\mu B$ is the standard kinetic energy term for a scalar field. Also, the term $c_2 e^2 \phi\phi^* \partial_\mu B \partial^\mu B$ takes the form of a kinetic energy term if ϕ develops a vacuum expectation value. Third, the term $-eb\partial_\mu(\phi^*\phi)(A^\mu - \partial^\mu B)$ will lead to C and CP violation. Let us now define exactly what will be the generalization of the unitary gauge appropriate to the situation here. In the presence of spontaneous symmetry breaking and where the field ϕ develops a VEV the unitary gauge eliminates cross terms like $A_\mu \partial^\mu \theta$ from the Lagrangian. In the present case the cross terms between the vector field A_μ and the scalars (in our case B and θ) are more involved. Explicitly the relevant cross terms that we wish to eliminate by a generalized unitary gauge are

$$\mathcal{L}_{cross} = -2c_5 A_\mu \partial^\mu B + ie(c_1 + a)[\phi\partial_\mu\phi^* - \phi^*\partial_\mu\phi]A^\mu + 2ae^2 \partial_\mu B A^\mu \phi^*\phi \ . \tag{6}$$

It is obvious why the first and third terms in the above equation are denoted as cross terms since they have the form $A_\mu \partial^\mu B$. To see why the second term above is considered a cross term between A_μ and θ in the presence of SSB (i.e. the scalar field develops a VEV $\langle\phi\phi^*\rangle = \rho_0^2$ where ρ_0 is a constant) we begin by approximating the scalar field as $\phi(x) \approx \rho_0 e^{i\theta(x)}$. With this the scalar current becomes $[\phi\partial_\mu\phi^* - \phi^*\partial_\mu\phi] \approx 2\rho_0^2 \partial_\mu\theta$. We have used the assumption that the amplitude of the scalar field is approximately constant – $\rho(x) \approx \rho_0$. Putting all this together show that the second term in (6) is a cross term between A_μ and θ of the form $A_\mu \partial^\mu \theta$. Thus (6) becomes

$$\mathcal{L}_{cross} = 2A_\mu \partial^\mu \left(-c_5 B + ec_1\rho_0^2\theta + ae\rho_0^2\theta + ae^2\rho_0^2 B\right) \ . \tag{7}$$

It is this more complex cross term that we want to eliminate via some generalized unitary gauge. Defining $F(x) = -c_5 B + c_1 e\rho_0^2\theta + ae\rho_0^2\theta + ae^2\rho_0^2 B$, one can see that the cross term in (7) takes the form $\propto A_\mu \partial^\mu F$ which is similar to the more common form $\propto A_\mu \partial^\mu \theta$. By means of a gauge transformation (i.e. $\theta \to \theta + e\Lambda$, $B \to B - \Lambda$) we can take some initial non-zero value $F = F_0$, and always arrive at a gauge $F = 0$. From (7) one can check this is possible by choosing the gauge function as $\Lambda = -F_0/(c_5 + c_1 e^2\rho_0^2)$. In this physical gauge, with $F = 0$, we can solve the θ field in terms of the B field as

$$\theta = \frac{c_5 - ae^2\rho_0^2}{e\rho_0^2(c_1 + a)} B \ . \tag{8}$$

What (8) shows is that θ and B are not independent fields – one is fixed in terms of the other. There is therefore only one physical scalar field in this generalized unitary gauge which one can call either θ or B. The above is different from the normal gauge procedure in the presence of symmetry breaking where the $\theta(x)$ field completely disappears. Here there is some left over hint of the Goldstone boson which we may call $B(x)$ (as we do here) or $\theta(x)$. At this stage the mixed θ/B field is massless and thus could be thought of as a true, massless Goldstone boson. However it is possible to add to the Lagrangian from (5), non-derivative potential terms for the B field. These terms will include a mass term and power law interaction terms. one can write

down the following general interacting potential for ϕ and B

$$V(e^{ieB}\phi) = -m^2\phi\phi^* + \lambda(\phi\phi^*)^2 + \lambda_1 e^{ieB}\phi + \lambda_1^* e^{-ieB}\phi^* + \lambda_2 e^{i2eB}\phi^2 + \lambda_2^* e^{-i2eB}(\phi^*)^2 \\ +\lambda_3 e^{i3eB}\phi^3 + \lambda_3^* e^{-i3eB}(\phi^*)^3 + \lambda_4 e^{i4eB}\phi^4 + \lambda_4^* e^{-i4eB}(\phi^*)^4 \ . \quad (9)$$

If the λ_i 's, have an imaginary part, then those terms will violate charge conjugation symmetry. Defining a canonically normalized field, rescaling the B field, expressing the interactions and effective potential in terms of this field, one can see that the interactions of the new B-particles can be very weak if certain expectation values are big and they can be massive [1], a possible candidate for dark matter?.

3 Global scalar QED and axion photon dynamics

We work here with the following lagrangian density [2]

$$\mathcal{L} = g^{\mu\nu}\frac{\partial\psi^*}{\partial x^\mu}\frac{\partial\psi}{\partial x^\nu} - U(\psi^*\psi) - \frac{1}{4}F^{\mu\nu}F_{\mu\nu} + j_\mu(A^\mu + \partial^\mu B) \quad (10)$$

where

$$j_\mu = ie(\psi^*\frac{\partial\psi}{\partial x^\mu} - \psi\frac{\partial\psi^*}{\partial x^\mu}) \quad (11)$$

and where we have also allowed an arbitrary potential $U(\psi^*\psi)$ to allow for the possibility of spontaneous breaking of symmetry. The model is separately invariant under local gauge transformations

$$A^\mu \to A^\mu + \partial^\mu\Lambda; \quad B \to B - \Lambda \quad (12)$$

and the independent global phase transformations

$$\psi \to exp(i\chi)\psi \quad (13)$$

A model of this type allows to couple electromagnetism to a global charge, it leads to a different version of scalar electrodynamics, without sea gull diagrams. Here also the correspondence between a scalar charged particle in an external electric field with the axion photon dynamics [3] is exact in this version of scalar electrodynamics as opposed to the standard scalar QED, where it is valid only to first order in the coupling constant.

4 Bibliography

References

[1] Eduardo I. Guendelman and Douglas Singleton, JHEP 1405 (2014) 096, "Scalar Gauge Fields", arXiv:1402.7334 [hep-th].

[2] E. Guendelman, Int. J. Mod. Phys. **A28**, 1350169 (2013), "Coupling Electromagnetism to Global Charge", arXiv:1350.6913.

[3] E. Guendelman, Phys. Lett. B **662**, 445 (2008); "Photon and Axion Splitting in an Inhomogeneous Magnetic Field", arXiv: 0802.0311 [hep-th].

Search for a new short-range spin-dependent force with polarized Helium 3

Mathieu Guigue[1], *David Jullien*[2], *Alexander K. Petukhov*[2], *Guillaume Pignol*[1]

[1]LPSC, Université Grenoble-Alpes, CNRS/IN2P3, Grenoble, France
[2]Institut Laue Langevin, 6 Rue Jules Horowitz, 38000 Grenoble, France

DOI: http://dx.doi.org/10.3204/DESY-PROC-2014-03/guigue_mathieu

Measuring the depolarization rate of a ^{3}He hyperpolarized gas is a sensitive method to probe hypothetical short-range spin-dependent forces. A dedicated experiment is being set up at the Institute Laue Langevin in Grenoble to improve the sensitivity. We present the status of the experiment.

1 Probing short-range spin-dependent interaction

Numerous theories beyond the Standard Model of particle physics predict the existence of new light scalar bosons such as the Axions theory [1] developed to solve the strong CP problem. The exchange of a new scalar boson of mass m_ϕ between a polarized probe particle and an unpolarized source particle, separated by r, would mediate a short-range monopole-dipole interaction defined by the potential:

$$V = g_s^N g_p^N \frac{\hbar\widehat{\sigma}.\widehat{r}}{8\pi Mc}\left(\frac{m_\phi}{r}+\frac{1}{r^2}\right)\exp(-m_\phi r) \tag{1}$$

where $\hbar\widehat{\sigma}/2$ is the spin of the probe particle, M the mass of the polarized particle, g_s^N and g_p^N the coupling constant at the vertices of polarized and unpolarized particles corresponding to a scalar and a pseudoscalar interactions. Finding a new boson or a new short-range interaction interaction would be a important discovery in fundamental physics, since it could solve problems such as the nature of the Dark Matter (as a WISP candidate [2]). This new force is thus actively searched for around the world through different kind of experiments (using torsion-balance, studying the Newton's inverse square law or looking at bouncing ultracold neutrons [3]).

Consider a spherical cell filled with polarized ^{3}He atoms with a gyromagnetic ratio γ immersed in a static magnetic field B_0. In the case of a light boson with $m_\phi \lesssim 1\,\mathrm{eV}$, the axion-like interaction given by Eq. (1) acts like a macroscopic pseudomagnetic field of typical size $\lambda = \frac{\hbar}{m_\phi c} \gtrsim 1\,\mu\mathrm{m}$, which is generated by the glass walls of the cell:

$$b_{\mathrm{NF}}(x) \quad = \quad \frac{\hbar\lambda}{2\gamma m_n} N g_s g_p \left(1-e^{-d/\lambda}\right) e^{-x/\lambda}, \tag{2}$$

where N is the nucleon density, m_n the nucleon mass, x the distance to the cell wall and d the thickness of the wall. This new pseudomagnetic field acting close and perpendicular to the

surface of the cell would provoke the depolarization of the gas, whose rate is, for a pressure of several bars and typical cell sizes L much larger than λ:

$$\Gamma_{1,\mathrm{NF}} \approx \sqrt{\frac{2}{\gamma B_0}} \frac{\lambda^2 \gamma^2 b_a^2}{L}, \tag{3}$$

where b_a is the the prefactor of the exponential in Eq. (2). This new relaxation channel adds to the the natural depolarization Γ_1 of the gas, which results from the three main contributions: the relaxation rate induced by collisions of polarized atoms on the cell walls Γ_w, the relaxation rate due to interparticles collisions Γ_{dd} and the depolarization rate due to the motion of polarized particles in an inhomogeneous magnetic field Γ_m. While Γ_1 behaves as $a + \frac{b}{B_0} + \frac{c}{B_0^2}$, the relaxation rate $\Gamma_{1,\mathrm{NF}}$ is proportional to $1/\sqrt{B_0}$ which is a non-standard dependence on the holding magnetic field B_0. The existence of a new short-range spin-dependent interaction can then be extracted from measurements of the relaxation rate at different values of the holding magnetic field.

A first test experiment [3, 4] measuring the spin longitudinal depolarization rate Γ_1 as a function of the applied field B_0 was performed in 2010 to demonstrate the sensitivity of the method. A new dedicated experiment is set up at the Institute Laue-Langevin, improving both (i) the magnetic environment of the experiment and (ii) the measurement of the decay of polarization.

2 An improvement of the magnetic field environment

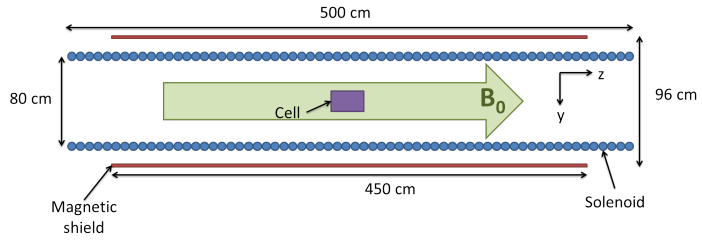

Figure 1: Scheme of the apparatus.

In order to suppress the magnetic field inhomogeneity depolarization channel Γ_m, the holding magnetic field should be as homogeneous as possible. The apparatus, represented on Fig. 1, is composed of a 5 m long and 80 cm diameter solenoid which provides a very homogeneous magnetic field. In order to shield its center from external magnetic fields, this solenoid is inserted into a μ-metal magnetic shield of 96 cm diameter and 4 m long from "n-nbar" experiment [5] which measured at the Institut Laue Langevin the neutron-antineutron oscillation.

In addition, we mapped the inner magnetic field using a three-axis fluxgate magnetometer, in order to extract the transverse gradients $g_\perp$ for different B_0 settings. Typically, $g_\perp$ is about 1.5 nT/cm to 2 nT/cm for magnetic field from 2 μT to 80 μT. The magnetic relaxation time $T_m = 1/\Gamma_m$ is then expected to be longer than 90 h. At low field ($B_0 = 3\,\mu$T), this is a factor 100 better than the previous experiment. This improvement will directly affect the duration of the experiment and so the precision of the relaxation rate measurement.

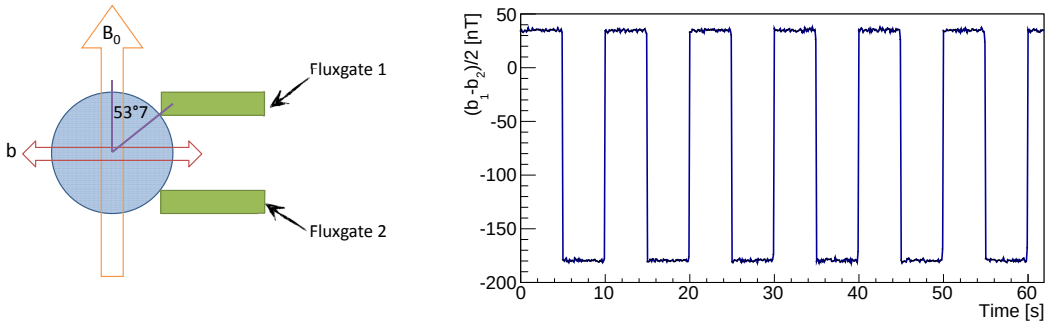

Figure 2: (Left) Scheme of the spin-flipping and measurement apparatus. The spherical cell is positioned in contact with the two magnetometers inside the spin-flip coil which generates an oscillating magnetic field transversely b to the holding magnetic field B_0. (Right) Typical sequence of measurement of the transverse magnetic field generated by a cylindrical cell at 4 bar with two fluxgate magnetometers. The upper (lower) points correspond to the spin up (down) state of the gas.

3 The polarization measurement technique

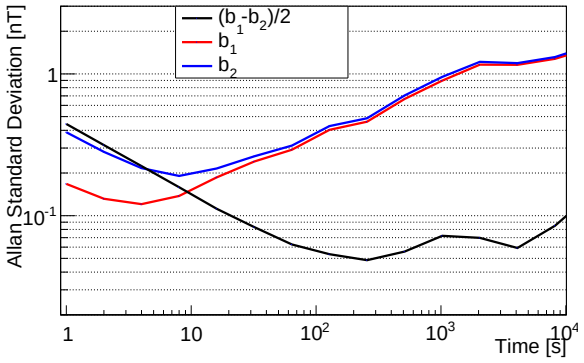

Figure 3: Allan Standard Deviation of the measurements of the transverse magnetic field generated by the solenoid with the two fluxgate magnetometers (in blue and red) and the Allan Standard Deviation of the differential measurement (in black).

Among all the way to measure the polarization and the relaxation rate of an hyperpolarized gas, the nuclear magnetic resonance (NMR) is the most widely used technique. One can measure at the percent level the amplitude of the NMR response signal or can also measure the frequency shift, both proportional to the polarization.

A better precision for the longitudinal relaxation rate measurement can be achieved with a direct polarimetry technique [6]: it consists in measuring, with two fluxgate magnetometers, the magnetic field generated by the gas itself which can be of order of tenths of nT at pressures of several bars. The magnetometers sensors are at a place where the dipolar field induced by the polarized gas is transverse relative of the B_0 field.

Applying spin-flips with a transverse oscillating magnetic field (Fig. 2) to reverse the polarization, one can remove magnetic offsets induced by long-term drift of the holding magnetic field or the misalignment of the magnetometers axis with B_0. Fig. 2 shows typical sequences of "up-down-down-up" measurements of the magnetic field induced by a spherical cell at 1 bar with the two magnetometers.

Fig. 3 shows the Allan Standard Deviation (ASD) of the holding field measurements with each magnetometers and of differential measurements. Since the magnetometers measure the same signal with an opposite sign, a differential acquisition between the two fluxgate magnetometers improves the precision of the measurement by suppressing the long-time correlated fluctuations of the holding magnetic field. Since the Allan Standard Deviation of the fluxgate magnetometers is 50 pT at 1 s when they are exposed to no magnetic field, the uncertainty on the polarization measurement mainly comes from the the holding magnetic field instability. This deviation is about 0.4 nT at 1 s; then, for a 1 bar cell of 70 % polarized helium, the typical magnetic field generated by the cell is 30 nT.

Since several measurements of magnetic field are performed for a single relative polarization determination, the relative uncertainties on the polarization is about 0.3 % which leads to relative uncertainties on relaxation rates lower than 1 %.

4 Expected constraints

The high quality of the magnetic environment decreases the dominant depolarization contribution at low magnetic field and the direct polarization measurement technique increases our sensitivity to any deviation from the classical behaviour of the longitudinal relaxation rate with the holding magnetic field B_0. From the expected Γ_1 curve as a function of B_0, one can extract the expected sensitivity (shown on Fig. 4) of the coupling constants product $g_s^N g_p^N$ from a new depolarization channel (3).

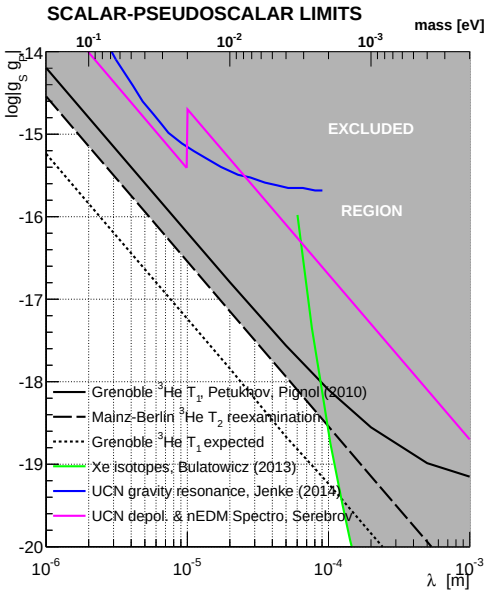

Figure 4: Constraints on the coupling constant product of axion-like particles to nucleons $g_s^N g_p^N$ as a function of the range λ of the macroscopic interaction. Bold black line, from ^{3}He T_1 measurement [4]; long-dashed line, ^{3}He T_2 reexamination [4]; short-dashed line, expected constraint from upgraded setup (present work); light green, from [7]; blue, from [8]; pink, from [9, 10].

References

[1] J. E. Moody and F. Wilczek, Phys. Rev. D 30, 130 (1984).

[2] P. Arias *et al.*, arXiv:1201.5902.

[3] I. Antoniadis *et al.*, Comptes Rendus Physique 12, 755 (2011).

[4] A. K. Petukhov *et al.*, Phys. Rev. Lett. 105, 170401 (2010).

[5] T. Bitter *et al.*, Nucl. Instrum. Methods Phys. Res. A 309, 521 (1991).

[6] E. Wilms *et al.*, Nucl. Instrum. Methods Phys. Res. A 401, 491 (1997).

[7] M. Bulatowicz *et al.*, arXiv:1301.5224.

[8] T. Jenke *et al.*, Phys. Rev. Lett. 112, 151105 (2014).

[9] A. P. Serebrov, Phys. Lett. B 680, 423 (2009).

[10] A. P. Serebrov *et al.*, Pis'ma Zh. Eksp. Tero. Fiz. 91, 8 (2010).

Light-Shining-Through-Walls with Lasers

Friederike Januschek[1]

[1]Deutsches Elektronen-Synchrotron (DESY), Hamburg, Germany

DOI: http://dx.doi.org/10.3204/DESY-PROC-2014-03/januschek_friederike

Light-Shining-Through-Walls experiments are the search experiments for weakly interacting slim particles (WISPs) with the smallest model dependence. They have the advantage that not only the detection, but also the production of the WISPs takes place in the laboratory and can thus be controlled. Using lasers is the preferred option for most of the mass region and has led to the world's most stringent laboratory limits (ALPS I) there. At CERN, OSQAR promises to surpass these and at DESY ALPS II is currently set up, which is planning to probe the axion-like particle to photon coupling down to $|g_{a\gamma}| \gtrsim 2 \cdot 10^{-11}$ GeV^{-1}, which is in a region favored by many astrophysical hints.

1 Motivation

WISPs are predicted by many extensions of the Standard Model. Most importantly, the axion provides the most elegant solution to the strong CP problem of quantum chromo dynamics [1, 2, 3]. In string theory inspired Standard Model extensions axion-like particles (ALPs) are expected [4]. These theoretical motivations would already make it worthwhile to look for WISPs experimentally, but the cause for their existence gets much stronger by pointing out that axions and ALPs are also well-motivated (cold) dark matter candidates.

Furthermore in the last years there have been several astrophysical phenomena, which could be explained by the existence of ALPs. Most prominently the reduced opacity of the universe for TeV photons compared to predictions [5, 6]: Extremely energetic γ-rays from cosmological sources should be attenuated by pair production through interaction with the extragalactic background light. Several studies have shown that the observed energy spectra do not fit this picture. This could be explained by the oscillation of photons into ALPs in ambient magnetic fields, which then travel unhinderedly due to their weak interaction and finally convert back to photons [7, 8]. For the relevant parameter region see Figure 1.

Recent observations like the unexplained 3.55 keV emission line from galaxy clusters and Andromeda, which could also be attributed to ALP-related decaying dark matter (see e.g. [10, 11]) or signatures of unexplained energy losses in stars [12, 13].

2 Experimental options

There are different prominent options looking for WISPs when employing $g_{a\gamma}$:

- Haloscopes
- Helioscopes and
- Light-Shining-Through-Walls experiments.

Haloscopes like ADMX [14] in Washington and WISPDMX [15] in Hamburg look for dark matter WISPs, typically using a resonant microwave cavity. This has the advantage of being very sensitive so that even the QCD axion is in reach, but only in a very narrow mass region (see Figure 1). Also the results are theoretically dependent on cosmology and astrophysics.

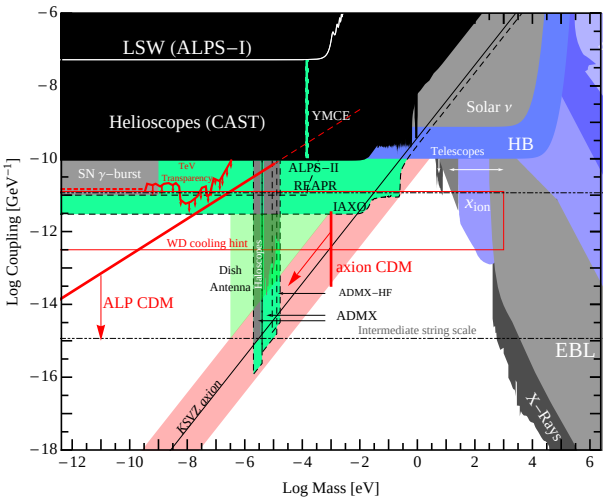

Figure 1: ALP parameter space with important hints and exclusion regions of past, present and future experiments [9].

Helioscopes (like CAST [16]) look for WISPs produced in the sun, thus their results only depend on astrophysics, but they are also less sensitive. As they are very broadband, their limits are the constraining factor in a wide mass region (see Figure 1).

In contrast to Haloscopes and Helioscopes, in Light-Shining-Through-Walls (LSW [17], see Figure 2) experiments the WISPs are produced (and detected) within the experiment. This has the distinct advantage that the theory dependence is kept at minimum and that the WISP production can be controlled and thus e.g. switched on and off.

In general the probability for a conversion between axions and photons $P_{\gamma\leftrightarrow a}$ due to the Primakoff effect is described by

$$P_{\gamma\leftrightarrow a} \propto (g_{a\gamma}BL)^2$$

where BL is the magnetic length and $g_{a\gamma}$ the coupling strength.

Thus the signal rate in a LSW experiment $\dot{N_{out}}$ is

$$|\dot{N_{out}}| \propto \dot{N_{in}} \cdot (g_{a\gamma})^4 \cdot (BL)^4 \cdot \epsilon_{det},$$

therefore depending on the number of incoming photons $\dot{N_{in}}$, the coupling strength, the magnetic length and the detection efficiency ϵ_{det}.

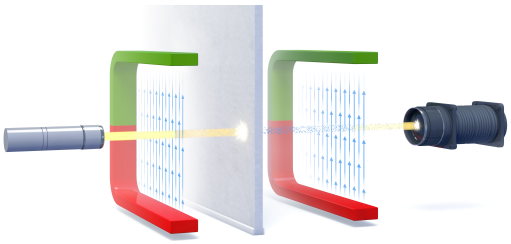

Figure 2: A diagram of a LSW setup [18]: A strong light source is shone on an opaque wall. On the other side of the wall there is a sensitive light detector. In addition, magnets are required on both sides for ALP searches.

LSW experiments can be done for all wavelengths, in principle. One example, using microwaves, is the CROWS experiment [19], having the advantage that operating low loss cavities

is comparatively easy for microwaves. Microwaves do have the disadvantage though that their relatively low energy restricts the probed mass region.

In contrast, LSW experiments can be (and have been [20, 21]) done using X-rays. In that case, high-mass regions can be investigated, but due to the impossibility of high-finesse cavities the number of photons and thus the sensitivity is rather limited.

Due to these reasons, LSW experiments in the visible/infrared with a laser as light source are the most common and several have been, are and will be performed (e.g. [22, 23, 24, 25, 26, 27, 18]), see also Figure 3 and the following Sections) since the suggestion of the principle [28, 29, 30].

3 ALPS I

The ALPS I experiment at DESY [22] was an LSW experiment at DESY from 2007 to 2010. It used an old HERA magnet of 5 T and about 1.2 kW of circulating laser power supplied by a laser power output of $\approx$ 4.6W of 512 nm green light and an optical resonator with a power build-up of about 300. The result of the data-taking in 2010 were the worldwide best laboratory limits (see Figure 3).

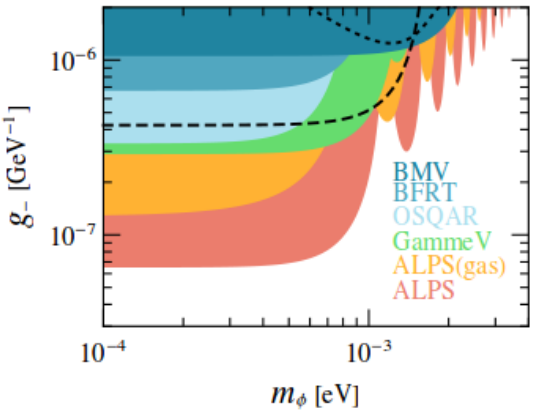

Figure 3: Exclusion limits (95% C.L.) or scalar axion-like-particles from the ALPS I [22], BFRT [24], BMV [23], GammeV [25] and OSQAR ([31], see Section 4) LSW experiments as of 2010, taken from [22].

4 OSQAR

OSQAR [27, 31] is an experiment of the LSW type currently taking place at CERN. The setup can be seen in the left part of Figure 4. At OSQAR an argon laser of 3-25 W and 488-514 nm is used in a 9 T transverse magnetic field of two LHC magnets over the unprecedented length of 2 $\times$ 14.3 m. For detection a CCD camera is used.

OSQAR was able to confirm the ALPS I limits [32].

Further improvements are planned so that OSQAR could in the near future probe even deeper $g_{a\gamma}$ regions and look at regions previously not covered by LSW experiments.

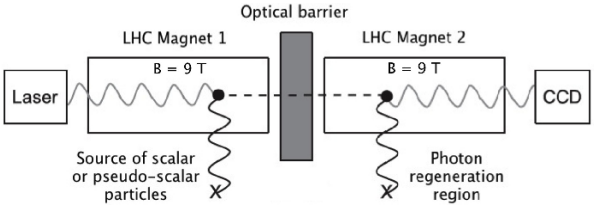

Figure 4: Setup of the OSQAR experiment, taken from [32].

5 ALPS II

The ALPS II experiment at DESY is the successor of ALPS I with the aim of increasing the sensitivity reaching down to the main region of the astrophysical ALP hints. Therefore, ALPS I is planned to be improved by three main factors:

- an additional regeneration cavity,
- an increase in magnetic length through usage of more magnets and
- a different detector system.

These changes, as described in the TDR [18], are supposed to lead to an increase in sensitivity to the coupling of a factor of about 3000 (see Table 1).

A simple scheme of the ALPS II setup is shown in Figure 5. In addition to an increase of the power build-up of the production cavity in front of the wall, leading to an effective power of 150 kW, the regeneration cavity behind the wall is built to enhance the probability of WISP to photon reconversion probability by a factor of 40,000.

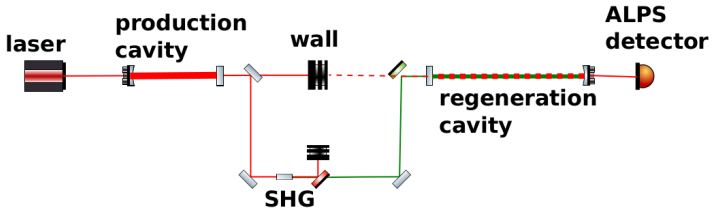

Figure 5: Setup of the ALPS II experiment, adapted from [18].

The most important factor with regards to a gain in sensitivity is the magnetic length increase. For that the usage of 20 HERA magnets (10 in front of and 10 behind the wall) is planned. As the HERA magnets are bent, the effective aperture -when using a long string of magnets- would be very small, leading to clipping losses and limiting the power build-up. Thus a method was devised, successfully tested and recently further improved to straighten the HERA magnets.

In contrast to ALPS I, the light used in ALPS II is near-infrared (1064 nm), which leads to the necessity of a different detector system as the quantum efficiency of a CCD would be very low (see [33]). Therefore, a Transition Edge Sensor (TES) detector system has been set up at the ALPS laboratory [34]. The system has been commissioned and calibrated with promising results, especially a low dark count rate, details see [35].

The first stage of ALPS II (ALPS IIa, with two 10 m cavities and without magnets, thus searching only for hidden photons) is planned to start taking data in the end of 2014/beginning of 2015. The planned second-stage (ALPS IIb, two 100 m cavities, but without magnets) had to be cut due to budget constraints. The final ALPS II data-taking with the complete setup is scheduled for 2018.

Parameter	Scaling	ALPS I	ALPS IIc	Sens. gain
Effective laser power P_{laser}	$g_{a\gamma} \propto P_{\text{laser}}^{-1/4}$	1 kW	150 kW	3.5
Rel. photon number flux n_γ	$g_{a\gamma} \propto n_\gamma^{-1/4}$	1 (532 nm)	2 (1064 nm)	1.2
Power built up in RC P_{RC}	$g_{a\gamma} \propto P_{reg}^{-1/4}$	1	40,000	14
BL (before& after the wall)	$g_{a\gamma} \propto (BL)^{-1}$	22 Tm	468 Tm	21
Detector efficiency QE	$g_{a\gamma} \propto QE^{-1/4}$	0.9	0.75	0.96
Detector noise DC	$g_{a\gamma} \propto DC^{1/8}$	$0.0018\,\text{s}^{-1}$	$0.000001\,\text{s}^{-1}$	2.6
Combined improvements				3082

Table 1: Sensitivity of ALPS II compared to ALPS I, taken from [18].

Exp.	Photon flux 1/s	E_γ eV	B T	L m	B·L Tm	PB	Sens. rel.
ALPS I	$3.5 \cdot 10^{21}$	2.3	5.0	4.4	22	1	0.0003
ALPS IIc	$1 \cdot 10^{24}$	1.2	5.3	106	468	40,000	1
Future	$3 \cdot 10^{25}$	1.2	13	400	5200	100,000	27

Table 2: Comparison of ALPS I, ALPS II and a possible future experiment.

6 Conclusion and outlook

LSW in the optical regime is an important tool for (relatively) model-independent searches for the well-motivated WISP particles. ALPS I has set stringent laboratory-based limits and OSQAR will be able to improve them in the near future. ALPS II, which is currently being set-up, will be able to reach the interesting region(s) with regards to the astrophysical hints.

In addition, another LSW experiment with a laser, REAPR, has been proposed at Fermilab [36], which is supposed to use a long string of Tevatron magnets and a production and a regeneration cavity similar to ALPS II. For REAPR a heterodyne signal detection scheme has been suggested.

Looking at what would be possible to achieve with a LSW setup in the near future, the sensitivity could be increased by about a factor of 27 compared to ALPS II (see Table 2) through the use of better magnet (e.g. magnets as designed for the LHC upgrade) und further increasing the power build-up of the cavities. This sensitivity increase would then cover the complete region covered by the leading astrophysical hints. Thus such an LSW experiment would either discover WISPs there or rule them out as an explanation for these phenomena.

Acknowledgements

The author would like to thank the organisers of the motivating workshop and the members of the ALPS II collaboration.

References

[1] R. D. Peccei and H. R. Quinn, Phys. Rev. Lett. **38** (1977) 1440.

[2] S. Weinberg, Phys. Rev. Lett. **40** (1978) 223.

[3] F. Wilczek, Phys. Rev. Lett. **40** (1978) 279.

[4] A. Ringwald, Phys. Dark Univ. **1** (2012) 116 [arXiv:1210.5081 [hep-ph]].

[5] D. Horns and M. Meyer, JCAP **1202** (2012) 033 [arXiv:1201.4711 [astro-ph.CO]].

[6] G. I. Rubtsov and S. V. Troitsky, JETP Lett. **100** (2014) 397 [arXiv:1406.0239 [astro-ph.HE]].

[7] A. De Angelis, M. Roncadelli and O. Mansutti, Phys. Rev. D **76** (2007) 121301 [arXiv:0707.4312 [astro-ph]].

[8] M. Meyer, D. Horns and M. Raue, Phys. Rev. D **87** (2013) 035027 [arXiv:1302.1208 [astro-ph.HE]].

[9] R. Essig *et al.*, arXiv:1311.0029 [hep-ph].

[10] M. Cicoli *et al.*, Phys. Rev. D **90** (2014) 023540 [arXiv:1403.2370 [hep-ph]].

[11] J. Jaeckel, J. Redondo and A. Ringwald, Phys. Rev. D **89** (2014) 103511 [arXiv:1402.7335 [hep-ph]].

[12] A. Ayala *et al.*, arXiv:1406.6053 [astro-ph.SR].

[13] N. Viaux *et al.*, Phys. Rev. Lett. **111** (2013) 231301 [arXiv:1311.1669 [astro-ph.SR]].

[14] L. Rosenberg, 10th Patras Workshop on Axions, WIMPs and WISPs, these proceedings.

[15] A. Lobanov, 10th Patras Workshop on Axions, WIMPs and WISPs, these proceedings.

[16] K. Zioutas *et al.* [CAST Collaboration], Phys. Rev. Lett. **94** (2005) 121301 [hep-ex/0411033].

[17] J. Redondo and A. Ringwald, Contemp. Phys. **52** (2011) 211 [arXiv:1011.3741 [hep-ph]].

[18] R. Bähre *et al.*, JINST **8** (2013) T09001 [arXiv:1302.5647 [physics.ins-det]].

[19] M. Betz *et al.*, Phys. Rev. D **88** (2013) 7, 075014 [arXiv:1310.8098 [physics.ins-det]].

[20] R. Battesti *et al.*, Phys. Rev. Lett. **105** (2010) 250405 [arXiv:1008.2672 [hep-ex]].

[21] T. Inada *et al.*, Phys. Lett. B **722** (2013) 301 [arXiv:1301.6557 [physics.ins-det]].

[22] K. Ehret *et al.*, Phys. Lett. B **689**, 149 (2010) [arXiv:1004.1313 [hep-ex]].

[23] M. Fouche *et al.*, Phys. Rev. D **78** (2008) 032013 [arXiv:0808.2800 [hep-ex]].

[24] R. Cameron *et al.*, Phys. Rev. D **47** (1993) 3707.

[25] A. S. .Chou *et al.* [GammeV (T-969) Collaboration], Phys. Rev. Lett. **100** (2008) 080402 [arXiv:0710.3783 [hep-ex]].

[26] A. Afanasev *et al.*, Phys. Rev. Lett. **101** (2008) 120401 [arXiv:0806.2631 [hep-ex]].

[27] P. Pugnat, 10th Patras Workshop on Axions, WIMPs and WISPs, these proceedings.

[28] L. B. Okun, Sov. Phys. JETP **56** (1982) 502 [Zh. Eksp. Teor. Fiz. **83** (1982) 892].

[29] A. A. Anselm, Yad. Fiz. **42** (1985) 1480.

[30] K. Van Bibber *et al.*, Phys. Rev. Lett. **59** (1987) 759.

[31] P. Pugnat *et al.* [OSQAR Collaboration], Phys. Rev. D **78** (2008) 092003 [arXiv:0712.3362 [hep-ex]].

[32] P. Pugnat *et al.* [OSQAR Collaboration], arXiv:1306.0443 [hep-ex].

[33] J. E. von Seggern, DESY-THESIS-2014-001.

[34] J. Dreyling-Eschweiler, DESY-THESIS-2014-016.

[35] J. Dreyling-Eschweiler for the ALPS II collaboration, 10th Patras Workshop on Axions, WIMPs and WISPs, these proceedings.

[36] G. Mueller *et al.*, Phys. Rev. D **80** (2009) 072004 [arXiv:0907.5387 [hep-ph]].

QCD Axion and Dark Energy

Jihn E. Kim
Department of Physics, Kyung Hee University, Seoul 130-701, Korea, and
Department of Physics, Seoul National University, Seoul 151-747, Korea

DOI: http://dx.doi.org/10.3204/DESY-PROC-2014-03/kim_jihn

String allowed discrete symmetry is the mother of acceptable effective global symmetries at low energy. With this philosophy, we discuss dark energy, QCD axion, and inflation, and speculate some implications of the recent BICEP2 data.

1 Pseudo-Goldstone Bosons from Discrete Symmetries

The ongoing QCD axion detection is based on the bosonic coherent motion (BCM). The QCD axion can be a fundamental pseudoscalar or a composite one [1]. But, after the discovery of the fundamental Brout-Englert-Higgs (BEH) boson, a fundamental QCD axion gain much more weight. This leads to a BEH portal to the high energy scale to the axion scale or even to the standard model (SM) singlets at the grand unification (GUT) scale. Can these singlets explain both dark energy (DE) and cold dark matter (CDM) in the Universe? Because the axion decay constant f_a, signifying the axion window, can be in the intermediate scale, axions can live up to now ($m_a < 24$ eV) and constitute DM of the Universe. In this year of a GUT scale VEV, can these explain the inflation finish in addition to DE and CDM?

But we have to worry about the quantum gravity effects which are known to break global symmetries, especially via the Planck scale wormholes. To resolve this dilemma, we can think of two possibilities of discrete symmetries below $M_{\rm P}$ [2]: (i) The discrete symmetry arises as a part of a gauge symmetry, and (ii) The string selection rules directly give the discrete symmetry. So,

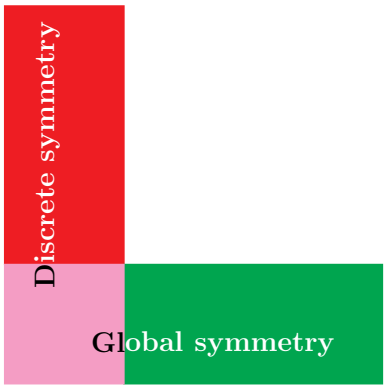

Figure 1: Terms respecting discrete and global symmetries.

we will consider discrete gauge symmetries allowed in string compactification. Even though the Goldstone boson directions in spontaneously broken gauge symmetries are flat, the Goldstone boson directions of spontaneously broken *global* symmetries are not flat, *i.e.* global symmetries are always *approximate*. The question is what is the degree of the *approximateness*. In Fig. 1, we present a cartoon separating effective terms according to string-allowed discrete symmetries. The terms in the vertical column represent exact symmmetries such as gauge symmetries and string allowed discrete symmetries. If we consider a few terms in the lavender part, we can consider a *global symmetry*. The global symmetry is broken by terms in the red part.

The most studied global symmetry is the Peccei-Quinn (PQ) symmetry $\mathrm{U}(1)_{\mathrm{PQ}}$. For $\mathrm{U}(1)_{\mathrm{PQ}}$, the dominant breaking term is the QCD anomaly term $(\overline{\theta}/32\pi^2)G_{\mu\nu}\tilde{G}^{\mu\nu}$ where $G_{\mu\nu}$ is the gluon field strength. Since $\overline{\theta}$ gives a neutron EDM (nEDM) of order $10^{-16}\overline{\theta}\,e$cm, the upper bound on nEDM restricts $|\overline{\theta}| < 10^{-10}$. "Why is $\overline{\theta}$ so small?" is the strong CP problem [3].

Axion osmology was started in 1982–1983. One key point I want to stress here is the axion domain wall (DW) problem [4, 5]. But the recent numerical study [6] of axion creation by decay of axionic DWs is too large, which gave a strong lower bound on the axion mass [7] from the BICEP2 data [8]. For the DW problem from string, there is a solution of Choi-Kim [9], which has been recently used for the anomalous U(1) from string [10, 11] in view of the GUT scale inflation implied by the BICEP2 data. A smoking gun for the axion CDM is detecting an oscillating $\overline{\theta}$. In this spirit, an oscillating nEDM was suggested to be measured 20 years ago [12, 13], and it got renewed interests recently [14, 15]. A guideline for the axion-photon-photon coupling is a string calculation, $c_{a\gamma\gamma} \simeq 0.91$ [16] in the $\mathbf{Z}_{12-I}$ model [17].

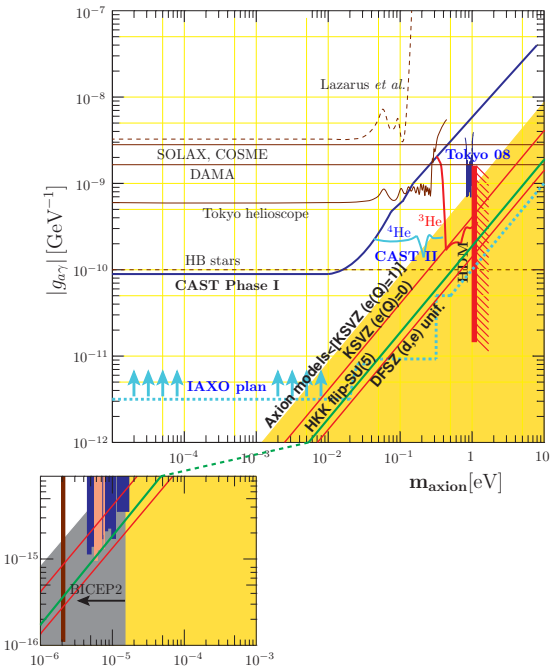

Figure 2: The $g_{a\gamma}$ coupling vs. axion mass. The green line is a string calculation [16].

2 Dark Energy from $U(1)_{de}$

The axion oscillation is just one example of BCM, classified as **BCM1** in [18]. The QCD axion naturally arises if one tries to interpret the DE scale by spontaneously breaking an *approximate* U(1) global symmetry, $U(1)_{de}$. A recent calculation of the cosmic axion density gives the axion window, 10^9 GeV $< f_a < 10^{12}$ GeV, including the anharmonic term carefully with the new data on light quark masses [19]. It is known that string axions from B_{MN} have GUT scale decay constants [20]. Therefore, the QCD axion from string theory is better to arise from matter fields originating from 10-dimensional adjoint representation of $E_8 \times E_8'$ [21]. Note that the global symmetry violating terms belong to the red part in Fig. 1. For the QCD axion, the dominant breaking is by the QCD anomaly term. The QCD anomaly term is too large to account for the DE scale of 10^{-46} GeV^4. Because the BEH scalar is known to be a fundamental one, we extend the fundamentality to the SM singlet scalars also. These singlets must couple to $H_u H_d$, *i.e.* a kind of BEH portal. So, to relate the DE scale to a pseudo-Goldstone boson from $U(1)_{de}$, we must forbid the coupling to the QCD anomaly term, which can be done only by introducing another *global* U(1), *i.e.* to remove the $U(1)_{de}$-G-G anomaly with G = QCD. Namely, another U(1) must be introduced so that one linear combination is free of the QCD anomaly. Thus, introduction of two global symmetries is inevitable to interpret the DE scale in terms of a potential of a pseudo-Goldstone boson [22]. Let us call these two global symmetries as $U(1)_{PQ}$ and $U(1)_{de}$.

The breaking scale of $U(1)_{de}$ is trans-Planckian [23]. With $U(1)_{PQ}$ and $U(1)_{de}$, one can construct a DE model from string compactification [24]. Using the SUSY language, the discrete and global symmetries below M_P are the consequence of the full superpotential W. So, the exact symmetries related to string compactification are respected by the full W, *i.e.* the vertical column of Fig. 1. Considering only the $d = 3$ superpotential W_3, we can consider an approximate PQ symmetry. For the MSSM interactions supplied by R-parity, one needs to know all the SM singlet spectrum. We need $\mathbf{Z}_2$ for a WIMP candidate.

The DE potential height is so small, 10^{-46} GeV^4, that the needed discrete symmetry breaking term of Fig. 1 must be small, implying the discrete symmetry is of high order. Now, we have a scheme to explain both 68% of DE and 27% of CDM via approximate *global* symmetries. With SUSY, axino may contribute to CDM also [25].

A typical example for the discrete symmetry is $\mathbf{Z}_{10\,R}$ as shown in [24]. The $\mathbf{Z}_{10\,R}$ charges descend from a gauge U(1) charges of the string compactification [17]. The U(1) defining terms, *i.e.* the lavender part of Fig 1, is W_6. Then, the height of the potential is highly suppressed and we can obtain 10^{-47} GeV^4, without the gravity spoil of the global symmetry. In this scheme with BEH portal, we introduced three VEV scales, TeV scale for $H_u H_d$, the GUT scale M_{GUT} for singlet VEVs, and the intermediate scale for the QCD axion. The other fundamental scale is M_P. The trans-Planckian decay constant f_{de} can be a derived scale [26].

Spontaneous breaking of $U(1)_{de}$ is via a Mexican hat potential with the height of M_{GUT}^4. A byproduct of this Mexican hat potential is the hilltop inflation with the height of $O(M_{GUT}^4)$. It is a small field inflation, consistent with the recent Planck data.

3 Gravity Waves from $U(1)_{de}$ and its Implications

With the surprising report from the BICEP2 group on a large tensor-to-scalar ratio r [8], we must consider the above hilltop inflation whether it leads to appropriate numbers on n_s, r and

the e-fold number e or not. With two U(1)'s, the large trans-Planckian $f_{\rm de}$ is not spoiled by the intermediate PQ scale f_a because the PQ scale just adds to the $f_{\rm de}$ decay constant only by a tiny amount.

Inflaton potentials with almost flat one near the origin, such as the Coleman-Weinberg type new inflation, were the early attempts for inflation. But any models can lead to inflation if the potential is flat enough as in the *chaotic inflation* [27]. A single field chaotic inflation survived now is the $m^2\phi^2$ scenario *chaotic inflation*. To shrink the field energy much smaller than $M_{\rm P}^4$, a *natural inflation* (mimicking the axion-type minus-cosine potential) has been introduced [28]. If a large r is observed, Lyth noted that the field value $\langle\phi\rangle$ must be larger than $15\,M_{\rm P}$, which is known as the Lyth bound [29]. To obtain this trans-Planckian field value, the Kim-Nilles-Peloso (KNP) 2-flation has been introduced with two axions [26]. It is known recently that the natural inflation is more than 2σ away from the central value of BICEP2, $(r, n_s) = (0.2, 0.96)$. In general, the hilltop inflation gives almost zero r.

Therefore, for the $\mathrm{U}(1)_{\rm de}$ hilltop inflation to give a large r, one must introduce another field which is called *chaoton* because it provides the behavior of $m^2\phi^2$ term at the BICEP2 point [30]. With this hilltop potential, the height is of order $M_{\rm P}^4$ and the decay constant is required to be $> 15\,M_{\rm P}$. Certainly, the potential energy is smaller than order $M_{\rm P}^4$ for $\phi = [0, f_{\rm de}]$. Since this hilltop potential is obtained from the mother discrete symmetry, such as $\mathbf{Z}_{10\,R}$, the flat valley at the trans-Planckian $f_{\rm de}$ is possible, for which the necessary condition is given in terms of quantum numbers of $\mathbf{Z}_{10\,R}$ [30].

With the GUT scale vacuum energy during inflation, the reheating temperature after inflation is most likely above 10^{12} GeV. This has led to the conclusion of Ref. [7] that f_a is around or smaller than 10^{11} GeV. But this study depends on the numerical calculation of [6]. That is the reason for the recent interests on axion string-DW system. A particular interest is the Choi-Kim mechanism [9] where several vacua are identified by a subgroup of the Goldstone boson direction. It is particularly useful in string compactification with the anomalous U(1) surviving as a global symmetry down to the axion window scale, because the model-independent axion corresponding to the anomalous U(1) has DW number one [10].

4 Acknowledgments

JEK is supported in part by the National Research Foundation (NRF) grant funded by the Korean Government (MEST) (No. 2005-0093841) and by the IBS(IBS CA1310).

References

[1] J. E. Kim, "A composite invisible axion," *Phys. Rev. D* **31**, 1733 (1985).

[2] J. E. Kim, "Abelian discrete symmetries Z_N and Z_{nR} from string orbifolds," *Phys. Lett. B* **726**, 450 (2013); "Natural Higgs-Flavor-Democracy Solution of the μ Problem of Supersymmetry and the QCD Axion," *Phys. Rev. Lett.* **111**, 031801 (2013).

[3] J. E. Kim and G. Carosi, "Axions and the Strong CP Problem," *Rev. Mod. Phys.* **82**, 557 (2010).

[4] A. Vilenkin and A. E. Everett, "Cosmic Strings and Domain Walls in Models with Goldstone and Pseudo-Goldstone Bosons," *Phys. Rev. Lett.* **48**, 1867 (1982).

[5] P. Sikivie, "Of Axions, Domain Walls and the Early Universe," *Phys. Rev. Lett.* **48**, 1156 (1982).

[6] T. Hiramatsu *et al.*, "Axion cosmology with long-lived domain walls," *Phys. Rev. D* **85**, 105020 (2012).

[7] D. J. E. Marsh *et al.*, "Tensor Detection Severely Constrains Axion Dark Matter," *Phys. Rev. Lett.* **113**, 011801 (2014); L. Vissineli and P. Gondolo, "Axion cold dark matter in view of BICEP2 results," *Phys. Rev. Lett.* **113**, 011802 (2014).

[8] P. A. R. Ade *et al.* (BICEP2 Collaboration), "BICEP2 I: Detection Of B-mode Polarization at Degree Angular Scales," *Phys. Rev. Lett.* **112**, 241101 (2014).

[9] K. Choi and J. E. Kim, "Domain Walls in Superstring Models," *Phys. Rev. Lett.* **55**, 2637 (1985).

[10] J. E. Kim, "High scale inflation, model-independent string axion, and QCD axion with domain wall number one," *Phys. Lett. B* **734**, 68 (2014).

[11] S. M. Barr and J. E. Kim, "New confining force solution of QCD domain wall problem," arXiv:1407.4311.

[12] J. Hong *et al.*, "Nuclear dipole radiation from $\bar{\theta}$ oscillations," *Phys. Rev. D* **42**, 1847 (1990).

[13] J. Hong and J. E. Kim, "New Method for the Detectability of Oscillating θ," *Phys. Lett. B* **265**, 197 (1991).

[14] J. Hong *et al.*, "Calculations of resonance enhancement factor in axion-search tube-experiments," arXiv:1403.1576.

[15] A. Arvanitaki and A. A. Geraci, "Resonant detection of axion mediated forces with Nuclear Magnetic Resonance," arXiv: 1403.1290.

[16] J. E. Kim, "Calculation of axion-photon-photon coupling in string theory," *Phys. Lett. B* **735**, 95 (2014).

[17] J.-H. Huh *et al.*, "$\mathrm{SU}(5)_{\mathrm{flip}} \times \mathrm{SU}(5)'$ from Z_{12-I}," *Phys. Rev. D* **80**, 115012 (2009).

[18] J. E. Kim *et al.*, "Bosonic Coherent Motions in the Universe", arXiv:1409.2497.

[19] K. J. Bae *et al.*, "Update of axion CDM energy density," *JCAP* **0809**, 005 (2008).

[20] K. Choi and J. E. Kim, "Harmful Axions in String Models," *Phys. Lett. B* **154**, 393 (1985); P. Svrcek and E. Witten, "Axions In String Theory," *JHEP* **0606**, 051 (2006).

[21] J. E. Kim, "Natural Higgs-flavor-democracy solution of the μ problem of supersymmetry and the QCD axion," *Phys. Rev. Lett.* **111**, 031801 (2013).

[22] J. E. Kim and H. P. Nilles, "Dark energy from approximate $\mathrm{U}(1)_{\mathrm{de}}$ symmetry," *Phys. Lett. B* **730**, 53 (2014).

[23] S. M. Carroll, "Quintessence and the Rest of the World," *Phys. Rev. Lett.* **81**, 3067–3070 (1998).

[24] J. E. Kim, "Modeling dark energy scale with quintessential pseudoscalar boson," *J. Korean Phys. Soc.* **64**, 795 (2014).

[25] H. Baer *et al.*, "Non-thermal dark matter: supersymmetric axions and other candidates," arXiv:1407.0017.

[26] J. E. Kim *et al.*, "Completing Natural Inflation," *JCAP* **0501**, 005 (2005).

[27] A. D. Linde, "Chaotic inflation," *Phys. Lett. B* **129**, 177 (1983).

[28] K. Freese *et al.*, "Natural inflation with pseudo Nambu–Goldstone bosons," *Phys. Rev. Lett.* **65**, 3233 (1990).

[29] D. H. Lyth, "What would we learn by detecting a gravitational wave signal in the cosmic microwave background anisotropy?," *Phys. Rev. Lett.* **78**, 1861 (1997).

[30] J. E. Kim, "The inflation point in $\mathrm{U}(1)_{\mathrm{de}}$ hilltop potential assisted by chaoton, BICEP2 data, and trans-Planckian decay constant," *Phys. Lett. B* **737**, 1 (2014).

WISP Dark Matter eXperiment and Prospects for Broadband Dark Matter Searches in the 1 μeV–10 meV Mass Range

Dieter Horns[1], *Axel Lindner*[2], *Andrei Lobanov*[3,1,†], *Andreas Ringwald*[2]

[1]Institut für Experimentalphysik, Universität Hamburg, Germany
[2]Deutsches Elektronen-Synchrotron (DESY), Hamburg, Germany
[3]Max-Planck-Institut für Radioastronomie, Bonn, Germany
[†]corresponding author.

DOI: http://dx.doi.org/10.3204/DESY-PROC-2014-03/lobanov_andrei

Light cold dark matter consisting of weakly interacting slim (or sub-eV) particles (WISPs) has been in the focus of a large number of studies made over the past two decades. The QCD axion and axion-like particles with masses in the 0.1 μeV–100 meV are strong candidates for the dark matter particle, together with hidden photons with masses below $\lesssim$ 100 meV. This motivates several new initiatives in the field, including the WISP Dark Matter eXperiment (WISPDMX) and novel conceptual approaches for broad-band WISP searches using radiometry measurements in large volume chambers. First results and future prospects for these experiments are discussed in this contribution.

1 WISP dark matter searches in the 1 μeV–10 meV mass range

Searches for light cold dark matter (DM) consisting of weakly interacting slim particles (WISPs) [1, 2, 3, 4] are gaining prominence, with a number of experiments conducted and proposed detecting hidden photons (HPs), QCD axions, and axion-like particles (ALPs) with astrophysical [5, 6, 7, 8, 9, 10, 11] and laboratory measurements [12, 13, 14, 15, 16, 17].

Best revealed by their coupling to standard model (SM) photons, WISPs can be non-thermally produced in the early Universe [18] and may give rise to dark matter for a broad range of the particle mass and the photon coupling strength [19, 20]. The photon coupling of axions/ALPs, $g_{a\gamma} \propto 1/f_a$, depends on the energy scale f_a of the symmetry breaking responsible for the given particle, while the hidden photon coupling, $\chi \propto g_h$, is determined by the hidden gauge coupling, g_h [19].

At particle masses above $\sim 10^{-3}$ eV, the existing constraints effectively rule out WISPs as DM particles, while cosmologically viable lower ranges of particle reach down to $\sim 10^{-6}$–10^{-7} eV for axions/ALPs and may extend to much lower masses with for HP and ALP, as well as with "fine tuning" of the axion models. The mass range 10^{-7}–10^{-3} eV corresponds to the radio regime at frequencies of 24 MHz–240 GHz where highly sensitive measurement techniques are developed for radioastronomical measurements, with typical detection levels of $\lesssim 10^{-22}$ W.

2 Narrowband experiments

The most sensitive laboratory HP and axion/ALP DM searches performed so far in the mass range 10^{-7}–10^{-3} eV have utilised the "haloscope" approach [21] which employs resonant microwave cavities lowering substantially the detection threshold in a narrow band around each of the cavity resonances [12, 13, 14, 22, 23, 24]. The WISP DM signal results from conversion of DM halo particles inside the cavity volume, V, into normal photons. This conversion is achieved via spontaneous kinetic mixing of HP with SM photons or via the Primakov process induced by an external magnetic field, $\mathbf{B}$, for axions/ALPs.

The output power of the axion/ALP conversion signal is $P_{\rm out} \propto G\,Q\,V\,|\mathbf{B}|^2$, where Q is the resonant enhancement factor (quality factor) of microwave cavity and G is the fraction of cavity volume (form factor) in which the electric field of the converted photon can be detected [25, 26]. Both G and Q depend on the cavity design and the resonant mode employed in the measurement. The respective $P_{\rm out}$ for the HP signal does not have a dependence on $\mathbf{B}$.

The fractional bandwidth of a haloscope measurement is $\propto Q^{-1}$, with typical values of Q not exceeding $\sim 10^5$. The WISP DM signal itself is restricted to within a fractional bandwidth of $Q_{\rm DM}^{-1} \approx \sigma_{\rm DM}^2/c^2 \approx 10^{-6}$, with $\sigma_{\rm DM}$ describing the velocity dispersion of the dark matter halo. A measurement made at a frequency, ν, and lasting for a time, t, can detect the WISP signal at an SNR $\propto \sqrt{t\,/\,W}\,P_{\rm out}/(k_{\rm b}\,T_{\rm n})$, where W is the signal bandwidth, $T_{\rm n}$ is the noise temperature of the detector, and $k_{\rm b}$ is the Boltzmann constant.

The exceptional sensitivity of microwave cavity experiments comes at the expense of rather low scanning speeds of $\lesssim 1$ GHz/year [12, 27], which makes it difficult to implement this kind of measurements for scanning over large ranges of particle mass. To overcome this difficulty, new experimental concepts are being developed that could relax the necessity of using the resonant enhancement and working in a radiometer mode with an effective $Q = 1$ [16, 17, 28, 29, 30].

2.1 WISP Dark Matter eXperiment

At frequencies below 1 GHz, the ADMX experiment[12, 13, 14] has employed the haloscope approach to probe the HP and axion/ALP dark matter in the 460–860 MHz (1.9–3.6 μeV) range [31], and a high frequency extension, ADMX-HF is planned for he 4–40 GHz frequency range [32, 33]. The WISP Dark Matter eXperiment (WISPDMX, Fig. 1) extends the haloscope searches to particle masses below 1.9 μeV, aiming to cover the range 200–600 MHz (0.8–2.5 μeV).

WISPDMX utilises a 208 MHz resonant cavity of the type used at the proton accelerator ring of the DESY HERA collider [34]. The cavity has a volume of 460 liters and a nominal resonant amplification factor $Q = 55000$ at the ground TM_{010} mode. The signal is amplified by a broad-band 0.2–1 GHz amplifier chain with a total gain of 40 dB. Broad-band digitization and FFT analysis of the signal are performed using a commercial 12-bit spectral analyzer, enabling simultaneous measurements at several resonant modes at frequencies of up to 600 MHz.

The main specific aspects of WISPDMX measurements are: 1) broadband recording in the 200–600 MHz band at a resolution of ≤ 150 Hz, 2) the use of multiple resonant modes tuned by a plunger assembly consisting of two plungers, and 3) the planned use of rotation of the cavity in the magnetic field in order to enable axion measurements at multiple resonant modes as well.

The WISPDMX measurements are split into three different stages: 1) HP DM searches at the nominal frequencies of the resonant modes of the HERA cavity; 2) HP DM searches with cavity tuning (covering up to 70% of the 200–600 MHz band); and 3) axion/ALP DM searches using the DESY H1 solenoid magnet which provides $B = 1.15$ T in a volume of 7.2 m^3.

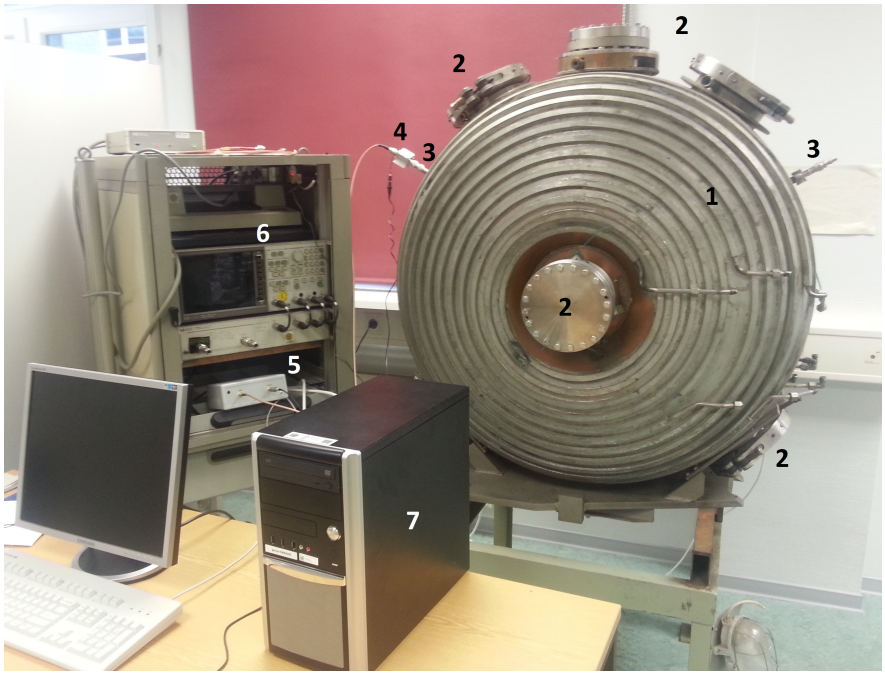

Figure 1: WISPDMX setup for the initial measurements made at nominal resonant frequencies of the microwave cavity. Indicated with numbers are: 1 – a 208-MHz microwave cavity of the type used in the proton ring of the DESY HERA collider; 2 - cavity ports (two on the axis of the cavity and five on the radial wall of the oblate cylinder; 3 – antenna ports for two magnetic-loop antennas inserted in the cavity; 4 – first stage amplifier (WantCom, 0.1-1.0 GHz, 22.5 dB gain, 0.6 dB noise figure); 5 – second stage amplifier (MITEQ, 0.1-0.9 GHz, 18.2 gain, 1.0 dB noise figure); 6 – network analyzer (HP 85047A); 7 – control computer, with a 12-bit digitizer Alazar ATS-9360 operated via a PCIe Gen2 interface.

The first phase of the WISPDMX measurements has been completed [15], and the final results are being prepared for publication. The WISPDMX setup used for these measurements is shown in Fig. 1. Table 2.1 lists preliminary exclusion limits obtained for five different resonant modes of the cavity. These limits reach below $\chi = 3 \times 10^{-12}$ at all of the modes used in the measurement, and already these limits probe the parameter space admitting HP DM. The expected exclusion limits for the HP and axion/ALP DM searches in the next two phases of WISPDMX are shown in Figs. 2-3.

3 Broadband experiments

The relatively low scanning speed (*e.g.*, $\approx 100\,\mathrm{MHz/yr}$ for WISPDMX and $\sim 1\,\mathrm{GHz/yr}$ for ADMX) and limited tunability of resonant experiments make them difficult to be used for covering the entire $1\,\mu\mathrm{eV}$–$10\,\mathrm{meV}$ range of particle mass. The gain in sensitivity provided by the resonant enhancement, Q, needs to be factored against the bandwidth reduction of the

Table 1: WISPDMX measurements at nominal resonant modes in the 200-600 MHz range

Mode	ν [MHz]	Q	$\mathcal{G}$	$P_{\rm det}$ [$\times 10^{-14}$W]	$m_{\gamma_{\rm s}}$ [μeV]	χ [$\times 10^{-13}$]
TM_{010}	207.87961	55405	0.429	1.08	0.85972093	17.0
TE_{111}	321.45113	59770	0.674	1.08	1.3294150	8.4
TE_{111}	322.74845	58900	0.671	1.08	1.3347803	8.5
TM_{020}	454.42411	44340	0.317	1.08	1.8793470	10.1
TE_{112}	510.62681	71597	0.020	1.09	2.1117827	28.2
TE_{112}	515.97110	67840	0.019	1.09	2.1338849	29.5
TE_{120}	577.59175	60350	0.036	1.10	2.3887274	20.4
TE_{120}	579.25126	66520	0.037	1.10	2.3955906	19.1

Column designation: resonant mode of the cavity, with its respective resonant frequency, ν, quality factor, Q, geometrical form factor, $\mathcal{G}$, measured noise power, $P_{\rm det}$, hidden photon mass, $m_{\gamma_{\rm s}}$, and 95% exclusion limit, χ, for hidden photon coupling to normal photons, calculated for the antenna coupling $\kappa = 0.01$ [15].

order of Q^{-1}, which may result in a somewhat counterintuitive conclusion that non-resonant, broadband approaches may be preferred when dealing with a mass range spanning over several decades.

Indeed, for axion/ALP searches, reaching a desired sensitivity to the photon coupling implies a measurement time $t \propto T_{\rm sys}^2 B^{-4} V^{-2} G^{-2} Q^{-2}$. A broadband measurement, with $Q_{\rm b} \equiv 1$, needs to last Q^2 times longer to reach the same sensitivity. However, the broadband measurement probes the entire mass range at once, while it would require a (potentially very large) number of measurements, $N_{\rm mes} = 1 + \log(\alpha) \,/\, \log[Q/(Q-1)]$, in order to cover a range of particle mass from m_1 to $m_2 = \alpha\, m_1$ (with $\alpha > 1$). Then, the broadband approach would be more efficient in case if $t_{\rm b} < t_{\rm n}\, N_{\rm mes}$. This corresponds to the following comparison between these two types of measurement:

$$1 + Q \log\, \alpha > \left(\frac{T_{\rm b}}{T_{\rm n}}\right)^2 \left(\frac{B_{\rm b}}{B_{\rm n}}\right)^{-4} \left(\frac{V_{\rm b}}{V_{\rm n}}\right)^{-2} \left(\frac{G_{\rm b}}{G_{\rm n}}\right)^{-2},$$

where the subscripts b and n refer to the respective parameters of the broadband and narrowband measurements. For typical experimental settings, one can expect that $T_{\rm b} \sim 100\, T_{\rm n}$, $B_{\rm b} \sim B_{\rm n}$, $V_{\rm b} \sim 100 V_{\rm n}$, and $G_{\rm b} \sim 0.01 G_{\rm n}$. In such conditions, a narrowband experiment with $Q > 10^4 / \log\, \alpha$ would be less efficient in scanning over the given range of mass. Applied to the entire 0.1 μeV–10 meV range of mass, this condition implies restricting the effective resonance enhancement of narrowband measurements to less than ~ 2000, which effectively disfavors the narrowband approach for addressing such a large range of particle mass.

The measurement bandwidth of radiometry experiments is limited only by the detector technology, with modern detectors employed in radio astronomy routinely providing bandwidths in excess of 1 GHz and spectral resolutions of better than 10^6.

One possibility for a radiometer experiment is to employ a spherical dish reflector that provides a signal enhancement proportional to the area of the reflector [16, 28, 29, 30]. This option is well-suited for making measurements at higher frequencies (shorter wavelengths, λ), as the effective signal enhancement is $\propto A_{\rm dish}/\lambda^2$, where $A_{\rm dish}$ is the reflecting area [16]. It is therefore expected that this concept would be best applicable at $\lambda \lesssim 1$ cm ($\nu \gtrsim 30$ GHz).

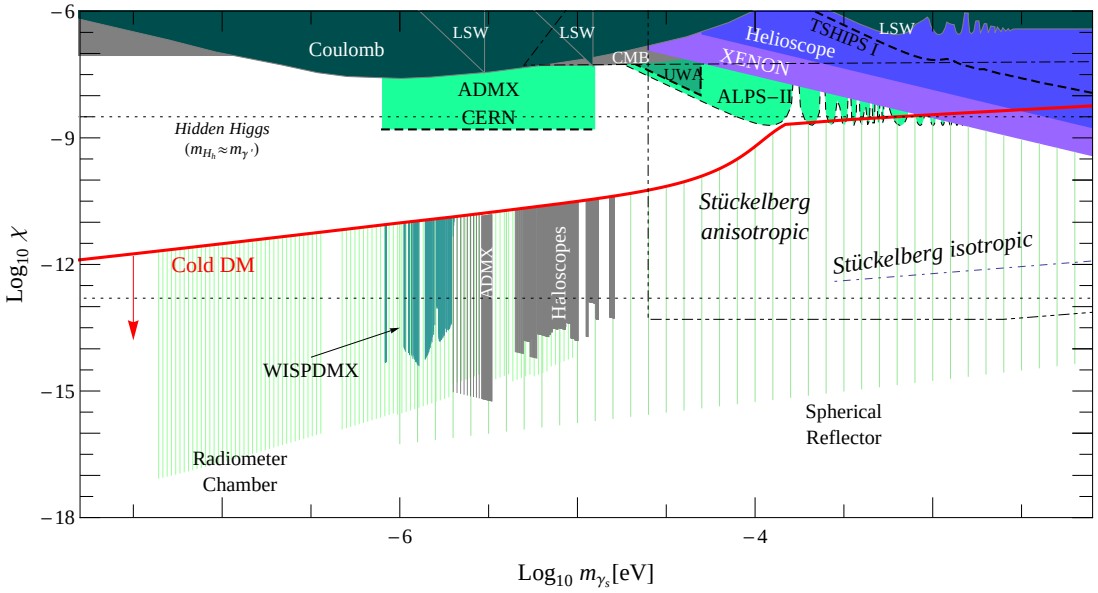

Figure 2: Exclusion limits for hidden photon coupling to normal photons from existing (white captions) and planned (black captions) experiments (adapted from [4]). Theoretical expectations for the hidden photon DM are indicated in red. The expected sensitivity limits of the second phase of the WISPDMX experiment are marked with turquoise color, reaching well into the DM favored range of photon coupling. The WISPDMX sensitivity is calculated for a setup with two tuning plungers operating simultaneously. The hatched areas illustrate the expected sensitivity of broadband experiments using the spherical reflector and the radiometry chamber approaches.

At lower frequencies, another attractive possibility for engaging into the broadband measurements is to use the combination of large chamber volume and strong magnetic field provided by superconducting TOKAMAKs or stellarators such as the Wendelstein 7-X stellarator [35] in Greifswald (providing $B = 3\,T$ in a $30\,\mathrm{m}^3$ volume).

3.1 Radiometry chamber experiments

More generally, the stellarator approach signifies a conceptual shift to employing a large, magnetized volume of space which can be probed in a radiometry mode (*radiometer chamber*), without resorting to a resonant enhancement of the signal. The exclusion limits expected to be achievable with the spherical reflector experiments and with the measurements made in a radiometer chamber with the volume and magnetic field similar to those of the Wendelstein stellarator are shown in Fig. 2-3.

Deriving from the stellarator approach, a large chamber can be designed specifically for the radiometer searches, with the inner walls of the chamber covered by multiple fractal antenna elements providing a broad-band receiving response in the 0.1-25 GHz frequency range with a high efficiency and a nearly homogeneous azimuthal receiving pattern [36, 37]. Combination

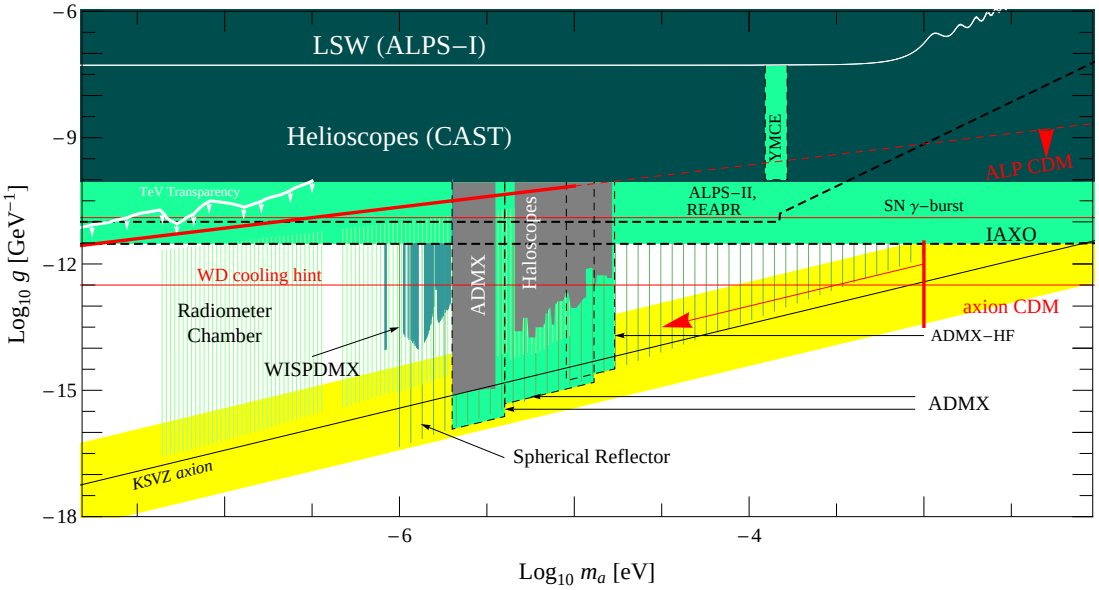

Figure 3: Exclusion limits for axion/ALP photon coupling to normal photons from existing (white captions) and planned (black captions) experiments (adapted from [4]). The yellow band corresponds to the parameter space allowed for the QCD axion. Theoretical expectations for the axion/ALP DM are indicated in red. The expected sensitivity limits of the second phase of the WISPDMX experiment are marked with turquoise color, reaching well into the DM favored range of ALP coupling. The WISPDMX sensitivity is calculated for a setup with two tuning plungers operating simultaneously. The hatched areas illustrate the expected sensitivity of broadband experiments using the spherical reflector and the radiometry chamber approaches.

of multiple receiving elements provides also the possibility for achieve directional sensitivity to the incoming photons.

The directional sensitivity can be realized through high time resolution enabling phase difference measurements between individual fractal antenna elements. Making such measurements is well within the reach of the present day data recording implemented for radio interferometric experiments with the recording rate as high as 16 Gigabit/sec [38]. This recording rate provides a time resolution down to 0.12 nanoseconds, thus enabling phase measurements over effective travel path difference $\delta_\mathrm{l} \approx 4$ millimetres. This corresponds to an angular resolution ϕ_p in the range of $R/(L/\delta_\mathrm{l}+1)[(R^2+L^2)^{1/2}-\delta_\mathrm{l}]^{-1} \lesssim \phi_\mathrm{p} \lesssim (2R/\delta_\mathrm{l}+1)^{1/2}/(R/\delta_\mathrm{l}+1)$, where R and L denote the smallest and largest dimensions of the chamber, respectively. For a chamber fitted into the HERA H1 magnet (assuming $R \approx 1\,\mathrm{m}$ and $L \approx 3\,\mathrm{m}$), this corresponds to angular resolutions of $0.05^\circ \lesssim \phi_\mathrm{p} \lesssim 5^\circ$. The radiometry chamber measurements could therefore provide an attractive experimental concept for performing WISP DM searches in the range of particle mass between 0.1 and $2\,\mu$eV, thus closing the low end of the parameter space still open for the axion dark matter.

Acknowledgments

AL acknowledges support from the Collaborative Research Center (Sonderforschungsbereich) SFB 676 "Particles, Strings, and the Early Universe" funded by the German Research Society (Deutsche Forschungsgemeinschaft, DFG). WISPDMX is performed in a collaboration between the University of Hamburg, DESY, and Max-Planck-Institut für Radioastronomie in Bonn. WISPDMX has been supported through an SFB 676 lump sum grant and a PIER 'Ideen Fonds' grant.

References

[1] R. Essig, J. A. Jaros, W. Wester *et al.*, "Dark Sectors and New, Light, Weakly-Coupled Particles", [arXiv:1311.0029 [hep-ph]].

[2] J. Jaeckel and A. Ringwald, Ann. Rev. Nucl. Part. Sci. **60** (2010) 405 [arXiv:1002.0329 [hep-ph]].

[3] A. Ringwald, Phys. Dark Univ. **1**, 116 (2012) [arXiv:1210.5081 [hep-ph]].

[4] J. L. Hewett, H. Weerts, R. Brock *et al.*, arXiv:1205.2671 [hep-ex].

[5] A. Mirizzi, J. Redondo and G. Sigl, JCAP **0903**, 026 (2009) [arXiv:0901.0014 [hep-ph]].

[6] A. Mirizzi, J. Redondo and G. Sigl, JCAP **0908**, 001 (2009) [arXiv:0905.4865 [hep-ph]].

[7] D. Chelouche, R. Rabadán, S.S. Pavlov, F. Castejón, ApJSS **180**, 1 (2009) [arXiv:0806.0411 [astro-ph]].

[8] M.S. Pshirkov, S.B. Popov, JETP **108**, 384 (2009) [arXiv:0711.1264 [astro-ph]].

[9] D. Horns, L. Maccione, A. Mirizzi, M. Roncadelli, Phys. Rev. D **85** 085021 (2012).

[10] D. Horns, M. Meyer, JCAP **2** 33 (2012).

[11] A. P. Lobanov, H.-S. Zechlin, D. Horns, Phys. Rev. D **87**, 065004 (2013) [arXiv:1211.6268 [astro-ph.co]]

[12] R. Bradley, J. Clarke, D. Kinion *et al.*, Rev. Mod. Phys. **75**, 777 (2003).

[13] [ADMX Collaboration], S. J. Asztalos *et al.*, Phys. Rev. Lett. **104**, 041301 (2010) [arXiv:0910.5914 [hep-ex]].

[14] A. Wagner, G. Rybka, M. Hotz *et al.*, Phys. Rev. Lett. **105**, 171801 (2010) [arXiv:1007.3766 [hep-ex]].

[15] S. Baum, *WISPDMX - Eine direkte Suche nach Dunkler Materie mit einer 208 MHz HERA-Kavität*, Universität Hamburg, 2013 (www.iexp.uni-hamburg.de/groups/astroparticle/de/forschung/BA_2013-12-04_final.pdf)

[16] D. Horns, J. Jaeckel, A. Lindner, *et al.*, JCAP **4**, 016 (2013) [arXiv:1212.2970 [hep-ph]].

[17] D. Horns, A. Lindner, A. P. Lobanov, A. Ringwald, Proc. of IX Patras Workshop *(in press)* (2014), [arXiv:1309.4170 [hep-ph]].

[18] Pierre Sikivie, Lect. Notes Phys. **741** 19 (2008), [astro-ph/0610440].

[19] P. Arias, D. Cadamuro, M. Goodsell, *et al.*, JCAP **1206**, 013 (2012) [arXiv:1201.5902 [hep-ph]].

[20] J. Redondo, B. Döbrich, arXiv:1311.5341 [hep-ex].

[21] P. Sikivie, Phys. Rev. Lett. **51** 1415 (1983).

[22] S. De Panfilis *et al.*, Phys. Rev. Lett. **59**, 839 (1987).

[23] W. Wuensch *et al.*, Phys. Rev. **D40**, 3153 (1989).

[24] C. Hagmann, P. Sikivie, N. S. Sullivan, and D. B. Tanner, Phys. Rev. **D42**, 1297 (1990).

[25] S. J. Asztalos *et al.*, Phys. Rev. **D64**, 092003 (2001).

[26] O. K. Baker, M. Betz, F. Caspers, *et al.*, [arXiv:1110.2180 [physics.ins-det]].

[27] C. Hagmann, P. Sikivie, N. Sullivan, D. B. Tanner and S. I. Cho, Rev. Sci. Instrum. **61** 1076 (1990)

[28] J. Jaeckel, J. Redondo, Phys. Rev. D **88** 115002 (2013) [arXiv:1308.1103 [hep-ph]].

[29] J. Jaeckel, J. Redondo, JCAP **11** 16 (2013) [arXiv:1307.7181 [hep-ph]].

[30] B. Döbrich, Proc. of X Patras Workshop *(this volume)* (2015).

[31] S. J. Asztalos, *et al.*, Phys. Rev. Lett. **104** 041301 (2010) [arXiv:0910.5914] [hep-ph]].

[32] K. van Bibber, G. Carosi, [arXiv:1304.7803 [physics.ins-det]] (2013).

[33] L. J. Rosenberg, Proc. of X Patras Workshop *(this volume)* (2015).

[34] A. Gamp, *Particle Accelerators* **29** 65 (1990)

[35] M. Hirsch, J. Baldzuhn, C. Beidler, *et al.*, Plasma Phys. Control. Fusion **50** 053001 (2008).

[36] A. Azari, R. Rowhani, Progr. in Electromag. Res. C **2** 7 (2008).

[37] S. N. Khan, J. Hu, J. Xiong, S. He, Progr. in Electromag. Res. Lett. **1** 19 (2008).

[38] A. R. Whitney, C. J. Beaudoin, R. J. Cappallo, *et al.*, arXiv:1210.5961 (2012).

Differences between Axions and Generic Light Scalars in Laboratory Experiments

Sonny Mantry[1]*, *Mario Pitschmann*[2] *and Michael J. Ramsey-Musolf*[3,4]

[1]Department of Physics, University of North Georgia, Dahlonega, GA, USA
[2]Institute of Atomic and Subatomic Physics, Vienna University of Technology, Vienna
[3]Amherst Center for Fundamental Interactions, Department of Physics, University of Massachussetts Amherst, Amherst, MA, USA
[4]California Institute of Technology, Pasadena, CA, USA

DOI: http://dx.doi.org/10.3204/DESY-PROC-2014-03/mantry_sonny

It is well-known that electric dipole moment (EDM) constraints provide the most stringent bounds on axion-mediated macroscopic spin-dependent (SD) and time reversal and parity violating (TVPV) forces. These bounds are several orders of magnitude stronger than those arising from direct searches in fifth-force experiments and combining astrophysical bounds on stellar energy loss with Eötvös tests of the weak equivalence principle (WEP). This is a consequence of the specific properties of the axion, invoked to solve the Strong CP problem. However, the situation is quite different for generic light scalars that are unrelated to the strong CP problem. In this case, bounds from fifth-force experiments and astrophysical processes are far more stringent than the EDM bounds, for the mass range explored in direct searches.

In this work [1], we consider the nature of constraints on macroscopic spin-dependent (SD) and T- and P-violating (TVPV) forces mediated by light scalar particles. In particular, we focus on differences between forces mediated by axions that solve the Strong CP problem and generic scalars that are unrelated to the Strong CP problem. Here macroscopic forces are understood to have an interaction range $r \gg 1$ Å. For example, such a force can arise at the microscopic level through a coupling of a light scalar φ with the light quarks $q = u, d$

$$\mathcal{L}_{\varphi qq} \quad = \quad \varphi\, \bar{q}\big(g_s^q + i g_p^q \gamma^5\big) q \quad , \tag{1}$$

which in turn can induce nucleon level couplings

$$\mathcal{L}_{\varphi NN} \quad = \quad \varphi\, \bar{N}\big(g_s + i g_p \gamma^5\big) N \quad , \tag{2}$$

where the nucleon-level couplings $g_{s,p}$ are related to the quark level couplings $g_{s,p}^q$ via nuclear matrix elements as determined by a matching calculation. For simplicity, we have assumed isoscalar couplings so that $g_{s,p}^u = g_{s,p}^d$ and ignored possible couplings to leptons. Such interactions give rise to a nucleon-nucleon monopole-dipole potential in the non-relativistic limit that has the form [2]

$$V(r) \quad = \quad g_s g_p \, \frac{\vec{\sigma}_2 \cdot \hat{r}}{8\pi M_2} \Big(\frac{m_\varphi}{r} + \frac{1}{r^2} \Big) e^{-m_\varphi r} \quad , \tag{3}$$

*Speaker at the 10^{th} PATRAS Workshop on Axions, WIMPs, and WISPs, 2014, CERN, Geneva, Switzerland.

where $\vec{\sigma}_2$ acts on the spin of the polarized nucleon and $\hat{r} = \vec{r}/r$ is the unit vector from the unpolarized nucleon to the polarized nucleon. Direct searches in fifth-force experiments and astrophysical bounds on stellar energy loss, yield (or plan to yield) upper limits [3, 4, 5, 6, 7, 8, 9, 10, 11, 12, 13, 14, 15] on the product of couplings $g_s g_p$. A summary of various experiments can be found in Ref. [16].

Since the nucleon-nucleon potential in Eq. (3) is TVPV, it will induce non-zero electric dipole moments (EDMs) in nucleons and nuclei. The EDM for an elementary fermion arises from a term in the Lagrangian of the form $\mathcal{L} = -i\,\frac{d}{2}\,\bar{\psi}\sigma^{\mu\nu}\gamma^5\psi\,F_{\mu\nu}$, which gives rise to the non-relativistic Hamiltonian of the form $H = -d\,\vec{E}\cdot\frac{\vec{S}}{S}$, where $\vec{S}$ is the spin of the particle and $\vec{E}$ is the electric field. For a non-zero value of d, TVPV or CP violation arises as a consequence of the CPT theorem and the time-reversal behavior of the interaction $T(\vec{E}\cdot\vec{S}) = -\vec{E}\cdot\vec{S}$. Current bounds from EDM experiments yield a bounds on the EDMs of the neutron $|d_n| < 2.9\times10^{-13}$ e-fm [17] and the diamagnetic mercury atom $|d_{Hg}| < 2.6\times10^{-16}$ e-fm [18]. SInce the TVPV nucleon-nucleon potential in Eq. (3) can induce non-zero EDMs, these EDM bounds translate into bounds on $g_s g_p$. Some examples of diagrams involving φ-exchange that contribute to nuclear EDMs and are proportional to $g_s g_p$ are shown in Fig. 1.

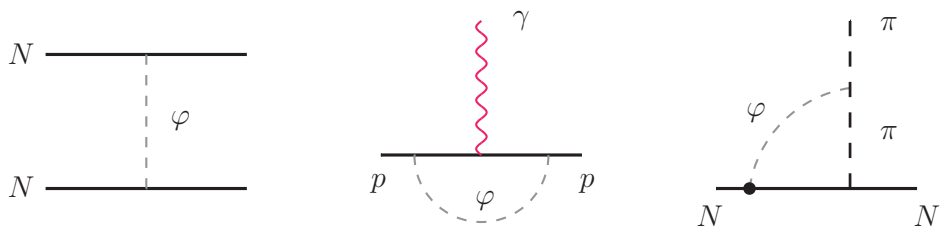

Figure 1: Example diagrams of φ-exchange that can contribute to nuclear EDMs.

We are then led to ask the question of how bounds on $g_s g_p$ arising from fifth-force experiments compare with those arising from EDM constraints. It is well-known that when φ is the axion(a) [19, 20, 21, 22] that solves the strong CP problem, EDM constraints on $g_s g_p$ are several orders of magnitude more stringent [23] than those derived from fifth-force experiments. As we explain below, this is result of the unique properties of the axion that arise from the need to solve the Strong CP problem. However, we show that for the case when φ is a generic scalar, unrelated to the Strong CP problem, the situation is quite different and the bounds from fifth-force experiments on $g_s g_p$ can be several orders of magnitude more stringent than those arising from EDM experiments.

1 Axion Scenario

We can understand the differences in the bounds on $g_s g_p$ between axions and generic scalars due to the unique properties of the axion couplings and their connection to the Strong CP problem. For the purposes of illustration, we consider QCD with one quark flavor. The terms relevant to the Strong CP problem are given by

$$\mathcal{L} \;=\; \bar{\theta}\,\frac{\alpha_s}{16\pi}\,G^a_{\mu\nu}\tilde{G}^{a\mu\nu} - m_q\,\bar{q}q \quad . \tag{4}$$

The $\bar{\theta}$-term is the source of flavor-diagonal CP violation in QCD. One can perform an axial $U(1)_A$ transformation so that the Lagrangian in Eq. (4) becomes

$$\mathcal{L} \;=\; -m_q \cos\bar{\theta}\;\bar{q}q + m_q \sin\bar{\theta}\;\bar{q}i\gamma^5 q \quad , \tag{5}$$

with strong CP violation now moved entirely into the quark mass terms. So far there has been no observable strong CP violation and current EDM bounds require $|\bar{\theta}| < 10^{-10}$. This is the well-known Strong CP problem. The axion provides a solution [19, 20, 21, 22] to the Strong CP problem by extending the Standard Model (SM) with new fields that are charged under a new anomalous $U(1)_{PQ}$ Peccei-Quinn symmetry, under which the SM fields are neutral. This symmetry can be used to completely rotate away the $\bar{\theta}$-term, thereby solving the Strong CP problem. However, in order to avoid additional light QCD degrees of freedom, the Peccei-Quinn symmetry must be broken at a high energy scale $10^9 \lesssim f_a \lesssim 10^{12}$ GeV. The axion field $\mathrm{a}(x)$ is the pseudo-Goldstone boson that arises from the spontaneously broken $U(1)_{PQ}$ symmetry. A $U(1)_{PQ}$ transformation results in the shifts $\bar{\theta} \to \bar{\theta} + 2\alpha\,, \frac{\mathrm{a}(x)}{f_a} \to \frac{\mathrm{a}(x)}{f_a} - 2\alpha$, so that the combination $\bar{\theta} + \frac{\mathrm{a}(x)}{f_a}$ is left invariant. Thus, in the low energy effective theory where all heavy degrees of freedom have been integrated and only the axion and the SM fields remain, all interactions involving the axion must be built out of this invariant combination. Thus, the low energy effective theory axion interactions can be obtained by making the replacement $\bar{\theta} \to \bar{\theta} + \frac{\mathrm{a}(x)}{f_a}$ in the QCD Lagrangian. Making this replacement in Eq. (5) we get the effective Lagrangian

$$\mathcal{L}_a \;=\; -\cos\left(\bar{\theta} + \frac{\mathrm{a}}{f_a}\right) m_q\,\bar{q}q + m_q \sin\left(\bar{\theta} + \frac{\mathrm{a}}{f_a}\right)\bar{q}i\gamma^5 q \quad , \tag{6}$$

which makes manifest the couplings of the axion to the SM quark. The axion can acquire a non-zero expectation value due to strong interaction quark condensates so that we can write the axion field as $\mathrm{a}(x) = \langle \mathrm{a}\rangle + a(x)$, where $a(x)$ denotes the axion field corresponding to excitations above the vev $\langle \mathrm{a}\rangle$. This gives rise to a new induced $\bar{\theta}$-parameter $\theta_{\rm eff} = \bar{\theta} + \frac{\langle \mathrm{a}\rangle}{f_a}$, so that the Lagrangian in Eq. (6) now takes the form

$$\mathcal{L}_a \;=\; -\cos\left(\theta_{\rm eff} + \frac{a}{f_a}\right) m_q\,\bar{q}q + m_q \sin\left(\theta_{\rm eff} + \frac{a}{f_a}\right)\bar{q}i\gamma^5 q \quad . \tag{7}$$

Non-perturbative QCD effects generate an axion potential via a non-zero quark condensate, given by $V\left(\theta_{\rm eff} + \frac{a}{f_a}\right) = -\chi(0)\cos\left(\theta_{\rm eff} + \frac{a}{f_a}\right)$, where $\chi(0) = -m_q\,\langle\bar{q}q\rangle$. Expanding the potential $V(\theta_{\rm eff})$ around its minimum gives $V(\theta_{\rm eff}) \simeq \frac{1}{2}\chi(0)\theta_{\rm eff}^2$. i.e. the minimum of the potential corresponds to $\theta_{\rm eff} = 0$, so that the dynamical relaxation of the ground state axion potential solves the strong CP problem.

The presence of higher dimensional CP-odd operators, like the quark chromo-electric dipole moment, can generate terms that are linear in $\theta_{\rm eff}$ so that the minimum of the potential is shifted to a small but non-zero value of $\theta_{\rm eff}$. This can occur via correlators of the type [24] $\chi_{\rm CP}(0) = -i\lim_{k\to 0}\int d^4x\; e^{ik\cdot x}\langle 0|T(G\tilde{G}(x), \mathcal{O}_{\rm CP}(0))|0\rangle$ so that the expanded potential now takes the form $V(\theta_{\rm eff}) \simeq \chi_{\rm CP}(0)\;\theta_{\rm eff} + \frac{\chi(0)}{2}\;\theta_{\rm eff}^2$. The potential is now minimized at a non-zero value $\theta_{\rm eff} = -\chi_{\rm CP}(0)/\chi(0)$. Thus, the axion scenario can generate non-zero EDMs while still providing a dynamical mechanism to explain the small size of strong CP effects in QCD. Expanding the axion Lagrangian in Eq. (7) in $\theta_{\rm eff}$ and $a(x)$, we arrive at

$$\mathcal{L}_a \;=\; \left(\frac{\theta_{\rm eff}}{f_a}a - 1\right) m_q\,\bar{q}q + \left(\theta_{\rm eff} + \frac{a}{f_a}\right) m_q\,\bar{q}i\gamma^5 q + \frac{m_q}{2f_a^2}\,a^2\,\bar{q}q + \cdots \quad . \tag{8}$$

The mass and the couplings of the axion to the quarks are now manifest

$$g^q_{a,s} = \frac{\theta_{\rm eff} m_q}{f_a}\,, \qquad g^q_{a,p} = \frac{m_q}{f_a}\,, \qquad m_a \simeq \frac{1}{f_a}|\chi(0)|^{1/2} \quad , \tag{9}$$

where $g^q_{a,s}$ and $g^q_{a,p}$ denote the scalar and pseudoscalar couplings respectively. Note that since the Peccei-Quinn symmetry breaking scale $f_a \gg |\chi(0)|^{1/2}$, the axion is very light and can mediate a macroscopic force. Note that based on the quark-level couplings in Eq. (9), the product of the nucleon-level couplings will be of the form

$$g^q_s g^q_p \propto \theta_{\rm eff}\, \frac{m_q^2}{f_a^2} \quad , \tag{10}$$

where the constant of proportionality will be determined by nucleon matrix elements. We can see that the size of the SD fifth-force is heavily suppressed by $m_q^2/f_a^2 \ll 1$.

However, note that the dominant contribution to the nucleon and nuclear EDMs arise from nuclear matrix elements of the CP-odd mass term $\theta_{\rm eff} m_q\, \bar{q} i\gamma^5 q$ in Eq. (8). This term does not suffer from the suppression factor $m_q^2/f_a^2 \ll 1$ that occurs in the context of fifth-force experiments via Eq. (10). In other words, the dominant effect that generates an EDM is independent of the product of couplings $g_s g_p$. Thus, the properties of the axion allow for a relatively large effect in EDMs and a heavily suppressed effect for fifth-force experiments.

Current EDM bounds require $\theta_{\rm eff} \lesssim 10^{-10}$. Using this value along with $m_q \sim 1$ MeV and a Peccei-Quinn scale $f_a \sim 10^9 - 10^{12}$ GeV, corresponding to the axion window, gives a bound on $g_s g_p$ for the axion as

$$g_s g_p \propto \theta_{\rm eff}\, \frac{m_q^2}{f_a^2} < 10^{-40} - 10^{-34} \quad . \tag{11}$$

For a more detailed discussion we refer the reader to Ref. [1]

2 Generic Scalar Scenario

The situation is quite different for a generic light scalar, unrelated to the strong CP problem. For a generic scalar, a non-zero nucleon or nuclear EDM is generated via the exchange of φ through diagrams. Thus, unlike the case of axions, the value of a non-zero nuclear EDM is proportional to $g_s g_p$ and arises through diagrams of the type shown in Fig. 1. However, for a generic scalar the product of couplings $g_s g_p$ is unrelated to the Strong CP parameter $\theta_{\rm eff}$ and are *a priori* unrestricted free parameters.

The computation of nuclear EDMs is a highly non-trivial many-body problem involving hadronic and nuclear effects (see Refs. [25, 24, 26] for recent reviews). We do not attempt to carry out rigorous computations and instead only aim to provide order of magnitude estimates. In particular, we estimate the contribution to the mercury (^{199}Hg) EDM from a generic scalar φ. The dominant contribution will arise from the first diagram in Fig. 1 that involves a tree-level exchange of φ, proportional to $g_s g_p$. However, we do not have the machinery to perform a many-body computation of this effect involving the spin-dependent potential in Eq. (3). In order to provide an order of magnitude estimate, we use the result that the nuclear EDM d_{Hg} is given in terms of the nuclear Schiff moment S_{Hg} as [27, 18]

$$d_{Hg} \simeq -2.8 \times 10^{-4}\, \frac{S_{Hg}}{\rm fm^2}. \tag{12}$$

Properties	Axion (a)	Generic Scalar (φ)
EDM Source	TVPV quark mass $\sim \bar{\theta}\, m_q\, \bar{q}\, i\gamma_5\, q$	φ -exchange
g_s	$\sim \bar{\theta}\, \frac{m_q}{f_a} \propto \bar{\theta}\, m_a$	arbitrary
g_p	$\sim\ \frac{m_q}{f_a} \propto\ m_a$	arbitrary
$g_s g_p$	$\sim \bar{\theta}\, \frac{m_q^2}{f_a^2} \propto \bar{\theta}\, m_a^2$	arbitrary

Table 1: Summary of differences between an axion (a) and a generic light scalar (φ) in terms of their couplings to quarks and contributions to non-zero EDMs.

The Schiff moment is a function of TVPV pion-nucleon couplings $S_{Hg} = g_{\pi NN}\left(a_0\, \bar{g}^{(0)}_{\pi NN} + a_1\, \bar{g}^{(1)}_{\pi NN} + a_2\, \bar{g}^{(2)}_{\pi NN}\right) e\ \text{fm}^3$ in the Lagrangian

$$\mathcal{L}_{\pi NN} \;=\; \bar{g}^{(0)}_{\pi NN}\, \bar{N}\tau^a N\pi^a + \bar{g}^{(1)}_{\pi NN}\, \bar{N}N\pi^0 + \bar{g}^{(2)}_{\pi NN}\left(\bar{N}\tau^a N\pi^a - 3\bar{N}\tau^3 N\pi^0\right) \quad , \tag{13}$$

where $g_{\pi NN} \simeq 13.5$ and $\bar{g}^{(0)}_{\pi NN}, \bar{g}^{(1)}_{\pi NN}, \bar{g}^{(2)}_{\pi NN}$ denote the isoscalar, isovector, and isotensor TVPV pion-nucleon couplings, respectively. We compute the third diagram in Fig. 1 and interpret the result as a contribution to the TVPV pion-nucleon couplings. In particular, we find that only the isoscalar component receives a non-zero result

$$\delta\bar{g}^{(0)}_{\pi NN} \simeq \frac{1}{16\pi}\frac{m_\pi^2 + m_\pi m_\varphi + m_\varphi^2}{m_\pi + m_\varphi}\frac{g_A m_\pi^2}{90\,\text{MeV}\,\text{m}_\text{N}\text{f}_\pi} g_s g_p \quad , \tag{14}$$

and is proportional to $g_s g_p$. We refer the reader to Ref. [1] for further details on the computation. The resulting shift in the nuclear Schiff moment and the current experimental constraint $|d_{Hg}| < 2.6 \times 10^{-16}$ e-fm [18], translates into a bound on $|g_s g_p| \lesssim 10^{-9}$. As noted earlier however, the dominant shift to the nuclear EDM will arise from the first diagram in Fig. 1, corresponding to a tree-level φ-exchange between nucleons and we expect it to be about two orders of magnitude larger than the loop-suppressed diagram that generates the shift $\delta\bar{g}^{(0)}_{\pi NN}$. Thus, we expect an upper bound on $g_s g_p$ in the range

$$|g_s g_p| \lesssim \left[10^{-11}, 10^{-9}\right] \quad . \tag{15}$$

Thus, we see that the EDM bound on $g_s g_p$ is much weaker for a generic scalar, compared to the case of an axion as seen in Eq.(11).

3 Conclusion

It is well-known that for axion-mediated macroscopic spin-dependent forces, the strongest bounds arise from electric dipole moment constraints. However, we have shown that for generic

scalars, unrelated to the Strong CP problem, fifth-force experiments and astrophysical constraints provide bounds that are several orders of magnitude more stringent than those arising from electric dipole moment constraints. A summary of the main relevant differences between axions and generic scalars is given in Table 1. Thus, these different experiments and observations can be complementary to each other in unraveling the true nature new macroscopic spin-dependent forces.

4 Acknowledgments

We acknowledge fruitful discussions with H. Abele, P. Chu, H. Gao, and T. G. Walker. This work was supported in part by: U. S. Department of Energy contracts DE-AC02-06CH11357 (MP), DE-FG02-08ER41531 (MP and MJRM), and DE-SC0011095 (MJRM), the Wisconsin Alumni Research Foundation (MP and MJRM), University of North Georgia (SM), and the theoretical program on the contract I689-N16 by the Austrian Fonds zur Förderung der Wissenschaftlichen Forschung (MP).

References

[1] S. Mantry, M. Pitschmann and M. J. Ramsey-Musolf, Phys. Rev. D **90** (2014) 054016 [arXiv:1401.7339 [hep-ph]].
[2] J. E. Moody and F. Wilczek, Phys. Rev. D **30** (1984) 130.
[3] E. G. Adelberger *et al.*, Phys. Rev. Lett. **98** (2007) 131104 [hep-ph/0611223].
[4] A. A. Geraci, S. J. Smullin, D. M. Weld, J. Chiaverini and A. Kapitulnik, Phys. Rev. D **78** (2008) 022002 [arXiv:0802.2350 [hep-ex]].
[5] M. Bordag, U. Mohideen and V. M. Mostepanenko, Phys. Rept. **353** (2001) 1 [quant-ph/0106045].
[6] R. S. Decca *el al.*, Phys. Rev. Lett. **94** (2005) 240401 [hep-ph/0502025].
[7] V. V. Nesvizhevsky, G. Pignol and K. V. Protasov, Phys. Rev. D **77** (2008) 034020.
[8] H. Abele, S. Baessler and A. Westphal, Lect. Notes Phys. **631** (2003) 355 [hep-ph/0301145].
[9] S. K. Lamoreaux, Phys. Rev. Lett. **78** (1997) 5 [Erratum-ibid. **81** (1998) 5475].
[10] G. L. Klimchitskaya and V. M. Mostepanenko, Phys. Rev. A **63** (2001) 062108.
[11] R. Horvat, D. Kekez, M. Krcmar, Z. Krecak and A. Ljubicic, Phys. Lett. B **699** (2011) 21.
[12] M. Bulatowicz *et al.*, Phys. Rev. Lett. **111** (2013) 102001 [arXiv:1301.5224 [physics.atom-ph]].
[13] K. Tullney *et al.*, Phys. Rev. Lett. **111** (2013) 100801 [arXiv:1303.6612 [hep-ex]].
[14] P. H. Chu *et al.*, Phys. Rev. D **87** (2013) 011105 [arXiv:1211.2644 [nucl-ex]].
[15] A. Arvanitaki and A. A. Geraci, arXiv:1403.1290 [hep-ph].
[16] I. Antoniadis *et al.*, Comptes Rendus Physique **12** (2011) 755.
[17] C. A. Baker *et al.*, Phys. Rev. Lett. **97** (2006) 131801 [hep-ex/0602020].
[18] W. C. Griffith*et al.*, Phys. Rev. Lett. **102** (2009) 101601.
[19] R. D. Peccei and H. R. Quinn, Phys. Rev. Lett. **38** (1977) 1440.
[20] R. D. Peccei and H. R. Quinn, Phys. Rev. D **16** (1977) 1791.
[21] S. Weinberg, Phys. Rev. Lett. **40** (1978) 223.
[22] F. Wilczek, Phys. Rev. Lett. **40** (1978) 279.
[23] L. J. Rosenberg and K. A. van Bibber, Phys. Rept. **325** (2000) 1.
[24] M. Pospelov and A. Ritz, Annals Phys. **318** (2005) 119 [hep-ph/0504231].
[25] J. Engel, M. J. Ramsey-Musolf and U. van Kolck, Prog. Part. Nucl. Phys. **71** (2013) 21.
[26] J. S. M. Ginges and V. V. Flambaum, Phys. Rept. **397** (2004) 63 [physics/0309054].
[27] J. H. de Jesus and J. Engel, Phys. Rev. C **72** (2005) 045503 [nucl-th/0507031].

Modelling γ-ray-axion-like particle oscillations in turbulent magnetic fields: relevance for observations with Cherenkov telescopes

Manuel Meyer

The Oskar Klein Center for CosmoParticle Physics, Department of Physics, Stockholm University, Albanova, SE-10691 Stockholm, Sweden

DOI: http://dx.doi.org/10.3204/DESY-PROC-2014-03/meyer_manuel

Axion-like particles (ALPs) are a common prediction of certain theories beyond the Standard Model and couple to photons in the presence of external magnetic fields. As a consequence, photon-ALP conversion could lead to an enhancement of the flux of extragalactic γ-ray sources that is otherwise attenuated due to the interactions with background radiation fields. The magnetic fields traversed by the γ rays are often turbulent and frequently modelled with a simple domain-like structure. Given a maximum mixing between photons and ALPs, we show that in such models realisations of the fields exist for which the photon-ALP oscillation probability vanishes. This behaviour does not occur in more sophisticated magnetic-field models.

1 Introduction

Very high energy γ rays (VHE; energy $E \gtrsim 100\,\mathrm{GeV}$) originating from extragalactic objects interact with photons of the extragalactic background light (EBL) leading to an exponential attenuation of the γ-ray flux emitted by the source [8]. Direct detections of the EBL are difficult due to foreground emission [11] and thus the exact level of the EBL photon density remains unknown. Recent EBL models (e.g. Refs. [15, 6, 10]) predict densities close to lower limits deduced from galaxy number counts [16, 9]. In simple emission models of blazars[1], no spectral hardening is expected at VHE and consequently spectra corrected for EBL absorption should not show such features. Nevertheless, evidence for such signatures has been found [4, 3, 7, 13, 24]. An explanation might be the oscillations of γ-rays into axion-like particles (ALPs), spin-0 pseudo-Nambu-Goldstone bosons that arise in certain Standard Model extensions. These particles couple to photons in external magnetic fields (see Ref. [14] for a review) and could lead to a flux enhancement as ALPs do not interact with EBL photons.

Several turbulent magnetic-field environments have been studied in this respect including the intergalactic magnetic field [22, 5], the AGN host galaxy [27], intra-galaxy-cluster fields [12], magnetic fields in AGN lobes [26], and in the Milky Way [25]. The turbulent fields are commonly modelled with a simple domain-like structure: the path length is split up into N domains of coherence length L_{coh}. While the field strength remains constant over all cells, the orientation

[1] Blazars are active galactic nuclei (AGN) with a jet closely aligned to the line of sight. It is the most common source class for extragalactic VHE γ-ray emitters, see e.g. `http://tevcat.uchicago.edu/`.

of the field is assumed to change randomly from one cell to the next. The random nature of the field makes it necessary to calculate the conversion probability for a large number of random realisations. As N grows, the photon-ALP oscillations can often only be calculated numerically. Here, we show analytically that in these simple models realisations exist for which the photon-ALP conversion probability vanishes.

2 Photon-ALP oscillations

The equations of motion of a monochromatic photon-ALP beam composed of the two photon polarisation states $A_{1,2}$ and the ALP field strength a, $\Psi = (A_1, A_2, a)^T$, of energy E propagating along the x_3 axis in a cold plasma with homogeneous magnetic field can be written as [23]

$$\left(i\frac{\mathrm{d}}{\mathrm{d}x_3} + E + \mathcal{M}_0\right)\Psi(x_3) = 0, \tag{1}$$

where the mixing is induced by off-diagonal elements of the mixing matrix $\mathcal{M}_0$. The resulting photon-ALP oscillations are similar to neutrino oscillations and we denote the mixing angle by α (see, e.g. Ref. [2] for the full expressions for $\mathcal{M}_0$ and α). Equation (1) can be solved with the transfer matrix $\mathcal{T}$, so that $\Psi(x_3) = \mathcal{T}(x_3, 0; \psi; E)\Psi(0)$, where ψ denotes the angle between the transversal magnetic field and the photon polarisation state along x_2 [3]. With the eigenvalues λ_j, $j = 1, 2, 3$, of the mixing matrix and introducing the notation $s_\theta = \sin\theta$ and $c_\theta = \cos\theta$, the transfer matrix can be written as [3]

$$\mathcal{T} = \sum_{j=1}^{3} e^{i\lambda_j x_3}\mathcal{T}_j \qquad \text{with} \qquad \mathcal{T}_1 = \begin{pmatrix} c_\psi^2 & -s_\psi c_\psi^2 & 0 \\ s_\psi c_\psi & s_\psi^2 & 0 \\ 0 & 0 & 0 \end{pmatrix},$$
$$\mathcal{T}_2 = \begin{pmatrix} s_\psi^2 s_\alpha^2 & c_\psi s_\psi s_\alpha^2 & -s_\psi c_\alpha s_\alpha \\ c_\psi s_\psi s_\alpha^2 & c_\psi^2 s_\alpha^2 & -c_\psi c_\alpha s_\alpha \\ -s_\psi c_\alpha s_\alpha & -c_\psi c_\alpha s_\alpha & c_\alpha^2 \end{pmatrix}, \quad \mathcal{T}_3 = \begin{pmatrix} s_\psi^2 c_\alpha^2 & c_\psi s_\psi c_\alpha^2 & s_\psi c_\alpha s_\alpha \\ c_\psi s_\psi c_\alpha^2 & c_\psi^2 c_\alpha^2 & c_\psi c_\alpha s_\alpha \\ s_\psi c_\alpha s_\alpha & c_\psi c_\alpha s_\alpha & s_\alpha^2 \end{pmatrix}. \tag{2}$$

For N consecutive domains with angle ψ_n in each domain, it can be shown that the total transfer matrix is given as a product over all domains,

$$\mathcal{T}(x_{3,N}, \ldots, x_{3,1}; \psi_N, \ldots, \psi_1; E) = \prod_{n=1}^{N} \mathcal{T}(x_{3,n+1}, x_{3,i}; \psi_n; E). \tag{3}$$

Present γ-ray experiments cannot measure the polarisation. Therefore, one has to generalise the problem at hand to the density matrix formalism, where $\rho = \Psi \otimes \Psi^\dagger$ [21]. The probability for an initially unpolarised photon beam, $\rho_{\mathrm{unpol}} = 1/2\mathrm{diag}(1, 1, 0)$, to oscillate into an ALP, $\rho_{aa} = \mathrm{diag}(0, 0, 1)$ is then given by [21]

$$P_{a\gamma} = \mathrm{Tr}\left(\rho_{aa}\mathcal{T}\rho_{\mathrm{unpol}}\mathcal{T}^\dagger\right). \tag{4}$$

The oscillation probability will take some value $0 \leqslant P_{a\gamma} \leqslant 1/2$ [20] depending on the realisation of the angles $\{\psi_n\}$ and the mixing angle. Interestingly, realisations exist for which $P_{a\gamma} = 0$ even though $\alpha > 0$. To show this we assume an even number of domains where $\psi = c\pi$ in one half of the domains and $(c+1)\pi$ in the other half (where c is a real non-zero number) ordered

randomly. A straightforward calculations shows that the commutator of the transfer matrices $C = [\mathcal{T}(\psi = (c+1)\pi), \mathcal{T}(\psi = c\pi)]$ is an anti-symmetric matrix with entries

$$C_{13} = -C_{31} = \frac{1}{2}\left(e^{i\lambda_2 x_3} - e^{i\lambda_3 x_3}\right)^2 s_{c\pi} s_{4\alpha} \quad (5)$$

$$C_{23} = -C_{32} = \frac{1}{2}\left(e^{i\lambda_2 x_3} - e^{i\lambda_3 x_3}\right)^2 c_{c\pi} s_{4\alpha} \quad (6)$$

and zero in all other entries. The matrix elements of the product $\mathcal{T}(\psi = (c+1)\pi)\mathcal{T}(\psi = c\pi)$ that induce mixing (i.e., the $i3$, $i = 1, 2$ elements in the current basis) are found to be equal to $2C_{i3}$. Above a critical energy $E_{\rm crit}$ the mixing becomes independent of energy. If in addition the mixing is strong so that $\alpha \to \pi/4$, the commutator and the mixing inducing matrix elements vanish. With the commutator equal to zero we can now combine all pairs of $c\pi$ and $(c+1)\pi$ transfer matrices and see that the resulting product of all matrices given in Eq. (3) does not induce any photon-ALP mixing.

As an example, we show this behaviour in Fig. 1, in which we assume magnetic-field parameters found in galaxy clusters. The conversion probability is calculated numerically following Eq. (4). Above the critical energy the probability goes to zero, however, around the critical energy oscillations still occur. Our findings still hold even if photon absorption is included as it is the case for conversions in the intergalactic magnetic field. However, as this magnetic field evolves with redshift, not all realisations lead to a conversion probability exactly equal to zero for all random permutations.

3 Conclusions

As shown in the previous section, the photon-ALP conversion probability can be exactly zero in special configurations of a turbulent magnetic field given that (a) it is modelled with a simple cell-like structure and (b) that the mixing occurs in the strong mixing regime, i.e. at energies $> E_{\rm crit}$ and $\alpha \to \pi/4$. Oscillations around the critical energy still occur making spectral features at this energy a universal prediction of photon-ALP oscillations. The absence of such signatures in γ-ray spectra has already been used to constrain the photon-ALP coupling [1]. In more realistic models of the turbulent field (that use, e.g., a Kolmogorov turbulence spectrum) we do not have the freedom to choose the ψ angles (see, e.g. Ref. [19]) and we cannot easily construct a scenario with vanishing mixing as done here. Utilizing such models, it can be shown that the future Cherenkov Telescope Array will be sensitive to detect a boost in the photon flux for photon-ALP couplings $\gtrsim 2 \times 10^{-11}\,{\rm GeV}^{-1}$ and ALP masses $\lesssim 100\,{\rm neV}$ [17], the same parameters that could explain evidence for a reduced opacity for VHE γ-rays [18].

Acknowledgments

MM is supported by a grant of the Knut and Alice Wallenberg Foundation, PI: Jan Conrad

References

[1] A. Abramowski, F. Acero, F. Aharonian, F. Ait Benkhali, A. G. Akhperjanian, E. Angüner, G. Anton, S. Balenderan, A. Balzer, A. Barnacka, and et al. Constraints on axionlike particles with H.E.S.S. from the irregularity of the PKS 2155-304 energy spectrum. Phys. Rev. D, 88(10):102003, 2013.

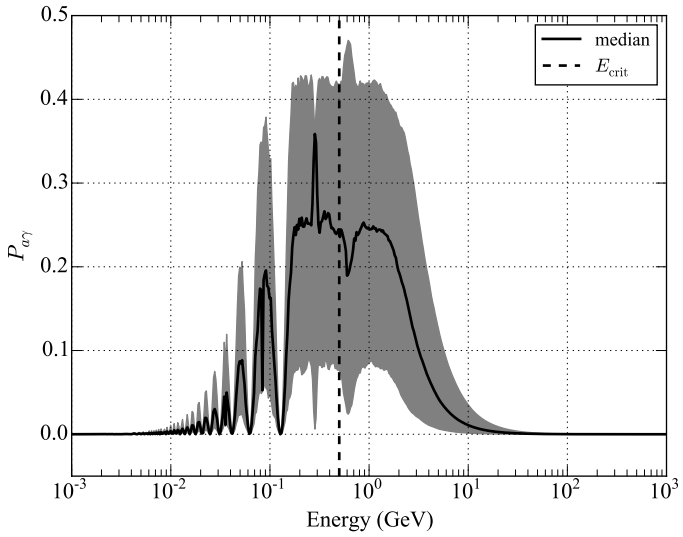

Figure 1: Conversion probability in 30 domains with $L_{\rm coh} = 10\,{\rm kpc}$ and $B = 1\,\mu{\rm G}$. Half of the domains have $\psi = 0$ while in the other half $\psi = \pi$ is chosen. The solid line shows the median of $P_{a\gamma}$ for 1000 random permutations of the angles. The shaded area gives the probability in the 68 % interval around the median. The dashed line shows $E_{\rm crit}$ above which $\alpha \to \pi/4$. An ALP mass of 1 neV and a photon-ALP coupling of $5 \times 10^{-11}\,{\rm GeV}^{-1}$ are assumed.

[2] N. Bassan, A. Mirizzi, and M. Roncadelli. Axion-like particle effects on the polarization of cosmic high-energy gamma sources. *JCAP*, 5:10, 2010.

[3] A. de Angelis, G. Galanti, and M. Roncadelli. Relevance of axionlike particles for very-high-energy astrophysics. Phys. Rev. D, 84(10):105030, 2011.

[4] A. De Angelis, O. Mansutti, M. Persic, and M. Roncadelli. Photon propagation and the very high energy γ-ray spectra of blazars: how transparent is the Universe? MNRAS, 394:L21–L25, 2009.

[5] A. de Angelis, M. Roncadelli, and O. Mansutti. Evidence for a new light spin-zero boson from cosmological gamma-ray propagation? Phys. Rev. D, 76(12):121301, 2007.

[6] A. Domínguez, J. R. Primack, D. J. Rosario, et al. Extragalactic background light inferred from AEGIS galaxy-SED-type fractions. MNRAS, 410:2556–2578, 2011.

[7] A. Domínguez, M. A. Sánchez-Conde, and F. Prada. Axion-like particle imprint in cosmological very-high-energy sources. *JCAP*, 11:20, 2011.

[8] E. Dwek and F. Krennrich. The extragalactic background light and the gamma-ray opacity of the universe. *Astroparticle Physics*, 43:112–133, 2013.

[9] G. G. Fazio, M. L. N. Ashby, et al. Number Counts at 3 μm $< \lambda <$ 10 μm from the Spitzer Space Telescope. ApJS, 154:39–43, 2004.

[10] R. C. Gilmore, R. S. Somerville, J. R. Primack, and A. Domínguez. Semi-analytic modelling of the extragalactic background light and consequences for extragalactic gamma-ray spectra. MNRAS, 422:3189–3207, 2012.

[11] M. G. Hauser, R. G. Arendt, et al. The COBE Diffuse Infrared Background Experiment Search for the Cosmic Infrared Background. I. Limits and Detections. ApJ, 508:25–43, 1998.

[12] D. Horns, L. Maccione, M. Meyer, A. Mirizzi, D. Montanino, and M. Roncadelli. Hardening of TeV gamma spectrum of active galactic nuclei in galaxy clusters by conversions of photons into axionlike particles. Phys. Rev. D, 86(7):075024, 2012.

[13] D. Horns and M. Meyer. Indications for a pair-production anomaly from the propagation of VHE gamma-rays. *JCAP*, 2:33, 2012.

[14] J. Jaeckel and A. Ringwald. The Low-Energy Frontier of Particle Physics. *Annual Review of Nuclear and Particle Science*, 60:405–437, 2010.

[15] T. M. Kneiske and H. Dole. A lower-limit flux for the extragalactic background light. A&A, 515:A19+, 2010.

[16] P. Madau and L. Pozzetti. Deep galaxy counts, extragalactic background light and the stellar baryon budget. MNRAS, 312:L9–L15, 2000.

[17] M. Meyer and J. Conrad. Sensitivity of the Cherenkov Telescope Array to the detection of axion-like particles at high gamma-ray opacities. *ArXiv e-prints*, 2014.

[18] M. Meyer, D. Horns, and M. Raue. First lower limits on the photon-axion-like particle coupling from very high energy gamma-ray observations. Phys. Rev. D, 87(3):035027, 2013.

[19] M. Meyer, D. Montanino, and J. Conrad. On detecting oscillations of gamma rays into axion-like particles in turbulent and coherent magnetic fields. *ArXiv e-prints*, 2014.

[20] Manuel Meyer. *The Opacity of the Universe for High and Very High Energy γ-Rays*. PhD thesis, University of Hamburg, 2013. `http://inspirehep.net/record/1254304`.

[21] A. Mirizzi and D. Montanino. Stochastic conversions of TeV photons into axion-like particles in extragalactic magnetic fields. *JCAP*, 12:4, 2009.

[22] A. Mirizzi, G. G. Raffelt, and P. D. Serpico. Signatures of axionlike particles in the spectra of TeV gamma-ray sources. Phys. Rev. D, 76(2):023001, 2007.

[23] G. Raffelt and L. Stodolsky. Mixing of the photon with low-mass particles. Phys. Rev. D, 37:1237–1249, 1988.

[24] G. I. Rubtsov and S. V. Troitsky. Breaks in gamma-ray spectra of distant blazars and transparency of the Universe. *ArXiv e-prints*, 2014.

[25] M. Simet, D. Hooper, and P. D. Serpico. Milky Way as a kiloparsec-scale axionscope. Phys. Rev. D, 77(6):063001, 2008.

[26] F. Tavecchio, M. Roncadelli, and G. Galanti. Photons into axion-like particles conversion in Active Galactic Nuclei. *ArXiv e-prints*, 2014.

[27] F. Tavecchio, M. Roncadelli, G. Galanti, and G. Bonnoli. Evidence for an axion-like particle from PKS 1222+216? Phys. Rev. D, 86(8):085036, 2012.

Mississippi State Axion Search: A Light Shining though a Wall ALP Search

Prajwal Mohanmurthy[1], *Dipangkar Dutta*[2], *Joseph Formaggio*[1], *Nicholas Fowler*[2], *Mikhail Gaerlan*[2], *Yipeng Jiang*[2], *John Madsen*[2], *Noah Oblath*[1], *Adam Powers*[2], *Amy Ray*[2], *Robertson Riehle*[2]
MASS Collaboration

[1]Laboratory for Nuclear Science, MIT, 77 Mass. Ave., Cambridge, MA 02139, U.S.A.
[2]Physics Department, Mississippi State University, Mississippi State, MS 39762-5167, U.S.A.

DOI: http://dx.doi.org/10.3204/DESY-PROC-2014-03/mohanmurthy_prajwal

The elegant solutions to the strong CP problem predict the existence of a particle called axion. Thus, the search for axion like particles (ALP) has been an ongoing endeavor. The possibility that these axion like particles couple to photons in presence of magnetic field gives rise to a technique of detecting these particles known as light shining through a wall (LSW). Mississippi State Axion Search (MASS) is an experiment employing the LSW technique in search for axion like particles. The apparatus consists of two radio frequency (RF) cavities, both under the influence of strong magnetic field and separated by a lead wall. While one of the cavities houses a strong RF generator, the other cavity houses the detector systems. The MASS apparatus looks for excesses in RF photons that tunnel through the wall as a signature of candidate axion-like particles. The concept behind the experiment as well as the projected sensitivities are presented here.

1 Introduction

The axion was proposed to solve the strong CP problem [1]. Axions have been proposed as a good cold dark matter candidate [2]. In addition to other super-symmetric dark matter candidates, axions are included as dark matter constituents especially in super symmetric extensions of the standard model [3].

A single parameter, the axion decay constant, f_a is sufficient to describe the physics of axions.

$$f_a = 6 \times 10^{-6} eV \frac{10^12 GeV}{m_a} \qquad (1)$$

where m_a is the mass of the axion. Axions and ALPs are characterized by small masses arising from the shift symmetry of the ALP

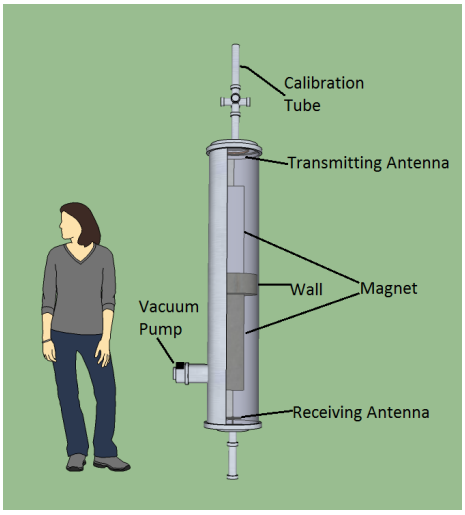

Figure 1: Basic schematic diagram of the MASS apparatus

field, $\phi(x)$. The shift symmetry $\phi(x) \rightarrow \phi(x)+const.$ prohibits explicit mass terms ($\propto m_\phi^2\phi^2$) in the ALP Lagrangian. The only way an ALP field could interact with standard model particles is via derivative couplings ($\propto \partial\phi/f_a$). This significantly suppresses their interactions below the f_a scale, effectively making ALPs weekly interacting sub-eV particle (WISP) candidates [4]. Furthermore, the two most relevant two photon couplings can be written for both pseudo-scalar and scalar ALPs respectively as;

$$\mathcal{L}_{\phi^{+(-)}\gamma\gamma} = -\frac{g_{+(-)}}{4} F_{\mu\nu}\tilde{F}^{\mu\nu}\phi^{+(-)} \tag{2}$$

where, $F_{\mu\nu}$ is the electromagnetic field, $g_{+(-)} = g_\gamma(\alpha/\pi f_a)$, $g_\gamma \approx -0.97$ in Kim-Shifman-Vainshtein-Zacharov (KSVZ) model [5] or $g_\gamma \approx -0.36$ in Dine-Fischler-Srednicki-Zhitnitskii (DFSZ) model [6] , and α is the fine structure constant.

2 Method

In the MASS experiment, Primakoff effect is employed to put the LSW technique to test where the incident photon couples with the magnetic field to create lightly interacting ALPs which pass through a barrier, regenerating to photons on the dark side of the barrier, while ideally no photons pass through the barrier. The regenerated photons have the same characteristics as the incident photons, *i.e.* they are of the same frequency, phase and couple to the same electromagnetic mode. Since photons are regenerated via an ALP, the rate of regeneration (R) is given by [7];

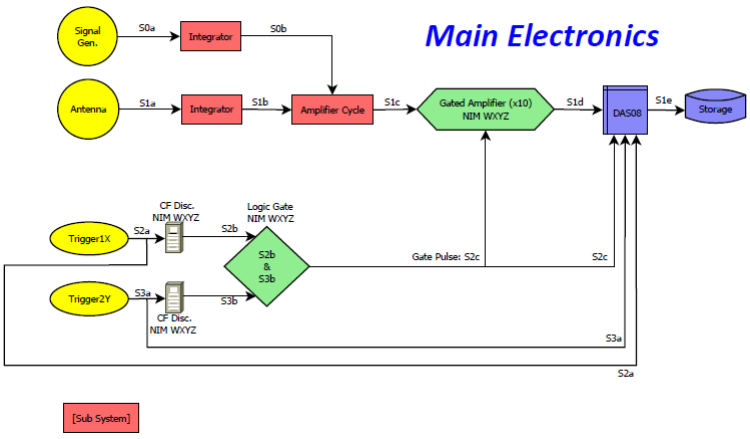

Figure 2: Schematic diagram showing the fast electronics in line before the data is written to disk.

$$R = N_\gamma \epsilon_c Q_d P_{\gamma\rightarrow ALP} P_{ALP\rightarrow\gamma} \tag{3}$$

$$P_{\gamma\rightarrow ALP} = P_{ALP\rightarrow\gamma} = \left(\frac{gB}{\frac{m^2}{2\omega}}\right)^2 Sin^2\left(\frac{m^2 L}{4\omega}\right) \tag{4}$$

where N_γ is the number rate of photons, ϵ_c is photon capture efficiency, Q_d is the detector quantum efficiency, $P_{\gamma\rightarrow ALP}$ is the probability of conversion of a photon to a scalar ALP, $P_{ALP\rightarrow\gamma}$ is the probability of conversion of a scalar ALP to a photon, g is the coupling constant, m is the mass of the ALP, B is the magnetic field strength, ω is the energy of the photons and L is the length of the cavity under magnetic field.

3 Apparatus

The MASS apparatus consists of two tunable evacuated cavities as shown in Figure 1. These two cavities are mutually isolated. The "light" cavity houses a StreakHouse ^{TM} transmission

antenna [8], capable of transmitting integral multiples of 410 MHz and the "dark" cavity houses an antenna capable of mapping local field in all three spatial axes. A compact dipole magnet bathes the two cavities in a magnetic field in the radial direction while a solenoid is used to create a magnetic field along the axis of the cavities (Z-direction). The radial magnetic field produced by the dipole magnet was mapped using a DPPH (Di-Phenyl Picryl Hydrazyl) probe and is presented in Figure 3. The solenoid is only used to tune the cavity and thereby has a low field strength output (< 0.5 T). The transmission antenna is mounted at the end of a calibration tube, precise to within 1 nm which allows for additional fine tuning of the cavity. The other end of the calibration tube provides for a number of electronic feed thoughts. Feed through for the receiving antenna electronics is completely separated from the feed through for the main transmission antenna.

The cavities are usually tuned simultaneously to TM_{010} and TM_{020} where the most fundamental mode corresponds to 410 MHz. About 120 W of RF power is dumped into the "light" cavity through the transmission antenna. The transmission power gives a measure of number rate of photons, N_γ, in Eq. (3). A precise measurement of the standing wave ratio (SWR) of the receiving antenna gives a measure of the product of photon capture efficiency and its quantum efficiency, $\epsilon_c Q_d$, in Eq. (3).

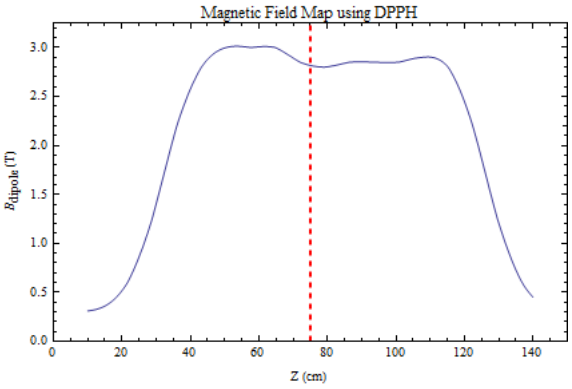

Figure 3: Plot showing the dipole magnetic field profile in the 2 cavities used in MASS. On the left hand side of the red line is the "light" cavity and on the right hand side of the red line is the "dark" cavity.

MASS experiment employs a redundant frequency lock-in technique to control signal to noise ratio in the apparatus. The primary signal is generated using a 16-bit programmable digital oscillator which is then amplified a number of times to reach 120 W of continuous transmission power. Both the receiver signal and the primary signal are rectified, integrated and normalized (hereby referred to as processed) such that their difference is ideally null except in the case of there being a regenerated photon (Figure 2). Processing involves continuous rectification which converts all negative components to positive. Furthermore, the rectified signal is integrated over 1 ms before the running integrand is reset to zero. The regenerated photons show up as small excesses in the running integrand at the end of the corresponding 1 ms time period. Integrating the receiver signal also reduces the amount of digitized data by a factor of 410×10^3, since the primary signal is 410 MHz and the integrated signal has a frequency of 1 kHz due to the integration time period being 1 ms. The difference between the processed primary signal and the processed receiver signal has the same frequency and phase information as that of the processed primary signal, therefore the processed primary signal also serves as the reference for the three SR 530 [9] lock-in amplifiers. The difference of the processed receiver signal and the processed primary signal is then subject to three sets of SR 530 lock-in amplifiers which use the processed primary signal as a reference providing a signal to noise ratio better than 10^{18} accounting for residual thermal noise and quantum fluctuations.

The processed and amplified receiver signal is then digitized and written to disk. A set of trigger antenna within the apparatus located around the "dark" cavity pickup on external

noises and creates a gate during which time the processed and amplified primary signal is not written to disk.

4 Conclusion

Taking into account the inhomogeneity of the magnetic field, the characteristics of the two main antennae, residual RF field on the "dark side of the cavity" and the thermal noise, all of which contribute to the uncertainity in measured rate of regenerated photons, the possible sensitivity of MASS to scalar and pseudo scalar ALPs is calculated using Eq. (3) & (4), as presented in Figure 4. It might be important to note that since the exclusions that MASS can provide for scalar and pseudo scalar ALPs are similar to each other, Figure 4 has plotted the sensitivities to two different cavity modes, each a multiple of the fundamental frequency of 410 MHz, both of which are accessible in the MASS apparatus.

Even though the sensitivity that MASS can provide in the low mass regime (10 μeV - 100 μeV) for both scalar and pseudo scalar ALPs will only be comparable to the currently available limits, and not any better, it shall demonstrate the feasibility of using the LSW technique with RF photons.

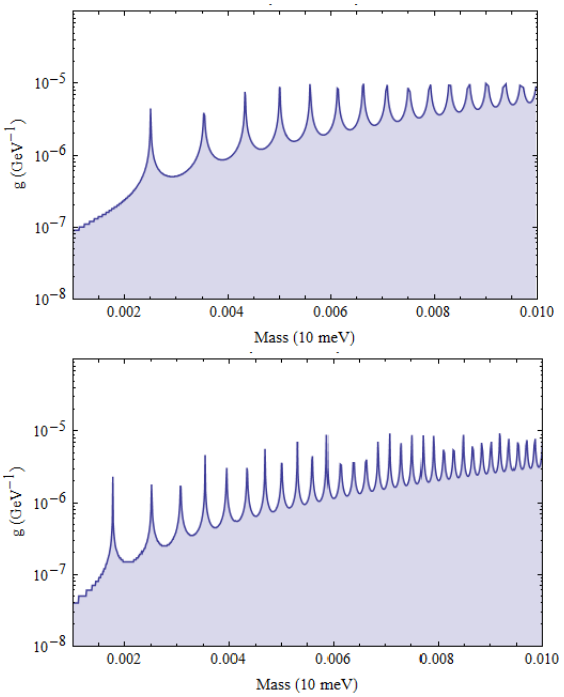

Figure 4: (Top) Plot showing the sensitivity of MASS to scalar ALPs when the cavities are tuned around 410 MHz with a C.L of 95%. (Bottom) Plot showing the sensitivity of MASS to pseudo-scalar ALPs when the cavities are tuned around 820 MHz with a C.L of 95%.

Acknowledgement

The authors would like to thank Dr. Torsten Clay for his help with setting the group up at the High Performance Computing Collaboratory, the resources of which are used for simulation and analysis. This work is supported by the Mississippi State Consortium and the Jefferson Science Associates through the Thomas Jefferson National Accelerator Facility.

References

[1] R. D. Peccei and H. R. Quinn, Phys. Rev. Lett. **38**, 1440 (1977).
[2] J. Preskill, M. Wise, and F. Wilczek, Phys. Rev. Lett. **120B**, 127 (1983).
[3] H. Baer, Particle Physics and Cosmology Meeting (PPC2013), (2013): arXiv.org: 1310.1859 .
[4] J. E. Kim, Phys. Rev. Lett. **43** 103 (1979).
[5] M. A. Shifman, A. I. Vainshtein, and V. I. Zakharov, Nucl. Phys. **B166**, 493 (1980).
[6] M. Dine, W. Fischler, and M. Srednicki, Phys. Rev. D **104B**, 199 (1985).
[7] K. Choi, Phys. Rev. D **62**, 043509 (2000).
[8] `http://www.streakwave.com/mmSWAVE1/Video/ANT-DS-FG16397.pdf`
[9] `http://www.thinksrs.com/downloads/PDFs/Manuals/SR530m.pdf`

Searches for axioelectric effect of solar axions with BGO-scintillator and BGO-bolometer detectors

V.N. Muratova[1], *A.V. Derbin*[1], *L. Giorni*[2,3], *S.S Nagorny*[4,5], *L. Pattavina*[4], *S.V. Bakhlanov*[1], *J.W. Beeman*[6], *F.Bellini*[7,8], *M. Biassoni*[2,3], *S. Capelli*[2,3], *M. Clemenza*[2,3], *I.S. Dratchnev*[1,5], *E. Ferri*[2,3], *A. Giachero*[2,3], *C. Gotti*[2,3], *A.S. Kayunov*[1], *C. Maiano*[2,3], *M. Maino*[2,3], *M. Pavan*[2,3], *S. Pirro*[4], *D.A. Semenov*[1], *M. Sisti*[2,3], *E.V. Unzhakov*[1]

[1]St.Petersburg Nuclear Physics Institute, Gatchina 188350 - Russia
[2]INFN - Sezione di Milano Bicocca, Milano 1-20126 - Italy
[3]Dipartimento di Fisica, Universita di Milano-Bicocca, Milano 1-20126 - Italy
[4]INFN - Laboratory Nazionale del Gran Sasso, Assergi (L'Aquila) I-67100 - Italy
[5]Gran Sasso Science Institute, INFN, L'Aquila (AQ) I-67100 - Italy
[6]Lawrence Berkeley National Laboratory, Berkley, California 94720 - USA
[7]INFN -Sezione di Roma, Roma I-00185 - Italy
[8]Dipartimento di Fisica - Universita di Roma La Sapienza, Roma I-00185 - Italy

DOI: http://dx.doi.org/10.3204/DESY-PROC-2014-03/muratova_valentina

A search for axioelectric absorption of 5.5 MeV solar axions produced in the $p+d \rightarrow {}^3\mathrm{He}+\gamma$ (5.5 MeV) reaction has been performed with a BGO detectors. A model-independent limit on the product of axion-nucleon g^3_{AN} and axion-electron g_e coupling constants has been obtained: $|g_{Ae} \times g^3_{AN}| < 1.9 \times 10^{-10}$ for 90% C.L..

1 Introduction

There are new possibilities for strong CP problem solution, which allow the existence of axions with a large mass (1 MeV), while their interaction with ordinary particles remain at the level of the invisible axions. The models rely on the hypothesis of mirror particles [1] and SUSY at the TeV scale [2]. The existence of these heavy axions is not forbidden by the laboratory experiments or astrophysical data.

This article describes the experimental search for 5.5 MeV solar axions, which can be produced by $p + d \rightarrow {}^3\mathrm{He} + \mathrm{A}$ reaction. Axion flux should be proportional to the *pp*-neutrino flux, which has been estimated with high accuracy [3]. The searches have been performed with the use of bismuth orthogermanate $Bi_4Ge_3O_{12}$ (BGO) scintillation and bolometric detectors. The solar axions are supposed to interact with atoms via the reaction of axioelectric effect $\mathrm{A} + e + Z \rightarrow e + Z$. This kind of interaction is governed by g_{Ae}-constant and the cross section depends on the charge as Z^5. From this point of view the BGO detector is a very suitable target, because of the high $Z_{Bi} = 83$ of bismuth nucleus.

The high energy solar axions and axions from a nuclear reactor have been looked by the Borexino [4, 5], the CAST [6] and the Texono [7] collaborations. This paper is based on the results of obtained with BGO scintillation [8] and BGO bolometer detectors [9].

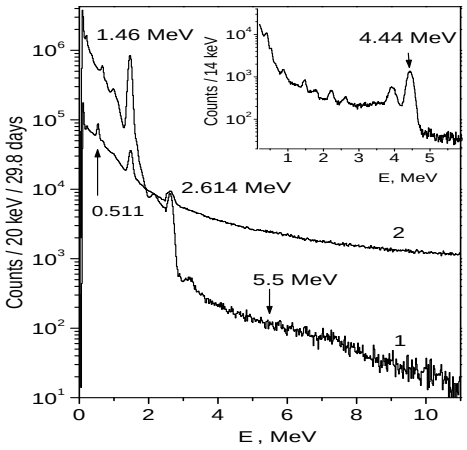

Figure 1: The energy spectrum of the BGO detector measured (1) in anticoincidence and (2) in coincidence with the muon veto signal.

The 5.5 MeV axion production probability ratio (ω_A/ω_γ) depends only on the isovector axion-nucleon coupling constant g^3_{AN} (see [9] and refs therein):

$$\frac{\omega_A}{\omega_\gamma} = \frac{\chi}{2\pi\alpha}\left[\frac{g^3_{AN}}{\mu_3}\right]^2\left(\frac{p_A}{p_\gamma}\right)^3 = 0.54(g^3_{AN})^2\left(\frac{p_A}{p_\gamma}\right)^3. \quad (1)$$

where p_γ and p_A are, respectively, the photon and axion momenta and μ_3 is isovector nuclear magnetic momenta. At the Earth's surface the axion flux is:

$$\Phi_A = \Phi_{\nu pp}(\omega_A/\omega_\gamma) \quad (2)$$

where $\Phi_{\nu pp}$ is the pp-neutrino flux. The cross section for the a.e. effect was calculated in [10].

2 BGO scintillation detector

BGO crystal with mass 2.46 kg contains 1.65 kg of Bi. The crystal was shaped as a cylinder, 76 mm in diameter and 76 mm in height. The detector signal was measured by an R1307 photoelectron multiplier, which had an optical contact with a crystal end surface. The external γ activity was suppressed using a passive shield that consisted of layers of lead and bismuth (Bi_2O_3) with the total thickness ≈ 110 g cm^{-2}. The setup was located on the Earth's surface. In order to suppress the cosmic-ray background we used an active veto, which consisted of five $50\times50\times12$ cm plastic scintillators. The measurements were performed over 29.8 days. The energy spectrum of the BGO detector in the range of (0–11) MeV is shown in Fig. 1. In inset the calibration spectrum measured with Pu-Be neutron source is shown.

In the spectrum, one can identify two pronounced peaks at 1.460 MeV and 2.614 MeV; these are due to the natural radioactivity of the ^{40}K and of ^{208}Tl from the ^{232}Th family. The positions and intensities of these peaks were used for monitoring of time stability of the detector.

3 BGO bolometers

Four cubic ($5\times5\times5$ cm^3) BGO bolometers, containing 1.65 kg of Bi, were arranged in a four-plex module, one single plane set-up. The scintillation light was monitored with an auxiliary bolometer made of high-purity germanium [12]. The detector was installed in the ^{3}He/^{4}He dilution refrigerator in the underground laboratory of L.N.G.S. and operated at a temperature of few mK. The four crystals were housed in a highly pure copper structure, the same described in [13]. Neutron Transmutation Doped (NTD) germanium thermistor was coupled to each bolometer, NTD acts as a thermometer: recording the temperature rises produced by particle interaction and producing voltage pulses proportional to the energy deposition. Details on electronics and on the cryogenic set-up can be found in [14, 15]. The detector was operated for a total live time of 151.7 days.

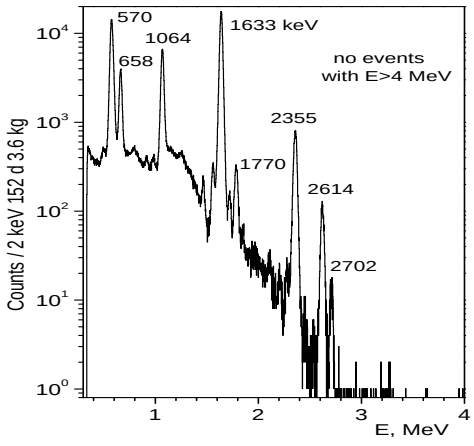

Figure 2: The energy spectrum of the four BGO detectors ($\beta-$ and $\gamma-$ events) measured for a 151.7 days.

The different light yield of interacting particles was used to discriminate $\alpha-$events from β/γ ones. This allowed to strongly increase the sensitivity, due to rejection of all $\alpha-$events in the region of interest. The total statistics in the range of (0.3-4) MeV for β/γ events are in shown in Fig.2. The most intense gamma lines are produced by ^{207}Bi decays. In first approximation, the energy resolution of large mass bolometric detector is independent of the energy - the FWHM is 33.7 ± 0.6 keV at 2614 keV (^{208}Tl) and 33.2 ± 0.1 keV at 570 keV (^{207}Bi).

4 Results

The expected number of axioelectric absorption events are:

$$S_{abs} = \varepsilon N_{Bi} T \Phi_A \sigma_{Ae} \qquad (3)$$

where σ_{Ae} is the axioelectric effect cross section; Φ_A is the axion flux (2); N_{Bi} is the number of Bi atoms; T is the measurement time; and ε is the detection efficiency for 5.5 MeV electrons.

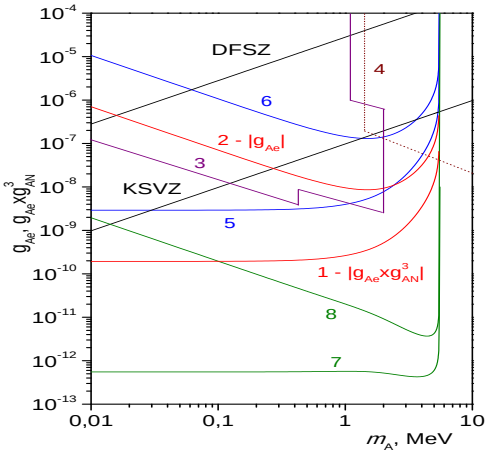

Figure 3: The limits on the g_{Ae} coupling constant obtained by 1,2 -BGO-bolometer [9] and 5,6-BGO-scintillator [8] for $|g_{Ae}|$ and $|g_{Ae} \times g^3_{AN}|$, correspondingly; 3- solar and reactor experiments, 4- beam dump experiments; 7,8 - Borexino results for $|g_{Ae} \times g^3_{AN}|$ and $|g_{Ae}|$ [5].

The axion flux Φ_A is proportional to the constant $(g^3_{AN})^2$, and the cross section σ_{Ae} is proportional to the constant g^2_{Ae}. As a result, the S_{abs} value depends on the product $(g_{Ae})^2 \times (g^3_{AN})^2$. The experimentally found condition $S_{abs} \leq S_{lim}$ imposes some constraints on the range of possible $|g_{Ae} \times g^3_{AN}|$ and m_A values.

The range of excluded $|g_{Ae} \times g^3_{AN}|$ values is shown in Fig. 3, at $m_A \to 0$ the limits

$$|g_{Ae} \times g^3_{AN}| \leq 2.9 \times 10^{-9} \quad \text{and} \qquad (4)$$

$$|g_{Ae} \times g^3_{AN}| \leq 1.9 \times 10^{-10} \quad \text{at } 90\% \text{ c.l.}. \qquad (5)$$

were obtained for BGO scintillating and BGO bolometer detectors, correspondingly. These constraints are completely model-independent and valid for any pseudoscalar particle with coupling $|g_{Ae}|$ less than $10^{-6(4)}$.

For hadronic axion model with concrete relation between g^3_{AN} and m_A one can obtain a constraint on the g_{Ae} constant, depending on the axion mass (Fig. 3). For $m_A = 1$ MeV, this limit corresponds to $|g_{Ae}| \leq 9.6 \times 10^{-9}$ at 90%c.l..

Figure 3 also shows the constraints which were obtained in the Borexino experiment for 478 keV ^{7}Li solar axions [4] and in the Texono reactor experiment for 2.2 MeV axions produced in the $n + p \to d + A$ reaction [7]. Borexino coll. reported new more stringent limits on g_{Ae} coupling for 5.5 MeV solar axions [5]. Unlike our work, these limits on g_{Ae} coupling were obtained in assumption that the axion interacts with electron through the Compton conversion process.

In the model of the mirror axion [1] an allowed parameter window is found within the P-Q scale $f_A \sim 10^4 - 10^5$ GeV and the axion mass $m_A \sim 1$ MeV. The limit (5) may be represented as a limit on the value f_A by taking the following relations into account: $g^3_{AN} = 0.5(g_{Ap} - g_{An}) = 1.1/f_A$ and $g_{Ae} = 5 \times 10^{-4}/f_A$. For axion masses about 1 MeV, the limit is $f_A > 1.7 \times 10^3$ GeV, which is close to the lower bound of mirror axion window.

Our results set constraints on the parameter space of the CP-odd Higgs (A^0), which arise in the next-to-minimal supersymmetric Standard Model due to the spontaneous breaking of approximate symmetries such as PQ-symmetry. The corresponding exclusion region can be obtained from Fig.3 using the conversion $C_{Aff} = g_{Ae} 2m_W/g_2 m_e$ where C_{Aff} is the coupling of the CP-odd Higgs to fermions and $g_2 = 0.62$ is the gauge coupling. The limit (5) translates into $C_{Aff} \times m_{A^0} \leq 3 \times 10^{-3}$ MeV for $m_{A^0} < 1$ MeV, which is compatible with the limits obtained in reactor experiments exploring Compton conversion.

This work was supported by RFBR grants 13-02-01199 and 13-02-12140-ofi-m.

References

[1] Z. Berezhiani et al., Phys. Lett. B500, 286 (2001).

[2] L.J. Hall and T. Watari, Phys. Rev. D70, 115001 (2004).

[3] G. Bellini et al., (Borexino coll.) Nature, 512, 7515, 383 (2014)

[4] G. Bellini et al., (Borexino coll.) EPJ, C54, 61 (2008).

[5] G. Bellini et al., (Borexino Coll.), Phys. Rev. D 85, 092003 (2012).

[6] S. Andriamonje et al., (CAST coll.) JCAP 1003, 032, (2010). arXiv:0904.2103

[7] H.M. Chang et al., (Texono Coll.) Phys. Rev. D75, 052004 (2007).

[8] A.V. Derbin et al., Europ. Phys. J. C73, 2490 (2013). arXiv:1306.4574

[9] A.V. Derbin et al., Europ. Phys. J. C74, 3035 (2014). arXiv:1405.3782

[10] A.R. Zhitnitskii and Yu.I. Skovpen, Yad. Fiz., 29b, 995 (1979).

[11] L. Cardani, S.Di Domizio, L. Gironi, JINST 7, P10022 (2012).

[12] J.W. Beeman et al., JINST 8, P05021 (2013).

[13] F. Alessandria et al., Astropart. Phys. 35, 839849 (2012).

[14] S. Pirro et al., Nucl. Instrum. Methods A 444, 331 (2000).

[15] C. Arnaboldi et al., Nucl. Instrum. Methods A 559, 826 (2006).

A fresh Look on the Limit on ultralight Axion-like Particles from SN1987A

Alexandre Payez

Deutsches Elektronen-Synchrotron (DESY), Hamburg, Germany

DOI: http://dx.doi.org/10.3204/DESY-PROC-2014-03/payez_alexandre

We revisit the limit on very light axion-like particles (ALPs) from the absence of gamma rays coincidental with the neutrino burst from SN1987A. We use updated supernova simulations, modern models for the magnetic field inside the Galaxy, and a Primakoff cross section which takes into account proton-degeneracy and mass-reduction effects.

We finally give an updated exclusion plot for the electromagnetic coupling of sub-eV ALPs, comparing our new bound with other limits as well as with future ALP searches.

1 Reminder

Axion-like particles (ALPs) are generic predictions of theories beyond the Standard Model of particle physics, where they essentially arise as pseudo-Nambu–Goldstone bosons of new spontaneously broken global symmetries. The case for such light particles is actually arguably getting even more interesting since the LHC discovered the scalar Higgs boson—and gave an experimental evidence of how important spontaneous symmetry breaking can be in particle physics— but has however so far found no new heavy particle beyond the Standard Model, and in particular no signs of SUSY where it was presumably expected.

Together with the long-sought QCD axion, there is also some interest for ultralight ALPs, somewhat driven by phenomenology: indeed, a number of observations in astrophysics have been claimed by various authors to hint at the existence of such nearly massless (pseudo)scalars, thereby defining another window of interest in the ALP parameter space. The reason why they would be so interesting is the electromagnetic coupling that they might have, that would affect in a number of ways the signals expected from astrophysical sources [1]. There of course exist strong constraints on the electromagnetic coupling of such light particles, and the aim of this work [2] is actually to revisit and update what has remained for almost 20 years the most stringent bound over a wide range of masses in the astrophysical window [3, 4].

When a very massive star undergoes a core-collapse, lots of neutrinos are quickly radiated by the proto-neutron star, leading to a short and intense neutrino burst that will arrive at Earth hours before the optical flash. Such supernova (SN) explosions are in fact also an ideal place to search for extremely light ($m_a \lesssim 10^{-9}$ eV) ALPs a with a generic two-photon interaction, of effective coupling $g_{a\gamma}$:

$$\mathcal{L}_{a\gamma\gamma} = \frac{1}{4} g_{a\gamma} F_{\mu\nu} \tilde{F}^{\mu\nu} a. \tag{1}$$

Produced with typical energies related to the core temperature via the Primakoff effect on p^+,

$$p^+ + \gamma \to p^+ + a, \tag{2}$$

these light spinless particles would then quickly escape the exploding star, and later convert in the Galactic magnetic field into γ-ray photons, coincidental with the neutrino burst [3, 4].

Such a signal has been searched for in February 1987, when it has been realised that the star Sanduleak had blown up as a core-collapse supernova in the Large Magellanic Cloud in an event known as SN1987A: the first supernova that could be observed with the naked eye for more than 300 years, located only 50 kpc away from us. As predicted, a burst of neutrinos was detected; however, only an upper limit could be obtained on the γ signal during this 10-s burst, leading to the well-known constraints on the coupling of light axion-like particles which we want to revisit: $g_{a\gamma} \lesssim 3 \times 10^{-12}$ GeV^{-1} [3] or $g_{a\gamma} \lesssim 10^{-11}$ GeV^{-1} [4], for $m_a \lesssim 10^{-9}$ eV.

2 Main updates

Supernova simulations & time resolution

The two original independent analyses have adopted different approaches: Ref. [3] relied on analytical results only and considered typical estimates of the conditions inside a SN core, while Ref. [4] considered both analytical and numerical results, using simulations of the conditions inside the star at 1 s, 5 s and 10 s after the core bounce and eventually making a linear regression to estimate the integrated photon flux at Earth over this time interval.

In our work, we use recently updated spherically symmetric supernova models [5] for two progenitor masses: 18 $M_\odot$ (resp. 10.8 $M_\odot$), with simulations up to 21 s (resp. 10 s) after bounce. Our main result is obtained with the 18 $M_\odot$ progenitor, while the 10.8 $M_\odot$ one allows us to investigate the dependence of our limit on the progenitor mass. In both cases, the simulation data consist of a collection of ~ 600 snapshots at different times giving the profiles of various physical quantities inside the proto-neutron star as a function of the radius. This also allows us to get a more precise timing evolution of the ALP production inside the supernova.

Magnetic field & conversion probability

We make a very significant improvement for the description of the magnetic field. Indeed, the original studies simply considered a homogeneous Galactic magnetic field of transverse field strength $B_T \sim 1$ μG over $L = 1$ kpc, while we now use the recent model of Jansson and Farrar of the Galactic magnetic field [6], and have also performed all our calculations using the one of Pshirkov *et al.* [7] for comparison. A major difference between these elaborate models and the original toy model is that they take into account the presence of a halo component over several kiloparsecs; the various bounds that we obtain are therefore actually more stringent.

Both the original papers [3, 4] also used an approximate expression of the conversion probability, with $\Delta\mu^2$ being the difference of the mass eigenvalues squared, and θ, the mixing angle:

$$P_{a\gamma} = \sin^2(2\theta)\sin^2\left(\frac{\Delta\mu^2 L}{4E}\right) \sim \frac{1}{4}\, g_{a\gamma}^2 B_T^2 L^2. \tag{3}$$

For the case at hand, this approximation would be valid in the massless limit and was estimated to hold for $m_a \leq 10^{-9}$ eV. In our calculations, we instead now consider the full conversion probability and are therefore able to directly derive the mass dependence of the limit.

Degeneracy & high density

We further include effects related to the conditions in the SN core that were mentioned but not included to calculate the ALP production in Refs. [3, 4]. The first one is to take into account the fact that the protons are partially degenerate. This affects the number of available targets and also the screening inside the plasma (somewhere between the Debye and the Thomas–Fermi regimes). The second is the fact that, due to the extremely high density during the first seconds ($\rho \sim 10^{14}$ g cm^{-3}), the p^+ effective mass can actually go down to about 50% of its value in vacuum. This makes the protons easier to be degenerate but also means that there are more targets available for a given mass density. We further take this mass reduction into consideration, and use the updated tables of equation of state for nuclear matter in a supernova (2010, 2011) based on Ref. [8], which were actually also used in the SN models themselves [5].

3 Bottom line

Putting together the improvements discussed above, the low-mass bound that we obtain is [2]

$$g_{a\gamma} \lesssim 5.3 \times 10^{-12}\ \text{GeV}^{-1}, \quad \text{for} \quad m_a \lesssim 4.4 \times 10^{-10}\ \text{eV}. \tag{4}$$

The results are very stable over a variety of changes mostly because the limit on $g_{a\gamma}$ essentially goes as the fourth root of the fluence. We give an exclusion plot for low-mass ALPs in Fig. 1, updating the one from Ref. [9] to include our main result, obtained using the model of Jansson and Farrar for the Galactic magnetic field. We also compare the new limit with the constraint from quasar polarisation measurements [10] that corresponds to the magnetic field and electron density assumed in Ref. [11] in the plane of the local supercluster.

Acknowledgments

We would like to thank all our collaborators on this project: Carmelo Evoli, Tobias Fischer, Maurizio Giannotti, Alessandro Mirizzi, and Andreas Ringwald. It is also a pleasure to thank Davide Cadamuro for sharing the data he used to produce his own exclusion plot. This work has been supported by the German Science Foundation (DFG) within the Collaborative Research Center SFB 676 "Particles, Strings and the Early Universe."

References

[1] See, for instance: P. Sikivie, "Experimental tests of the invisible axion," Phys. Rev. Lett. **51**, 1415 (1983) [Erratum-ibid. **52**, 695 (1984)]; G. Raffelt and L. Stodolsky, "Mixing of the photon with low-mass particles," Phys. Rev. D **37**, 1237 (1988); D. Harari and P. Sikivie, "Effects of a Nambu–Goldstone boson on the polarization of radio galaxies and the cosmic microwave background," Phys. Lett. B **289**, 67 (1992).

[2] A. Payez, C. Evoli, T. Fischer, M. Giannotti, A. Mirizzi, and A. Ringwald, "Revisiting the SN1987A gamma-ray limit on ultralight axion-like particles," DESY 14-164 (to appear).

[3] J. A. Grifols, E. Massó and R. Toldrà, "Gamma-rays from SN1987A due to pseudoscalar conversion," Phys. Rev. Lett. **77**, 2372 (1996) [astro-ph/9606028].

[4] J. W. Brockway, E. D. Carlson and G. G. Raffelt, "SN1987A gamma-ray limits on the conversion of pseudoscalars," Phys. Lett. B **383**, 439 (1996) [astro-ph/9605197].

[5] T. Fischer, S. C. Whitehouse, A. Mezzacappa *et al.*, "Protoneutron star evolution and the neutrino driven wind in general relativistic neutrino radiation hydrodynamics simulations," Astron. Astrophys. **517**, A80 (2010) [arXiv:0908.1871 [astro-ph.HE]].

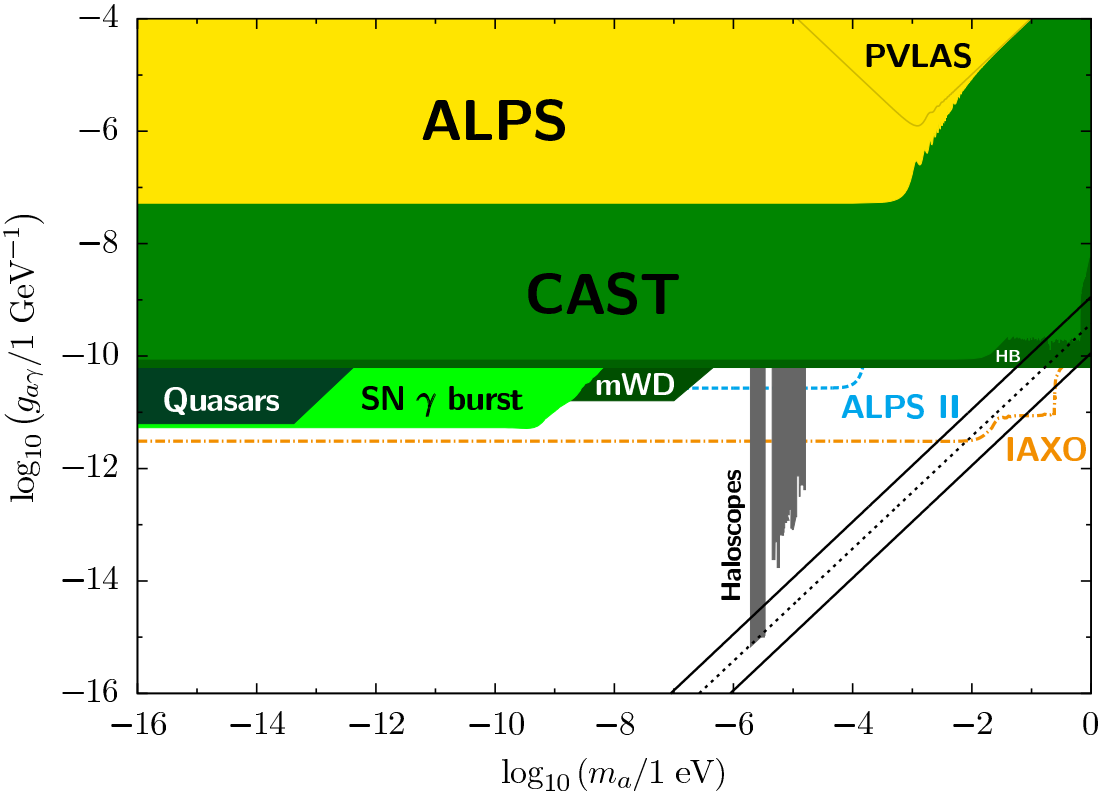

Figure 1: Update of the exclusion plot of Ref. [9] for sub-eV ALPs. We compare our updated bound with some other limits that apply in this region of the parameter space. We also indicate the projected sensitivities of the forthcoming ALPS II experiment [12] and of the proposed IAXO experiment [13].

[6] R. Jansson and G. R. Farrar, "A New model of the galactic magnetic field," Astrophys. J. **757**, 14 (2012) [arXiv:1204.3662 [astro-ph.GA]].

[7] M. S. Pshirkov, P. G. Tinyakov, P. P. Kronberg and K. J. Newton-McGee, "Deriving global structure of the Galactic magnetic field from Faraday rotation measures of extragalactic sources," Astrophys. J. **738**, 192 (2011) [arXiv:1103.0814 [astro-ph.GA]].

[8] H. Shen, H. Toki, K. Oyamatsu, K. Sumiyoshi, "Relativistic equation of state of nuclear matter for supernova and neutron star" Nucl. Phys. A **637**, 435 (1998) [arXiv:9805035 [nucl-th]].

[9] D. Cadamuro, "Cosmological limits on axions and axion-like particles," arXiv:1210.3196 [hep-ph].

[10] A. Payez, J.R. Cudell and D. Hutsemékers, "New polarimetric constraints on axion-like particles," JCAP **1207** (2012) 041 [arXiv:1204.6187 [astro-ph.CO]]; A. Payez, "Constraining ALPs with linear and circular polarisation measurements of quasar light," arXiv:1309.6114 [astro-ph.CO].

[11] J. P. Vallée, "Faraday screen and reversal of rotation measure in the Local Supercluster Plane," Astron. J. **124**, 1322 (2002).

[12] R. Bähre, B. Döbrich, J. Dreyling-Eschweiler *et al.*, "Any light particle search II Technical Design Report," JINST **8**, T09001 (2013) [arXiv:1302.5647 [physics.ins-det]].

[13] J. K. Vogel, F. T. Avignone, G. Cantatore *et al.*, "IAXO - The International Axion Observatory," arXiv:1302.3273 [physics.ins-det].

Latest Results of the OSQAR Photon Regeneration Experiment for Axion-Like Particle Search

Rafik Ballou[1,2], *Guy Deferne*[3], *Lionel Duvillaret*[4], *Michael Finger, Jr.*[5], *Miroslav Finger*[5], *Lucie Flekova*[5], *Jan Hosek*[6], *Tomas Husek*[5], *Vladimir Jary*[6], *Remy Jost*[7,8], *Miroslav Kral*[6], *Stepan Kunc*[9], *Karolina Macuchova*[6], *Krzysztof A. Meissner*[10], *Jérôme Morville*[11,12], *Pierre Pugnat*[13,14], *Daniele Romanini*[7,8], *Matthias Schott*[15], *Andrzej Siemko*[3], *Miloslav Slunecka*[5], *Miroslav Sulc*[9], *Guy Vitrant*[4], *Christoph Weinsheimer*[15], *Josef Zicha*[6]

[1]CNRS, Institut Néel, F-38042 Grenoble, France
[2]Université Grenoble Alpes, Institut Néel, F-38042 Grenoble, France
[3]CERN, CH-1211 Geneva-23, Switzerland
[4]Grenoble INP - Minatec & CNRS, IMEP-LAHC, F-38016 Grenoble, France
[5]Charles University, Faculty of Mathematics and Physics, Prague, Czech Republic
[6]Czech Technical University, Prague, Czech Republic
[7]Université Grenoble Alpes, LIPhy, F-38000 Grenoble, France
[8]CNRS, LIPhy, F-38000 Grenoble, France
[9]Technical University of Liberec, 46117 Liberec, Czech Republic
[10]University of Warsaw, Institute of Theoretical Physics, 00-681 Warsaw, Poland
[11]Université Claude Bernard Lyon-1, Institut Lumière Matière, F-69622 Villeurbanne, France
[12]CNRS, Institut Lumière Matière, F-69622 Villeurbanne, France
[13]CNRS, LNCMI, F-38042 Grenoble, France
[14]Université Grenoble Alpes, LNCMI, F-38042 Grenoble, France
[15]University of Mainz, Institute of Physics, 55128 Mainz, Germany

DOI: http://dx.doi.org/10.3204/DESY-PROC-2014-03/pugnat_pierre

The OSQAR photon regeneration experiment searches for pseudoscalar and scalar axion-like particles by the method of "Light Shining Through a Wall", based on the assumption that these weakly interacting sub-eV particles couple to two photons to give rise to quantum oscillations with optical photons in strong magnetic field. No excess of events has been observed, which constrains the di-photon coupling strength of both pseudoscalar and scalar particles down to $5.7 \cdot 10^{-8}$ GeV^{-1} in the massless limit. This result is the most stringent constraint on the di-photon coupling strength ever achieved in laboratory experiments.

1 Introduction

Embedding the Standard Model (SM) of particle physics into more general unified theories often results in postulating new elementary particles in unexplored parameter space. A number of weakly interacting sub-eV particles (WISPs) are thus predicted besides the weakly interacting massive particles (WIMPs). The most prominent example of WISPs is the axion [1], first anticipated from the breaking at the quantum level of an additional $U(1)_{PO}$ global symmetry

postulated to provide a natural solution of the strong CP problem [2]. This light spin-zero particle is one of the basic outputs of the string theory, where a number of axions and axion-like particles (ALPs), either pseudoscalar or scalar, naturally emerge [3]. It moreover constitutes a non-supersymmetric candidate of the so far unobserved dark matter in the universe [4].

The detection of WISPs requires dedicated low energy experiments, in contrast to the WIMPs which are suitably searched in the facilities of the high energy frontier such as the CERN Large Hadron Collider (LHC). A number of methods have been proposed and implemented in the recent years, based on lasers, microwave cavities, strong electromagnetic fields or torsion balances [5]. The OSQAR experiment at CERN combines high intensity laser beams and strong magnetic fields to search for WISPs at this low energy frontier. One of its setups uses the "Light Shining Through a Wall" (LSW) method for the search of the WISPs, as considered in a pioneering work which excluded ALPs with a di-photon coupling constant $g_{\mathrm{A}\gamma\gamma}$ larger than $6.7 \cdot 10^{-7}$ GeV^{-1} for ALPs masses below 10^{-3} eV [6]. These exclusion limits were extended in later LSW experiments, which now excludes ALPs with a di-photon coupling constant $g_{\mathrm{A}\gamma\gamma}$ larger than $6.5 \cdot 10^{-8}$ GeV^{-1} in the massless limit [7]. We present here, following our previous work [8], the analysis of the latest dataset taken in 2013, including advanced techniques for the data treatments. As a result we will tighten the current exclusion limits for the ALPs di-photon coupling constant down to $g_{\mathrm{A}\gamma\gamma} < 5.7 \cdot 10^{-8}$ GeV^{-1} in the massless limit.

2 Experimental Setup and Data Taking

LSW experiments are based on the combination of photon-to-WISP and WISP-to-photon double quantum oscillations and interaction weakness of the WISPs with the fermions of the SM. The method in the case of ALPs takes advantage of the ALPs di-photon coupling to create ALPs from polarized photons traversing a magnetic field, which will propagate across the optical barrier where the photons are blocked (see Fig. 1). A magnetic field of same strength is applied in the regeneration domain where the opposite process occurs meaning the ALP produces a photon that is subsequently detected by a CCD. The Lagrangian density of the interaction of a pseudoscalar ALPs field $\mathcal{A}$, such as the axion field, with the electromagnetic field $F_{\mu\nu}$ has the generic form $\mathcal{L}_{int} = -\frac{1}{4} g_{\mathrm{A}\gamma\gamma}\, \mathcal{A}\, F_{\mu\nu}\widetilde{F}^{\mu\nu} = g_{\mathrm{A}\gamma\gamma}\, \mathcal{A}\, \mathbf{E}\cdot\mathbf{B}$, where $\widetilde{F}^{\mu\nu} = \frac{1}{2}\epsilon^{\mu\nu\alpha\beta}F_{\alpha\beta}$ is the dual of $F_{\mu\nu}$ and $g_{\mathrm{A}\gamma\gamma}$ the ALP di-photon coupling constant. This points out that the photons from the incoming laser beam must be polarized parallel to the magnetic field for optimum conversion. With a scalar ALPs field $\mathcal{A}$ the interaction takes the generic form $\mathcal{L}_{int} = -\frac{1}{4} g_{\mathrm{A}\gamma\gamma}\, \mathcal{A}\, F_{\mu\nu}F^{\mu\nu} = g_{\mathrm{A}\gamma\gamma}\, \mathcal{A}\, \frac{1}{2}(\mathbf{E}^2 - \mathbf{B}^2)$, in which case the photons from the incoming laser beam must be polarized perpendicular to the magnetic field for optimum conversion. In all cases the probability of an ALP-to-photon ($A \to \gamma$) or of a photon-to-ALP ($\gamma \to A$) conversion is given by [9]:

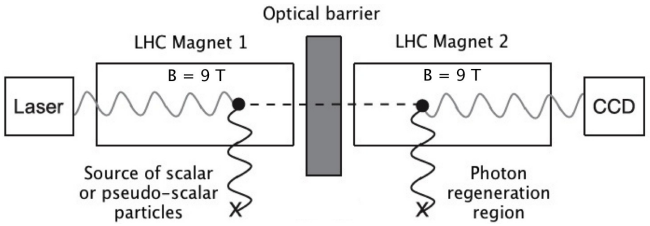

Figure 1: Principle of a LSW experiment for ALPs search.

$$P_{\gamma\leftrightarrow A} = \frac{1}{4}(g_{\mathrm{A}\gamma\gamma}BL)^2\left(\frac{2}{qL}\sin\frac{qL}{2}\right)^2 \tag{1}$$

in units of Heaviside-Lorentz system ($\hbar = c = 1$). $q = |k_\gamma - k_A|$ stands for the momentum transfer, where $k_\gamma = \omega$ is the momentum of the photon of energy ω and $k_A = \sqrt{(\omega^2 - m_A^2)}$ the momentum of the ALP of mass m_A. The concept of LSW experiments inherits the probability given in Eq. (1) twice so the overall probability for photon regeneration is $P_{\gamma\to A\to\gamma} = (P_{\gamma\leftrightarrow A})^2$. This one being proportional to the $4-th$ power of (BL) stresses the necessity of the strongest magnetic field B over the longest optical path length L. Taking η as the photon detection efficiency and P as the optical power, the flux of detected reconverted photons is then given by

$$\frac{dN}{dt} = \frac{P}{\omega}\eta \left(P_{\gamma\leftrightarrow W}\right)^2 \tag{2}$$

The experimental setup of the OSQAR photon regeneration consists of two LHC dipole magnets separated by an optical barrier as schematized in Fig. 1. Each magnet is cooled down to 1.9 K with superfluid He and provides an uniform transverse magnetic field with a strength of 9 T over a magnetic length of 14.3 m. A diode-pumped solid-state laser from Coherent, Inc. has been used to deliver 15 W of optical power at a single wavelength of 532 nm (2.33 eV). The photon beam is linearly polarized with a vertical orientation parallel to the magnetic field, which is suited for the search of axions and pseudoscalar ALPs. A $\lambda/2$ wave-plate with antireflective coating layers oriented at 45° was inserted at the laser exit to align the polarization in the horizontal direction for the search of scalar ALPs. The laser light after the second magnet was focussed by an optical lens on a Spectrum One LN_2-cooled CCD detector from Instrument SA, Inc. The CCD chip is composed by a 2D array of 1152×298 square pixels with a $26\,\mu m$ size. Dark current and readout noise are given as 1 - 3 e^-/pixel/hour and 4 - 10 e^- rms/pixel. The overall quantum efficiency, including the gain factor, is measured to $33.7 \pm 0.7\%$.

The data-taking was performed in August 2013. Each run consisted typically of nine *frames* of recorded signal distribution on the CCD. The first three frames are taken during one minute with strongly attenuated laser power and without the optical barrier to record the laser position on the CCD, which defines the expected signal region and ensures the alignment of the experimental setup. The laser power then is set to maximum and the optical barrier positioned for the actual measurements. To receive as high as possible signal to noise ratio, with acceptable risk of cosmic rays contamination of the region of interest, three consecutive frames were recorded with exposure time of 2700 s for each. The run ends by removing the optical barrier and recording again the laser position on the CCD in three independent frames of one minute. Considering conservatively only runs with very stable laser position on the CCD the whole collected data amounts to integrated measuring time of 19.5 h for pseudoscalar ALPs search and 26.25 h for scalar ALPs search. Background frames were also recorded with laser beam switched off.

3 Data Analysis

The laser-beam was focused on one pixel of the CCD. It however might show a tiny displacement, owing to thermal or mechanical noise around the experimental installation. This was scrutinized to avoid enlarging the area of the possible reconverted photons on the CCD, which degrades the precision of the data analysis. No displacement was observed during the three consecutive one minute recorded laser positions either before or after signal recording. Hence the signal region is defined per run by the recorded laser positions before and after the signal exposure. If no displacement is observed then the signal region is exactly one pixel wide. If the laser-position before and after the signal recording are apart then the sensitive signal area is determined by a linear interpolation in time. The runs with a displacement exceeding 2 pixels are discarded.

The basic idea of the data analysis is to compare the recorded photon counts in the signal region to the recorded photon counts outside this region, i.e. the background region not exhibited to possible ALPs signals. The sensitivity of the experiment is determined by the width of the distribution of these background counts, which thus must be first cleaned from contamination by cosmic ray events and corrected for possible defect of flatness. An impact of cosmic ray reveals itself as a series of contiguous pixels with photon counts exceeding a certain threshold in terms of standard deviation. Cosmic ray events are removed in each data frame separately. A median filtered copy is calculated, with fixed median-filter kernel size of 8×8 pixels, for the purpose of replacing areas of hot pixels in the original data frame with its median filtered correspondents. The signal region is explicitly excluded from this procedure in order to preserve possible ALPs signatures. The recorded frames also show a wavelike structure evolving over the whole CCD chip, as displayed in Fig. 2, which was confirmed to be inherent to the used CCD detector by recorded frames without laser beam. It was important to correct this lack of flatness since it decreases the sensitivity of the experiment by broadening the width of the distribution of the background counts. A filter technique based on Fast-Fourier-Transformations (FFT) has been applied to each data frame individually. The two dimensional FFT of the frame is created and the power spectrum $|A(f_x, f_y)|^2$ is calculated[1]. A subset $\Omega \subset \{\, A(f_x, f_y)\,\}$ of the frequency spectrum, subject to cause the wavelike structure in the spatial domain is identified by comparing the amplitudes with an artificial amplitude spectrum of pure gaussian white noise with same mean and standard deviation (Fig. 3 Left). $\Omega = \{A(f_x, f_y) \;\big|\; |A(f_x, f_y)|^2 > \text{cutOff}\,\}$ where *cutOff* is defined as the highest amplitude occur-

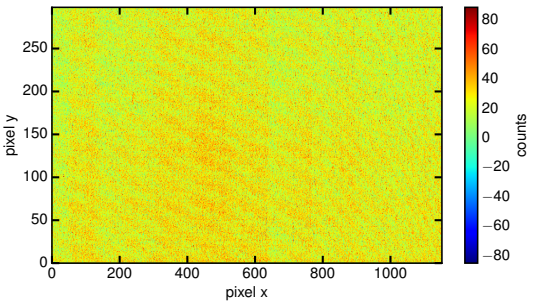

Figure 2: Example frame after removal of the contamination by cosmic ray events. A wavelike structure spread over whole chip reveals itself.

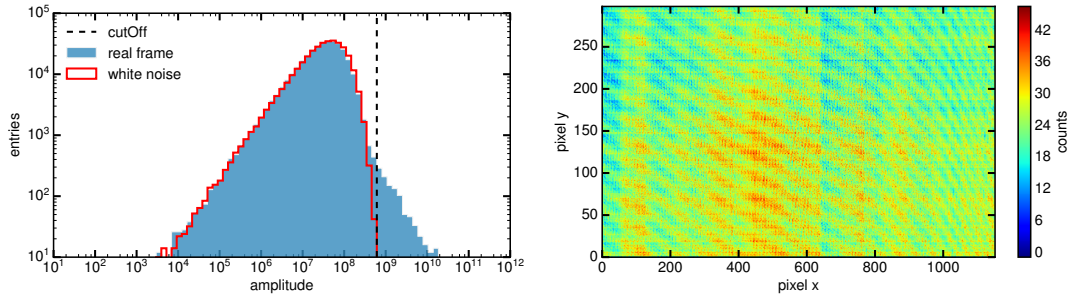

Figure 3: Left: Comparison of the FFT amplitude spectrum of a real frame (blue) with gaussian white noise (red). Right: Inverse transform into spatial domain of the subset Ω (see text).

[1]It is pointed out that the frequency spectrum of a real valued distribution is point symmetric to the origin frequency $A(0,0)$, which corresponds to the sum of all pixels in spatial domain. $A(0,0)$ may represent the average depending on the normalization convention of the FFT.

ring in the white noise spectrum and is individually determined for each frame. The frequency set Ω is then transformed back into spatial domain exposing the shape of the wavelike structure (Fig. 3 Right) and is subtracted from the original data frame. Since the origin frequency $A(0,0)$ is per definition contained in Ω, this procedure also results in the normalization of the data frames in terms of setting their average pixel count to zero. To ensure that no possible ALPs signal will be impacted by this procedure, an artificial 2σ *fake signal* imposed to the signal region of a dedicated copy of the frame is checked to be still present after the filtering.

The whole treatment, i.e. cosmic events removal and defect of flatness correction, was tested on the background frames to which an artificial signal was imposed corresponding to $m_A = 10^{-4}$ eV and $g_{A\gamma\gamma} = 8.5 \cdot 10^{-8}$ GeV^{-1}. It has then been applied to all data-frames, corresponding to a specific laser polarization. The distribution of the recorded photon count in an example background region and also the imposed signal are shown in Fig. 4. The counts in the signal regions are evaluated and the resulting background distributions are fitted by the sum of two gaussian functions with a shared parameter for the mean value. Typical χ^2/n.d.f values resulting from the fitting procedure are in the range of 0.8 to 1.5 documenting a good parametric description.

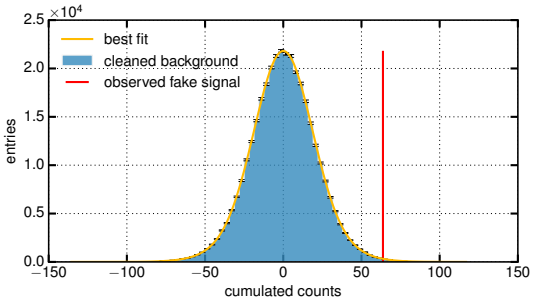

Figure 4: An example of background distribution obtained after cosmic events removal and defect of flatness correction (blue) and signal counts (red) of beforehand imposed fake signal.

4 Exclusion Limits

No excess of counts is detected in the signal region whatever the polarization of the photons, parallel or perpendicular to the magnetic field. Exclusion limits on the ALP di-photon coupling strength $g_{A\gamma\gamma}$ and the ALP mass m_A were then derived via Eq. (1) & Eq. (2). The 95% confidence limits (C.L.) are based on the Bayesian inference with the likelihood function $\mathcal{B} = \prod_i \mathcal{B}_i(n_{obs;i}|\frac{dN}{dt}) \cdot \pi(\frac{dN}{dt})$ and a flat prior $\pi(dN/dt)$ for the signal parameter. The index i runs over the integer number of runs corresponding to a certain polarization state and $\mathcal{B}_i(n_{obs;i}|\frac{dN}{dt})$ represents the background parametrization of the i-th frame including an additional poissonian signal contribution of expectation value dN/dt times the frames exposure time. From the posterior distribution for the signal parameter dN/dt the 95%C.L. limit on the reconverted photon flux can be set. Table 1 summarizes the obtained values and the resulting limit on $g_{A\gamma\gamma}$ for a vanishing ALP mass ($m_A \to 0$). The functional relation of Eq. (1) leads to limits of $g_{A\gamma\gamma}$ in dependence of the ALP mass m_A as illustrated in Fig. 5 for the scalar- and pseudoscalar search, where also results of the previous experiments are shown.

		PSEUDOSCALAR	SCALAR
$dN_{95\%C.L.}/dt$	[Hz]	$2.07 \cdot 10^{-3}$	$2.14 \cdot 10^{-3}$
$g_{A\gamma\gamma}^{m_A \to 0}$	[Gev^{-1}]	$5.71 \cdot 10^{-8}$	$5.76 \cdot 10^{-8}$

Table 1: 95%C.L. limit on flux of reconverted photons and resulting limit on di-photon coupling constant in massless limit.

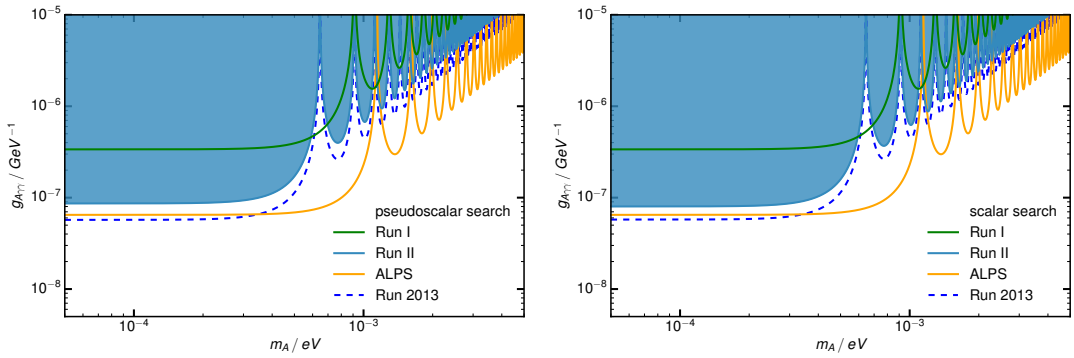

Figure 5: Exclusion limits inferred from the pseudoscalar and scalar search in vacuum for the present experiment compared to previous runs and the latest ALPS result in vacuum [7].

5 Conclusion

We have reported on the latest results obtained from a conservative analysis of the OSQAR LSW experiment for ALPs search conducted in the year 2013. No signal was detected. The 95% derived confidence limits exclude di-photon coupling strength above $5.7 \cdot 10^{-8}$ GeV^{-1} in the massless limit, giving the so far most stringest constraints on ALPs in LSW-type experiments.

6 Bibliography

References

[1] S. Weinberg, "A New Light Boson?", Phys. Rev. Lett. **40**, 223 (1978); F. Wilczek, "Problem of Strong P and T Invariance in the Presence of Instantons", Phys. Rev. Lett. **40**, 279 (1978).

[2] R. D. Peccei and H. R. Quinn, "CP Conservation in the Presence of Pseudoparticles", Phys. Rev. D **16**, 1791 (1977);

[3] P. Svrek, and E. Witten, "Axions in string theory", J. High Energy Phys. **06**, 051 (2006), arXiv:0605206 [hep-th]; M. Cicoli, M. Goodsell and A. Ringwald, "The type IIB string axiverse and its low-energy phenomenology", J. High Energy Phys. **2012**, (10) 146 (2012), arXiv:1206.0819 [hep-th].

[4] R. Bradlay, *et al.*, "Microwave cavity searches for dark-matter axions", Rev. Mod. Phys. **75**, 777-817 (2003); P. Arias, *et al.*, "WISPy Cold Dark Matter", J. Cosmol. Astropart. Phys. **06**, 013 (2012), arXiv:1201.5902 [hep-ph]; A. Ringwald, "Ultralight Particle Dark Matter", arXiv:1310.1256 [hep-ph].

[5] J. Jaeckel and A. Ringwald, "The Low-Energy Frontier of Particle Physics", Ann. Rev. Nucl. Part. Sci. **60**, 405 (2010), arXiv:1002.0329 [hep-ph]; R. Essig *et al.*, Report of the Community Summer Study 2013 (Snowmass) Intensity Frontier "New Light, Weakly Coupled Particles", arXiv:1311.0029 [hep-ph].

[6] R. Cameron *et al.*, "Search for nearly massless, weakly coupled particles by optical techniques", Phys. Rev. D **47**, 3707 (1993)

[7] K. Ehret *et al.* (ALPS collaboration),"New ALPS Results on Hidden-Sector Lightweights," Phys. Lett. B **689**, 149 (2010), arXiv:1004.1313 [hep-ex].

[8] P. Pugnat, *et al.* (OSQAR collaboration), "Search for Weakly Interacting Sub-eV Particles with the OSQAR Laser-based Experiment: Results and Perspectives", Eur. Phys. J. B **74**, 3027 (2014).

[9] P. Sikivie, Phys. Rev. Lett. 51 1415 (1983); K. Van Bibber, N.R. Dagdeviren, S.E. Koonin, A.K. Kerman and H.N. Nelson, Phys. Rev. Lett. 59 759 (1987); P. Arias *et al.*, Phys. Rev. D **82**, 115018 (2010).

Production and Evolution of Dark Matter Axions in the Early Universe

Ken'ichi Saikawa[1], *Takashi Hiramatsu*[2], *Masahiro Kawasaki*[3,4], *Toshifumi Noumi*[5], *Ryosuke Sato*[6], *Toyokazu Sekiguchi*[7], *Masahide Yamaguchi*[1]

[1]Department of Physics, Tokyo Institute of Technology, Tokyo, Japan
[2]Yukawa Institute for Theoretical Physics, Kyoto University, Kyoto, Japan
[3]Institute for Cosmic Ray Research, The University of Tokyo, Chiba, Japan
[4]Kavli Institute for the Physics and Mathematics of the Universe (WPI), Todai Institutes for Advanced Study, The University of Tokyo, Chiba, Japan
[5]Mathematical Physics Laboratory, RIKEN Nishina Center, Saitama, Japan
[6]Theory Center, High Energy Accelerator Research Organization (KEK), Ibaraki, Japan
[7]Helsinki Institute of Physics, University of Helsinki, Finland

DOI: http://dx.doi.org/10.3204/DESY-PROC-2014-03/saikawa_kenichi

Production mechanisms and interaction properties of dark matter axions are investigated. The decay of string-wall systems gives an additional contribution to the dark matter abundance, which implies that the axion becomes dark matter in the high mass range of $\mathcal{O}(10^{-4}$–$10^{-2})$eV. The structure of gravitational self-interactions of coherently oscillating axions is also evaluated, and it turns out that their self-interaction rate can be relevant in their late time evolution.

1 Introduction

The axion [1, 2] is a hypothetical particle predicted by the Peccei-Quinn (PQ) mechanism as a solution of the strong CP problem of quantum chromodynamics (QCD) [3, 4]. Since it has tiny couplings with ordinary matter and it is highly non-relativistic at the time when it was produced, it can be a good candidate of the cold dark matter of the universe. Identifying the cosmological behavior of the dark matter axions is important not only to understand the early history of the universe, but also to distinguish them from other dark matter candidates.

In this work, we investigate the production and evolution of the axions in the early universe. For the cold dark matter axions, there are three major production mechanisms: One is the misalignment mechanism [5, 6, 7], which induces the coherent oscillation of the axion field. The second is the production from global strings [8], which occurs during the epoch between the PQ phase transition and the QCD phase transition. The last one is the production from the string-wall systems [9, 10], which occurs after the QCD phase transition. The latter two become relevant only if the PQ symmetry is broken after inflation. In the following sections, we first discuss the recent development on the estimation of the abundance of axions produced from the string-wall systems. After that, we switch our attention to the evolution of axions, and address the question whether they form a Bose-Einstein condensate (BEC).

2 Axion production from topological defects

In the invisible axion models [11], we must introduce an additional $SU(2)_L \times U(1)_Y$ singlet scalar field Φ. Let us call this field the PQ field. This field is charged under the global $U(1)_{\rm PQ}$ symmetry, which is spontaneously broken due to the potential of the form $V(\Phi) = \frac{\lambda}{4}(|\Phi|^2 - \eta^2)^2$. This occurs when the temperature of the universe becomes less than the scale η, and at that time the line-like objects called strings are formed. Then, the axion field $a(x)$ can be identified as the phase direction of the PQ field: $\Phi = |\Phi| e^{ia(x)/\eta}$.

The axion acquires a mass m_a due to the non-perturbative effect of QCD when the temperature of the universe becomes $T \lesssim \mathcal{O}(1)$GeV. We can model this effect by considering the following potential for the axion field:

$$V(a) = \frac{m_a^2 \eta^2}{N_{\rm DW}^2} \left(1 - \cos\left(N_{\rm DW} \frac{a}{\eta}\right)\right), \tag{1}$$

where $N_{\rm DW}$ is an integer number called the domain wall number. There are $N_{\rm DW}$ degenerate vacua, and $N_{\rm DW}$ domain walls are formed around the boundary of different vacua [12]. Since the field a is the phase direction of Φ, these domain walls are attached to strings. We call such configurations the string-wall systems.

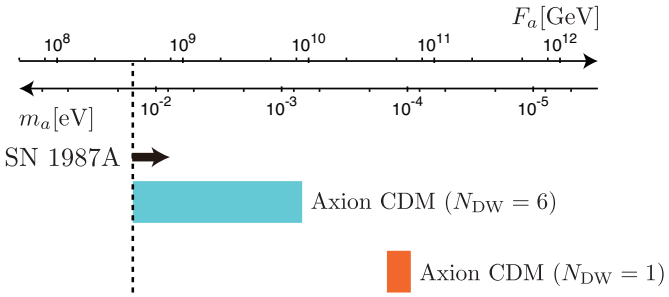

Figure 1: The mass ranges where the QCD axion explains the cold dark matter for the models with $N_{\rm DW} = 1$ (orange interval) and $N_{\rm DW} = 6$ (light blue interval).

The subsequent history after the QCD phase transition is different according to the value of the domain wall number. If $N_{\rm DW} = 1$, the string-wall systems are unstable, and they decay immediately after the formation. On the other hand, if $N_{\rm DW} > 1$, they are stable and come to overclose the universe, causing a problem in the standard cosmology [13]. This problem can be avoided by introducing an explicit symmetry breaking term in the potential of the PQ field [12], which induces the annihilation of domain walls at a late time.

We investigate these scenarios based on the lattice simulations of the PQ field. The simulations are executed by solving the classical field equation of Φ in the expanding universe. Using the results of the simulations, we estimate the spectrum of axions radiated from the string-wall systems. In the models with $N_{\rm DW} = 1$, the inclusion of the wall decay contribution [9] leads to the upper bound on the axion decay constant $F_a \lesssim (4.2\text{–}6.5) \times 10^{10}$GeV [14], which corresponds to the lower bound on the axion mass: $m_a \gtrsim (0.9\text{–}1.4) \times 10^{-4}$eV. The constraint becomes more severe for the models with $N_{\rm DW} > 1$, but there still exists a loophole if we allow a mild tuning of a theoretical parameter [10]. We note that there is a large systematic uncertainty on the determination of the lifetime of the domain walls in the models with $N_{\rm DW} > 1$ [15]. This kind of uncertainty is not reduced straightforwardly even in the recent numerical simulations with improved dynamical ranges [14].

In Fig. 1, we show the parameter range in which the axion can be dominant component of the cold dark matter for the models with $N_{\rm DW} = 1$ and $N_{\rm DW} = 6$. Here, we also show the lower bound on the axion decay constant $F_a > 4 \times 10^8$GeV obtained from the observation of

the supernova (SN) 1987A [16]. Since the decay of the string-wall systems amplifies the energy density of dark matter axions, they explain the cold dark matter in the higher mass range [$m_a \approx \mathcal{O}(10^{-4}$–$10^{-2})$eV]. More extensive studies will be required to reduce the uncertainties of these theoretical predictions.

3 Evolution of axion dark matter in the condensed regime

Next, let us turn our attention to the evolution of the cold dark matter axions. Although their mass is as small as $\mathcal{O}(10^{-4}$–$10^{-2})$eV, they have an extremely small velocity dispersion because of the non-thermal production mechanisms. The smallness of the velocity dispersion implies that they have a large occupation number in the phase space. Regarding this fact, the authors of Refs. [17, 18] claimed that the axions exist in the form of a BEC. The point in Ref. [18] was that the BEC is defined in the thermal equilibrium state and that the system of dark matter axions can reach the thermal equilibrium due to the gravitational self-interactions. This phenomenon might lead to some observable signatures such as effects on the phase space structure of galactic halos [19] and those on the cosmological parameters [20].

Our aim here is to discuss the above issues more carefully. At this stage, we just expect that the system of dark matter axions develops toward the thermal equilibrium when the transition rate Γ between different momentum states exceeds the cosmic expansion rate H. The rate Γ can be estimated in terms of the time derivative of the expectation value of the operator $\mathcal{N}_{\mathbf{p}}$ corresponding to the occupation number of axions with the three-momentum $\mathbf{p}$. As a result of the calculation in the second quantized field theory, we obtain the following expression [21]:

$$\Gamma \simeq \frac{4\pi G m_a^2 n_a}{(\delta p)^2}, \tag{2}$$

where G is the Newton's constant, n_a is the number density of axions, and δp is their typical momentum dispersion. This rate indeed exceeds the expansion rate when the temperature of the universe becomes $T \sim$ keV [18, 21]. Although the above result was obtained for the Newtonian approximation for the gravitational interactions, we can obtain the similar result when we take account of the general relativistic corrections [22].

We note that the estimation given by Eq. (2) holds only if the initial state is given by the coherent state [21]. With the assumption that the axion field produced by the misalignment mechanism is described as the coherent state, we conclude that the gravitational self-interaction is relevant only for the misalignment axions. This result implies that the misalignment axions evolve differently from those produced by strings and domain walls, and it will be important to see how this difference affects the dynamics of Large Scale Structure [23].

4 Summary

We have investigated the production and evolution of axions in the early universe. Their total abundance is given by the sum of three contributions: axions produced from the misalignment mechanism, the decay of strings, and the decay of string-wall systems. We showed that the contribution from the decay of string-wall systems can be considerable and that the axion can be responsible for dark matter in the high mass range. We also showed that the gravitational self-interaction of the misalignment axions becomes relevant in their late time evolution. Further studies are needed to evaluate the observational consequences of these results.

Acknowledgments

K. S. is supported by the Japan Society for the Promotion of Science (JSPS) through research fellowships. Numerical computation in this work was carried out at the Yukawa Institute Computer Facility.

References

[1] S. Weinberg, "A New Light Boson?," Phys. Rev. Lett. **40**, 223 (1978).

[2] F. Wilczek, "Problem of Strong P and T Invariance in the Presence of Instantons," Phys. Rev. Lett. **40**, 279 (1978).

[3] R. Peccei and H. R. Quinn, "CP Conservation in the Presence of Instantons," Phys. Rev. Lett. **38**, 1440 (1977).

[4] R. Peccei and H. R. Quinn, "Constraints Imposed by CP Conservation in the Presence of Instantons," Phys. Rev. **D16**, 1791 (1977).

[5] J. Preskill, M. B. Wise, and F. Wilczek, "Cosmology of the Invisible Axion," Phys. Lett. **B120**, 127 (1983).

[6] L. Abbott and P. Sikivie, "A Cosmological Bound on the Invisible Axion," Phys. Lett. **B120**, 133 (1983).

[7] M. Dine and W. Fischler, "The Not So Harmless Axion," Phys. Lett. **B120**, 137 (1983).

[8] T. Hiramatsu, M. Kawasaki, T. Sekiguchi, M. Yamaguchi, and J. Yokoyama, "Improved estimation of radiated axions from cosmological axionic strings," Phys. Rev. **D83**, 123531 (2011) [arXiv:1012.5502 [hep-ph]].

[9] T. Hiramatsu, M. Kawasaki, K. Saikawa, and T. Sekiguchi, "Production of dark matter axions from collapse of string-wall systems," Phys. Rev. **D85**, 105020 (2012), Erratum-ibid. **D86**, 089902 (2012) [arXiv:1202.5851 [hep-ph]].

[10] T. Hiramatsu, M. Kawasaki, K. Saikawa, and T. Sekiguchi, "Axion cosmology with long-lived domain walls," JCAP 1301 (2013) 001 [arXiv:1207.3166 [hep-ph]].

[11] J. E. Kim, "Weak Interaction Singlet and Strong CP Invariance," Phys. Rev. Lett. **43**, 103 (1979).

[12] P. Sikivie, "Of Axions, Domain Walls and the Early Universe," Phys. Rev. Lett. **48**, 1156 (1982).

[13] Y. Zeldovich, I. Y. Kobzarev, and L. Okun, "Cosmological Consequences of the Spontaneous Breakdown of Discrete Symmetry," Sov. Phys. JETP 40, 1 (1974).

[14] M. Kawasaki, K. Saikawa, and T. Sekiguchi, "Axion dark matter from topological defects," arXiv:1412.0789 [hep-ph].

[15] T. Hiramatsu, M. Kawasaki, and K. Saikawa, "Evolution of String-Wall Networks and Axionic Domain Wall Problem," JCAP 1108 (2011) 030 [arXiv:1012.4558 [astro-ph.CO]].

[16] G. G. Raffelt, "Astrophysical axion bounds," Lect. Notes Phys. **741**, 51 (2008) [arXiv:hep-ph/0611350].

[17] P. Sikivie and Q. Yang, "Bose-Einstein Condensation of Dark Matter Axions," Phys. Rev. Lett. **103**, 11301 (2009) [arXiv:0901.1106 [hep-ph]].

[18] O. Erken, P. Sikivie, H. Tam, and Q. Yang, "Cosmic axion thermalization," Phys. Rev. **D85**, 063520 (2012) [arXiv:1111.1157 [astro-ph.CO]].

[19] N. Banik and P. Sikivie, "Axions and the Galactic Angular Momentum Distribution," Phys. Rev. **D88**, 123517 (2013) [arXiv:1307.3547 [astro-ph.GA]].

[20] O. Erken, P. Sikivie, H. Tam, and Q. Yang, "Axion Dark Matter and Cosmological Parameters," Phys. Rev. Lett. **108**, 061304 (2012) [arXiv:1104.4507 [astro-ph.CO]].

[21] K. Saikawa and M. Yamaguchi, "Evolution and thermalization of dark matter axions in the condensed regime," Phys. Rev. **D87**, 085010 (2013) [arXiv:1210.7080 [hep-ph]].

[22] T. Noumi, K. Saikawa, R. Sato, and M. Yamaguchi, "Effective gravitational interactions of dark matter axions," Phys. Rev. **D89**, 065012 (2014) [arXiv:1310.0167 [hep-ph]].

[23] S. Davidson, "Axions: Bose Einstein Condensate or Classical Field?," arXiv:1405.1139 [hep-ph].

A new test of the transparency of the Universe

Grigory Rubtsov, Sergey Troitsky

Institute for Nuclear Research of the Russian Academy of Sciences, Moscow, Russia

DOI: http://dx.doi.org/10.3204/DESY-PROC-2014-03/troitsky_sergey

We present a brand new quantitative test of the degree of transparency of the Universe to gamma rays, confronting existing models of pair production on the extragalactic background light with observational data. We discuss this result in the context of various scenarios of photon mixing with axion-like particles.

In this note, written along the lines of a poster presented at the Patras workshop and based on Ref. [1], we give a proof that the so-called "infrared-TeV crisis" is back: gamma-ray observations of distant blazars indicate that the Universe is much more transparent for energetic photons than suggested by the lowest-absorbtion models. Indeed, energetic gamma rays scatter on soft background radiation when propagating through the Universe, producing electron-positron pairs [2]. Gamma rays with energies between 100 GeV and a few TeV interact mostly with infrared background photons whose amount is poorly known experimentally but safely constrained from below by account of the contribution of observed light from known galaxies [3]. The expected opacity of the intergalactic space limits the mean free path of TeV gamma rays to dozens of Megaparsecs. However, TeV photons from numerous more distant sources have been detected [4]. One does not know what flux was emitted in the source, so the observation of photons may be made consistent with strong absorbtion if the emitted spectrum breaks upwards at high energies. This interpretation works in every particular case, though it requires presently unknown mechanisms to work in the sources [5]. Here we show that this interpretation is not supported by the analysis of the ensemble of all observed sources. In the frameworks of an infrared-background model with the lowest opacity [6], we reconstruct the emitted spectra of distant blazars and find that upward spectral breaks appear precisely at those energies where absorption effects are essential. Since these energies are very different for similar sources located at various distances, we conclude that the breaks are nothing but artefacts of the incorrect account of absorption and, therefore, the opacity of the Universe for gamma rays is overestimated even in the most conservative model. This implies that some novel physical or astrophysical phenomena should affect long-distance propagation of gamma rays.

All observed distant sources are blazars, that is belong to a certain class of active galactic nuclei whose relativistic jets point to the observer. While the mechanism of high-energy emission of blazars is disputable, the bulk of their spectral energy distribution is well studied. The overall shape of the distribution is to a large extent determined by the energy scale of the electron population. One often distinguishes two large classes of blazars, namely flat-spectrum radio quasars (FSRQs) with the synchrotron peak in the radio to infrared and BL Lac type objects (BLLs) with the peak in optical to X-ray bands. However, deabsorbed spectra of distant blazars often exhibit high-energy hardening which is not seen in nearby objects. Even a visual inspection of the deabsorbed blazar spectra leads to a conclusion that both the position and

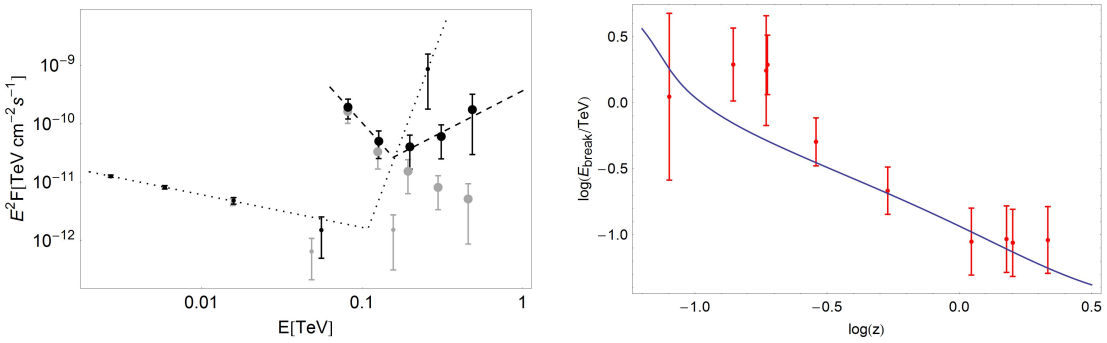

(a) (b)

Figure 1: (a). Example of two spectra with breaks: 3C 279 (redshift $z = 0.536$, large points) and PKS J0730-1141 (redshift $z = 1.591$, small points). Grey points represent the observed spectrum, dark points are corrected for the EBL absorption with the most conservative model. (b). Positions of individual significant upward breaks versus redshift z. The line represents the energy $E_0(z)$ at which the optical depth with respect to the pair production $\tau = 1$.

the strength of the spectral hardening differ for similar blazars located at different distances, see Fig. 1(a) for an example.

We consider a sample of blazars, located at various distances but with fluxes measured beyond the energies where absorption on EBL is significant, compiled from published data of atmospheric Cerenkov telescopes by making use of the TeVCat catalog [4] and supplemented with a set of more distant objects observed by Fermi. For each of the objects in the sample, we construct a deabsorbed spectrum.

First, we fit each spectrum with a power law and, independently, with two power laws with a break, keeping the break position arbitrary. We select these (few) objects for which the fit with a break is better than without it and the break corresponds to a spectral hardening (it is not so for a few nearby sources). Then we compare the break positions with the values of energy at which the absorption is expected to be significant (namely, with the energy E_0 for which the optical depth due to pair production $\tau = 1$). The results are shown in Fig. 1(b), where we plot the positions of these significant upward breaks versus the redshift z. The break positions are statistically consistent with $E = E_0$. A further test of this relation constitutes the main part of our study and results in our principal conclusion.

We assume that the position of the break is fixed at $E = E_0$ and study how the strength of the break, determined as the difference $\Delta\Gamma$ between power-law indices below and above the break, depends on z. In this approach, we use the information from all sources, even if their individual breaks are not statistically significant. The results are presented in Fig. 2, together with the best-fit approximation. The absence of distance-dependent spectral hardening is excluded at the 12.4 standard deviations (12.4σ) level. This gives a serious argument in favour of the hypothesis that the upward breaks in deabsorbed blazar spectra are unphysical and are caused by incorrect account of absorbtion. Potential systematic errors and statistical biases are discussed in Ref. [1]; it is unlikely that they might affect our result.

Among previous studies of gamma-ray blazars in the context of the EBL opacity, two groups went beyond the discussion of individual objects and used a sample, like we do here. The first

one is the Fermi LAT collaboration [9] which discovered a spectrum suppression by comparison of stacked BLL spectra grouped in large redshift bins, interpreted as the effect of the EBL absorption. This result does not exclude the opacity below the lowest model and even favours it for high energies, cf. Fig. 1 of Ref. [9]. Horns and Meyer [10] concentrated on the sample of blazars detected at very large optical depths, $\tau \geq 2$, and found a 4-sigma evidence for the pair-production anomaly which lead them to conclusions similar to ours. The differences of our approach from Ref. [10] are in the choice of the sample, in the use of simultaneous data only and in the method of the analyzis. They also did not take into account the shift of the mean energy in the bin in the deabsorbed versus observed spectrum, important at large opacities.

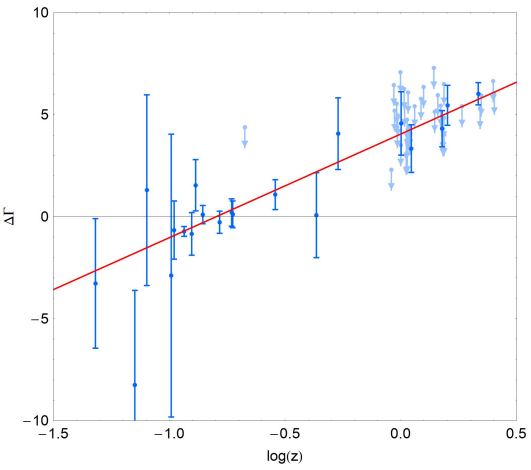

Figure 2: Value $\Delta\Gamma$ of the break in the spectrum deabsorbed with the most conservative model, assumed to happen at $E = E_0$, versus redshift z. The line gives the best fit; its slope is non-zero at the 12σ significance.

How to explain the fact that the most conservative EBL model is likely to overestimate the absorption? The probability of the pair-production process cannot be questioned: it is calculated in quantum electrodynamics at the center-of-mass energies where no unknown effects are expected to contribute, and has been measured experimentally. The downward change in the amount of target photons is hardly acceptable because the EBL model we use is already saturated by lower limits of Ref. [3]. One should consider new processes which affect the observed photon flux and are not accounted for in the absorption model which takes into account pair production only. Several models of this kind have been suggested; they invoke either new physical processes or very unusual astrophysical assumptions.

Two quite different scenarios invoke similar extensions of the particle-physics Standard model, the so-called axion-like particles (ALPs; see Ref. [11] for a review and a list of references). In external magnetic fields, these particles may convert to photons and vice versae. Applied to our problem, this conversion may happen [12] in intergalactic magnetic fields provided they are sufficiently strong ($> 10^{-9}$ G). In this regime, VHE photons convert to ALPs and back during propagation in a way similar to neutrino oscillations. In a rough approximation and for the maximal possible photon/ALP mixing, the path becomes longer by a factor of $\sim 3/2$. Assuming this in our analysis, we obtain the reduction in significance of the distance dependence of breaks from $\sim 12\sigma$ to $\sim 6\sigma$ which suggests that this scenario may not explain the entire observed effect, though a detailed analyzis is required for a firm conclusion.

In the second scenario, intergalactic magnetic fields are assumed to be weaker, $\lesssim 10^{-10}$ G, and therefore insufficient for the photon/ALP transitions which may happen instead in the regions of stronger field around both the source and the observer. The conversion may happen on magnetic fields of galaxies [13], galaxy clusters or superclusters [14]. A rough account of this mechanism in our study reduces the effect to $\sim 2\sigma$ thus making it insignificant. We conclude that our result may be explained in this scenario.

The third option [15] does not require new physics beyond the Standard Model; however,

it invokes some non-conventional astrophysical assumptions. In this approach, a competitive source of VHE photon *production* along the path from the source to the observer feeds the photon flux which is, in parallel, absorbed in the usual way. These additional photons may be created in interactions of ultra-high-energy cosmic protons, which are assumed, in this model, to be produced in the very same source, with the background radiation. It is not possible to perform a simple rough test of this model in our study because this scenario is necessarily based on rather arbitrary parameters of the hypothetical proton flux. This scenario requires very low values of the intergalactic magnetic fields, $\lesssim 10^{-14}$ G, otherwise charged particles would be deflected and secondary photons would not point back to the source.

While detailed tests of these scenarios versus our results will be presented elsewhere, our preliminary considerations thus favour the ALP convertion/reconvertion scenario [13, 14] for the explanation of the effect we observe.

S.T. thanks the organizers of the Patras workshop for an excellent scintific meeting they built up. The authors are indebted to O. Kalashev for discussions. This work was supported in part by the RFBR grant 13-02-01293 (G.R. and S.T.), by the Dynasty foundation (G.R.), by the grants of the President of Russia MK-1170.2013.2 (G.R.) and NS-2835.2014.2 (G.R. and S.T.). We acknowledge the use of data and software provided by the Fermi Science Support Center.

References

[1] Rubtsov, G. & Troitsky, S. Breaks in gamma-ray spectra of distant blazars and transparency of the Universe *JETP Lett.* **100**, 397-401 (2014) [arXiv:1406.0239].

[2] Nikishov, A.I. Absorption of high-energy photons in the Universe. *Sov. Phys. JETP* **14**, 393-394 (1962).

[3] Keenan, R.C., Barger, A.J., Cowie, L.L. & Wang, W.-H. The Resolved Near-infrared Extragalactic Background. *Astrophys. J.* **723**, 40-46 (2010) [arXiv:1102.2428].

[4] Wakely, S.P. & Horan, D. TeVCat, http://tevcat.uchicago.edu/ .

[5] Archambault,S. *et al.* [VERITAS and Fermi LAT Collaborations]. Deep Broadband Observations of the Distant Gamma-ray Blazar PKS 1424+240. *Astrophys. J.* **785**, L16 (2014) [arXiv:1403.4308].

[6] Gilmore, R.C., Somerville, R.S., Primack, J.R. & Dominguez, A. Semi-analytic modeling of the EBL and consequences for extragalactic gamma-ray spectra. *Mon. Not. Roy. Astron. Soc.* **422**, 3189-3207 (2012) [arXiv:1104.0671].

[7] Hauser, M.G. & Dwek, E. The cosmic infrared background: measurements and implications. *Ann. Rev. Astron. Astrophys.* **39**, 249-307 (2001) [astro-ph/0105539].

[8] Costamante, L. Gamma-rays from Blazars and the Extragalactic Background Light. *Int. J. Mod. Phys. D* **22**, 1330025 (2013) [arXiv:1309.0612].

[9] Ackermann, M. *et al.* [Fermi-LAT Collaboration], The Imprint of The Extragalactic Background Light in the Gamma-Ray Spectra of Blazars. *Science* **338**, 1190-1192 (2012) [arXiv:1211.1671].

[10] Horns, D. & Meyer, M. Indications for a pair-production anomaly from the propagation of VHE gamma-rays. *JCAP* **1202**, 033 (2012) [arXiv:1201.4711].

[11] Jaeckel, J. & Ringwald, A. The Low-Energy Frontier of Particle Physics. *Ann. Rev. Nucl. Part. Sci.* **60**, 405-437, (2010) [arXiv:1002.0329].

[12] De Angelis, A., Mansutti, O. & Roncadelli, M. Axion-Like Particles, Cosmic Magnetic Fields and Gamma-Ray Astrophysics. *Phys. Lett. B* **659**, 847-855 (2008) [arXiv:0707.2695].

[13] Simet, M., Hooper, D. & Serpico, P. The Milky Way as a Kiloparsec-Scale Axionscope. *Phys. Rev.* **D77**, 063001 (2008) [arXiv:0712.2825].

[14] Fairbairn, M., Rashba, T. & Troitsky, S. Photon-axion mixing and ultra-high-energy cosmic rays from BL Lac type objects: Shining light through the Universe. *Phys. Rev.*, **D84**, 125019 (2011) [arXiv:0901.4085].

[15] Essey, W. & Kusenko, A. A new interpretation of the gamma-ray observations of active galactic nuclei. *Astropart. Phys.* **33** 81-85 (2010) [arXiv:0905.1162].

Chapter 3

Astrophysical Observations

Periodicities in the soft X-ray emission from the solar corona during descending phase of cycle 23

Partha Chowdhury[1]

[1]University College of Science & Technology, Calcutta University, Kolkata 700009, West Bengal, India
parthares@gmail.com

DOI: http://dx.doi.org/10.3204/DESY-PROC-2014-03/chowdhury_partha

We have studied the time series of full disk integrated soft X-ray emission from the solar corona during January 2004 to December 2008, covering the entire descending phase of solar cycle 23 from a global point of view. We employ the daily X-ray index (DXI) derived from 1s cadence X-ray observations from the Si detector of "Solar X-ray Spectrometer (SOXS)" mission in four different energy bands ranging between $6 - 25\ KeV$. The daily time series is subjected to power spectrum analysis after appropriate correction for noise. Lomb-Scargle periodogram technique has shown prominent periods of $\sim$ 13.5 days, $\sim$ 27 days, and near Rieger period of $\sim$ 181 days and $\sim$ 1.24 years in all energy bands. Further to this, other periods like $\sim$ 31, $\sim$ 48, $\sim$ 57, $\sim$ 76, $\sim$ 96, $\sim$ 130, $\sim$ 227 and $\sim$ 303 days are also detected in different energy bands. We discuss our results in the light of previous observations and existing numerical models.

1 Introduction

Solar activity as a whole is known to exhibit a wide range of periodicities on different time scales ranging from minutes to centuries. As long-term periodicity, the Sun exhibits the $\sim$ 11yr sunspot cycle (Schwabe cycle) and for short-term variations, the near 27 day periodicity is the most prominent. The former is related to the polarity reversal of solar magnetic field and the latter reflects the modulation imposed on the solar flux at the Earth by solar rotation. The regime between these extremes of time-scales (between 27 day and 11 year) is called the "mid-range" or "intermediate-term" periodicities. Studies of short and mid-term variations in solar activity and their solar-cycle dependence may help to achieve a better understanding of the basic processes of solar activity cycle, dynamics and mechanisms of generation of the solar magnetic field and for predicting the level of solar activity [2, 11, 12], and hence the variation in space weather. The helioseismic probing of the solar interior using SOHO/MDI data has shown that the rotation rate of the Sun near the base of its convective zone changes with a period of roughly 1.3 years [7]. The 1.3yr periodicity has also been detected in variations of the interplanetary magnetic field and geomagnetic activity [13, 14] in the variation of photospheric magnetic flux [11] and in the solar wind speed [16]. In this context, investigation of $\sim$ 1.3yr periodicity in the solar corona would strengthen or weaken the case for associated changes in the layers harbouring the dynamo as well as may enable to understand any connection between

convective zone and the corona.

The structure and evolution of the solar magnetic field is believed to be produced by a magneto-hydro-dynamic (MHD) dynamo operating inside the Suns convection zone [4], which induces various solar activities that exhibit periodic variations on different time scales. We consider that any fluctuation in the dynamo process will manifest itself most clearly in relatively freshly emerged flux [12], whose signatures could be visible in the solar corona when viewed in the X-ray waveband. The X-ray intensity of the solar corona, however, varies as a function of emerging flux, sunspots, and flares etc, which are changing over 11-year sunspot cycle. The X-ray corona refers to different plasma temperature and density for different solar features, observed in different X-ray energy bands [8]. In this investigation, for this purpose, we exploit the "Solar X-ray Spectrometer (SOXS)" data [9, 10] for the period of January 2004 to December 2008, declining phase of sunspot cycle 23.

2 The Data

We employ the observations from the "Solar X-ray Spectrometer (SOXS): Low Energy Detector (SLD)" mission for current investigation (http://www.prl.res.in/ soxs-data/).

3 Analysis techniques

The daily variation of coronal X-ray emission recorded as DXI data sets was analyzed by the LombScargle method by calculating the Scargle normalized periodogram $P_N(\omega)$ [17].

4 Results

During 2004 to 2006, we find ∼four sharp peaks in both soft X-rays in consistence to [3] who reported a high flare activity in the early descending phase of cycle 23. The application of Lomb-Scargle periodogram technique on the time series of (DXI) observed by Si detector in $6-7$, $7-10$, $10-20$ and $4-25$ KeV, energy bands reveals several short and intermediate term periodicities of the X-ray corona. The Si detectors explicitly show the most prominent periods of ~ 27 days related to prominent solar rotation, $13-14$ days related to 1800 oppositely directed active longitudes [6] or hotspots [1], and Rieger type period of ~ 181 days proposed to be related to the change in the rotation rate of the Sun near the base of its convective zone [12]. We report the 1.24-year period detected for the first time in the X-ray emission form the solar corona in wide energy band during the declining phase of sunspot cycle 23. We further propose that variation in the solar rotation below techocline due to tensional oscillations [5] manifests to up flowing magnetic flux to corona with variety of periods to cause the solar activity as seen by us in the various X-ray energy bands. Further, we have observed significant power at ~ 31 days periodicity in all energy bands, which, however, becomes stronger with increasing energy. Perhaps this may be related to solar activity at higher latitudes.

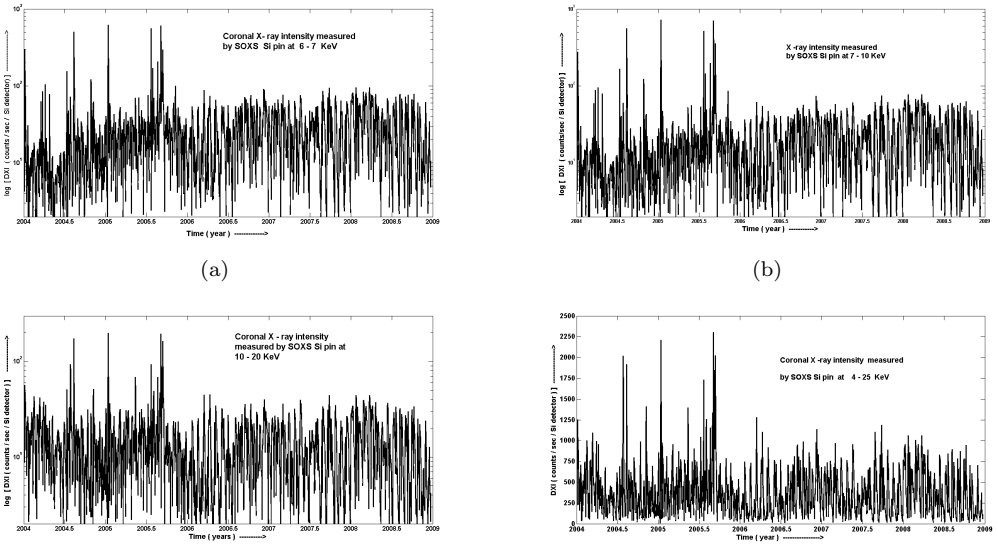

Figure 1: Time series of daily X-ray index (DXI) in (a) $6-7$, (b) $7-10$, (c) $10-20$ and (d) $4-25keV$ bands of SOXS Si detector for the period from 1 January 2004 to 31 December 2008.

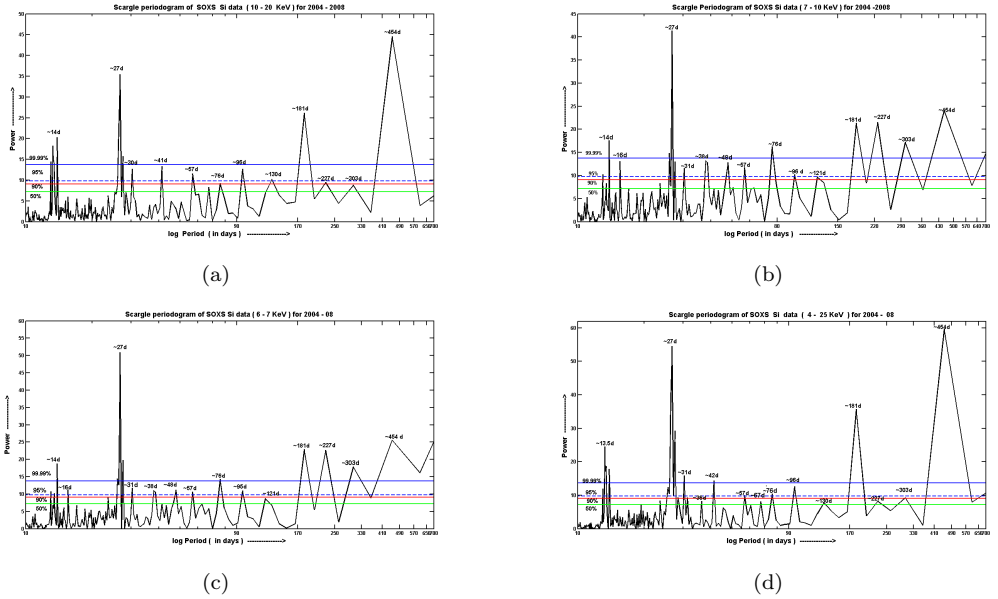

(a) (b) (c) (d)

Figure 2: Lomb - Scargle periodogram of the DXI data from the Si detector for 2004 - 2008. (a) $10-20keV$, (b) $7-10keV$, (c) $6-7keV$, (d) $4-25keV$.

5 Discussions and Conclusion

The results presented in section 4 refer to the first investigation of short and intermediate-term oscillations revealing the occurrence rate in the daily X- Ray index (DXI) that obtained from 1s cadence observations made by the Si detectors of the SOXS mission from 1 January 2004 to 31 December 2008 covering the descending phase of solar cycle 23. However, the detection of 1.24 year periodicity in the X-ray corona suggests coupling of this outermost layer with the rotation of the innermost core. It is generally suggested that the $1.24-1.3$ year periodicity is associated with variation in equatorial speed of the rotation in the convective zone, which is in anti-phase with an oscillation in the corresponding speed of rotation of the core, on the other side of the tachocline. However, our current discovery of 1.24-yr periodicity from solar coronal X-ray emission suggests that variation in equatorial speed of the solar rotation beneath convective zone and perhaps at the core level is also manifested in the coronal plasma, and suggests exploring the physical processes that couple the core to corona.

The other prominent periodicities seen in our dataset are $\sim$ 13.5 and 27 days. The 13.5 days periodicity is a result of 180° oppositively directed longitudes as many scientists have also shown earlier. On the other hand, 27 day periodicity refers to the solar rotation, which is most prominent due to all the active centers or exciters hotspot are very close to the equator particularly during the declining phase of the solar cycle. Our results endorse earlier conclusion of [15] that this periodicity arises because active regions and their magnetic field are better organized and are long lived during the maximum and declining portion of the solar cycle than its rising portion. Our discovery of 31 days periodicity though not prominent but observed

in all the energy bands suggests that many sunspot regions did not approach close to equator during declining phase of cycle 23. This indicates that the length of the declining phase of cycle 23 should be longer which is in agreement to sunspot observations that report decay phase to be ~ 8 years.

The present investigation reveals the prominent existence of a near 26 day periodicity (with 13.5 day period as sub harmonic) and a similar kind of period has been reported in the photospheric magnetic-field evolution. This is important because it represents a link among the sub-photospheric magnetic field evolution, coronal activity, and the loss of magnetic flux through coronal X-ray emission. In conclusion, after studying the periodic behavior of coronal X-ray emission data during descending phase of cycle 23, we have detected a number of short and inter-mediate term oscillations which are consistent with several other studies during cycle 23. In particular, we found that the group of peaks ranges from $26 - 41$ day period may be due to a single quasi-periodic process that is shifting in frequency through the cycle. It is possible that, this intermittent behavior may be due to a random process of magnetic flux emergence through the photosphere. We assume that magnetic Rossby type waves are responsible for this short and mid-term periods.

The present investigation suggests a scenario of emergence and escape of magnetic flux from the solar convection zone to the interplanetary medium through the photosphere and corona. Therefore we may conclude that X-ray emission from the corona is one of the most important solar parameters crucial to probe the Sun Earth coupling and terrestrial climate. However, more observations and theoretical investigations on the dynamics of the solar interior, corona, flare producing active regions and mechanism of the Rossby type waves within solar atmosphere may shed new light on the origin of these short and intermediate-term periodicities.Along with it we should be careful about the gravitational lensing effect by the planets as they revolve with a constant orbital period around the Sun.

Acknowledgements

The author is grateful to the Organizers of 10^{th} Patras workshop and Prof. Konstantin Zioutas, for invitation to deliver the talk. The author acknowledges Prof. Rajmal Jain, Physical Research Laboratory for SOXs data and discussion.

References

[1] Bai, Taeil., "Solar 'hot spots' are still hot," Astrophysical Journal, Part 2 - Letters (ISSN 0004-637X),364, L17-L20 (1990)

[2] Bai T., ApJ, 397, 584 (1992)

[3] Bai, Taeil, "High Flare Activity in the Late Declining Phase of Cycle 23," Solar Physics, 234(2),409-419 (2006)

[4] Charbonneau, P. "Dynamo Models of the Solar Cycle," Living Reviews in Solar Physics, 7, 3 (2010)

[5] Christensen-Dalsgaard, Jrgen., "Helioseismology, Reviews of Modern Physics," 74(4),1073 (2002)

[6] Donnelly, R. F., Puga, L. C., "Thirteen-day periodicity and the center-to-limb dependence of UV, EUV, and X-ray emission of solar activity1990," Sol. Phys., 130, 369 (1990).

[7] Howe R. et al., Science, 287, 2456 (2000)

[8] Jain, Rajmal ; Aggarawal, Malini and Sharama, Raghunandan, "X-ray emission from solar flares," JApA, 29,125 (2008)

[9] Jain, Rajmal *et al.*, "Solar X-ray Spectrometer (Soxs) Mission on Board GSAT2 Indian Spacecraft: The Low-Energy Payload," Sol. Phys., 227, 89 (2005).

[10] Jain, Rajmal *et al.*, "Solar X-ray Spectrometer (SOXS) Mission - Low Energy Payload - First Results," JApA, 27,175 (2006)

[11] Knaack R., Stenflo J. O., Berdyugina S. V., "Evolution and rotation of large-scale photospheric magnetic fields of the Sun during cycles 21-23. Periodicities, north-south asymmetries and r-mode signatures," A&A, 438, 1067 (2005)

[12] Krivova N. A., Solanki S. K., "The 1.3-year and 156-day periodicities in sunspot data: Wavelet analysis suggests a common origin," A&A, 394, 701 (2002)

[13] Lockwood, M., "Long-term variations in the magnetic fields of the Sun and the heliosphere: Their origin, effects, and implications," Journal of Geophysical Research, 106(A8), 16021 (2001)

[14] Mursula, K., Zieger, B., Vilppola, J. H., "Mid-term quasi-periodicities in geomagnetic activity during the last 15 solar cycles," Sol.Phys, 212(1), 201 (2003)

[15] Pap J., Tobiska W. K., Bouwer S. D., "Periodicities of solar irradiance and solar activity indices," Sol. Phys., 129, 165 (1990)

[16] Richardson, J. D.*et al.* "Solar wind oscillations with a 1.3 year period," Geophys. Res. Lett., 21(14), 1559,doi: 10.1029/94GL01076 (1994).

[17] Scargle J. D., "Studies in astronomical time series analysis. II - Statistical aspects of spectral analysis of unevenly spaced data," ApJ, 263, 835 (1982)

[18] Sturrock P. A., Bai T., "Search for evidence of a clock related to the solar 154 day complex of periodicities," ApJ, 397, 337 (1992)

An InGrid based Low Energy X-ray Detector

Christoph Krieger[1], *Klaus Desch*[1], *Jochen Kaminski*[1], *Michael Lupberger*[1] *and Theodoros Vafeiadis*[2]

[1]Physikalisches Institut, University of Bonn, Germany
[2]CERN, Geneva, Switzerland

DOI: http://dx.doi.org/10.3204/DESY-PROC-2014-03/krieger_christoph

An X-ray detector based on the combination of an integrated Micromegas stage with a pixel chip has been built in order to be installed at the **C**ERN **A**xion **S**olar **T**elescope. Due to its high granularity and spatial resolution this detector allows for a topological background suppression along with a detection threshold below 1 keV.

Tests at the CAST Detector Lab show the detector's ability to detect X-ray photons down to an energy as low as 277 eV. The first background data taken after the installation at the CAST experiment underline the detector's performance with an average background rate of 5×10^{-5} /keV/cm^2/s between 2 and 10 keV when using a lead shielding.

1 InGrid - An integrated Micromegas stage

To enhance the performance of Micromegas detectors, it is necessary to match the granularity of the readout to the highly granular gas amplification stage. Taking into account the rising number of readout channels per area when following this approach, a pad based readout is impractical. This drawback can be bypassed by using integrated electronics in form of a pixel chip, e.g. the Timepix ASIC [1]. This pixel chip offers 256×256 pixels with a pixel pitch of 55 µm and thus an active area of 2 cm^2. Each of the pixels contains a charge sensitive amplifier and a discriminator plus complete counting logic needed for time or charge measurements.

In order to achieve a precise alignment between the mesh holes and the pixels, to avoid the appearance of Moiré patterns, it is suitable to produce the Micromegas mesh directly on top of the pixel chip by means of photolithographic postproceesing technologies [2, 3]. A scanning electron microscope picture of the resulting structure can be seen in Figure 1a. When building such an **In**tegrated **Grid** on top of a Timepix ASIC a resistive layer made of 4 µm silicon nitride is deposited between ASIC and InGrid to protect the chip and its electronics from discharges occurring during operation of the Micromegas stage [4].

2 The InGrid based X-ray Detector

The InGrid based X-ray detector constructed at Bonn uses a Timepix ASIC with an InGrid stage as central charge multiplication and readout device. The design of the detector (see Figure 1c for an exploded view) has been based on the recent Micromegas detectors [5] used at the Sunset stations of the **C**ERN **A**xion **S**olar **T**elescope [6]. The detector body is made of acrylic glass and contains the modular readout assembly which houses the Timepix ASIC, with

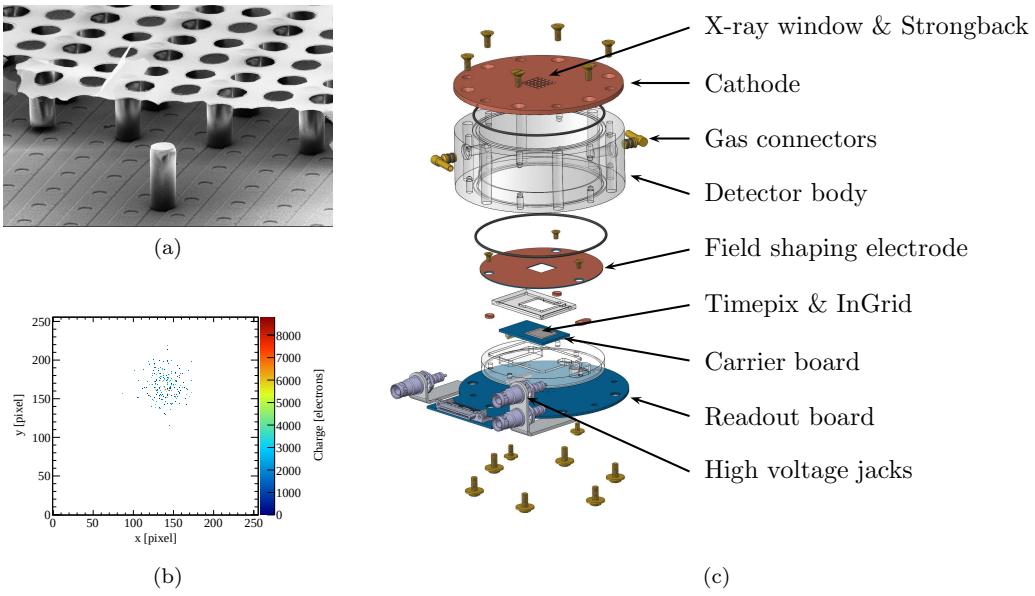

Figure 1: Scanning electron microscope picture of an InGrid structure (a), taken from [7]. Event display showing an X-ray photon of 5.9 keV from an ^{55}Fe source as recorded with the InGrid based X-ray detector (b), depicted area shows the complete active area of the Timepix ASIC. Z-axis shows the charge collected on each pixel. An exploded view of the detector, with main parts labeled, is shown in (c). Drawing is taken from [8].

the InGrid stage, mounted on a small carrier board. The chip is covered by a field shaping electrode, closing the readout assembly. The electrode features a cutout matching the size of the chip's active area and is leveled a bit above the mesh of the InGrid structure and set to the electric potential according to its position within the drift field. This helps to reduce electric field distortions arising at the chip's borders and the wire bonds connecting the chip's electronics to the underlying carrier board.

The drift volume featuring a drift distance of 3 cm at a drift field of 500 V/cm is closed by a cathode plate made of copper. To allow especially low energy X-ray photons to enter the detector, a 2 µm thick aluminized Mylar film is used as entrance window. The material of the cathode plate above the instrumented area of the detector has therefore been removed except for a small grid like structure to support the thin window. The support for the window is necessary as it has to withstand a pressure difference of 1050 mbar. Additionally only a small leak rate is allowed so the detector can be operated connected to vacuum. Considering these requirements the choice of a 2 µm Mylar film represents a good compromise between robustness and transparency.

Readout of the Timepix ASIC is done with an FPGA based readout system developed at Bonn [7] which allows for full access to firm- and software for customization. The detector is filled with a gas mixture composed of 97.7 % Argon and 2.3 % isobutane as quencher gas.

The detection of X-rays with this detector is based on the fact that X-rays entering the detector will hit a gas atom and produce a bunch of primary electrons through ionization.

These will drift towards the readout. The initial bunch of electrons is spread to a cloud of approximately circular shape due to diffusion. Then they get multiplied in the InGrid stage and are afterwards detected on the Timepix's pixels. This allows for a low X-ray energy threshold along with a topological background suppression by application of an event shape analysis. A typical X-ray event recorded with the detector is depicted in Figure 1b.

3 Installation & first background rates

To replace the pnCCD detector behind the X-ray telescope [9] at one of the four detector stations of CAST, a vacuum system has been constructed and built which allows for differential pumping and provides the necessary safety interlocks. For the differential pumping a 0.9 µm thick Mylar window is used. In April and May of 2014 the vacuum system and the InGrid based detector were installed including a laser guided alignment with the X-ray telescope. A lead shielding designed and manufactured by our colleagues from the University of Zaragoza was added mid of May. In two months of operation no detector related problems occurred.

Prior to the installation, the detector was characterized at the X-ray generator of the CAST Detector Lab which provides a complete vacuum beamline connected to the X-ray generator [10]. With the appropriate combination of targets of the X-ray tube and filters, characteristic X-ray lines can be produced in the energy range from a few hundred eV up to 8 keV. Additionally the lab provides the necessary infrastructure for operating Micromegas detectors. The lab tests underlined the detector's low energy threshold through successful detection of photons down to the Carbon K_α line at 277 eV (see Figure 2a for the spectrum containing the Carbon K_α line).

To achieve a low background rate a background discrimination routine was created, based on a likelihood algorithm and reference data sets for different energy ranges recorded during the tests in the CAST Detector Lab. The applied likelihood method utilizes event shape properties making benefit of the Timepix ASIC's high spatial resolution resulting in a topological background suppression to identify real X-ray photons in the recorded data. The energy of a recorded event is calculated via a calibration curve from the total charge of an event. To built the likelihood, event shape properties of this event are being compared to the corresponding distributions for events of similar energy. These sample distributions are obtained from the lab tests' data. The likelihood cut value is adjusted for each energy range so that a signal efficiency of roughly 90 % is kept over all energies. The background rates achieved during first operation period were in the order of a few 10^{-5} /keV/cm^2/s, occurring peaks could be explained by the characteristic fluorescence line of the copper cathode and misidentified cosmic rays traversing the detector perpendicular to the chip and therefore resulting in an X-ray like, circular, structure.

4 Summary

A gaseous detector based on the combination of a pixel chip and an integrated Micromegas stage has been successfully built and commissioned. The detector was installed at the CAST experiment along with its infrastructure and has up to now been successfully operated. First background rates achieved in the CAST environment look promising and are in agreement with the results obtained with a first prototype in the lab at Bonn [11]. Together with the measurements carried out at an X-ray generator facility which provided proof of the detector's low

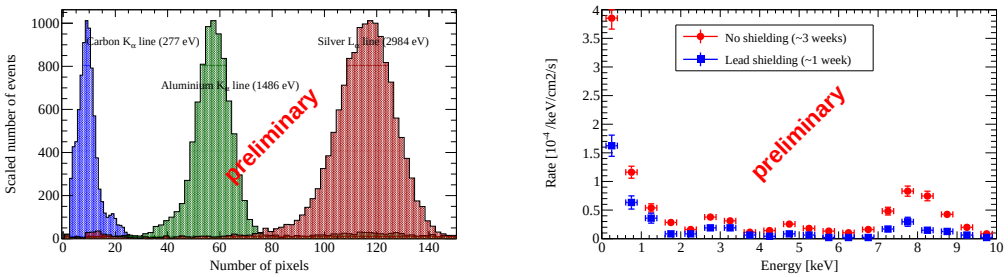

(a) (b)

Figure 2: Spectrum showing the Carbon K_α line at 277 eV together with the Aluminum K_α and the Silver L_α line at 1486 eV and 2984 eV respectively (a). Lines have been recorded separately. Number of pixels corresponds to the number of electrons in the charge cloud created by the initial X-ray photon which is proportional to the photon's energy. First background spectra obtained with and without lead shielding in the CAST environment (b).

energy detection threshold of a few hundred eV, the detector's performance could be underlined and demonstrated.

Further improvement to the background discrimination algorithm will be done as well as future detector upgrades, which should include a decoupling and recording of the signal induced on the mesh, as it is done for the CAST Micromegas detectors. The latter one should give access to further event properties to be utilized for background suppression.

References

[1] X. Llopart *et al.*, "Timepix, a 65k programmable pixel readout chip for arrival time, energy and/or photon counting measurements", Nucl. Instr. Meth. Phys. Res. A **581** (2007) pp 485-494.

[2] M. Chefdeville *et al.*, "An electron-multiplying 'Micromegas' grid made in silicon wafer post-processing technology", Nucl. Instr. Meth. Phys. Res. A **556** (2006) pp 490-494.

[3] H. van der Graaf, "GridPix: An integrated readout system for gaseous detectors with a pixel chip as anode", Nucl. Instr. Meth. Phys. Res. A **580** (2007) pp 1023-1026.

[4] Y. Bilevych *et al.*, "Spark protection layers for CMOS pixel anode chips in MPGDs", Nucl. Instr. Meth. Phys. Res. A **629** (2011) pp 66-73.

[5] S. Aune *et al.*, "New Micromegas detectors in the CAST experiment", Nucl. Instr. Meth. Phys. Res. A **604** (2009) pp 15-19.

[6] K. Zioutas *et al.*, "A decommissioned LHC model magnet as an axion telescope", Nucl. Instr. Meth. Phys. Res. A **425** (1999) pp 480-487.

[7] M. Lupberger, "The Pixel-TPC: first results from an 8-InGrid module", J. Instrum. **9** (2014) C01033.

[8] C. Krieger *et al.*, "An InGrid based Low Energy X-ray Detector for the CAST Experiment", in proceedings of TIPP2014 conference, PoS(TIPP2014)060.

[9] M. Kuster *et al.*, "The x-ray telescope of CAST", New J. Phys. **9** (2007) 169 [arXiv: 0702188 [physics]].

[10] T. Vafeiadis, "Contribution to the search for solar axions in the CAST experiment", CERN, Aristotle University, Thessaloniki 2012 [CERN-THESIS-2012-349].

[11] C. Krieger *et al.*, "InGrid-based X-ray detector for low background searches", Nucl. Instr. Meth. Phys. Res. A **729** (2013) pp 905-909.

Cosmologically Probing Ultra-light Particle Dark Matter using 21 cm Signals

Yi Mao[1], *Kenji Kadota*[2,3], *Kiyomoto Ichiki*[4] *and Joseph Silk*[1,5,6]

[1] Institut d'Astrophysique de Paris, Institut Lagrange de Paris, CNRS, UPMC Univ Paris 06, UMR7095, 98 bis, boulevard Arago, F-75014, Paris, France
[2] Department of Physics, Nagoya University, Nagoya 464-8602, Japan
[3] Center for Theoretical Physics of the Universe, Institute for Basic Science, Daejeon 305-811, Korea
[4] Kobayashi-Maskawa Institute for the Origin of Particles and the Universe, Nagoya University, Nagoya 464-8602, Japan
[5] The Johns Hopkins University, Department of Physics and Astronomy, Baltimore, Maryland 21218, USA
[6] Beecroft Institute of Particle Astrophysics and Cosmology, University of Oxford, Oxford OX1 3RH, UK

DOI: http://dx.doi.org/10.3204/DESY-PROC-2014-03/mao_yi

Ubiquitous ultra-light scalar fields may make a partial contribution to the dark matter and affect the large scale structure of the Universe. While their properties are heavily model dependent, we develop a model-independent analysis to forecast the constraints on their mass and abundance using futuristic 21 cm observation as well as CMB lensing measurements. We demonstrate that the 21 cm power spectrum are most sensitive to the ultra-light dark matter with mass $m \sim 10^{-26}$ eV for which the precision attainable on mass and abundance bounds can be of the order of a few percent.

1 Introduction

The existence of light scalar fields has been explored from both particle phenomenology and cosmological aspects. As an astrophysical example, the ultra-light particles (ULPs) with mass of the order of the current Hubble scale $H_0 \approx 2 \times 10^{-33}$ eV [1] may contribute to a small fraction of the total matter in our Universe. Those ultra-light scalar fields can have an imprint on the matter power spectrum due to *free-streaming*, similar to that due to massive neutrinos. Since the range of possible mass is wide, so is the range of the suppression scale in the matter power spectrum. In this proceeding paper, we forecast cosmological constraints on two free parameters of the ULPs, their mass and abundance, with CMB lensing and futuristic 21 cm observations. We aim to clarify the range of the mass and abundance of ULPs which 21 cm observations will be most sensitive to.

In what follows, §2 outlines the effect of the ULPs on the matter power spectrum. §3 gives a brief review of the Fisher forecast formalism, followed by the results in §4. The main results

[1] Throughout this paper, the mass is in units of $H_0 \approx 2 \times 10^{-33}$ eV.

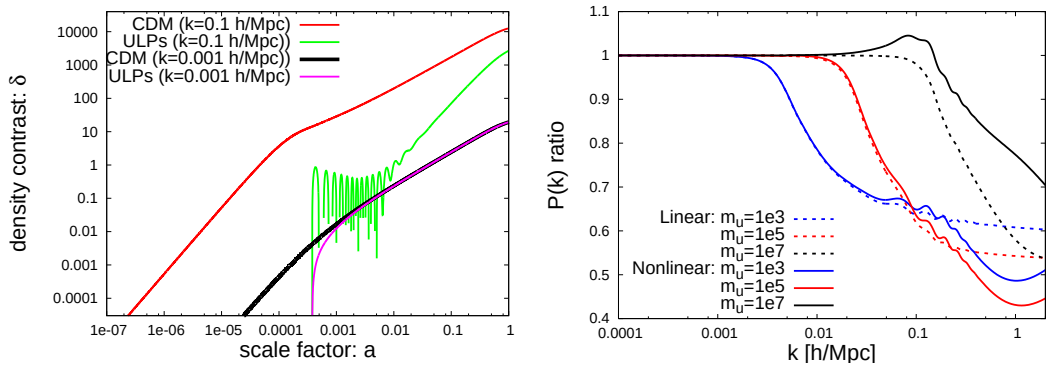

Figure 1: (Left) The evolution of perturbations for ULPs ($m_u = 10^5 H_0, f_u = 0.05$) and for CDM only. (Right) The ratio of the power spectrum $P(k)$ with ULPs ($f_u = 0.05$) to that with CDM only. Figures are reused from [1].

of this proceeding have been published in [1].

2 Suppression in the Matter Power Spectrum

For the leading order perturbation equation, $\ddot{\delta_k} + 2H\dot{\delta_k} + \left(\frac{c_s^2 k^2}{a^2} - 4\pi G\rho_m\right)\delta_k = 0$, there exists a gravitationally stable solution for short wave-length mode $k \gg k_J$ and an unstable (growing) one for $k \ll k_J$, with the Jeans wave number $k_J = (a/c_s)\sqrt{4\pi G\rho_m}$. For the ULPs, its effective sound speed is $c_s \approx k/2m_u a$ for $a \gg k/2m_u$, and $c_s \approx 1$ below the Compton scale $a \ll k/2m_u$, where m_u is the ULP mass [2, 3]. Therefore, $k_J(a) = 2a(\pi G\rho_m(a))^{1/4} m_u^{1/2}$ for $a \gg k/2m_u$. We consider scenarios in this paper where the ULP behaves like dark energy due to the large Hubble friction for $H > m_u$, and starts oscillations like dark matter, once $H \leq m_u$. We implement ULPs into CAMB [4] accordingly. The evolution of the ULP fluctuations $\delta_u = \delta\rho_u/\rho_u$ is shown in the left panel of Fig. 1 for the ULP mass and fraction $m_u = 10^5 H_0$, $f_u = \Omega_u/\Omega_m = 0.05$. The fluctuations $\delta(k)$ cannot grow when they behave like a cosmological constant and can start growing once the ULPs start to oscillate. The perturbation growth however is suppressed inside the Jeans scale and the perturbation growth has to wait till it goes outside the Jeans scale for a large enough value of a. We also plotted the CDM perturbation evolution which illustrates that the ULP perturbations can catch up with the CDM perturbations for small k but not for large k, analogously to the well-known behavior of the baryon perturbation evolution. The nonlinearity becomes important when $k^3 P(k)/(2\pi^2)$ becomes of order unity. We estimate that $m_u \sim 10^5 H_0$ leads to the oscillation starting around the matter-radiation equality epoch $z_{osc} \sim 3200 (\sim z_{eq})$. For the modes which enter the horizon during matter domination, the suppression in the matter power spectrum starts around the scale corresponding to the Jeans scale when the ULP starts oscillating $k \sim \left(H_0^2\Omega_m\right)^{1/3} m_u^{1/3}$. Similarly, when the oscillations start during radiation domination, the suppression is expected to occur for scales smaller than the Jeans scale at matter-radiation equality $k \sim (m_u^2 H_0^2 \Omega_m a_{eq})^{1/4}$. The suppression scales for different masses are illustrated in the right panel of Fig. 1 which shows the transfer function

$T^2(k) = P(k)_{\rm ULPs}/P(k)_{\rm no\ ULPs}$ representing the ratio of the power spectrum including the ULPs to that without ULPs. We are particularly interested in the ULP masses which affect the matter power at the 21 cm-observable scales of $0.055 \lesssim k \lesssim 0.15$ Mpc^{-1}. We can see that the baryon acoustic oscillation effects are more prominent in the nonlinear matter power spectrum than in the linear one and $m_u \sim 10^7 H_0$ lets the suppression start right in the 21 cm observable range.

3 Forecast Formalism

To forecast the constraints on the cosmological parameters including those relevant to the ULPs, we perform the Fisher likelihood analysis for future 21 cm experiments. We also use the CMB observables including CMB lensing which help remove the parameter degeneracies that the 21 cm signals would otherwise suffer from. We briefly outline the formalism of the likelihood analysis here, and present the results in the next section.

The 21 cm radiation comes from the atomic transition between the two hyperfine levels of the hydrogen $1s$ ground state. In the linear regime, the power spectrum of 21 cm brightness temperature fluctuations can be written as $P_{\Delta T}(\mathbf{k}, z) = \widetilde{\delta T_b}^2 \overline{x}_{H_I}^2 [b_{H_I}(z) + \mu_{\mathbf{k}}^2]^2 \ P_{\delta\delta}(k, z)$, where $\widetilde{\delta T_b}(z) = (23.88{\rm mK}) \left(\frac{\Omega_b h^2}{0.02}\right) \sqrt{\frac{0.15}{\Omega_m h^2} \frac{1+z}{10}}$. Here we consider $z \lesssim 10$ when the spin temperature $T_S \gg T_{CMB}$. We define the neutral and ionized density bias, $b_{H_I}(z)$ and $b_{H_{II}}(z)$, as $b_{H_I} \equiv \delta_{\rho_{H_I}}(k)/\delta_\rho(k)$, $b_{H_{II}} \equiv \delta_{\rho_{H_{II}}}(k)/\delta_\rho(k)$. They are related by $b_{H_I} = (1 - \overline{x}_{H_{II}} b_{H_{II}})/\overline{x}_{H_I}$. We use the excursion set model of reionization [5] to obtain the fiducial values of ionized density bias $b_{H_{II}}(z)$ and the mean ionized fraction $\overline{x}_{H_{II}}(z)$. The Fisher matrix for 21 cm power spectrum measurements is [6, 7] $F_{\alpha\beta}^{21{\rm cm}} = \sum_{\mathbf{u}} \frac{1}{[\delta P_{\Delta T}(\mathbf{u})]^2} \left(\frac{\partial P_{\Delta T}(\mathbf{u})}{\partial p_\alpha}\right) \left(\frac{\partial P_{\Delta T}(\mathbf{u})}{\partial p_\beta}\right)$, where $\{p_\alpha\}$ represents the free parameters in our model. We assume a logarithmic pixelization $du_\perp/u_\perp = du_\parallel/u_\parallel = 0.1$. The error in power spectrum measurement is $\delta P_{\Delta T}(\mathbf{u}) = [P_{\Delta T}(\mathbf{u}) + P_N(u_\perp)]/\sqrt{N_c}$, where $N_c = u_\perp du_\perp du_\parallel \Omega B/(2\pi^2)$ is the number of independent modes in each pixel (Ω is a field of view solid angle and B is the bandwidth of a redshift bin). P_N is the noise power spectrum $P_N(\mathbf{u}_\perp, z) = (\lambda T_{sys}/A_e)^2/(t_0 n(\mathbf{u}_\perp))$, where $T_{sys} \approx (280{\rm K})[(1+z)/7.4]^{2.3}$ is the system temperature [8], A_e is the effective collecting area of each antenna tile, and t_0 is the total observation time. We assume an Omniscope-like instrument [9] consisting of a million 1m $\times$ 1m dipole antennae with a field of view of 2π steradians and we assume $t_0 = 4000$ hours for each redshift bin of bandwidth $B = 6$MHz. We also assume the residual foregrounds can be neglected for $k_\parallel \geq k_{\parallel,{\rm min}} = 2\pi/(yB)$ [6], and the minimum baseline L_{min} sets $k_{\perp,{\rm min}} = 2\pi L_{min}/(\lambda d_A)$ (for example, for an Omniscope-like array, $k_{min} \approx k_{\parallel,{\rm min}} = 0.055\,{\rm Mpc}^{-1}$ at $z = 10.1$). We conservatively restrict our studies to large scale $k \leq 0.15\,{\rm Mpc}^{-1}$ for the sake of the linear treatment of 21 cm observables, to avoid any scale-dependent bias at the nonlinear regime and the nonlinear effects due to reionization patchiness at the scale of the typical size of ionized regions [10].

The CMB can also be affected by light dark matter through the change in matter-radiation equality and also via the Sachs-Wolfe effect. The CMB is also helpful in removing the degeneracies among the cosmological parameters. The CMB lensing is in particular helpful in removing the so-called geometric degeneracy which the primary CMB observables would otherwise suffer from. We consider the CMB observables T, E, d which represent the CMB temperature, polarization and CMB deflection angle respectively. We assume the Planck-like specifications [11]

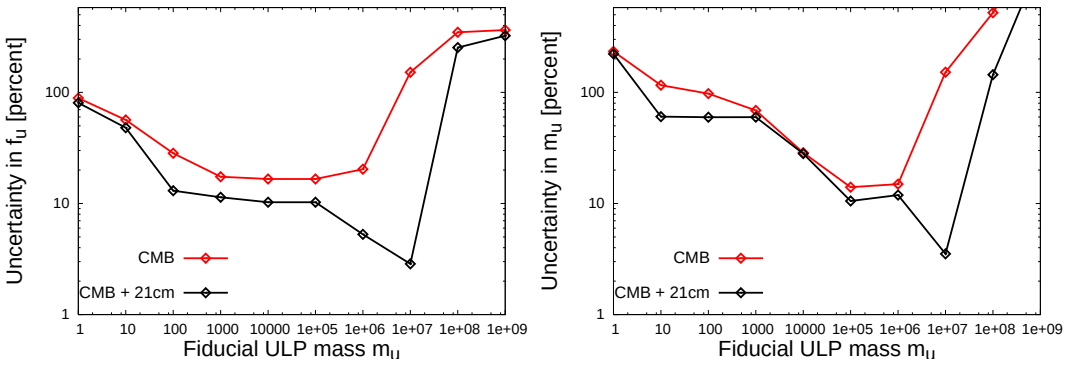

Figure 2: 1σ errors in f_u (left) and m_u (right) for several fiducial values of m_u in units of $H_0 \approx 2 \times 10^{-33}$ eV, with fiducial value $f_u = 0.05$. Figures are reused from [1].

including the CMB lensing measurements covering up to the multipole $l_{max} = 2500$, three channels $100, 143, 217$ GHz and the sky coverage $f_{sky} = 0.65$. The Fisher matrix for CMB lensing is $F^{CMB}_{\alpha\beta} = \sum_{l=2}^{l_{max}} \frac{f_{sky}(2l+1)}{2} Tr[\mathbf{C}_{,\alpha}\, \mathbf{C}^{-1} \mathbf{C}_{,\beta}\, \mathbf{C}^{-1}]$, where $,_\alpha$ refers to the partial derivative with respect to a cosmological parameter p_α, and $\mathbf{C}$ is the covariance matrix. We assume the noise in the auto-correlation spectra is dominated by detector noise represented by the photon shot noise [12, 13], and the CMB lensing statistical noise is estimated using the optimal quadratic estimator method of Hu & Okamoto [14, 15]. The total Fisher matrix was obtained by adding the 21 cm and CMB Fisher matrix $F \approx F^{21cm} + F^{CMB}$. The modified version of the CAMB [4] was used to obtain the CMB and matter power spectra where the ultra-light fluid component was implemented in the Boltzmann equations.

4 Results

We vary 12 parameters in our Fisher analysis Ω_Λ, $\Omega_m h^2$, $\Omega_b h^2$, n_s, A_s (scalar amplitude), τ (reionization optical depth), N_{eff} (the effective number of relativistic neutrino species), m_u (mass of ULPs), f_u (ratio of ULP abundance to total matter), f_ν (ratio of neutrino abundance to total matter), $x_{H_I}(z)$ (mean neutral fraction at redshift z), $b_{H_{II}}(z)$ (H II density bias at redshift z). For the fiducial models, unless stated otherwise, we use $x_{H_I} = 0.5$ at the redshift bin of $z = 10.10$ and $b_{H_{II}} = 5.43$ obtained by the excursion set model of reionization [5], and the power spectrum up to the scale $k_{max} = 0.15\,\mathrm{Mpc}^{-1}$ was used.

Our main results are summarized in Fig. 2 which shows the 1σ uncertainties in the ULP parameters for several representative ULP masses for $f_u = 0.05$. The 1σ errors on the ULP parameters f_u, m_u can be of order a few percent for the mass range, around $m_u \sim 10^7 H_0$, to which the 21 cm signals are most sensitive. This ULP mass lets the ULPs start oscillations at $0.055 \lesssim k \lesssim 0.15\mathrm{Mpc}^{-1}$ which, as Fig. 1 shows, is where the matter power spectrum has the significant change with respect to that of the CDM only. On the other hand, the sensitivity of the CMB observables to the ULPs increases up to the ULP mass of about $10^5 H_0$ which corresponds to the oscillation starting around the CMB last scattering epoch. For instance, we found numerically $2 \times 10^4 H_0 \sim H(z = 1100)$ and we can indeed see that $\sigma(m_u)$ does not

improve so much by adding the 21 cm observables for the mass around $m_u \sim 10^{4\sim5} H_0$. This implies that the CMB constraint on m_u is dominant over that from the 21 cm observables for this mass range. The CMB, however, starts losing its sensitivity to the ULPs significantly for the larger ULP masses $m_u \gtrsim 10^6 H_0$ which initiate the oscillations well before the last scattering epoch.

In short, we find that the CMB measurements are most sensitive to the ULP mass range of $10^4 H_0 \sim 10^6 H_0$, and the 21 cm measurements are most sensitive to $m_u \sim 10^7 H_0$. We forecast that the future 21 cm can constrain the ULP density fraction and the mass with an accuracy of the order of a few percent. Because of the complications due to nonlinearity, however, the ULPs with $m_u \gg 10^7 H_0$ would be hard to probe by the large-scale structure of the Universe, even though these mass ranges can be well probed by other probes such as black holes and dwarf galaxies. Further studies on the complementarity between different observables are left for future work.

Acknowledgments

We thank K. Choi and D. Marsh for the useful discussions. This work was supported by the MEXT of Japan and by French state funds managed by the ANR within the Investissements d'Avenir programme under reference ANR-11-IDEX-0004-02. The research of JS has been supported at IAP by the ERC project 267117 (DARK) hosted by Université Pierre et Marie Curie - Paris 6 and at JHU by NSF grant OIA-1124403. K.K. thanks the hospitality of IAP where this work was initiated.

References

[1] K. Kadota, Y. Mao, K. Ichiki and J. Silk, JCAP **1406**, 011 (2014) [arXiv:1312.1898 [hep-ph]].

[2] W. Hu, R. Barkana and A. Gruzinov, Phys. Rev. Lett. **85**, 1158 (2000) [astro-ph/0003365].

[3] W. Hu, Astrophys. J. **506**, 485 (1998) [astro-ph/9801234].

[4] A. Lewis, A. Challinor, A. Lasenby Astrophys. J. **538**, 473 (2000) [astro-ph/9911177].

[5] S. Furlanetto, M. Zaldarriaga and L. Hernquist, Astrophys. J. **613**, 1 (2004) [astro-ph/0403697].

[6] M. McQuinn, O. Zahn, M. Zaldarriaga, L. Hernquist and S. R. Furlanetto, Astrophys. J. **653**, 815 (2006) [astro-ph/0512263].

[7] Y. Mao, M. Tegmark, M. McQuinn, M. Zaldarriaga and O. Zahn, Phys. Rev. D **78**, 023529 (2008) [arXiv:0802.1710 [astro-ph]].

[8] S. Wyithe and M. F. Morales, [astro-ph/0703070 [ASTRO-PH]].

[9] M. Tegmark and M. Zaldarriaga, Phys. Rev. D **82**, 103501 (2010) [arXiv:0909.0001 [astro-ph.CO]], M. Tegmark and M. Zaldarriaga, Phys. Rev. D **79**, 083530 (2009) [arXiv:0805.4414 [astro-ph]].

[10] P. R. Shapiro, Y. Mao, I. T. Iliev, G. Mellema, K. K. Datta, K. Ahn and J. Koda, Phys. Rev. Lett. **110**, 151301 (2013) [arXiv:1211.2036 [astro-ph.CO]].

[11] P. A. R. Ade *et al.* [Planck Collaboration], arXiv:1303.5062 [astro-ph.CO].

[12] J. R. Bond, G. Efstathiou and M. Tegmark, Mon. Not. Roy. Astron. Soc. **291**, L33 (1997) [astro-ph/9702100].

[13] L. Knox, Phys. Rev. D **52**, 4307 (1995) [astro-ph/9504054].

[14] W. Hu and T. Okamoto, Astrophys. J. **574**, 566 (2002) [astro-ph/0111606].

[15] T. Okamoto and W. Hu, Phys. Rev. D **67**, 083002 (2003) [astro-ph/0301031].

Status of CAST and Solar Chameleon searches

T. Vafeiadis[1], *M. Arik*[2], *S. Aune*[3], *K. Barth*[1], *A. Belov*[4], *S. Borghi*[1], *H. Bräuninger*[5], *G. Cantatore*[6], *J.M. Carmona*[7], *S. A. Cetin*[2], *J. I. Collar*[8], *E. Da Riva*[1], *T. Dafni*[7], *M. Davenport*[1], *C. Eleftheriadis*[9], *N. Elias*[1], *G. Fanourakis*[10], *E. Ferrer-Ribas*[3], *P. Friedrich*[5], *J. Galán*[7,3], *J. A. Garcia*[7], *A. Gardikiotis*[11], *J. G. Garza*[7], *E. N. Gazis*[12], *T. Geralis*[10], *E. Georgiopoulou*[11], *I. Giomataris*[3], *S. Gninenko*[4], *H. Gomez*[7], *M. Gomez Marzoa*[1], *E. Gruber*[13], *T. Guthörl*[13], *R. Hartmann*[14], *S. Hauf*[15], *F. Haug*[1], *M. D. Hasinoff*[16], *D. H. H. Hoffmann*[15], *F. J. Iguaz*[7], *I. G. Irastorza*[7], *J. Jacoby*[17], *K. Jakovčić*[18], *M. Karuza*[6], *K. Königsmann*[13], *R. Kotthaus*[19], *M. Krčmar*[18], *M. Kuster*[5,15], *B. Lakić*[18], *P. M. Lang*[15], *J. M. Laurent*[1], *A. Liolios*[9], *A. Ljubičić*[18], *V. Lozza*[6], *G. Luzon*[7], *S. Neff*[15], *T. Niinikoski*[1], *A. Nordt*[5,15], *T. Papaevangelou*[3], *M. J. Pivovaroff*[20], *G. Raffelt*[19], *H. Riege*[15], *A. Rodriguez*[7], *M. Rosu*[15], *J. Ruz*[1,20], *I. Savvidis*[9], *I. Shilon*[1], *P. S. Silva*[1], *S. K. Solanki*[21], *L. Stewart*[1], *A. Tomas*[7], *M. Tsagri*[11,1], *K. van Bibber*[20], *J. Villar*[7], *J. K. Vogel*[13,20], *S. C. Yildiz*[2], *K. Zioutas*[1,11].

[1]European Organization for Nuclear Research (CERN), Genève, Switzerland
[2]Dogus University, Istanbul, Turkey
[3]IRFU, Centre d Etudes Nucléaires de Saclay (CEA-Saclay), Gif-sur-Yvette, France
[4]Institute for Nuclear Research (INR), Russian Academy of Sciences, Moscow, Russia
[5]Max-Planck-Institut fúr Extraterrestrische Physik, Garching, Germany
[6]INFN, Sezione di Trieste and Università di Trieste, Trieste, Italy
[7]Instituto de Física Nuclear y Altas Energías, Universidad de Zaragoza, Zaragoza, Spain
[8]Enrico Fermi Institute and KICP, University of Chicago, Chicago, IL, USA
[9]Aristotle University of Thessaloniki, Thessaloniki, Greece
[10]National Center for Scientific Research Demokritos, Athens, Greece
[11]Physics Department, University of Patras, Patras, Greece
[12]National Technical University of Athens, Athens, Greece
[13]Albert-Ludwigs-Universität Freiburg, Freiburg, Germany
[14]MPI Halbleiterlabor, München, Germany
[15]Technische Universität Darmstadt, IKP, Darmstadt, Germany
[16]Department of Physics and Astronomy, University of British Columbia, Vancouver, Canada
[17]J. W. Goethe-Universität, Institut fúr Angewandte Physik, Frankfurt am Main, Germany
[18]Rudjer Bošković Institute, Zagreb, Croatia
[19]Max-Planck-Institut fúr Physik (Werner-Heisenberg-Institut), München, Germany
[20]Lawrence Livermore National Laboratory, Livermore, CA, USA
[21]Max-Planck-Institut fúr Sonnensystemforschung, Katlenburg-Lindau, Germany

DOI: http://dx.doi.org/10.3204/DESY-PROC-2014-03/vafeiadis_theodoros

CERN Axion Solar Telescope (CAST) is the most powerful axion helioscope searching for axions and axion-like particles produced in the Sun. CAST completed its search for solar axions with ^{3}He buffer gas in the magnet bores, covering axion masses up to 1.2 eV. In the absence of excess X-rays it has set the best experimental limit on the axion-photon

coupling constant over a broad range of axion masses. In 2013 CAST has improved its sensitivity to solar axions with rest mass below 0.02 eV by using Micromegas detectors and it will continue in 2014 with the implementation of a second X-ray optic and a new type detector (InGrid). In 2013 CAST has extended its sensitivity into the sub-keV energy range using a silicon detector (SDD), to search for solar chameleons, extending its searches to the dark energy sector. This search will be continued in 2014 and 2015 as well with the InGrid detector. Future axion searches can improve the current axion sensitivity by 1 to 1.5 orders of magnitude with a new generation axion telescope (IAXO).

1 Introduction

Axions are stable pseudoscalars that arise from the compelling Peccei-Quinn mechanism [1] to solve the CP problem in quantum chromodynamics. Most of axion experimental searches rely on the axion coupling to two photons, allowing for axion-photon conversion in external electric or magnetic fields.

The CAST experiment is based on the axion helioscope technique [2], orienting a magnet towards the Sun. Axions could be generated in the solar center via the Primakoff effect: a photon converts into an axion in the presence of the electric field of a charged particle. The axion can be back-converted into a photon in the presence of a laboratory magnetic field. The differential solar axion flux at Earth is given by:

$$\frac{d\Phi_a}{dE_a} = 6.02 \times 10^{10} \left(\frac{g_{a\gamma}}{10^{-10}\ \mathrm{GeV}^{-1}} \right)^2 E_a^{2.481} e^{-E_a/1.205} \quad \left[\mathrm{cm}^{-2}\mathrm{s}^{-1}\mathrm{keV}^{-1}\right] \ , \tag{1}$$

where $g_{a\gamma}$ is the axion-photon coupling constant, and E_a is the axion energy (the mean axion energy is 4.2 keV). The probability of axion-photon conversion in the general case of a uniform optical medium inside a transverse and homogeneous magnetic field, which extends for length L is [3]:

$$P_{a\to\gamma} = \left(\frac{B\, g_{a\gamma}}{2} \right)^2 \frac{1}{q^2 + \Gamma^2/4} \left[1 + e^{-\Gamma L} - 2e^{-\Gamma L/2} \cos(qL) \right] \ , \tag{2}$$

with Γ the inverse photon absorption length of the medium, and the momentum transfer q given by

$$q = \left| \frac{m_\gamma^2 - m_a^2}{2E_a} \right| \ , \tag{3}$$

with m_γ being the effective photon mass in the medium,

$$m_\gamma \left[\frac{\mathrm{eV}}{c^2} \right] = 28.77 \sqrt{\frac{Z}{A} \rho \left[\frac{\mathrm{g}}{\mathrm{cm}^3} \right]} \ , \tag{4}$$

given as a function of the density ρ, the atomic number Z and atomic mass A of the medium.

The conversion probability in Eq.(2) becomes maximum when the coherence condition $qL < \pi$ is satisfied. Therefore, the experimental sensitivity is restricted to a range of axion masses. If the medium inside the magnetic field is vacuum ($\Gamma = 0$, $m_\gamma = 0$), the sensitivity is limited to masses $m_a < \sqrt{2\pi E_a/L}$ (for the CAST experimental setup, $m_a < 0.02$ eV). In order to extend the sensitivity to higher axion masses, the conversion region has to be filled with a medium

which provides an effective photon mass m_γ. As a result, the coherence is restored for a narrow mass window around $m_a = m_\gamma$.

The expected number of photons reaching an X-ray detector can be calculated as

$$N_\gamma = \int \frac{d\Phi_a}{dE_a} P_{a\to\gamma} S\ t\ dE_a \ , \tag{5}$$

where S is the effective area, and t the observation time.

2 Strategy and scientific program

The main component of the CAST experiment is the 10 m long, twin aperture LHC prototype dipole magnet, with the magnetic field of 9 T. The magnet is mounted on a moving platform which allows it to move it to follow the Sun for approximately 1.5 h during the sunrise and 1.5 h during the sunset, throughout the year. Four low-background X-ray detectors (until the end of 2012 three Micromegas and one pn-CCD/Telescope system [4]) are installed in each end of the cold bore tubes to identify the converted photons exclusively at times of alignment between the magnet and the core of the Sun (tracking), providing an axion signature. The remaining hours of the day the magnet stays idle and reference background measurements are taken.

The CAST experiment has been searching for solar axions since 2003. During 2003 and 2004, it operated with vacuum inside the magnet bores (Phase I). From the absence of excess of X-ray signal, while pointing to the Sun, it set the best experimental limit [5, 6] for the axion-photon coupling constant for axion masses up to 0.02 eV. To extend the sensitivity to higher axion masses, the experiment underwent a large upgrade in 2005 in order to operate with a buffer gas of variable density in the magnet bores (Phase II). The first part of Phase II was completed with ^{4}He as buffer gas. With 160 different pressure settings, CAST scanned the region of axion masses up to 0.39 eV, entering for the first time in the QCD axion model band in the electronvolt range [7]. In 2007 CAST upgraded again the buffer gas system, to accommodate ^{3}He as a buffer gas. In the second part of Phase II, which started in 2008 and finished in 2011, the range of axion masses up to 1.18 eV was scanned [8, 9]. Figure 1 shows the CAST published limits on the axion-photon coupling constant.

3 Status

In the period 2013 - 2015 CAST will revisit the vacuum phase to search for axion-like particles (ALPs) with improved detectors with very low background ($\sim 1 \times 10^{-6}$ s^{-1} cm^{-2} keV^{-1}). In addition, a new X-ray optics will be installed for the sunrise Micromegas line in 2014. The strategy for achieving low background detectors includes new electronics which provide more information (pulse shape analysis extended to every strip), a cosmic veto with 75% coverage in the sunset line, new shielding design and new generation Micromegas detectors specifically designed for CAST. All the detectors are calibrated in the variable energy X-ray generator line, in the PH-DT detector lab at CERN [10]. Additionally, CAST will continue searching for solar chameleons and axion-like particles, something that no other helioscope has undertaken before.

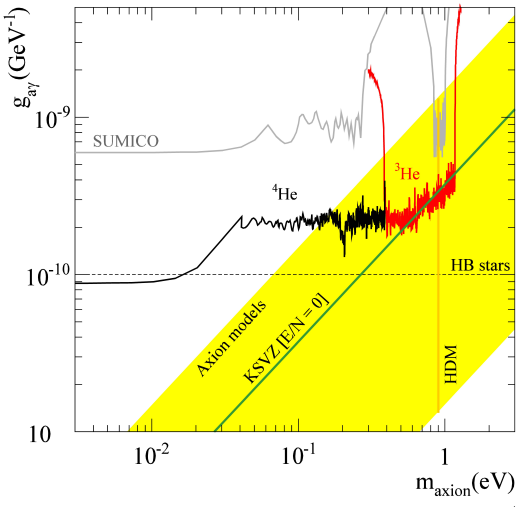

Figure 1: Exclusion regions in the $m_a - g_{a\gamma}$ plane achieved by CAST in the vacuum, ^{4}He, and ^{3}He phase. We also show constraints from the Tokyo helioscope (Sumico), horizontal branch (HB) stars, and the hot dark matter (HDM) limit. The yellow band represents typical theoretical models while the green solid line corresponds to the benchmark KSVZ model.

4 Chameleon searches

Chameleons are dark energy candidates to explain the accelerated expansion of the Universe. Their main characteristic is that their mass depends on the energy density of the environment. They can be created by the Primakoff effect in the presence of a strong magnetic field and can be converted to X-ray photons in CAST via the inverse Primakoff effect (like axions) [11].

In 2013 CAST extended its search to these dark energy particles. For this program, a windowless silicon drift detector (SDD) was chosen with high quantum efficiency, good energy resolution and a relatively large area. The detector collected 15.2 hours of tracking data and 108 hours of background in the energy range of interest from 400-1500 eV. The result of the data analysis is compatible with the null hypothesis. Figure 2 shows the expected number of counts in our detector, the subtracted counts (tracking - background) and the best fit to the data. The compatibility of the data with the absence of excess of X-rays allows the derivation of a preliminary limit to the chameleon to photon coupling constant, over a range of β_m from 1 to 10^6 (Figure 3):

$$\beta_\gamma \leq 9.20 \times 10^{10} \text{ at } 95\% \text{ CL.} \tag{6}$$

In 2014 and 2015, a new InGrid Micromegas detector will be installed on the sunrise side to search for chameleons and ALPs [13]. The effective area of the detector is 2 cm^2 , and the energy threshold well below 1 keV. It will work in combination with the existing X-ray telescope in CAST.

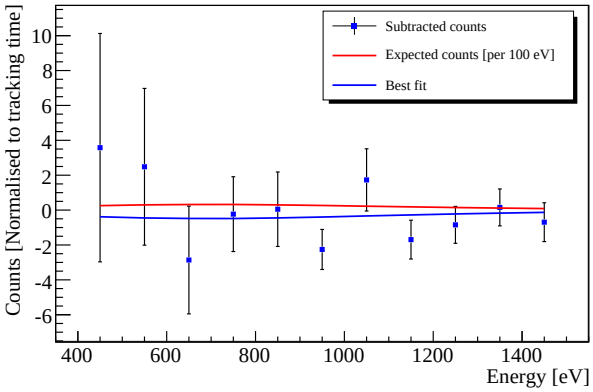

Figure 2: The expected number of photons from chameleon conversion inside the CAST magnet, that reaches the SDD is calculated from the theoretical photon spectrum arriving at the detector, from the conversion of chameleons, taking into account the total tracking time, the quantum efficiency of the detector, the magnetic length that the chameleons travel inside CAST, the absorption phenomena on the cold surface of the bSDD due to the absence of window and the area of the detector.

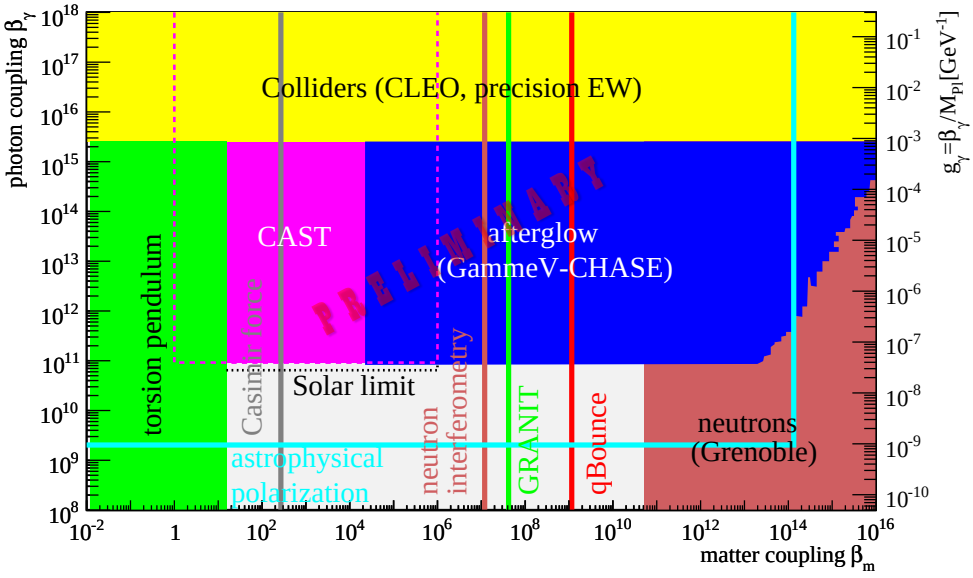

Figure 3: Constraints on the coupling of the chameleons to matter and photons [12]. The current constraints are shown as shaded regions and the future ones as solid lines. The preliminary result of CAST appears as a solid purple area. The black dashed line shows the solar limit whereas the dashed purple one shows the actual limits of sensitivity of CAST.

5 Future searches: CAST and beyond

In the following years the scientific program of CAST involves searches for chameleons and ALPs with improved sensitivity and also the R&D and feasibility study of new types of detectors like a Radiation Pressure detector, a Relic axion dish antenna and dielectric waveguide detectors destined to work inside the cold bores. In the first semester of 2017 CAST could be reconfigured to install Relic axion detectors. In addition a new generation axion telescope, IAXO (International AXion Observatory) [14] is currently at the level of the Conceptual Design. It will look for solar axions or ALPs with about 4-5 orders of magnitude higher sensitivity than CAST.

References

[1] R. D. Peccei, "The Strong CP Problem and Axions", Lect. Notes Phys. **741**, 3 (2008).

[2] P. Sikivie, "Experimental Tests of the "Invisible" Axion", Phys. Rev. Lett. **51**, 1415 (1983) [Erratum-ibid. **52**, 695 (1984)].

[3] K. van Bibber *et al*, "Design for a practical laboratory detector for solar axions", Phys. Rev. D **39**, 2089 (1989).

[4] M. Kuster *et al*, "The X-ray telescope of CAST ", New J. Phys. **9**, 169 (2007).

[5] K. Zioutas *et al* [CAST Collaboration], "First Results from the CERN Axion Solar Telescope", Phys. Rev. Lett. **94**, 121301 (2005).

[6] S. Andriamonje *et al* [CAST Collaboration], "An improved limit on the axionphoton coupling from the CAST experiment", JCAP **0704**, 010 (2007).

[7] M. Arik *et al* [CAST Collaboration], "Probing eV-scale axions with CAST", JCAP **0902**, 008 (2009).

[8] M. Arik *et al* [CAST Collaboration], "CAST search for sub-eV mass solar axions with 3He buffer gas", Phys. Rev. Lett. **107**, 261302 (2011).

[9] M. Arik *et al* [CAST Collaboration], "Search for Solar Axions by the CERN Axion Solar Telescope with He3 Buffer Gas: Closing the Hot Dark Matter Gap", Phys. Rev. Lett. **112**, 091302 (2014).

[10] T. Vafeiadis, "Contribution to the search for solar axions in the CAST experiment", CERN/Aristotle University of Thessaloniki, 2012 [CERN-THESIS-2012-349].

[11] P. Brax *et al*, "Detection prospects for solar and terrestrial chameleons", Phys. Rev. D **85**, 043014 (2012).

[12] A. Weltman, "Chameleon fields near and far", Proceedings of the PATRAS 2013 conference.

[13] C. Krieger *et al*, "An InGrid based low energy X-ray detector", Proceedings of the PATRAS 2014 conference.

[14] I. G. Irastorza *et al*, *JCAP* **1106**, 013 (2011).

Chapter 4

Neutrinos, Hidden Sector Photons and other Topics

Dark sector searches using the Higgs boson in ATLAS

Oliver K. Baker and Theodota Lagouri

Yale University, New Haven, CT USA
for the ATLAS collaboration

DOI: http://dx.doi.org/10.3204/DESY-PROC-2014-03/baker_oliver

Observational and experimental data from astrophysics, cosmology, and particle physics strongly support the possible existence of new phenomena that are beyond the standard model of particle physics. The Higgs boson may provide sensitivity to this new sector which has remained inaccessible up to now. We provide an overview of an analysis strategy to determine the ATLAS detector sensitivity to couplings of the Higgs boson to dark or hidden sector vector bosons, Z_d, that decay to leptons (muons and electrons).

Theories of fundamental interactions that are beyond the standard model (BSM) of particle physics are believed to be necessary in order to explain much natural phenomena. The standard model (SM), while extremely powerful as a theory of the strong, electromagnetic and weak interactions [1, 2, 3], does not appear to provide a natural candidate to explain Dark Matter (DM), Dark Energy, the θ term in the QCD Lagrangian, or the reason for so many free parameters in the theory. The SM may be part of or embedded in a more fundamental structure of particles and interactions at a new mass scale or with couplings that have not been previously accessible experimentally. In this case, new particles, dynamics, and symmetries that are beyond the SM could appear and signal the new physics associated with it. When the SM is embedded in a larger unified theory based, for example, on superstrings or supergravity, a hidden or "dark" sector of particles and interactions usually results [4]. Much recent attention in the theoretical community on this "dark sector" physics has been focussed on massive particles with MeV to TeV mass scales [5, 6, 7]. In astro-particle physics, the most recent satellite data from Fermi-LAT [8] and AMS-02 [9] indicate a stiffening of the positron spectra with energy from about 10 GeV up to a few hundred GeV (AMS-02: 8-275 GeV) where a behavior that decreases with energy is expected. Possible explanations for this excess are that it is attributed to more mundane phenomena such as radiation from nearby pulsars, or molecular cloud ionization. However, a strong possibility is that this excess is due to DM annihilation that proceeds through the exchange of a dark force or dark matter particle. These ideas are thus suitable for testing at the Large Hadron Collider (LHC) [10]. The bosons of the dark sector would couple only very feebly to SM fields that were used previously, in order to be consistent with observations. There could be several types of dark sector particles, with scalar, pseudoscalar, and vector intrinsic spin assignments [11].

A new probe of this hypothetical hidden or dark sector may have become available at the energy frontier opened up by the LHC. The experimental search for a Higgs boson has resulted in a new discovery at the LHC, a boson with a mass in the vicinity of 125 GeV [12, 13]. This was interpreted as a clear evidence for the production of a neutral particle and found to be

compatible with the production and decay of the SM Higgs boson. If there is a family of dark sector particles and interactions, they may couple to this Higgs boson in a unique manner that is not possible with other SM fields. This physics may therefore be accessible experimentally in a way that did not exist previously [14, 15, 4, 16, 17]. In this work, we consider the effect of the Higgs boson (H) couplings to both a dark sector (Z_d) and a SM weak vector (Z), $H \to ZZ_d \to 4l$, as well as the SM process, $H \to ZZ^* \to 4l$, where $l = e, \mu$ in both cases. Only four lepton events resulting in the new Higgs boson at approximately 125 GeV are used in the study. The search is for a narrow peak or excess above background in the Z^* spectrum (the Z^* can propagate off-shell), resulting from decays to di-leptons. An example of the process described in this work can be seen in the top process of Figure 1. The Higgs boson is produced via gluon-gluon fusion, the dominant production mechanism at the LHC. The Higgs boson would then decay into a SM Z^0 boson and a hidden sector gauge boson Z_d that subsequently decays directly into two leptons, in this case either a di-muon or di-electron pair. It is possible that the dark sector gauge boson would kinetically mix with the SM Z^* boson (if it is itself a vector boson) that then decays into di-leptons as shown in the top process of Figure 1.

Several groups in ATLAS [18] have or are presently engaged in related searches, but with very different strategies and signatures than those used in the analysis described here. Invisible Higgs searches may be used to set limits on its couplings to hidden sector particles and interactions. Analyses that attempt a search for Higgs invisible decays to a hidden sector will include an incoming gluon or quark in the production channel that radiate a single gluon or photon (mono-X events), for instance [19, 20]. The mono-X events include large amounts of missing transverse energy, and a high energy jet or photon, unlike this present study. Invisible decays of the Higgs boson may also be studied in events that include associated production with or without vector bosons, such as $q\bar{q} \to q\bar{q}H$, $gg \to ZH$ [21]. SM fields may couple to a supersymmetric hidden valley of BSM particles via a mediator messenger dark boson that itself decays to pairs of highly collimated leptons (lepton jets) [22]. The final states in those processes are similar to those of the present study, except that the former are highly collimated. Several new BSM vector bosons are predicted in models that are tested in the analysis of di-lepton decays [23]. These studies focus on high invariant mass di-lepton events so as to be consistent with LEP constraints. The direct production and decays of these predicted resonances are considered, unlike in the present study where the new hypothetical resonance couples directly to the Higgs boson and decays to

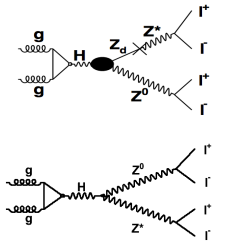

Figure 1: The Higgs boson (H) may decay into an on-shell SM Z^0 boson plus a dark sector vector boson Z_d, with kinetic mixing, as indicated in the top diagram. The bottom diagram shows the SM process where the Higgs boson decays into a Z^0 boson as well as an off-shell Z^* boson.

two leptons in the process shown at the top of Figure 1.

The process $H \to 4l$ was one of the two "discovery modes" in the search for the Higgs boson (the other being $H \to \gamma\gamma$) [12, 13, 24]. The present analysis makes use of this clear discovery channel in the search for a new dark vector boson. The search strategy is as follows:

1. The $H \to ZZ^* \to 4l$ events are the starting point for the analysis. Only those $4l$ final state events that reconstruct the resonance near 125 GeV are used in the subsequent analysis to search for Z_d.

2. The Z^0 boson invariant mass is fully reconstructed in the intermediate state and this selection is shown to agree with the Particle Data Group value.

3. Decays of the Z^* boson that propagates off the mass shell are then considered. These invariant mass events are not expected to exhibit a peak for SM events. Thus, a narrow peak or excess of events above background in this spectrum signals the new particle state, Z_d.

4. The Profile Likelihood ratio based on the the frequentist ATLAS statistical procedure [25] is used to quantify any narrow peak or excess of events above background in the subleading di-lepton invariant mass spectrum. In the absence of a signal, the search results are presented as a limit of the ratio

$$\frac{BR(H \to ZZ_d \to 4l)}{BR(H \to 4l)} \tag{1}$$

in the mass range considered.

The authors gratefully acknowledge funding support from the US Department of Energy and from the Deborah Fine Fellowship at Yale University.

References

[1] S. Weinberg, Phys. Rev. D**19**, 1264 (1967).

[2] A. Salam, in "Elementary particle theory", Almqvist and Wiksell, Stockholm, 367 (1968).

[3] S.L. Glashow, Nucl. Phys. 22, 579 (1961).

[4] M. Ahlers et.al., Phys. Rev. D**79**, 075005 (2008).

[5] Proceedings of "Dark forces at accelerators", http://www.lnf.infn.it/conference/dark/ (2010).

[6] A. Ringwald, in "Physics of the dark universe", Elsevier, Netherlands, 116 (2012).

[7] E. Dudas et.al., arXiv:1205.1520 [hep-ph] (2012).

[8] A. Abdo et.al., Phys. Rev. Lett. **102**, 181101 (2009).

[9] M. Aguilar et.al., Phys. Rev. Lett. **110**, 141102 (2013).

[10] J. Jaeckel, in "Physics of the dark universe 2", Elsevier, Netherlands, 111 (2013).

[11] R. Essig et.al., arXiv:1311.0029 [hep-ph] (2013).

[12] ATLAS collaboration, Phys. Lett. B**716**, 1 (2012).

[13] CMS collaboration, Phys. Lett. B**716**, 30 (2012).

[14] B. Patt and F. Wilczek, arXiv:0605188 [hep-ph] (2006).

[15] S. Gopalakrishna, S. Jung, and J.D. Wells, Phys. Rev. D**78**, 055002 (2008).

[16] H. Davoudiasl et.al., Phys. Rev. D**88**, 015022 (2013) .

[17] J.F. Kamenik and C. Smith, Phys. Rev. D**85**, 093017 (2012) .

[18] ATLAS collaboration, JINST **3** S08003 (2008).

[19] ATLAS collaboration, Phys. Lett. B**705**, 294 (2012).

[20] J.F. Gunion, Phys. Rev. Lett. **72**, 147 (1964).

[21] D. Choudhury and D.P. Roy, Phys. Lett. B**322**, 368 (1994).

[22] C. Cheung et.al., JHEP **1004**, 116 (2010).

[23] ATLAS collaboration, JHEP **1211**, 138 (2012).

[24] ATLAS Collaboration, arXiv:1408.5191 [hep-ex] (2014).

[25] ATLAS collaboration, Phys. Lett. B**726**, 88 (2013).

Dark Matter in Minimal $U(1)_{B-L}$ Model

Tanushree Basak[1], *Tanmoy Mondal*[1,2]

[1]Theoretical Physics Division, Physical Research Laboratory, Ahmedabad 380009, India.
[2]Department of Physics, Indian Institute of Technology, Gandhinagar, Ahmedabad, India.

DOI: http://dx.doi.org/10.3204/DESY-PROC-2014-03/basak_tanushree

We study the $B-L$ gauge extension of the Standard Model which contains a singlet scalar and three right-handed neutrinos. The third generation right-handed neutrino is qualified as the dark matter candidate, as an artifact of Z_2-charge assignment. Relic abundance of the dark matter is consistent with WMAP9 and PLANCK data, only near scalar resonances. Requiring correct relic abundance, we restrict the parameter space of the scalar mixing angle and mass of the heavy scalar boson of this model.

1 Gauged $U(1)_{B-L}$ Model

The minimal $U(1)_{B-L}$ extension of the SM [1, 2, 3, 4] contains in addition to SM : a SM singlet S with $B-L$ charge +2, three right-handed neutrinos $N_R^i (i = 1, 2, 3)$ having $B-L$ charge -1. The assignment of $\mathbb{Z}_2$-odd charge ensures the stability of N_R^3 [5, 4] which qualified as a viable DM candidate. Scalar Lagrangian of this model can be written as,

$$\mathcal{L}_s = (D^\mu \Phi)^\dagger D_\mu \Phi + (D^\mu S)^\dagger D_\mu S - V(\Phi, S)\,, \tag{1}$$

where the potential term is,

$$V(\Phi, S) = m^2 \Phi^\dagger \Phi + \mu^2 |S|^2 + \lambda_1 (\Phi^\dagger \Phi)^2 + \lambda_2 |S|^4 + \lambda_3 \Phi^\dagger \Phi |S|^2\,,$$

with Φ and S as the SM-scalar doublet and singlet fields, respectively. After spontaneous symmetry breaking (SSB) the singlet scalar field can be written as, $S = \frac{v_{B-L}+\phi'}{\sqrt{2}}$ with v_{B-L} real and positive. The mass eigenstates (H_1, H_2) are linear combinations of ϕ and ϕ' with mixing angle α. We identify H_2 as the SM-like Higgs boson with mass 125.5 GeV.

The RH neutrinos interact with the singlet scalar field S through interaction term of the lagrangian:

$$\mathcal{L}_{int} \;=\; \sum_{i=1}^{3} \frac{y_{n_i}}{2} \overline{N_R^i} S N_R^i. \tag{2}$$

Here we define, λ_{DM} as the coupling between DM candidate and the SM Higgs boson, which is effectively the Yukawa coupling of the N_R^3. Thus, the mass of dark matter is given by, $m_{DM} = m_{N_R^3} = \frac{y_{n_3}}{\sqrt{2}} v_{B-L}$.

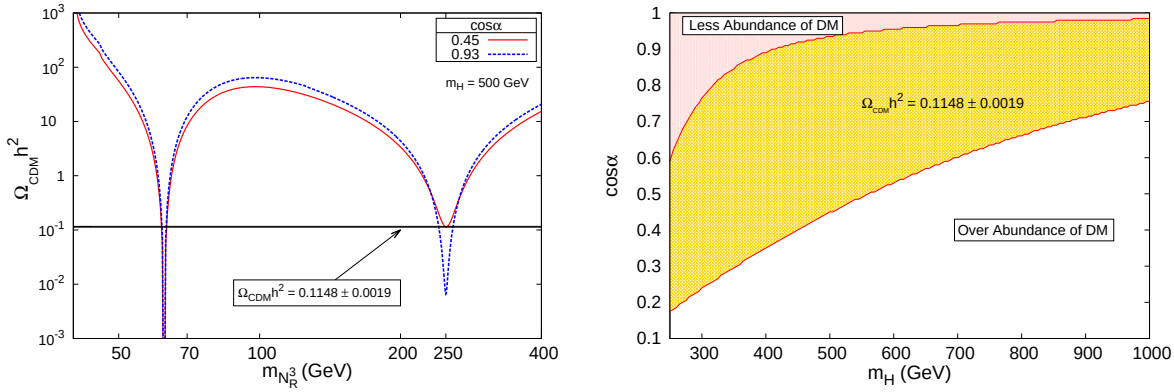

Figure 1: Left : Plot of relic abundance as a function of DM mass for $m_H = 500$ GeV with specific choices of scalar mixing angle $\cos\alpha = 0.935$ (blue-dashed), 0.45 (red-solid). The straight line shows the WMAP9 value, $\Omega_{CDM}h^2 = 0.1148 \pm 0.0019$. Right : Yellow region (in the middle) shows the allowed range of $\cos\alpha$ and m_H consistent with correct relic abundance as reported by WMAP9. The above-pink (below-white) region is disallowed due to under-abundance (over-abundance) of dark matter.

2 Dark Matter Observations

2.1 Relic Abundance

m_h	Γ_h	v_{B-L}	g_{B-L}
125 GeV	4.7×10^{-3} GeV	7 TeV	0.1

Table 1: Choice of Parameters

A specific set of benchmark values chosen is shown in Table.1. The relic abundance of DM can be formulated as [6],

$$\Omega_{CDM}h^2 = 1.1 \times 10^9 \frac{x_f}{\sqrt{g^*} m_{Pl} \langle\sigma v\rangle_{ann}} \text{GeV}^{-1} \,, \tag{3}$$

where $x_f = m_{N_R^3}/T_D$ with T_D as decoupling temperature. m_{Pl} is Planck mass $= 1.22 \times 10^{19}$ GeV, and, g^* is effective number of relativistic degrees of freedom. $\langle\sigma v\rangle_{ann}$ is the thermal averaged value of DM annihilation cross-section times relative velocity. DM interacts with the SM particles via Z'-boson and h, H. But, Z'-boson being heavy ($m_{Z'} \geq 2.33$ TeV [7]), the annihilation of DM into the SM particles takes place via h and H only. Thus, effectively we

obtain a Higgs-portal DM model. $\langle\sigma v\rangle_{ann}$ can be obtained using the well known formula [8],

$$\langle\sigma v\rangle_{ann} = \frac{1}{m^2_{N^3_R}} \left\{ w(s) - \frac{3}{2}\Big(2w(s) - 4m^2_{N^3_R} w'(s)\Big)\frac{1}{x_f} \right\}\Bigg|_{s=\left(2m_{N^3_R}\right)^2} , \tag{4}$$

where prime denotes differentiation with respect to s ($\sqrt{s}$ is the center of mass energy). Here, the function $w(s)$ depends on amplitude of different annihilation processes,

$$N^3_R N^3_R \longrightarrow b\bar{b},\ \tau^+\tau^-,\ W^+W^-,\ ZZ,\ \ hh. \tag{5}$$

In Figure. 1 the relic density is plotted against DM mass for two specific choices of scalar mixing angles. The resultant relic abundance is found to be consistent with the reported value of WMAP-9 and PLANCK experiment only near resonance when, $m_{N^3_R} \sim (1/2)\ m_{h,H}$. The reason for the over abundance of DM except at the resonance can be understood in the following way : The annihilation cross-section of DM, being proportional to $y^2_{n_3}$ (where, $y_{n_3} = (\sqrt{2}m_{N^3_R})/v_{_{B-L}}$), is heavily suppressed due to large value of $v_{_{B-L}}$.

Relic abundance near the second resonance depends on the following model parameters (unknown) : scalar mixing angle (α), heavy scalar mass (m_H) and decay width (Γ_H). For large mixing angle, the total decay width of heavy scalar is large and hence the annihilation cross-section $\langle\sigma v\rangle_{ann}$ is less compared to that with minimal mixing scenario. This behavior is observed in Figure. 1, where $\Omega_{_{CDM}}h^2$ is large for smaller value of $\cos\alpha$ (at $m_{N^3_R} \sim (1/2)\ m_H$) and vice-versa. We therefore perform a scan over the entire parameter range of m_H (300-1000 GeV) and $\cos\alpha$ (shown in Fig. 1) to find the allowed region consistent with the 9-year WMAP data [9].

2.2 Spin-independent scattering cross-section

The effective Lagrangian describing the elastic scattering of the DM off a nucleon is given by,

$$L_{eff} = f_p \bar{N^3_R} N^3_R \bar{p}p + f_n \bar{N^3_R} N^3_R \bar{n}n\ , \tag{6}$$

We obtain the scattering cross-section (spin-independent) for the dark matter off a proton or neutron as,

$$\sigma^{SI}_{p,n} = \frac{4m^2_r}{\pi} f^2_{p,n} \tag{7}$$

where, $f_{p,n}$ is the hadronic matrix element and m_r is the reduced mass.

We observe that, $\sigma^{SI}_{p,n} \propto (\sin 2\alpha)^2 f(m_H)$, which is maximum at $\alpha = \pi/4$ (or $\cos\alpha = 0.707$) irrespective of the choice of m_H. Figure. 2 shows the maximum value of spin-independent scattering cross-section (i.e, with $\cos\alpha = 0.707$) of the DM off proton (σ^{SI}_p) as a function of DM mass. We observe that the value of the resultant cross-section with two different values of m_H for the entire range 6 GeV $\leq m_{N^3_R} \leq$ 500 GeV lies much below the XENON100 and latest LUX exclusion limits. But, as the value of m_H is increased, the spin-independent cross-section becomes larger at higher values of DM mass and approaches the limits as reported by LUX and XENON100. As shown in Figure. 2, in future XENON1T data might severely restrict the choice of allowed m_H.

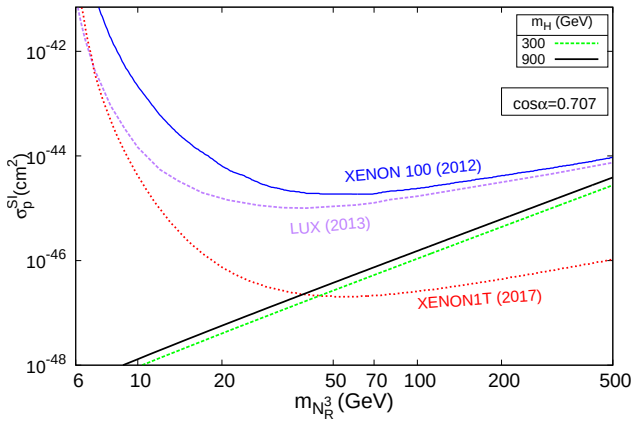

Figure 2: Variation of σ_p^{SI} with $m_{N_R^3}$ for $m_H = 300$ GeV (green-dashed) and 900 GeV (black-solid) with $\cos\alpha = 0.707$. The blue and violet curves show the bound from XENON100 [10] and LUX [11] data respectively. Red curve shows the projected limits for XENON1T [12] .

Acknowledgements

We would like to thank Joydeep Chakrabortty, Partha Konar and Subhendra Mohanty for most useful comments and discussions.

References

[1] Shaaban Khalil. Low scale B - L extension of the Standard Model at the LHC. *J.Phys.*, G35:055001, 2008.

[2] Lorenzo Basso, Stefano Moretti, and Giovanni Marco Pruna. A Renormalisation Group Equation Study of the Scalar Sector of the Minimal B-L Extension of the Standard Model. *Phys.Rev.*, D82:055018, 2010.

[3] Lorenzo Basso. Phenomenology of the minimal B-L extension of the Standard Model at the LHC. 2011.

[4] Tanushree Basak and Tanmoy Mondal. Constraining Minimal $U(1)_{B-L}$ model from Dark Matter Observations. *Phys.Rev.*, D89:063527, 2014.

[5] Nobuchika Okada and Osamu Seto. Higgs portal dark matter in the minimal gauged $U(1)_{B-L}$ model. *Phys.Rev.*, D82:023507, 2010.

[6] Edward W. Kolb and Michael S. Turner. The Early universe. *Front.Phys.*, 69:1–547, 1990.

[7] J. Beringer et al. Review of particle physics. *Phys. Rev. D*, 86:010001, Jul 2012.

[8] Mark Srednicki, Richard Watkins, and Keith A. Olive. Calculations of Relic Densities in the Early Universe. *Nucl.Phys.*, B310:693, 1988.

[9] G. Hinshaw et al. Nine-Year Wilkinson Microwave Anisotropy Probe (WMAP) Observations: Cosmological Parameter Results. 2012.

[10] E. Aprile et al. Dark Matter Results from 225 Live Days of XENON100 Data. *Phys.Rev.Lett.*, 109:181301, 2012.

[11] D.S. Akerib et al. First results from the LUX dark matter experiment at the Sanford Underground Research Facility. 2013.

[12] Elena Aprile. The XENON1T Dark Matter Search Experiment. 2012.

Hidden Photon Dark Matter Search with a Large Metallic Mirror

Babette Döbrich[1], *Kai Daumiller*[2], *Ralph Engel*[2], *Marek Kowalski*[1,3], *Axel Lindner*[1], *Javier Redondo*[4], *Markus Roth*[2]

[1]Deutsches Elektronen-Synchrotron (DESY), 22607 Hamburg and 15738 Zeuthen, Germany
[2]Karlsruher Institut für Technologie (KIT), IKP, 76021 Karlsruhe, Germany
[2]Humboldt Universität, Institut für Physik, 12489 Berlin, Germany
[4]Zaragoza University, Pedro Cerbuna 12, E-50009 Zaragoza, Spain

DOI: http://dx.doi.org/10.3204/DESY-PROC-2014-03/doebrich_babette

If Dark Matter is composed of hidden-sector photons that kinetically mix with photons of the visible sector, then Dark Matter has a tiny oscillating electric field component. Its presence would lead to a small amount of visible radiation being emitted from a conducting surface, with the photon frequency given approximately by the mass of the hidden photon. Here, we report on experimental efforts that have started recently to search for such hidden photon Dark Matter in the (sub-)eV regime with a prototype mirror for the Auger fluorescence detector at the Karlsruhe Institute for Technology.

1 Ultralight Dark Matter and the dish principle

In the literature there is no shortage of well-motivated candidates for cold Dark Matter (DM) particles. Without going into details of their respective theoretical motivation, it is however clear that there is more experimental work needed in the search for its ultra-light candidates below the eV regime: Although different detection schemes have been proposed, only a few laboratory Dark Matter searches are actively searching for low-mass particles such as QCD Axions, see, e.g., recent progress of the Axion Dark Matter eXperiment (ADMX) [1] and EDM-based techniques [2].

Considerations of general classes of ultra-light particles, dubbed 'weakly interacting slim particles' (WISPs) [3] have shown that such particles could make up the Dark Matter in a rather large parameter space: particularly axion-like particles (ALPs) and massive hidden photons (HPs) [4] can in principle constitute all of the cold Dark Matter mainly through the misalignment mechanism which is also invoked for Axions, see [5]. Whilst the viable parameter space for such ultra-light Dark Matter is likely to be further constrained from cosmological observables, ultimately laboratory experiments should be performed to have certainty on its existence.

On the experimental side, set-ups like ADMX are based on a *resonant* conversion of axions (and WISPs) and are thus ideal to find extremely weakly coupled particles in a rather narrow mass region. This is ideal for a QCD axion Dark Matter search. For covering a wider mass-range, the search for ALP and HP Dark Matter with a spherical mirror has been recently proposed [6]: Here the conversion is *not resonantly amplified* and thus the most immediate

experimental setups are less sensitive with respect to the coupling (but have the advantage of broad-band frequency/mass coverage).

Let us recapitulate the idea of the 'dish setup' for HP Dark Matter, analogous considerations hold then for ALPs[1]: The relevant term for HP DM $\tilde{\gamma}$ is photon-to-hidden-photon coupling, parameterized by the kinetic mixing parameter χ, see, e.g. [4]. It eventually leads to electromagnetic power being emitted by a conducting surface (e.g. mirror) at angular frequencies approximately corresponding to the HP mass, $\omega \simeq m_{\tilde{\gamma}}$ [6]. This is due to the presence of the HP DM together with the usual requirement that for electric fields at the conducting surface $\vec{E}|_{\parallel} = 0$. To first order, photons are emitted perpendicular to the surface, with small corrections stemming from directionality of the DM inflow (which can be used to verify its DM origin).

To detect photons induced by this process, the advantage of using a spherical mirror is imminent: photons from far away background sources impinging on the mirror will be focused in the focal point $f = R/2$ whilst the Dark-Matter-induced photons will propagate to the center of the 'mirror sphere'. There, a detector can be mounted. A small off-set away from the center can be understood as follows: Be $\vec{p}$ the momentum of the incoming DM, and $\vec{k}$ the outgoing photon momentum, then $k_{\parallel} = p_{\parallel}$ along an infinitely extended surface because there is no boundary change (the approximation is then valid as long as λ is much smaller then the surface diameter). With energy conservation $\vec{k} = \sqrt{m^2 + |\vec{p}_{\perp}|^2}\vec{n} + \vec{p}_{\parallel}$, with normal $\vec{n}$ to the surface. As for the DM $|\vec{p}| \ll m$, the angular off-set of the signal away from the center of the 'dish-sphere' is $\psi \simeq |\vec{p}_{\parallel}|/m$ and the off-set on the detector is $d_i \simeq \frac{p_i}{m} R$ when the detector is at center R and i labels directions along the surface.

Nicely, thus, such a setup has a directional sensitivity [7], which is easy to retrace within the common DM halo models. E.g., assuming an isotropic velocity distribution of the DM with respect to the galactic frame, a global off-set of the signal on the order of $\Delta d \sim \Delta v_{\text{detector}} R$ is expected due to the movement of the sun in the galactic rest frame as well as a daily modulation on the same order of magnitude (the yearly modulation is negligible due to the small velocity of the earth w.r.t. the sun). Besides the signal-spot movement, a likely velocity distribution $\Delta v_{\text{DM}} \sim 10^{-3}$ of the DM leads to a broadening of the signal spot. Ultimately, it is nice that this directional sensitivity can help to verify the Dark Matter nature of a signal.

2 Prospective sensitivity with the KIT mirror

The Pierre Auger Observatory uses two types of mirrors (coated glass and coated aluminum) [8]. Both are are segmented due to their rather large overall area of $A \simeq 13\text{m}^2$, see Fig. 2. One prototype aluminum mirror for this experiment is kept at the Karlsruhe Institute for Technology (KIT). As the mirrors are spherical with $R = 3.4$m, the metallic mirror is ideal for the Dark Matter search described above. Assuming a Dark Matter density of $\rho_{\text{CDM}} \simeq 0.3\text{GeV/cm}^3$ and assuming that HPs make up all of the Dark Matter the power emitted to the center is

$$P = \langle \alpha^2 \rangle \, \chi^2 \rho_{\text{CDM}} A_{\text{dish}} \approx \chi^2 \ (1.87 \times 10^5 \text{ Watt}) \ , \tag{1}$$

where $\langle \alpha^2 \rangle$ is a $\mathcal{O}(1)$-factor related to the polarization of the HPs [6], which we have taken to be one for simplicity. As mentioned, the experimental advantage now is that the power is concentrated at the center R of the 'mirror sphere', and not at the focal point $f = R/2$.

[1] From the experimental point of view, to look for ALP DM with this technique is rather involved, since for a decent sensitivity the mirror has to be strongly magnetized with field strengths on the order of a few Tesla [6]. For the experimental setup at KIT described here, this will likely not be possible.

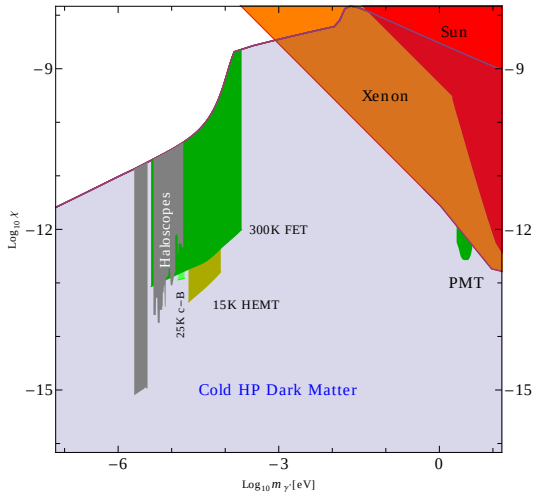

Figure 1: Hidden photon DM parameter space (blue) and exclusion regions (red/orange). In green some parameter regions accessible with the metallic mirror setup with different detector options. See text for details and [4] for a comprehensive review of the parameter space.

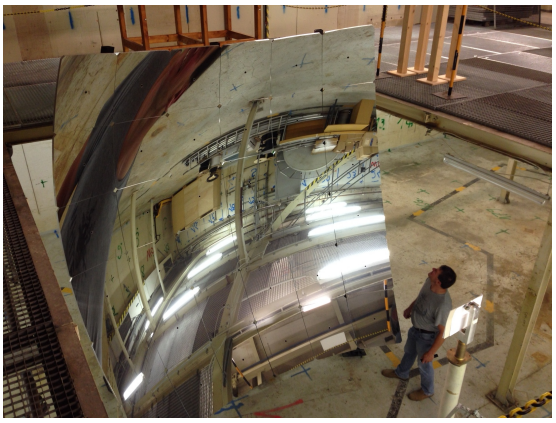

Figure 2: Spherical prototype mirror for AUGER housed at KIT (campus north). The grey post at the lower right hand side is the detector mount located in the center of curvature.

As benchmark number, one would like to probe the parameter space below $\chi = 3 \times 10^{-12}\ 1/m[\mathrm{eV}]$, which is the limit inferred from the XENON10 experiment [9], see the orange region labeled 'Xenon' in Fig. 1.

The setup described above is sensitive to all HP masses whose associated wavelength $\lambda = 2\pi/m$ can be: 1) detected by the sensor and 2) properly focused by the mirror (here we assumed $\lambda \ll R$ to use light-ray approximation and neglect diffraction, which would affect our estimates approximately below the mass range at which we cut Fig. 1).

For technological simplicity, measurements in the visible are a good starting point, although their range is a limited. As an example, labeled 'PMT' in Fig. 1, we have plotted the sensitivity range of a readily available[2], low-noise ($\lesssim$1Hz) cooled PMT with $\sim$ 25% quantum efficiency in the (300-500)nm regime at a SNR of 3 and 30h measurement time (assuming we are noise-limited by the detector, which is conceivable in the optical).

One can see that even this most simple and realistic setup is quickly sensitive to uncharted parameter space and with a set of PMTs, the near-infrared to UV range can be explored down to $\chi \sim 10^{-13}$ (the overall coverage is a bit limited in the eV-range due to the strong bounds imposed by [9]).

Since the mirror is by default set up in a room with $\mathcal{O}$(m)-thick concrete walls and further shielding can be constructed if required, measurements down to the GHz-range can be envisioned and are sensitive to larger parameter regions of HP DM. The gray regions in Fig. 1 indicate the exclusion set through a null-result of different QCD axion haloscopes as described in Sect 1.

[2]see, e.g. `http://my.et-enterprises.com/pdf/9893_350B.pdf`.

In green and yellow, again we plot parameter space accessible in principle to our set-up, here within a few minutes in an idealized situation where we are limited by detector noise (if the mirror has high reflectivity for the corresponding frequencies, its thermal emission should be low). We sketch the accessible parameter region using the Dicke radiometer equation for a 25K c receiver at hand ($\sim 3.2 - 4.2$GHz) (lighter green). For slightly higher frequencies we employ the noise figure provided in [10]. One sees that even non-cryogenic options (300K FET, darker green) can cover a neat section of parameter space, we also plot in lighter green the accessible region for a 15K HEMT (yellow).

Note the in the above considerations we have left out implications of directionality discussed in Sect 1. In the final analysis, the data sets have to be evaluated in a particular DM model in which off-set and modulation can be computed.

In summary, one sees that this rather simple setup offers many options to look for HP Dark Matter. Fig. 1 just sketches the most immediate options for this setting for good experimental conditions. If we are successful in these first steps, measurements in also in intermediate frequency ranges could be conceived. In the following months, the results of ongoing background measurements and budgetary considerations will determine our next steps.

3 Summary

Hidden Photons could constitute (part of) Dark Matter. To test this possibility, cosmological guidance and laboratory experiments are needed. A novel setup with a large metallic mirror that can probe HP masses in the $10^{-5} - 10^{0}$ eV-regime down to kinetic mixing values of $\chi \sim 10^{-13}$ is being set up at Karlsruhe. This experiment can nicely complement other broadband efforts [11] to probe even lower HP DM mass-scales with microwave cavities.

The authors acknowledge the support of the Helmholtz Alliance for Astroparticle Physics, the lasting support of many 'light-movers' [12] and the kind collaboration of I. G. Irastorza, J. Jaeckel, D. Horns, H. Krüger, A. Lobanov, H.-J. Mathes, A. Ringwald, J.-E. v. Seggern, G. Woerner and D. Veberic on different aspects of this experiment. BD would like to thank the PATRAS 2014 workshop organizers for a topical and motivating conference.

References

[1] I. P. Stern, AIP Conf. Proc. **1604**, 456 (2014) [arXiv:1403.5332 [physics.ins-det]].

[2] D. Budker *et al.*, Phys. Rev. X **4**, 021030 (2014) [arXiv:1306.6089 [hep-ph]].

[3] K. Baker *et al.*, Annalen Phys. **525**, A93 (2013) [arXiv:1306.2841 [hep-ph]].

[4] J. Jaeckel, Frascati Phys. Ser. **56**, 172 (2012) [arXiv:1303.1821 [hep-ph]].

[5] P. Arias *et al.*, JCAP **1206**, 013 (2012) [arXiv:1201.5902 [hep-ph]].

[6] D. Horns *et al*, JCAP **1304**, 016 (2013) [arXiv:1212.2970].

[7] J. Jaeckel and J. Redondo, JCAP **1311**, 016 (2013) [arXiv:1307.7181].

[8] J. Abraham *et al.* [Pierre Auger Collaboration], Nucl. Instrum. Meth. A **620**, 227 (2010).

[9] H. An, M. Pospelov and J. Pradler, Phys. Rev. Lett. **111**, 041302 (2013) [arXiv:1304.3461 [hep-ph]].

[10] S. Weinreib, W. Pospieszalski and W. Norrod, 1988 IEEE MTT-S Digest

[11] P. W. Graham, J. Mardon, S. Rajendran and Y. Zhao, arXiv:1407.4806 [hep-ph].

[12] J. Redondo and B. Döbrich, arXiv:1311.5341 [hep-ph].
`https://indico.desy.de/conferenceDisplay.py?confId=7975`

Search for Hidden Sector and Dark Matter Particles produced at Fermilab's NuMI Target.

Athanasios Hatzikoutelis[1], *Sergey Kotelnikov*[2], *Bindu A. Bambah*[3], *Siva P. Kasetti*[3]

[1]University of Tennessee Knoxville, Knoxville, TN, USA
[2]Fermi National Accelerator Laboratory, Batavia, IL, USA
[3]University of Hyderabad, Hyderabad, India

DOI: http://dx.doi.org/10.3204/DESY-PROC-2014-03/hatzikoutelis_athanasios

In the long tradition of exotic searches at fixed-target experiments, we plan to use the NuMI beam-target and the NOvA Near Detector to observe potential signatures of Hidden Sector or Dark Matter particles, either directly produced within the target or through theoretically postulated mediators. Expecting mostly scattering events on electrons or nucleons as their signatures, an example of a mediator generated scalar dark matter particles is used to discuss the target production profile of a dark matter beam. This channel explores the capabilities of the detector to observe neutral-current events from electron-neutrino scattering interactions.

1 Introduction

Worldwide, the search for New Physics particles is getting more intense. Global broken symmetries may give rise to the elusive Axion (meV) and other Axion-like-particles (ALPs) which do not bind their masses with the weak scale coupling. Particles from these *Hidden* or *Dark Sectors* (HS) are not charged under the Standard Model and they are generically referred to as *Dark Matter candidates* (DM). A brand new particle discovery will be overwhelming proof of the existence of the postulated New Sectors in nature. It will not only define the High Energy Physics research in this century, but will also give us either the first dynamic coupling, (in the case of Axions), or a view into nature's intentions, (in the case of HS), where there are no reasons to have any anthropic motivated fine tuning of parameters.

The lowest dimension operator through which HS couple to the Standard Model is called a *portal*. Several models exist such as *Vector Portal, Heavy Neutrinos Portal, Axion Portal*, and others that may explain a very weak coupling of these sectors to the standard model. Search ideas born from these portals appear in a community-wide study in [1]. Several model independent plans in this literature utilize the proximity of neutrino near detectors to intense fixed-target setups that drive accelerator-based neutrino measurements. In this work, and in [2], we estimate an example of the DM flux to a near detector. We use the Vector portal to simulate the production of a vector mediator V_χ that decays into a pair of scalar DM particles $(\chi, \chi^\dagger)$.

2 NuMI and NOνA

Currently, the most intense neutrino source is the NuMI (Neutrinos at the Main Injector) ν_μ beam. It is a fixed-target system at the end of the Main Injector (MI) accelerator complex at Fermi National Accelerator Laboratory. Neutrinos are the tertiary beam coming out of the target complex used to feed the MINOS and MINERνA experiments with a baseline power of 320 kW.

For the needs of the new flagship experiment of Fermilab called NOνA (NuMI Off-axis electron-neutrino Appearance), MI has been upgraded to 500 kW. It delivers multiple proton groups (bunches) stored in each burst (spill) of 10 μsec (Fig. 1) every 1.67 sec. Since September of 2013, it has delivered almost 3.25×10^{20} protons on the target (POT). Further upgrades to the Booster accelerator that feeds MI are expected to bring the intensity to 700 kW within a year. The projected integral beam is 5×10^{21} POT within the 6 years of the NOνA run plan. This is more intense than the most severe constraints for the production of dark matter particles in the literature (see [2]).

The main function of the NOνA Near Detector (ND) [3] is to measure, near the source, the energy spectrum and profile of the ν_μ beam and the ν_e background expectation within the range of 1-3 GeV. Its segmented design of $4cm \times 6cm$ cells and its construction of low-Z plastic material gives it an estimated energy loss of about 10 MeV/cell or $0.18X_o$/plane. This makes it very competitive for detecting electron tracks for a wide range of energies 0.1-60 GeV as shown in the study in [2].

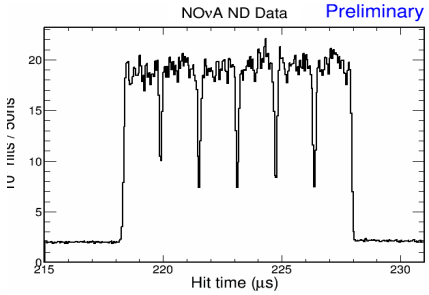

Figure 1: The NOνA timing peak (all hits) seen at the Near Detector. The full *spill* is shown arriving to the detector after the hardware imposed delay of 218 μsec and the beam structure is from the individual *bunches* of 18.8 ns each.

3 Dark matter production and flux simulation

The MI proton beam with 120 GeV on the NuMI carbon fixed target provides all of the available energy of 15 GeV for the mass of a directly produced vector mediator particle. Therefore, the sensitivity of the ND to DM extends up to 7.5 GeV. In this work, we present one example of a calculation of DM flux into the NOνA ND. We use a model of scalar DM production $(\chi, \chi^\dagger)$ for three mass cases m_χ=100, 300, and 450 MeV through the Vector Portal by the direct creation of a vector mediator particle (V_χ) of mass 1 GeV. The interaction $p + p \rightarrow V_\chi \rightarrow \chi + \chi^\dagger$ from [5] is the input to PYTHIA 8 calculation framework [6] producing the angular and energy distributions of the dark matter flux profile in Fig. 2. We chose this example so we can compare

the product distributions to a similar analytical estimation by deNiverville *et al.* in [5]. As the ND is off axis and its angular acceptance is $0.6^o - 0.8^o$ [2], we compare the 300 MeV case distribution to the same one from [5] for the forward lab-angles less than 2^o ignoring the dependence on angles away from the direction of the initial proton beam direction (Fig. 2, left). This gives us a handle for the size of production rate of DM as is estimated in [5] from various astrophysical and cosmological constraints. The energy spectrum of χ in Figure 2 right comes from events that have an angle to the beam in the lab frame within the ND acceptance range. The distributions are normalized to the total events in the 300 MeV case. The two distributions of Figure 2 make the DM beam profile.

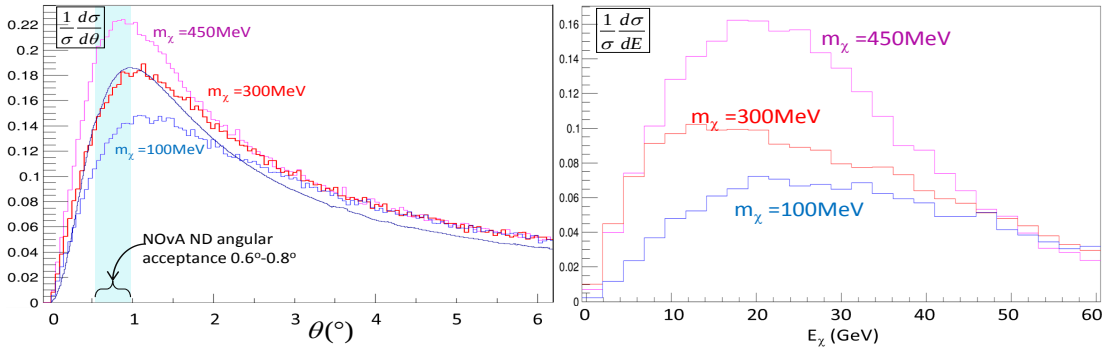

Figure 2: (left) The angular distributions of the χ's in the lab frame. The distributions are labeled by the m_χ. The 300 MeV curve is compared to the smooth curve taken from [5] and fits well for $\theta < 2^o$ within only a normalization factor. (right) The energy spectrum of the χ's that cross into the NOνA ND is normalized to the number of events from the 300 MeV curve.

4 Discussion

Figure 2 (right) shows that the energy spectrum of the dark matter extends from few to 60 GeV, peaking at around 20 GeV. This covers the complete range of the detector response to high energy signatures as seen in [2]. The large DM masses from NuMI and the ns resolution expected from the NOνA system may also allow us to use time-of-flight techniques in the DM signature reconstruction. That can keep the detection efficiency [2] be around 10^{-3}, depending only on detector acceptance and software reconstruction capabilities. Of course, in order to make a model independent measurement, the analysis of the data will proceed in the backward direction. That is, identifying any regions of excess events and attempting to interpret them from their kinematics (energy transfer to the scattered particle, direction of the scattered product, time of flight with respect to the prompt neutrino beam coincident with the accelerator cycle, etc.) and then, attempt to compare which are the most probable models predicting such distributions.

Future experiments, like LBNE [7] (expected to start in 2022), with an on-axis detector can potentially have improved time resolution, efficiency and finer granularity in the tracks but also they must compensate for the neutrino background that will be over the full energy range

of signals in the near detector. In the meantime, NOνA will have the advantage of having the neutrino background energy spectrum peeled back below 5 GeV. This may allow us to see several events in excess to the predicted neutral current spectrum, and so probing models of DM production in the order of a pico-barn of cross section for each detected event during the 6-year of the NOνA run plan.

5 Conclusions

The weak coupling of the Hidden/Dark Sectors to Standard Model make fixed target neutrino experiments sensitive to dark matter mass below 10 GeV. In anticipation to the first NOνA production runs, at the world's most intense fixed-target beam during the fall and winter of 2014 with the newly commissioned Near Detector, we have presented an example of our expectations of the source and the kinematics of the dark matter particles that could be seen in the NOνA near detector. The debate on the sensitivity is critically dependent on the model that each favors but we expect a model agnostic attidude can help find the answers within the data.

6 Acknowledgments

Operated by Fermi Research Alliance, LLC under Contract No. De-AC02-07CH11359 with the United States Department of Energy.

References

[1] E. Rouven *et al.* "Dark Sectors and New, Light, Weakly-Coupled Particles," arXiv:1311.0029 [hep-ph]. B. Batell, W. Wester, P. deNiverville, R. Dharmapalan, A. Hatzikoutelis, D. McKeen, M. Pospelov, A. Ritz and R. Van de Water, "New, light, weakly-coupled particles with Project X" chapter VII pp 142-152 of the Project-X book, editor Henderson S *et al.* (Batavia, IL: Fermi National Accelerator Laboratory).

[2] A. Hatzikoutelis, S. Kotelnikov, B. A. Bambah, S. P. Kasetti, "New light weakly-coupled particle searches in a neutrino detector." IOP Journal of Physics: Conference Series 490 (2014) 012070.

[3] A. Hatzikoutelis, "Neutrino oscillations at the intensity frontier: The NOνA experiment" IOP Journal of Phys.: Conf. Series, 410 (2013) 012146.

[4] P. deNiverville *et al.* (2011) Phys. Rev. D 84 075020.

[5] P. deNiverville *et al.* (2012) Phys. Rev. D 86 035022.

[6] T. Sjstrand, S. Mrenna, and P. Skands, "A Brief Introduction to PYTHIA 8.1" CERN-LCGAPP-2007-04, LU TP 07-28, FERMILAB-PUB-07-512-CD-T, arXiv:0710.3820 [hep-ph].

[7] LBNE Collaboration, "LBNE Science Opportunities" arXiv:1307.7335 and `http://lbne.fnal.gov/`

Do radioactive decay rates depend on the distance between the Earth and the Sun?

Karsten Kossert, Ole Nähle

Physikalisch-Technische Bundesanstalt (PTB), Bundesallee 100, 38116 Braunschweig, Germany

DOI: http://dx.doi.org/10.3204/DESY-PROC-2014-03/kossert_karsten

The potential influence of solar neutrinos on beta decay rates was investigated at PTB. To this end, new experiments have been carried out for the beta emitters ^{36}Cl and ^{90}Sr/^{90}Y, respectively. The measurements were performed using custom-built liquid scintillation counters with three photomultiplier tubes (PMTs). The data were analyzed applying the TDCR method which yields information on the counting efficiency and the activity. The activities corrected for decay were found to be stable and no oscillation could be observed. Also frequency analyses do not show any significant periodicity. Thus, we disprove the findings from several previous works of a research group working with Fischbach, Jenkins, Sturrock et al. who used data from relative measurement methods only. The data they use are not suitable to claim evidence for variations of decay rates, since the measurement techniques do not provide information on the instrument efficiency. That group also used data from our laboratory which were obtained by means of ionization chambers. We can show that the observed effects cannot be explained with an influence of solar neutrinos, whereas an influence of climate data in the corresponding measurement room appears to be a more plausible reason.

1 Introduction

In the past few years, a group of US American scientists has analyzed data of long-term measurements of several radioactive isotopes. Some of the data sets showed fluctuations with reference to the seasons, which the researchers explained by corresponding changes in the decay rate of the radionuclides (see, e.g., [1] and references therein). They attributed these fluctuations to the changes in the distance between the Earth and the Sun. With this distance, also the flux of solar neutrinos at the surface of the Earth changes which, according to these scientists, allegedly influences the decay rates. What the publications by the group have in common is that their theory is based on experimental data which were obtained by means of detector types that are known to be particularly sensitive to environmental parameters. For instance, the measurements performed on ^{32}Si, ^{36}Cl and ^{226}Ra are based on gas detectors. Moreover, these experiments were never designed to precisely measure potential variations of decay rates; some data were even taken by detectors used for radiation protection procedures.

In a recently published article [1], the American scientists have now used measurements of ^{36}Cl, which were obtained with a Geiger counter used for wipe testing of contaminations at the Ohio State University Research Reactor (OSURR). These, too, show clear fluctuations which

the authors interpret as further evidence of their theory.

Measurements on ^{90}Sr/^{90}Y were carried out by Parkhomov using a Geiger-Müller counter [2]. The data, which were later analyzed by Sturrock et al., show also timely variation with a frequency of about 1 y^{-1} [3].

2 New experiments at PTB

The beta emitter ^{36}Cl has also been investigated at PTB [4] by means of a liquid scintillation counter. For this purpose, a small amount of the radioactive material is put directly in the organic liquid scintillator, which rules out any potential problems with the self-absorption of the radiation originating from the radioactive decay inside the source itself and in the air layer between the source and the detector. The TDCR procedure allows the detection probability to be determined without an additional reference source [5]. The method compensates to a large extent for fluctuations of the detection probability due to changes in the properties of the source or of the detector and due to environmental influences. In this way, the TDCR liquid scintillation measurements exhibit a clear advantage compared to simple counting experiments with gas detectors.

The new PTB data fluctuate far less than those from the OSURR and, thus, refute a dependence of the ^{36}Cl decay rate on the distance between the Earth and the Sun. The new PTB data were also analyzed by means of a Lomb-Scargle frequency analysis before and after removing a trend which can be explained by slight colour quenching. The corresponding power spectra are shown in Fig. 1.

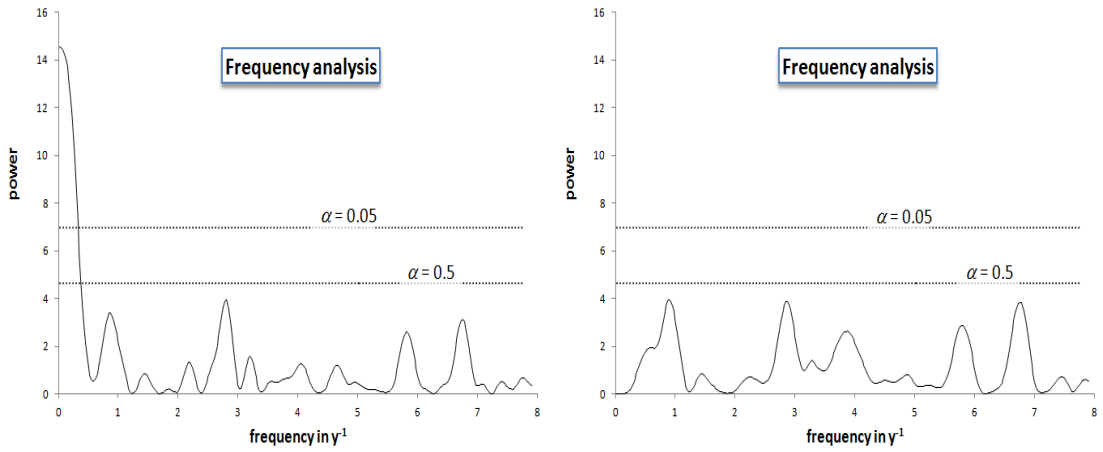

Figure 1: Periodograms obtained from a Lomb-Scargle frequency analysis applied to ^{36}Cl activity data from [4] before (left) and after (right) removal of a trend which is ascribed to colour quenching.

From April 2013 to May 2014, additional long-term TDCR measurements were carried out at PTB using ^{90}Sr/^{90}Y [6] and using a new counter with an automated sample changer. The data show no dependence on the season (Fig. 2) and, thus, refute the results published in [2] and [3] which are, again, based on measurements with a gas detector. When analyzing the data

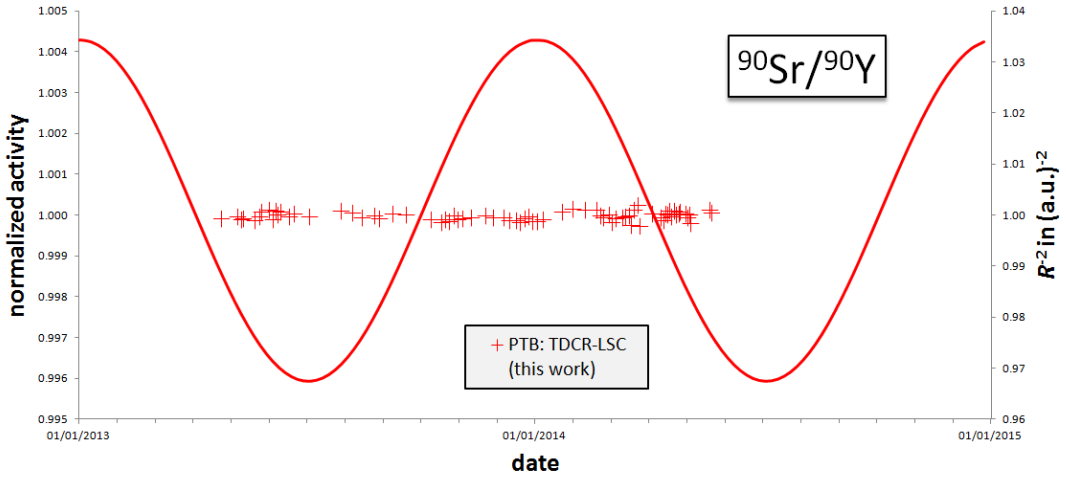

Figure 2: Normalized ^{90}Sr/^{90}Y activities measured by means of TDCR at PTB [6]. The solid line represents the squared inverse Sun-Earth distance (right ordinate).

with a frequency analysis technique, the new PTB data show no significant peak and, thus, an influence of the Moon or the Sun, as suggested in [2] and [3], can be excluded.

3 Ionization chamber measurements at PTB

In several articles, Fischbach, Jenkins, Sturrock et al. use data which were obtained by means of ionization chamber measurements in our laboratory. In a recent article [7], our laboratory is even mentioned in the article title, and we emphasize here that this does not mean that we agree with the assertions. On the contrary, we found several serious errors and the conclusions are definitely false. The main fault is that the authors of [7] equate instrument readings with decay rates. Of course, the two parameters are related via the detection efficiency. However, a claim that the decay rates vary with time would only be possible if one can ensure that the detection efficiency is constant which cannot be proved for these data. We find clear correlations between the instrument readings and the temperature or the air humidity in the corresponding measurement room. In addition, we find variations with different amplitude, different phase and different frequency when using another instrument. Thus, we can exclude the Sun or solar neutrinos as a common reason for the observed variations.

The papers from Fischbach, Jenkins, Sturrock et al. also make clear that they have only limited knowledge about the experimental data they use. For example, they report on ‘count rates’ (see, e.g., Figs. 1 to 8 in [7]) obtained from our ionization chambers whilst we are measuring ionization currents, i.e. we cannot count single events.

4 Discussion

In conclusion, our results from primary activity measurements strongly refute timely variations of decay rates. Moreover we have shown that variation in instrument reading (not in decay rates!) is more likely due to changes of other parameters such as temperature, air pressure and humidity.

In many articles by Fischbach, Jenkins, Sturrock and coworkers (we cannot cite them all) several mistakes were made. The main error is that the authors equate instrument readings with decay rates without showing clear experimental evidence that the detection efficiency is a constant. We also criticize their findings which ignore the fact that some of the data they use are in contradiction. For example, they used ^{36}Cl data from BNL to support their theory and later they used data from OSURR for the same isotope. However, both data sets do neither agree in amplitude nor do the power spectra agree. Another example is ^{90}Sr/^{90}Y: For this isotope, data from ionization chamber measurements at PTB were used which are in contradiction to the data from Parkhomov.

In our opinion, a sophisticated investigation of a potential influence of solar neutrinos to decay rates requires accurate measurements by means of primary activity standardization techniques like the TDCR method or the $4\pi\beta - \gamma$ coincidence counting method, whereas relative methods based on gas counters, scintillation counters or gamma-ray spectrometers are not sufficient.

Finally, we emphasize that a correlation does not necessarily imply causality. For example, we can also find a correlation between the flux of solar neutrinos on the Earth's surface and the mean gas consumption in Germany. However, this correlation certainly does not mean that the gas consumption is influenced by solar neutrinos.

References

[1] J.H. Jenkins, K.R. Herminghuysen, T.E. Blue, E. Fischbach, D. Javorsek II, A.C. Kauffman, D.W. Mundy, P.A. Sturrock and J.W. Talnagi, "Additional experimental evidence for a solar influence on nuclear decay rates," Astropart. Phys. 37 (2012), 81-88.

[2] A.G. Parkhomov, "Deviations from beta radioactivity exponential drop," J. Mod. Phys. 2 (2011) 1310-1317.

[3] P.A. Sturrock, A.G. Parkhomov,E. Fischbach, J.H. Jenkins, "Power spectrum analysis of LMSU (Lomonosov Moscow State University) nuclear decay-rate data: Further indication of r-mode oscillations in an inner solar tachocline," Astropart. Phys. 35 (2011) 755-758.

[4] K. Kossert, O.J. Nähle, "Long-term measurements of ^{36}Cl to investigate potential solar influence on the decay rate," Astropart. Phys. 55 (2014) 33-36.

[5] R. Broda, P. Cassette, K. Kossert, 2007. "Radionuclide metrology using liquid scintillation counting," Metrologia 44 (2007) S36-S52 (Special issue on radionuclide metrology).

[6] K. Kossert, O.J. Nähle, "Disproof of solar influence on the decay rates of ^{90}Sr/^{90}Y," submitted to Astropart. Phys., arXiv:1407.2493.

[7] P.A. Sturrock, E. Fischbach, D. Javorsek II, J.H. Jenkins, R.H. Lee, J. Nistor, J.D. Scargle, "Comparative study of beta-decay data for eight nuclides measured at the Physikalisch-Technische Bundesanstalt," Astropart. Phys. 59 (2014) 47-58.

Astroparticles and extra dimensions

A. Nicolaidis

Theoretical Physics Department
Aristotle University of Thessaloniki
54124 Thessaloniki, Greece
nicolaid@auth.gr

DOI: http://dx.doi.org/10.3204/DESY-PROC-2014-03/nikolaidis_argyris

In theories with large extra dimensions, besides the graviton living in the bulk, particles which are singlets under the standard model may live in extra dimensions. A singlet neutrino can live in the bulk and its mixing with a standard flavor neutrino offers unconventional patterns of neutrino matter oscillations. These oscillations depend upon two parameters: the brane-bulk coupling ξ and the effective mass μ of the flavor neutrino inside matter. With a 1 km^3 neutrino telescope, extra dimensions with a radius down to 1 μm can be tested directly. An axion particle can live also in extra dimensions. We consider the photon axion mixing and analyze the eigenvalues and eigenstates of the mixing matrix. A resonance condition for the total conversion of a high energy photon into a Kaluza-Klein (KK) axion state is established. This resonant transition may provide a plausible explanation for the transparency of the universe to energetic photons. If the brane we live in is curved, then there are shortcuts through the bulk, which the axion can take. We suggest that such axionic shortcuts are at the root of the dispersion of time arrival of photons.

1 Introduction

The standard model (SM) of strong and electroweak interactions has been extremely successful. It provides a consistent theoretical framework within which we can analyze and understand all available experimental data. Still we know that it cannot be regarded as the final theory. Any attempt to include quantum gravity leads to a unified theory where two disparate scales coexist: the electroweak scale ($M_W \sim 1$ TeV) and the Planck scale ($M_{Pl} \sim 10^{19}$ GeV). Quantum radiative corrections then, especially in the scalar sector (Higgs field) of the theory, tend to mix the scales and, without an incredible amount of fine-tuning, will always equalize them (the hierarchy problem). A novel approach has been suggested to alleviate the hierarchy problem [1]. Our four-dimensional world is embedded in a higher dimensional space with D dimensions ($D = 4+n$). While the SM fields are constrained to live on the 4-dimensional brane, gravity can freely propagate in the higher-dimensional space (bulk). The fundamental scale M_f of gravity in D dimensions is related to the observed 4-dimensional Planck scale M_{Pl} by

$$M_{Pl}^2 = M_f^{2+n} V_n, \tag{1}$$

where V_n is the volume of the extra space. For a torus configuration

$$V_n = (2\pi)^n \, R_1 R_{2...} R_n, \tag{2}$$

with R_i $(i = 1, 2, ...n)$ the radii of extra dimensions. Then for a sufficiently large volume V_n the fundamental scale of gravity M_f can become as low as M_W . In this radical way the hierarchy problem ceases to exist as such.

Besides the graviton, fields which are standard-model singlets, like a sterile neutrino [2-4] or an axion [5-7] can freely propagate in the bulk. These particles accrue then an infinite tower of Kaluza-Klein (KK) excitations and the issue of mass eigenstates and mixing has to be revisited.

In the next part we consider how the Yukawa coupling of the standard lepton doublet, the Higgs scalar and the right-handed bulk neutrino, will provide a mixing between the left handed neutrino of the standard model and the KK modes. We focus our attention on neutrino oscillations, inside matter. Compared to the usual oscillations, novel features appear since now we have a coupled system of infinite degrees of freedom. The pattern of oscillations depends upon two parameters: the coupling ξ between the left-handed neutrino and the KK states and the effective mass μ of the flavor neutrino. We study in detail this dependence.

In the third part we consider the photon-axion mixing, induced by a magnetic field. Compared to the usual oscillations, novel features appear linked to the presence of the new scale, the radius of the extra dimension (or its inverse, the mass of the Kaluza-Klein excitation). We study in detail the eigenvalues and eigenstates of the mixing matrix and establish the resonance condition for the total conversion of a high energy photon into a KK axion state. We examine also the astrophysical implications of our formalism, notably the production and propagation of photons in sites of strong magnetic fields (neutron stars, GRBs). A photon-generated KK axion can take a "shortcut" through the bulk and appear earlier, compared to a photon traveling along a geodesic on the brane. We quantify this effect and analyze its relevance for the timing of photons observed by the MAGIC telescope during an activity of Markarian 501. At the end we present our conclusions.

2 Sterile neutrino in large extra dimensions

There is already an extensive literature on neutrinos living in extra dimensions [8–20]. We start by considering the action for a massless bulk fermion Ψ living in 5 dimensions

$$S_\Psi = \int d^4x dy \bar{\Psi} \Gamma^\mu \partial_\mu \Psi, \qquad M = 0, 1 \ldots 5. \tag{3}$$

Ψ is decomposed as

$$\Psi = \begin{pmatrix} N_R \\ N_L \end{pmatrix}, \tag{4}$$

with each component admitting a Fourier expansion

$$N(x, y) = \frac{1}{\sqrt{2\pi R}} N_0(x) + \sum_{n=1}^{\infty} \frac{1}{\sqrt{\pi R}} \left(N_n(x) \cos\left(\frac{ny}{R}\right) + \hat{N}_n(x) \sin\left(\frac{ny}{R}\right) \right). \tag{5}$$

Thus at the brane the bulk fermion appears as a KK tower. Since the momentum in the extra compact dimension is quantized, each KK mode appears as having a mass n/R $(n = 1, 2, \ldots)$. Consider now the coupling of the standard left-handed lepton doublet to the bulk neutrino

$$\frac{h}{\sqrt{M_f}} \bar{L} H N_R \delta(y), \tag{6}$$

where H is the Higgs scalar doublet and h a dimensionless Yukawa coupling. After the Higgs field develops a vacuum expectation value (v), we get the mass terms

$$m\bar{\nu}_L \left(N_{R0} + \sqrt{2} \sum_{n=1}^{\infty} N_{Rn} \right), \tag{7}$$

with $m \sim hvM_f/M_{Pl}$. Notice that for $M_f \sim 1$ TeV, $h \sim 1$, we obtain $m \sim 10^{-4}$ eV [8-13]. Also, the left-handed zero mode N_{L0} decouples from the spectrum and remains massless. Denoting

$$\Psi_R = \begin{pmatrix} N_{R0} \\ N_{Ri} \end{pmatrix}, \qquad \Psi_L = \begin{pmatrix} \nu_L \\ N_{Li} \end{pmatrix}, \quad i = 1, 2, \ldots, \tag{8}$$

the mass term is $\bar{\Psi}_L M \Psi_R$ with the mass matrix M given by [10]

$$M = \begin{pmatrix} m & \sqrt{2m} & \sqrt{2m} & \cdots \\ 0 & 1/R & 0 & \cdots \\ 0 & 0 & 2/R & \cdots \\ \vdots & \vdots & \vdots & \ddots \end{pmatrix}. \tag{9}$$

The evolution of the neutrino states is determined by the Hamiltonian

$$H = \frac{1}{2E_\nu} M M^T. \tag{10}$$

We define $\xi = mR$. For a muon neutrino traveling inside matter the effective mass takes the form $\mu = \sqrt{2} E_v R^2 G_F N_n$ with N_n the neutron density. The eigenvalues λ_n^2 of the mass matrix satisfy the equation

$$\left[\mu - \lambda^2 + \xi^2 (\lambda\pi) \cot (\lambda\pi) \right] \prod_{n=1}^{\infty} \left(n^2 - \lambda^2 \right) = 0. \tag{11}$$

A resonance occurs whenever the condition is satisfied

$$\mu_R = \lambda_n^2 \tag{12}$$

For $n = 1$, the condition becomes [20]

$$\left(\frac{\rho}{10 \frac{g}{cm^3}} \right) \left(\frac{E_\nu}{100\, GeV} \right) \left(\frac{R}{1\, \mu m} \right) \simeq 1, \tag{13}$$

with ρ the density of the medium, E_ν the neutrino energy and R the radius of the large extra dimension.

Notice at figure 1, that an impressive resonance structure appears and by reading the energy and using Equ.(13) we can extract the value of the radius R.

3 Axion in large extra dimensions

Pecci-Quinn (PC) solution to the strong CP problem in QCD [7], predicts the existence of a neutral, spin-zero pseudoscalar particle, the axion. Axions and photons oscillate into each other in an external magnetic field [21, 22] due to the interaction term

$$\mathcal{L}_{int} = \frac{1}{f_{PQ}} \alpha F_{\mu\nu} \tilde{F}_{\mu\nu} = \frac{4}{f_{PQ}} \alpha \vec{E} \cdot \vec{B} \tag{14}$$

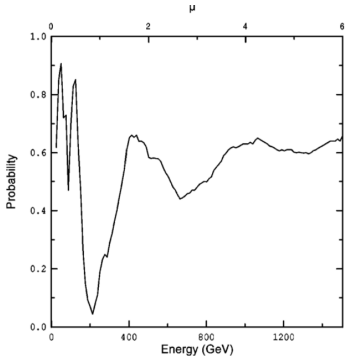

Figure 1: The probability $P(\nu_\mu \to \nu_\mu)$ for a neutrino traversing 10649 Km through the mantle of the Earth (with density $\rho \sim 4.4\, g/cm^3$), as a function of energy.

where $F_{\mu\nu}$ is the electromagnetic field tensor, $\tilde{F}_{\mu\nu}$ is its dual, α is the axion field. The mass m_{PQ} of the standard axion, as well as the axion-photon coupling is inversely proportional to the scale f_{PQ}. For a recent account of the axion searches see ref [23].

To simplify the calculation for the higher-dimensional case, we consider one extra compact dimension y and a singlet axion field $\alpha(x^\mu, y)$. Projected into the brane the axion field will appear as a collection of KK modes $a_n(x^\mu)$, each having a mass $m_n = \frac{n}{R}$, where R is the compactification radius. The coupling of the KK axions to the photon is universal [5, 6, 24, 25]

$$\mathcal{L}_{int} = \frac{1}{f_{PQ}} \sum_n \alpha_n F_{\mu\nu} \tilde{F}_{\mu\nu} \tag{15}$$

The mixing matrix M between the photon state $A_{||}$ parallel to the magnetic field B, the standard PQ axion α_0 and the KK axions α_n is [6]

$$M = \begin{pmatrix} \Delta_\gamma & \Delta_B & \Delta_B & \cdots & \Delta_B \\ \Delta_B & \Delta_0 & 0 & \cdots & 0 \\ \Delta_B & 0 & \Delta_1 & \cdots & 0 \\ \vdots & \vdots & \vdots & \ddots & \vdots \\ \Delta_B & 0 & 0 & & \Delta_N \end{pmatrix} \tag{16}$$

where

$$\Delta_\gamma = \frac{\omega_{pl}^2}{2E}, \quad \Delta_0 = \frac{m_{PQ}^2}{2E}, \quad \Delta_n = \frac{n^2}{2ER^2}, \quad \Delta_B = \frac{4B}{f_{PQ}} \tag{17}$$

The plasma frequancy is $\omega_{pl}^2 = (4\pi\alpha n_e)/m_e$ for an electron density n_e.

The next step is to establish the eigenvalues and the eigenvectors of the mixing matrix M. The resonant condition for the transition of the photon to the first KK axion (the most dominant transition) takes the form, in actual units [27]

$$\left(\frac{E}{500\, GeV}\right)\left(\frac{R}{10^{-3}\, cm}\right)^2\left(\frac{B}{10^7 G}\right)\left(\frac{10^{12}\, GeV}{f_{PQ}}\right) = 1.0 \tag{18}$$

Within this scheme, photons of high energy produced in an active nucleus are transformed through an MSW type resonance into KK axions, which travel unimpeded before being reconverted back into photons. For photons not satisfying the resonance condition, the probability to transit as KK axions is reduced and therefore these photons are limited by the opacity of two photon annihilation into an electro-positron pair. Our approach offers a plausible explanation for the transparency of the universe to energetic photons [26]. Photons of the appropriate energy, are transformed into KK axions, travel freely in the bulk space, before returning back into the brane and observed again as photons [27]. The same mechanism may provide also high energy photons escaping the GZK cutoff [28].

The advent of imaging atmospheric Cerenkov telescope like HESS, MAGIC, VERITAS, FERMI, CTA, allows the detection of photons from astrophysical sources (neutron stars, GRB, AGN) in the high energy window from 100 GeV to few TeV .The MAGIC telescope analyzed the timing of photons originating from the Mkn 501 source [29]. It was found that the photons in the $0.25-0.6\,TeV$ energy range precede by 4 minutes the photons in the $1.2-10\,TeV$ energy band. The observed features might be possible to be explained within an astrophysical context [30]. A particle physics solution, within the framework of quantum gravity [31, 32] has been suggested also. Quantum fluctuations of space-time lead to a speed of light dependent upon energy, thus creating a dispersion in the time arrival of photons [33].

The transition of a photon to a KK axion, offers another alternative to analyze the observed dispersion in time arrival of high energy photons [27]. A particle, travelling from a point on the brane to another point on the brane, may take a "shortcut" by following a geodesic in the bulk and arriving earlier compared to a particle which follows a geodesic on the brane [34]. In our case a photon, transformed into a KK axion traveling through the bulk, may reappear earlier on the brane, compared to a photon stuck in the brane. There are a number of ways shortcuts emerge in theories with extra dimensions. In a brane containing matter and energy, self-gravity will induce a curvature to the brane, so that the brane becomes concave towards the bulk in the null direction. Then we can find geodesics in the bulk propagating signals faster compared to the geodesics in the brane [34]. A phenomenology, with a sterile neutrino shortcuting through the bulk has been developed [35, 36], accounting for all neutrino oscillation data. A $1+1$ dimensional toy model may exhibit the expected behavior [35]. In a Minkowski metric

$$ds^2 = dt^2 - dx_1^2 - dx_2^2 \tag{19}$$

the curved brane is represented by

$$x_2 = A\sin(kx_1) \tag{20}$$

while the bulk geodesic is given by $x_2 = 0$. A signal transmitted through the bulk will appear as having a superluminal speed. Equivalently a difference in time arrival will be observed given by

$$\frac{t_\gamma - t_\alpha}{t_\gamma} \simeq \left(\frac{Ak}{2}\right)^2 \tag{21}$$

where t_γ is the time it takes for the photon in the brane and t_α is the corresponding time for the photon which uses the axionic shortcut. Within our model, the photons having the resonance energy, eq.(18), use the axionic shortcut and arrive earlier compared to the other photons of different energies which propagate along the brane. From the MAGIC experimental data we infer that the $0.25 - 0.6\,TeV$ photon energy brackets the aforementioned resonance energy. The amount of the time difference is determined by the brane shape-parameter Ak and the

rauge of the magnetic field B. The magnetic field near the core of a GRB or a blazar reaches high values. We adopt the average value of $B = 10^7\,G$. By appealing to the Hillas criterion [37] we obtain a range for the magnetic field of the order of $10^9\,km$. Then the set of values $R = 10^{-3}\,cm$, $f_{PQ} = 10^{12}\,GeV$, $B = 10^7\,G$, $E = 500\,GeV$, $\Delta t = 4\,min$, implies for the shape parameter the value $Ak \simeq 1$ [27]. Monitoring the astrophysical sites, where high energy photons are produced in the presence of strong magnetic fields, might be revealing. We might observe the disappearance of high energy photons connected to the photon-KK axion transition. Or, we might notice the sudden appearance of high energy photons, connected to the intrusion of KK axions from the bulk into the brane.

4 Conclusions

We analyzed the situation where the left-handed muon neutrino of the standard model mixes with a right-handed neutrino experiencing a large extra space dimension. This mixing induces neutrino oscillations, even if the neutrino itself is massless. We encountered novel features compared to the standard oscillations, since the mixing involves an infinity of KK states. A rich resonance structure appears accompanied by many spikes. We emphasized that the 1 km^3 neutrino telescope may be used as an instrument to explore the bulk space and establish unambiguously the existence of extra dimensions with $R > 1\,\mu m$.

We studied also the photon-axion oscillation in the presence of extra dimensions. Next to the standard scales, a new scale is introduced, the size R of the extra dimension, or its inverse the KK mass excitation. An MSW-type resonance occurs at high energies between the photon and the KK axion. This resonance transition $A\,(\gamma \to \alpha \to \gamma)$ allows the photon to travel unimpeded from a dense and opaque medium, offering the ground for a rich phenomenology. It is highly plausible that our brane is curved creating the possibility of shortcut through the bulk. We suggested that an axionic shortcut may be at the origin of the dispersion in the time arrival of the photons observed by the MAGIC telescope.

References

[1] I. Antoniadis, Phys. Lett. **B246**, 377 (1990); N. Arkani-Hamed, S. Dimopoulos, and G. Dvali, *ibid.* **429**, 263 (1998); I. Antoniadis, N. Arkani-Hamed, S. Dimopoulos, and G. Dvali, *ibid.* **436**, 257 (1998).

[2] R. Barbieri, P. Creminelli, and A. Strumia, Nucl. Phys. **B585**, 28 (2000).

[3] R. Mohaparta, S. Nandi, and A. Perez-Lorenzana, Phys. Lett. **B466**, 115 (1999).

[4] A. Lukas, P. Ramond, A. Romanino, and G. Ross, Phys. Lett. **B495**, 136 (2000).

[5] S. Chang, S. Tazawa and M. Yamaguchi, *Axion model in extra dimensions with TeV scale gravity*, Phys. Rev. **D61**, 084005 (2000)

[6] C. Deffayet and J.-P. Uzan, *Photon mixing in universes with large extra-dimensions*, Phys. Rev. **D62**, 063507 (2000)

[7] R.D. Peccei and H.R. Quinn, *CP conservation in the presence of instantons*, Phys. Rev. Lett. **38**, 1440 (1977); *Constraints imposed by CP conservation in the presence of instantons*, Phys. Rev. **D16**, 1791 (1977).

[8] N. Arkani-Hamed, S. Dimopoulos, G. Dvali, and J. March- Russsell, Phys. Rev. **D65**, 024032 (2002).

[9] K. Dienes, E. Dudas, and T. Ghergetta, Nucl. Phys. **B557**, 25 (1999).

[10] R. Barbieri, P. Creminelli, and A. Strumia, Nucl. Phys. **B585**, 28 (2000).

[11] R. Mohaparta, S. Nandi, and A. Perez-Lorenzana, Phys. Lett. **B466**, 115 (1999).

[12] A. Lukas, P. Ramond, A. Romanino, and G. Ross, Phys. Lett. **B495**, 136 (2000)

[13] G. Dvali and A. Smirnov, Nucl. Phys. **B563**, 63 (1999).

[14] K. Dienes and I. Sarcevic, Phys. Lett. **B500**, 133 (2001).

[15] A. Das and O. Kong, Phys. Lett. **B470**, 149 (1999).

[16] D. Caldwell, R. Mohaparta, and S. Yellin, Phys. Rev. **D64**, 073001 (2001).

[17] N. Cosme, J. Frere, Y. Gouverneur, F. Ling, D. Monderen, and V. Van Elewyck, Phys. Rev. **D63**, 113018 (2001).

[18] C.S. Lam and J.N. Ng, Phys. Rev. **D64**, 113006 (2001).

[19] A. de Gouvea, G. Giudice, A. Strumia, and K. Tobe, Nucl. Phys. **B623**, 395 (2002).

[20] A. Nicolaidis and D. T. Papadamou, Phys. Rev. **D66**, 013005 (2002)

[21] P. Sikivie, *Experimental tests of the "invisible" axion*, Phys. Rev. Lett. 51, 1415 (1983) [Erratum *ibid.* **52** (1984) 695]

[22] G. Raffelt and L. Stodolsky, *Mixing of the photon with low mass particles*, Phys. Rev. **D37**, 1237 (1988)

[23] K. Zioutas, M. Tsagri, T. Papaevangelou and T. Dafni, *Axion searches with helioscopes and astrophysical signatures for axion(-like) particles*, New J. Phys. **11**, 105020 (2009)

[24] S. Chang, S. Tazawa and M. Yamaguchi, *Axion model in extra dimensions with TeV scale gravity*, Phys. Rev. **D61**, 084005 (2000)

[25] L. Di Lella, A. Pilaftsis, G. Raffelt and K. Zioutas, *Search for solar Kaluza-Klein axions in theories of low-scale quantum gravity*, Phys. Rev. **D62**, 125011 (2000)

[26] A. De Angelis, O. Mansutti and M. Roncadelli, *Evidence for a new light spin-zero boson from cosmological gamma-ray propagation?*, Phys. Rev. **D76,** 121301 (2007)

[27] A. Nicolaidis, *Axionic shortcuts for high energy photons*, JCAP04, 013, 2010

[28] D.S. Gorbunov, G.G. Raffelt and D.V. Semikoz, *Axion-like particles as ultrahigh-energy cosmic rays?*, Phys. Rev. **D64,** 096005 (2001)

[29] J. Albert et al., *Variable VHE gamma-ray emission from Markarian 501*, Astrophys. J. **669,** 862 (2007)

[30] A. Mastichiadis and K. Moratis, *On the rapid TeV flaring activity of Markarian 501*, Astron. Astrophys. **491**, L37 (2008)

[31] G. Amelino-Camelia, J. Ellis, N. Mavromatos, D. Nanopoulos and S. Sarkar, *Tests of quantum gravity from observations of γ-ray bursts*, Nature **393**, 763 (1998) [Erratum ibid. **395** (1998) 525]

[32] J.R. Ellis, K. Farakos, N.E. Mavromatos, V.A. Mitsou and D.V. Nanopoulos, *Astrophysical probes of the constancy of the velocity of light*, Astrophys. J. **535**, 139 (2000)

[33] MAGIC collaboration, J. Albert et al., *Probing quantum gravity using photons from a flare of the active galactic nucleus Markarian 501 observed by the MAGIC telescope*, Phys. Lett. **B668**, 253 (2008)

[34] H. Ishihara, Causality of the brane universe, Phys. Rev. Lett. 86 (2001) 381

[35] H. Päs, S. Pakvasa and T.J. Weiler, Sterile-active neutrino oscillations and shortcuts in the extra dimension, Phys. Rev. D 72 (2005) 095017

[36] S. Hollenberg, O. Micu, H. P¨ as and T.J. Weiler, Baseline-dependent neutrino oscillations with extra-dimensional shortcuts, Phys. Rev. D 80 (2009) 093005

[37] A.M. Hillas, The origin of ultrahigh-energy cosmic rays, Ann. Rev. Astron. Astrophys. 22 (1984) 425

Status report of Microwave Cavity Hidden Sector Photon searches at The University of Western Australia

Stephen R. Parker[1]*, Michael E. Tobar*[1]

[1]School of Physics, The University of Western Australia, Australia

DOI: http://dx.doi.org/10.3204/DESY-PROC-2014-03/parker_stephen

We report on the latest work on microwave frequency hidden sector photon searches performed at The University of Western Australia (UWA). This includes recent efforts to design an experiment to try and constrain the strength of photon / hidden sector photon mixing via measurements of resonance frequency shifts in a pair of microwave resonant cavity structures.

1 Light shining through a wall

One of the most sensitive laboratory-based search techniques for hidden sector photons (and similar particles) is the Light Shining through a Wall (LSW) experiment, whereby photons are generated on one side of an impenetrable barrier and then photon detection is attempted on the other side, presumably having crossed the barrier by mixing with hidden sector photons. In the microwave domain, mode-matched resonant microwave cavities can be used for the generation and detection of photons (Fig. 1). Experimental sensitivity is ultimately dictated by cavity design and losses, amount of power in the emitting cavity and noise in the detecting cavity and readout electronics.

In our most recent work the emitting cavity was a room temperature copper cavity housed in a vacuum chamber. A loop oscillator circuit and temperature control was used to prevent frequency drifting. The detector cavity was a superconducting niobium cavity operated at 4 K, the first stage amplifier had a noise temperature of 4 K. The TM_{020} resonant mode was used with a frequency of 12.8 GHz. Bounds obtained for photon-hidden sector photon mixing are shown in Fig. 2 [1].

2 Hidden Sector Photon coupling of resonant cavities

LSW experiments focus on the one way flow of hidden sector photons from a driven emitter cavity to an undriven detection cavity. However, it is also possible to treat the two-way exchange of hidden sector photons as a weak coupling between the cavities, creating a system analogous to two spring-mass oscillators connected via a third weak spring. When both cavities are actively driven the hidden sector photon mediated coupling will cause a phase-dependent

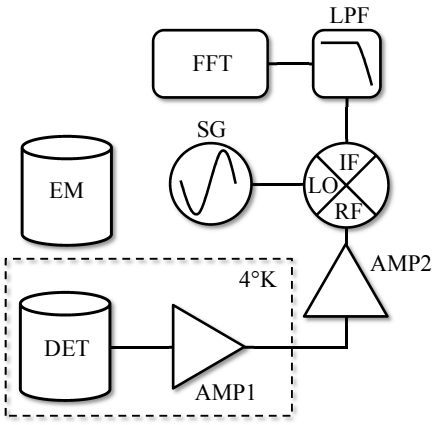

Figure 1: Schematic of detector cavity and readout circuit for a LSW search. FFT = Fast Fourier transform vector signal analyzer, LPF = low pass filter, SG = signal generator and AMP = amplier. The dashed rectangle represents the cryogenic environment..

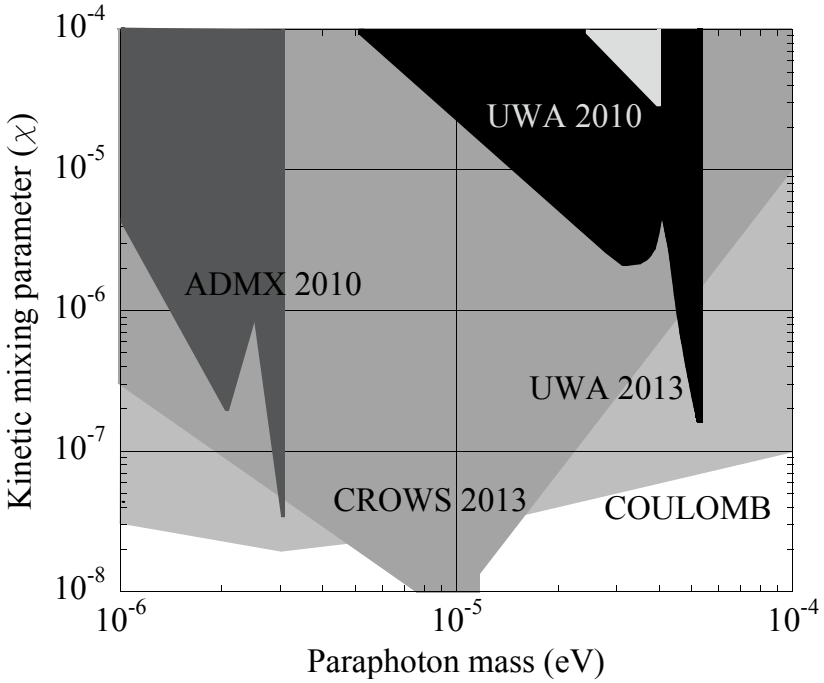

Figure 2: Limits on the kinetic mixing parameter, χ, as a function of hidden sector photon mass. The mass range corresponds to frequencies from 240 MHz to 24 GHz. Different shaded regions correspond to bounds obtained by other experiments, with the bounds from this work presented in black.

shift in the resonance frequencies and quality factors of the system. This opens up the possibility of conducting experiments that constrain the strength of photon-hidden sector photon mixing by observing this coupling induced resonant frequency shift. With careful experimental design these searches could be more sensitive than standard LSW measurements [2].
The effect on the cavity resonance frequencies due to coupling is demonstrated in Fig. 3. Strength of the coupling can be manipulated through alterations or modulations of the two cavity fields, geometries and relative positions. Figure 4 sketches out how an experiment could be made to constrain the kinetic mixing parameter, χ, with a measurement of frequency.

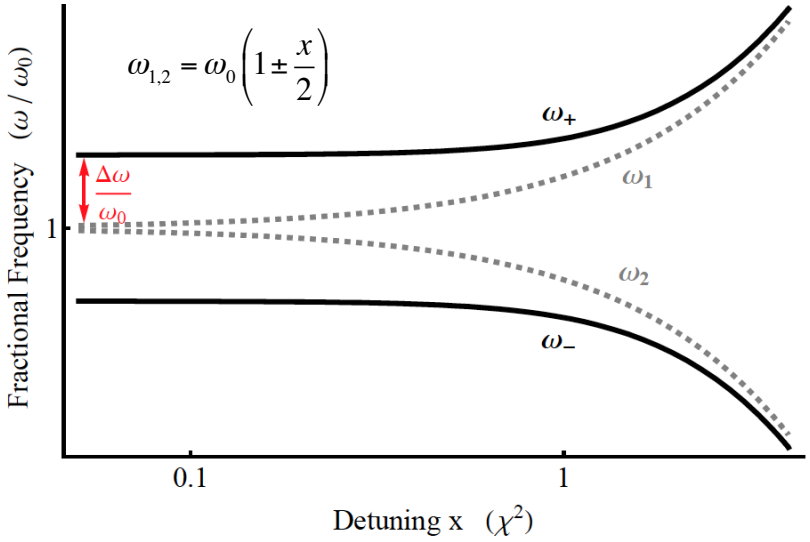

Figure 3: Log-Log plot of resonant frequencies relative to a common central frequency, ω_0, as a function of detuning for a pair of cavities that are coupled (black, full) and uncoupled (gray, dashed). The detuning, x, is given as a factor of the square of the hidden sector photon kinetic mixing parameter, χ.

3 Other work

Ongoing areas of research include new measurement techniques for microwave cavity-based axion and WISP searches and further development of hidden sector photon resonant cavity coupling and LSW experiments.

4 Acknowledgments

This work was partially funded by Australian Research Council grants DP130100205, FL0992016 and a UWA Research Collaboration Award.

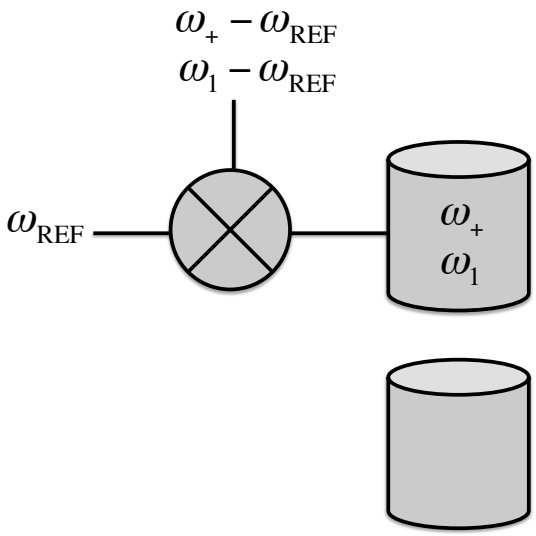

Figure 4: Sketch of experimental concept. The top cavity is compared against a stable frequency reference while the bottom cavity is used to manipulate / modulate the strength of the coupling. The resonance frequency of the top cavity will change between ω_+ and ω_1.

References

[1] S. R. Parker, J. G. Hartnett, R. G. Povey and M. E. Tobar, "Cryogenic resonant microwave cavity searches for hidden sector photons," Phys. Rev. D **88**, 112004 (2013) [arXiv:1410.5244 [hep-ex]].

[2] S. R. Parker, G. Rybka and M. E. Tobar, "Hidden sector photon coupling of resonant cavities," Phys. Rev. D **87**, 115008 (2013) [arXiv:1304.6866 [hep-ph]].

Dark Radiation from a hidden U(1)

Hendrik Vogel[1], *Javier Redondo*[1,2]

[1]Max Planck Institute for Physics, Munich, Germany
[2]Arnold Sommerfeld Center, Ludwig-Maximilians-Universität, Munich, Germany

DOI: http://dx.doi.org/10.3204/DESY-PROC-2014-XX/vogel_hendrik

We discuss the impact of a hidden sector consisting of Minicharged Particles (MCPs) and massless hidden photons on the expansion history of our Universe. We present parameter scans for the amount of extra relativistic particles ($N_{\rm eff}$) and the abundance of light nuclei for fermionic MCPs with masses between ∼100 keV and 10 GeV and minicharges in the range $10^{-11} - 1$. Current CMB and BBN data significantly constrain the available parameter space of MCPs. The shown results are a valuable indicator for future experimental searches and are presented in a flexible way so that more accurate results on $N_{\rm eff}$ can be easily interpreted.

1 Minicharged particles

Minicharged Particles (MCPs) naturally arise in extensions of the Standard Model (SM) with an additional local hidden gauge group $U(1)_{\rm h}$. The hidden photon (HP) associated with this $U(1)_{\rm h}$ does not couple to any SM particle but mixes kinetically with the SM photon

$$\mathcal{L} = -\frac{\chi}{2} F_{\mu\nu} F'^{\mu\nu},$$

where χ is the kinetic mixing parameter, $F_{\mu\nu}$ is the photon field strength tensor and $F'^{\mu\nu}$ is the field strength tensor of the HP. We assume that the $U(1)_{\rm h}$ is unbroken. Hence, the HP is massless. It would be unobservable because the mixing can be removed through a field redefinition. The kinetic mixing becomes unphysical.
The HP field has observable consequences in a minimal extension of this model with a (fermionic) field f, the hidden fermion. It is only charged under the $U(1)_{\rm h}$ with a coupling strength g'. This makes χ a physical parameter because transforming the kinetic mixing away induces an effective coupling of the hidden fermion to the SM photon with a coupling strength $g'\chi$. Since the hidden fermion couples to the SM photon, it carries an effective electric charge. It is useful to define

$$g'\chi = e\epsilon,$$

where e is the electron charge and ϵ is the minicharge. Since ϵ can be small, f is called a minicharged particle. It is fully characterized by g', ϵ and its arbitrary mass m_f.

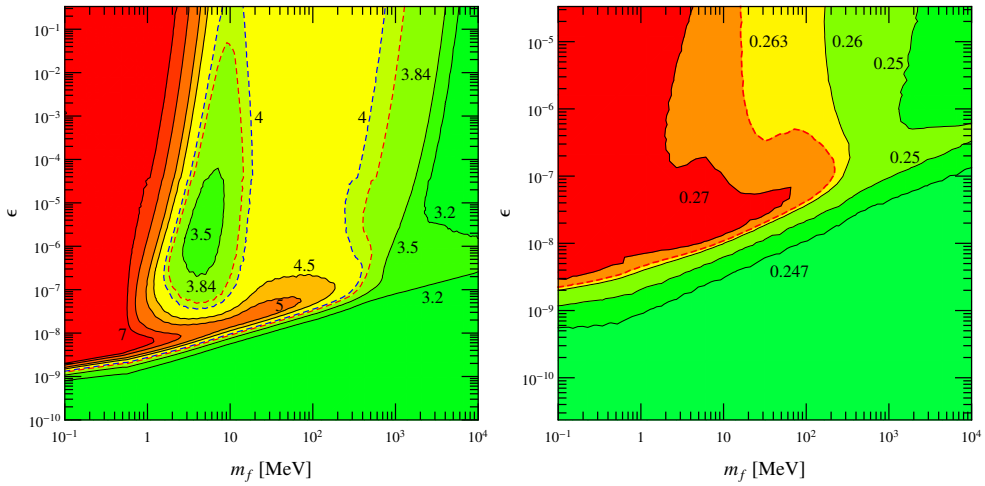

Figure 1: Isocontours of $N_{\rm eff}$ at the CMB epoch (left) and primordial Helium yield Y_p (right) as a function of m_f and ϵ, for $g' = 0.1$. Numbers correspond to the value of the closest contour line. *Left:* Dark green: $N_{\rm eff} \sim 3$, light green and yellow $N_{\rm eff} \sim 3.5 - 4.5$, Orange and red $N_{\rm eff} > 4.5$. The red dashed line shows the 95% upper exclusion limit $N_{\rm eff} = 3.84$ (Planck+WP+highL+BAO) by Planck [1]. The blue dashed line gives the best fit value $N_{\rm eff} = 4$ from a combination of BICEP2 and Planck data [2]. *Right:* Dark green coloring denotes regions far away from the upper limit $Y_p < 0.263$ [4]. The limit is given by the red dashed contour line. Orange and red regions are excluded on more than a 95% CL.

2 Impact on the CMB and BBN

Due to the small charge, HPs and MCPs will be produced in the early Universe to some extent. Both of them will then contribute to the energy density of radiation during the formation of the CMB anisotropies. The impact of light degrees of freedom on the CMB is parametrized with the effective neutrino degrees of freedom $N_{\rm eff}$. They are defined as

$$N_{\rm eff} = \frac{\rho_{\rm DR}}{\rho_{1\nu *}},$$

where $\rho_{\rm DR}$ is the energy density of dark radiation (DR), i.e. all relativistic particles that are not strongly coupled to the SM photon at the CMB epoch, $\rho_{1\nu *}$ is the energy density of one neutrino species which instantly decoupled from the electron-photon plasma before BBN. All densities are evaluated at times corresponding to the formation of the CMB anisotropies. $N_{\rm eff}$ scales like $(T_{\rm DR}/T_\gamma)^4$. It is, hence, very sensitive to temperature changes.
In the SM the three neutrinos contribute $N_{\rm eff} = 3.04$ [5] after correcting for non-instantaneous decoupling. The most precise observations to date come from the PLANCK collaboration. They set an upper limit of $N_{\rm eff} < 3.84$ at 95 % CL on the number of relativistic degrees of freedom at the CMB epoch. This value is obtained by fitting a Cosmological model to the data. The limit is conservative since it does not use the controversial value for the Hubble rate today, H_0, obtained from local astrophysical measurements. Local measurements prefer a higher value for $N_{\rm eff}$. Also the disputed result obtained by BICEP2 [6] suggests a higher value, $N_{\rm eff} = 4$ [2].

In order to compare the predictions of models with minicharged particles to the observations, we have to accurately compute the energy density of dark radiation at the CMB epoch. We numerically solve a set of Boltzmann-like equations that parametrize the energy transport between SM particles and the dark sector (DS) consisting of HPs and MCPs

$$\dot{\rho}_{\mathrm{SM}} + 3H\left(\rho_{\mathrm{SM}} + P_{\mathrm{SM}}\right) = -\mathcal{W},$$
$$\dot{\rho}_{\mathrm{DS}} + 3H\left(\rho_{\mathrm{DS}} + P_{\mathrm{DS}}\right) = \mathcal{W},$$

where ρ (P) is the energy density (pressure) of the DS and the SM particles, H is the Hubble parameter, the dot is a derivative with respect to physical time and $\mathcal{W}$ is a generalized collision term that gives the energy transported from one sector to the other.
For the computation we assume that the DS is always in thermal equilibrium with itself. It is fully characterized by a common temperature T_{DS} and m_f. Following the spirit of a dark, weakly coupled sector we initially set $T_{\mathrm{DS}} = 0$. The DS is then produced by the SM particles during the evolution of the Universe. In order to compute this thermalization as accurately as possible we include all SM particles and light mesons and all relevant processes in our computations. It turns out that for $T_{\mathrm{DS}} \ll T_\gamma$ DS particles are most efficiently produced by SM particle pair annihilation ($e\bar{e} \to f\bar{f}$). When T_{DS} approaches the SM temperature Coulomb-like scattering ($ef \to ef$), regularized by plasma screening, and (for large g') Compton-like scattering ($\gamma f \to \gamma' f$) become the most important processes.
We scan over a wide range of parameters m_f, ϵ for $g \in \{10^{-2}, 0.1, 1\}$. The constraints for $g' = 0.1$ are the most conservative. For $g = 10^{-2}$ the results are indistinguishable from the results with $g' = 0.1$ because in this case the dominant processes are $\propto e\epsilon = g'\chi$. A change in g' can be compensated by a corresponding change in χ but leaves ϵ unchanged. The bounds for $g' = 1$ are stronger because Compton-like scattering ($\gamma f \to \gamma' f$), which is $\propto g'^4\chi^2 \sim g'^2\epsilon^2$, becomes dominant for high g'. Increasing g' cannot be compensated by a shift in χ anymore if ϵ is fixed. For $g' = 1$ the DS and SM particles equilibrate faster.
Our result for $g = 0.1$ is presented in Fig. 1 (left). The sudden increase for small kinetic mixing $\epsilon \sim 10^{-8}$ corresponds to partial thermalization of the DS with the SM photon. The behavior for large ϵ can be understood analytically. The DS fully thermalizes and after decoupling its temperature at the CMB epoch is given by entropy conservation. For more details see [3].
Another primordial probe is BBN. The DS changes the formation of nuclei. The most sensitive probe is the yield of primordial helium Y_p. By adjusting the BBN code of [7], we computed Y_p using the data of our CMB simulation. The result is shown in Fig. 1 (right). We use $Y_p < 0.263$ at 95% CL [4] as a conservative upper bound.

3 Conclusions

Figure 1 shows that, using PLANCK's limit, the CMB anisotropies still allow for light minicharged particles in the range $m_f \sim 5$ MeV for a wide range of minicharges ϵ. This parameter space is, however, disfavored by the abundance of primordial helium. Using these two results we set a lower limit on the hidden fermion mass of $m_f \gtrsim 390$ MeV for $\epsilon > 10^{-7}$. A compilation of this result with earlier approaches using astrophysics, Cosmology or laboratory experiments is shown in Fig. 2.
If BICEP2 has observed primordial gravitational waves, the limit on MCPs from the CMB anisotropies vanishes and BBN gives the most stringent bounds. Further research is needed to clarify the role of BICEP's observations. Since the question of the existence of additional light

degrees of freedom cannot be settled with the current data, we present our results in a flexible way. Future more accurate values of $N_{\rm eff}$ are to be expected. Using the predicted accuracy of CMBPol [8], PLANCK's current mean value $N_{\rm eff} = 3.30$ [1] could be detected at $\sim 5\sigma$.

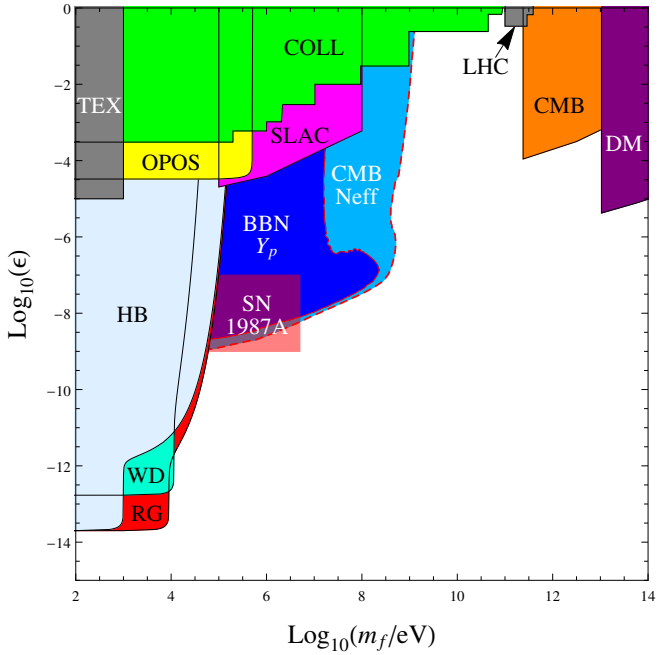

Figure 2: Exclusion plot for MCPs from various experiments and observations. The constraint from the amount of helium Y_p produced during BBN (dark blue) and from light extra degrees of freedom $N_{\rm eff}$ by Planck (light blue) described here have been obtained in [3].

References

[1] P.A.R. Ade *et al.*, "Planck 2013 results. XVI. Cosmological parameters", Astron. Astrophys. 2014 [arXiv:1303.5076 [astro-ph.CO]].

[2] E. Giusarma *et al.*, "Relic Neutrinos, thermal axions and cosmology in early 2014", Phys. Rev. D90 043507 (2014), [arXiv:1403.4852 [astro-ph.CO]]

[3] H. Vogel and J. Redondo, "Dark Radiation constraints on minicharged particles in models with a hidden photon", JCAP 1402 029 (2014), [arXiv:1311.2600 [hep-ph]]

[4] G. Mangano and P. Serpico, "A robust upper limit on $N_{\rm eff}$ from BBN, circa 2011", Phys.Lett. B701 296-299 (2011), [arXiv:1103.1261 [astro-ph.CO]]

[5] G. Mangano, G. Miele, S. Pastor and M. Peloso, "A Precision calculation of the effective number of cosmological neutrinos", Phys.Lett. B534 8-16 (2002), [arXiv:astro-ph/0111408]

[6] P.A.R. Ade *et al.*, Detection of B-Mode Polarization at Degree Angular Scales by BICEP2, Phys.Rev.Lett. 112 241101 (2014), [arXiv:1403.3985 [astro-ph.CO]]

[7] D. Cadamuro and J. Redondo, "Cosmological bounds on pseudo Nambu-Goldstone bosons", JCAP (1202), [arXiv:1110.2895]

[8] S. Galli *et al.*, "Constraining Fundamental Physics with Future CMB Experiments" Phys.Rev. D82 123504 (2010), [arXiv:1005.3808 [astro-ph.CO]]

List of Authors

List of Participants

Albuquerque, Ivone – University of So Paulo
Andreas, Sarah – Institut Astrophysique de Paris
Antoniadis, Ignatios – CERN
Arbey, Alexandre – CERN
Arias, Paola – Pontificia Universidad Catolica de Chile
Arvanitaki, Asimina – Perimeter Institute For Theoretical Physics
Bailey, Ian – Lancaster University
Baker, Oliver – Yale University
Balakin, Alexander – Kazan Federal University
Balazs, Csaba – Monash University
Ballou, Rafik – CNRS - Institut Nel
Basak, Tanushree – PHYSICAL RESEARCH LABORATORY
Baudis, Laura – University of Zurich
Baum, Sebastian – Uppsala Universitet
Betz, Michael – CERN
Boyarsky, Alexey – Leiden University
Burrage, Clare – University of Nottingham
Cantatore, Giovanni – Universita' e INFN - Trieste
Chowdhury, Partha – University of Calcutta
Chung, WooHyun – Institute for Basic Science
Coderre, Daniel – LHEP, Uni Bern
Conlon, Joseph – Oxford University
Covi, Laura – Institute for theoretical Physics
Cui, Xingzhu – Institute of high energy physics,CAS
Dagnolo, Raffaele Tito – IAS Princeton
Davenport, Martyn – CERN
Davidson, Sacha – IPNL
Decowski, Patrick – Nikhef amp; GRAPPA / University of Amsterdam
Derbin, Alexander – St. Petersburg Nuclear Physics Institute
Di Stefano, Philippe – Queen's University
Dias, Alex Federal – University of ABC
Dreyling-Eschweiler, Jan – DESY
Dbrich, Babette – DESY
Fradette, Anthony – University of Victoria
Galloway, Michelle – University of Zürich
Garcia Irastorza, Igor – Universidad de Zaragoza
Gavela , Belen – UAM (Madrid) and IFT
Giannotti, Maurizio – Barry University
Giomataris, Ioanis – CEA/IRFU,Centre d'etude de Saclay Gif-sur-Yvette
Gondolo, Paolo – University of Utah
Guendelman, Eduardo – Ben Gurion University
Guigue, Mathieu – LPSC

Hatzikoutelis, Athanasios – University of Tennessee
Henning, Reyco – University of North Carolina at Chapel Hill
Hong, Jooyoo – Hanyang University at Ansan
Horns, Dieter – Universitaet Hamburg
Hosek, Jiri – Nuclear Physics Institute, ASCR
Hugle, Thomas – Institute for Theoretical Physics
Ichimura, Koichi – Institute for Cosmic Ray Research, University of Tokyo
Jacques, Thomas – Universite de Geneve
Jaeckel, Joerg – ITP Heidelberg
Januschek, Friederike – DESY
Kahlhoefer, Felix – University of Oxford
Katori, Teppei – Queen Mary University of London
Keum, Yong-Yeon – IBS/Seoul National University
Kilminster, Ben – University of Zürich
Kim, Jihn E. – Kyung Hee University
Kiritsis, Elias – University of Crete and CERN and APC
Kossert, Karsten – Physikalisch-Technische Bundesanstal
Kozlov, Valentin – Karlsruhe Institute of Technology
Kreslo, Igor – LHEP, Uni-Bern
Krieger, Christoph – University of Bonn
Krmer, Michael – RWTH Aachen University
Kunc, Stepan – Technical university of Liberec
Lagouri, Theodota – Yale
Lindner, Axel – DESY
Lobanov, Andrei – MPIfR Bonn / Uni. Hamburg
Machado, Ana – IFT-UNESP
Mantry, Sonny – Northwester University and Argonne National Laboratory
Mao, Yi – Institut d'Astrophysique de Paris
Maroudas, Marios – University of Patras
Masso Soler, Eduard – Universitat Autnoma de Barcelona
Merlo, Luca – UAM-IFT
Messineo, Giuseppe – University of Ferrara and INFN-Ferrara
Meyer, Manuel – Oskar Klein Centre, Stockholm University
Miceli, Lino – IBS
Mohanmurthy, Prajwal – Massachusetts Institute of Technology
Montaruli, Teresa – University of Geneva
Muratova, Valentina – St. Petersburg Nuclear Physics Institute
Nesvizhevsky, Valery – Institut Max von Laue - Paul Langevin
Nicolaidis, Argyris – Theoretical Physics Department
Ni, Kaixuan – Shanghai Jiao Tong University
Ortolan, Antonello – INFN-National Labs of Legnaro
Ostrovskiy, Igor – Stanford University
Parker, Stephen – The University of Western Australia
Payez, Alexandre – DESY
Pinfold, James – University of Alberta
Priel, Nadav – Weizmann Institute of Science
Pugnat, Pierre – CNRS/LNCMI
Read, Justin – University of Surrey
Riffard, Quentin – LPSC/CNRS

Ringwald, Andreas – DESY
Rosenberg, Leslie – University of Washington
Rybka, Gray – University of Washington
Saikawa, Ken'ichi – Tokyo Institute of Technology
Saldanha, Richard – University of Chicago
Santos, Daniel – Laboratoire de Physique Subatomique et de Cosmologie
Schulz, Oliver – MPI for Physics, Munich
Schumann, Marc – Albert Einstein Center for Fundamental Physics, University of Bern
Semertzidis, Yannis – KAIST and CAPP/IBS
Speake, Clive – University of Birmingham
Spooner, Neil – University of Sheffield
Strauss, Raimund – Max Planck Institut München
Sulc, Miroslav – Technical University of Liberec
Tapia Oregui, Beatriz – ITP University Heidelberg
Tihinen, Ulla – CERN
Tobar, Michael – The University of Western Australia
Tripathi, Mani – UC Davis
Troitsky, Sergey – INR
Tsesmelis, Emmanuel – CERN and University of Oxford
Ugo, Gastaldi – INFN-Ferrara
V. Sivers, Moritz – Technische Universität München
Vafeiadis, Theodoros – CERN
Verma, Murli – Lucknow University
Villalba Chavez, Selym – Heinrich-Heine University of Dsseldorf
Vogel, Hendrik – Max Planck Institute for Physics
Wang, Huanyu – Institute of High Energy Physics,CAS
Wester, William – Fermilab
Woollett, Nathan – Lancaster University
Zaharijas, Gabrijela – ICTP and INFN
Zayats, Alexey – Kazan Federal University
Zioutas, Konstantin – University of Patras

122 participants

Faces & Places

ASTROPARTICLE PHYSICS

CERN hosts Patras Workshop on Axions, WIMPs and WISPs

The Patras Workshop returned to CERN in July for its 10th anniversary, having begun there in 2005. The initial aim was to provide academic training to the new generations of scientists working within the EU's Integrated Large Infrastructure for Astroparticle Science network, which covered the already mature field of astroparticle physics (*CERN Courier* July/August 2006 p19). Following increasing worldwide interest in the workshop, the organizers widened its agenda, inspired by the possibilities that are opening up in ongoing searches for exotica such as axions, WIMPs, etc. Results from direct and indirect searches for axion-like particles (ALPs), also dubbed weakly interacting slim (light) particles (WISPs), and new, more sensitive searches for electric-dipole moments, were also covered in the latest workshop. Participants from more than 40 institutions around the world had the opportunity to present their latest results and discuss detector-upgrade plans and exciting new ideas for future research. As a result of the high number of participants, the programme also included a poster session for the first time.

Speakers covered diverse new approaches in dark-matter, dark-energy and neutrino physics, including astrophysical observations, as well as novel ideas for detection using state-of-the-art instrumentation. In his opening address, CERN's director-general, Rolf Heuer, emphasized that following the discovery of a Higgs boson, there remain big questions related to the hidden side of the universe. The talks that followed demonstrated the breadth in experimental searches for constituents of dark matter and dark energy, from direct searches for WIMPs in underground experiments with the lowest noise, axion or WISP searches with cavity and "light-shining-through-a-wall" experiments, and not-so-indirect searches in specific solar or cosmic observations with orbiting equipment, to searches at the LHC. Hidden photons and gauge bosons of various kinds are also being searched for with accelerators and solar observations. Theories span an even greater breadth, as manifest in the mass range of the expected exotica.

The Patras programme traditionally features results, theoretical ideas and exciting projects beyond the main focus of the meeting. This time, participants heard about the latest results from space X-ray missions, the Indian SOXs and the Chinese Chang 'E1. Data from both missions are being re-analysed to search for overlooked signatures of dark-matter or dark-energy constituents in their solar X-ray observations.

Upgrade plans were also presented at the workshop. The performance of experimental techniques – either in use or suggested – to unravel the nature of the enigmatic dark sector is advancing impressively, with a remarkable overlap between LHC physics and astroparticle physics. The state-of-the-art equipment used faces two extreme situations: the LHC experiments have to deal with unprecedented high background rates, while the dark-matter/dark-energy searches with the lowest signal levels require ever increasing background screening. Here, equipment developed for high-energy physics and other disciplines finds an increasing number of applications in astroparticle physics. Micromegas detectors, powerful magnets and high-sensitivity antennae in the sub-electron-volt range, for example, are typical of the interdisciplinary character of many experiments that are being upgraded or are in the conceptual-design phase.

In the spirit of the workshop series, discussions were lively and the atmosphere friendly, although occasionally not without scientific controversy. A number of new ideas were presented, mostly highly interdisciplinary in character, profiting from the strong synergies developed between theory and experiment. By bringing together experts working on so many diverse topics, the workshop continues to contribute to the ongoing scientific revolution in astroparticle physics to uncover the unknown universe.

● For more information, visit http://axion-wimp2014.desy.de/.